2009

Optical Properties of Nanostructures and Applications to Surface-Enhanced Spectroscopy

Daniel Ross
University of Windsor

Follow this and additional works at: https://scholar.uwindsor.ca/etd

OPTICAL PROPERTIES OF NANOSTRUCTURES AND APPLICATIONS TO

SURFACE-ENHANCED SPECTROSCOPY

BY

DANIEL JOSEPH ROSS

A Dissertation

Submitted to the Faculty of Graduate Studies through the

Department of Physics in Partial Fulfillment of the

Requirements for the Degree of Doctor of Philosophy at

The University of Windsor

Windsor, Ontario, Canada

2009

Optical Properties of Nanostructures and Applications to Surface Enhanced
Spectroscopy.

By

Daniel Joseph Ross

APPROVED BY

_____
Dr. Cecilia Noguez, External Examiner
Instituto de Fısica, UniVersidad Nacional Autonoma de Mexico,

_____
Dr. S. Holger Eichorn
Department of Chemistry and Biochemistry

_____
Dr. Chitra Rangan
Department of Physics

_____
Dr. Roman Maev
Department of Physics

_____
Dr. Ricardo Aroca, Advisor
Department of Chemistry and Biochemistry

_____
Dr. Jichang Wang
Chair of Defence

DECLARATION OF CO-AUTHORSHIP

I hereby declare that this dissertation incorporates material that is result of joint research, as follows:

This dissertation incorporates the outcome of joint research undertaken with Mathew Halls, under the supervision of Ricardo Aroca and Gholam Abbas Nazri of GM Research laboratories. The results of this collaboration are detailed in Chapter 8, section B of this dissertation. In this case the primary contributions, data analysis, and interpretation were all performed by the author. Contribution of Mathew Halls was primarily through advice on use of high level computational tools in cluster based research, while Gholam Abbas Nazri provided the materials, as well as details and expertise on synthesis.

This dissertation also includes the outcome of joint research undertaken with Dr. R. E. Clavijo of the University of Chile. The results of this collaboration are detailed in chapter 8, section C. In this case, the experimental Raman, SERS, and infrared spectra were obtained by Dr. Clavijo, who granted permission for their use.

I am aware of the University of Windsor Senate Policy on Authorship and I certify that I have properly acknowledged the contribution of other researchers to my thesis, and have obtained written permission from each of the co-author(s) to include the above material(s) in my thesis.

I certify that, with the above qualification, this thesis, and the research to which it refers, is the product of my own work.

DECLARATION OF PREVIOUS PUBLICATION

This thesis includes 2 original papers that have been previously published/submitted for publication in peer reviewed journals, as follows:

Thesis Chapter	Publication title/full citation	Publication status
Chapter 8, section C	Surface Enhanced Raman Scattering of trans-p-Coumaric and Syringic Acids	Accepted
Chapter 8, Section B	Raman scattering of complex sodium aluminum hydride for hydrogen storage/Daniel J Ross, Mathew D Halls, Abbas G Nazri and Ricardo F Aroca, Chemical Physics Letters, **388**, 430, 2004	Published
Chapter 7	Surface enhanced infrared spectroscopy /R.F. Aroca, D. Ross, and C. Domingo, Applied Spectroscopy, **58,** 324-338A., 2004.	Published

I certify that I have obtained a written permission from the copyright owner(s) to include the above published material(s) in my thesis. I certify that the above material describes work completed during my registration as graduate student at the University of Windsor.

I declare that, to the best of my knowledge, my thesis does not infringe upon anyone's copyright nor violate any proprietary rights and that any ideas, techniques, quotations, or any other material from the work of other people included in my thesis, published or otherwise, are fully acknowledged in accordance with the standard referencing practices. Furthermore, to the extent that I have included copyrighted material that surpasses the bounds of fair dealing within the meaning of the Canada Copyright Act, I certify that I have obtained a written permission from the copyright owner(s) to include such material(s) in my thesis.

I declare that this is a true copy of my thesis, including any final revisions, as approved by my thesis committee and the Graduate Studies office, and that this thesis has not been submitted for a higher degree to any other University or Institution.

ABSTRACT

Metallic nanoparticles, in particular silver and gold nanostructures, are at the centre of the development of plasmon enhanced optical signals. There is a flurry of activities in the fabrication and testing of these nanostructures, especially in surface enhanced Raman scattering (SERS) and surface enhanced-infrared absorption (SEIRA), the two branches of surface-enhanced vibrational spectroscopy. The need to develop an understanding of this general subject matter for practicing spectroscopists cannot be questioned. This work is a unique undertaking intended to examine some of the elements that give rise to surface-enhanced spectroscopy.

The optical properties of nanoparticles are discussed in detail, beginning with a discussion of the electromagnetic theory describing the interaction of light and matter. Exact solutions to the electromagnetic equations are used to model and calculate plasmonics of nanoparticles. These methods include Mie theory, and extensions to Mie such as for concentric spheres and interacting spheres. Approximate methods are also discussed, such as the dipolar model for ellipsoids of rotation, and the coupled dipole equations for irregular or interacting particles. These models are used to obtain optical properties as well as enhanced electromagnetic fields, applied to surface enhanced vibrational spectroscopy. The origin of vibrational spectroscopy is briefly described, and quantum mechanical calculations are performed to describe a variety of the molecular possibilities arising through surface enhanced spectroscopy, such as aggregation, chemical adsorption, and surface selection rules.

DEDICATION

To my wife, Reagan

ACKNOWLEDGEMENTS

TABLE OF CONTENTS

LIST OF TABLES

LIST OF FIGURES

LIST OF APPENDICIES

LIST OF SYMBOLS, ABBREVIATIONS, AND NOMENCLATURE

AFM: Atomic Force Microscopy

LSPR: Localized Surface Plasmon Resonance

RRS: Resonance Raman Scattering

RS: Raman Scattering

SAW: Self Avoiding Walk

SEF: Surface Enhanced Fluoresence

SEIRA: Surface Enhanced Infrared Absorption

SERRS: Surface Enhanced Resonance Raman Scattering

SERS: Surface Enhanced Raman Scattering

STM: Scanning Tunnelling Microscopy

CHAPTER ONE

INTRODUCTION

A. Plasmonics and Optical Properties of Nanoparticles

The following dissertation may best be understood to be part of the field of plasmonics. Plasmonics is the study of the electronic oscillation, or plasmon, which is created by the interaction of light with a nanostructured material.[1] It is the optical response of noble metals, dominated by the behavior of their conduction electrons, which can produce collective oscillations of the electrons, or, plasmon. The interaction between electromagnetic radiation (from infrared to the ultraviolet) and a metal surface may lead to surface plasmon excitation, as this interaction creates electronic plasma oscillations on the surface of the metal. When speaking of a plasmon, it is necessary to differentiate whether the collective excitation of electrons of the metal is contained *within* the metal or is a *surface* excitation.

Should the excitation be found within the metal (e.g., bulk plasmons), the oscillations due to fluctuations in the electronic density of the metal are longitudinal[2-4]. In this case, the condition for plasmon formation is that the real part of the dielectric function is zero, which is only true at a specific frequency of light. This frequency is termed the plasma frequency, and, in practice, is very distinctive among different materials. For metallic surfaces, however, there exists a surface plasmon with an amplitude that dies off quickly away from the surface. This surface excitation is a coupling of the incident photons with the oscillation of the conduction electrons and it polarizes the surface. The surface plasmon is often thus referred to as the surface plasmon-polariton, clearly indicating that this excitation is a coupling of the light and a material. This concept is shown in Figure 1.1, which is an idealized image of the charge, and the decay of the electric field away from the surface.
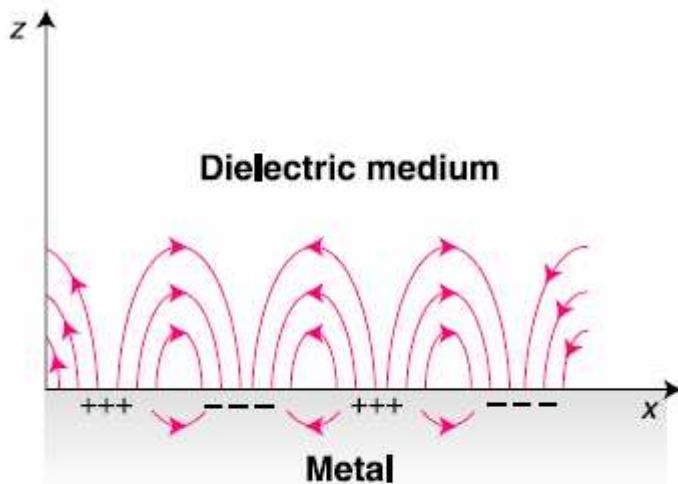
Figure 1.1 Illustration of surface charge and electric field in a surface plasmon.

The electromagnetic field of a surface plasmon at the metal/dielectric interface is the evanescent solution of Maxwell's equations, applying the correct continuity conditions at the surface. This work deals with the surface plasmons in a specific size regime: that of metal nanoparticles. These excitations depend strongly on both the size and shape of the particle or particles involved, and thus are very different from the surface plasmon created in a flat surface. These are often termed localized surface plasmons, or localized surface plasmon resonances (LSPR), as they are confined to nanometric particles, leading to resonances that depend on the size, shape, and dielectric function of the material that the particle is made up of. Discussing the solution of Maxwell's equations for this problem will be one of the main subjects of this work.

Although plasmonics is a relatively new field, (the term was first appeared in the literature in 2001)[5] , the study of plasmons has had a much longer history. For example, the use of colloidal gold and silver particles in the Lycurgus cup give it unique optical properties[6]. These gold and silver particles, as will be shown in detail later (See chapter 2, p.18) absorb and scatter light primarily in the shorter wavelengths of the visible region. When viewed using reflected light, the cup is a green colour. When lit from inside, however, the gold and silver particles embedded in the glass matrix allow only the red light to transmited[7]. Another

2

historic application for the scattering of light by metal particles is seen in the windows of temples, churches, and other buildings, as well as in other forms of stained glass artwork. The bright colours of the stained glass are due to metallic nanoparticles, the specific colour depending on the size and material of the particle.

The first systematic understanding of the phenomenon that would later develop into the field of plasmonics was through Mie's solution to Maxwell's equations for a dielectric sphere[8]. The exact solution of the interaction of light with a spherical body was now understood, given that the optical properties of the specific material were known. In addition to colloidal metal particles, Mie's solution applies to a wide variety of problems [9]: atmospheric dust, interstellar particles, solar coronas, scattering by raindrops[10], and others. The theory of electromagnetic absorption and scattering by small particles, as well as applications and computational techniques has been summarized by Kerker[11] and Bohren and Huffman[10].

Given the wide variety of techniques to fabricate nanoparticles, there are a plethora of possible shapes and sizes, even for the two most common materials, silver and gold. Although spheres are probably the most common (due to the relative ease of synthesis through colloidal suspensions of gold and silver) some of the geometrically simple, yet interesting shapes include nanoshells[12-15], ellipsoids of revolution[16], triangles[17], cubes[18], and hexagons[19]. These latter shapes make up a fairly small sample that reveals possibility of modifying the nanoparticle shape. Fortunately, this modification of shape allows for control over the resonance wavelength, amplitude, and bandwidth. Another important development is that of interacting particles, such as dimers of spheres and shells[20], and of triangles[17], forming nano 'bow-ties'. The problem of two interacting particles is one of the few that can be treated exactly, or at least approximated well, while still having some of the essential features of a system of particles.

The confinement of electromagnetic field to the particle gives the surface plasmon an extraordinary sensitivity to surface features. This sensitivity is widely

used for studying adsorption on the surface, as well as surface roughness and related phenomena. Devices based on the surface plasmon are used in chemical and biological sensors[21]. The enhancement of the electromagnetic field at the interface is responsible for phenomena such as optical amplification surface: the intensification of the surfaces by Raman scattering (SERS), where it is possible to detect a single molecule; second harmonic generation; fluorescence, and so on. In addition, the two-dimensional nature of the surface plasmon makes it particularly interesting in building plasmon circuits, where the information is transmitted through a surface plasmon, with potential applications in optical computing. The fabrication, manipulation, and characterization of nanometric surfaces has recently become relatively easier, thanks to developments in techniques such as high resolution electron microscopy, AFM, and STM, allowing for novel opportunities in optoelectronics and photonic devices, with length scales much smaller than traditional electronic or optical methods, down to the scale of nanometers. As a result of these developments, as well as increasing knowledge of other characteristics of surface plasmon, there is now more interest in new technologies, as well as in the study of new physical phenomena in which plasmons play a leading role. Taken together, this interest has lead the the field known as plasmonics.

B. Definition of The Optical Constants

The optical constants arise from Maxwell's equation with a time harmonic field. Starting from the derivative form[22]:

$$\nabla \cdot \mathbf{D} = \rho \tag{1.1}$$

$$\nabla \cdot \mathbf{B} = 0 \tag{1.2}$$

$$\nabla \times \mathbf{H} - \mathbf{J} - \frac{\partial \mathbf{D}}{\partial t} = 0 \tag{1.3}$$

$$\nabla \times \mathbf{E} + \frac{\partial \mathbf{B}}{\partial t} = 0 \tag{1.4}$$

In general, the macroscopic manifestation of the fields, **D** and **H**, called the electric displacement and magnetic field, respectively, depend on the electric or magnetic polarization of the medium, **P** and **M**. Assuming that the contribution of the quadrupole and higher moments to the polarization are small compared to the dipole, and can be neglected, these are:

$$\mathbf{D} = \varepsilon_0 \mathbf{E} + \mathbf{P} \tag{1.5}$$

$$\mathbf{H} = \frac{\mathbf{B}}{\mu_0} - \mathbf{M} \tag{1.6}$$

For a proof of the above, please refer to Jackson, Classical Electrodynamics, chapter 6, section 6.[22]

In any media besides vacuum, constitutive relations are used to describe the fields. Assuming linear, isotropic, and homogeneous media, the derived fields **D** and **H** can take simple forms. The linearity implies that an electric or magnetic field induces a polarization proportional to the field. For the sake of consistency, the permittivity will be symbolized by $\hat{\varepsilon}$, rather than ε, which will be reserved for the relative permittivity, or the dielectric function.

$$\mathbf{D} = \hat{\varepsilon}\mathbf{E} \tag{1.7}$$

$$\mathbf{B} = \mu\mathbf{H} \tag{1.8}$$

Finally, Ohm's law is used to describe the flow of current in the medium.

$$\mathbf{J} = \sigma\mathbf{E} \tag{1.9}$$

Although the above restrictions to the medium seem stringent, they are applicable to a large class[10]; however, they are not appropriate for ferroelectric or ferromagnetic materials, or when the applied fields are very high.

Optical properties and spectroscopic studies necessarily use oscillating fields. A harmonic oscillating field can be used without loss of generality, as different oscillating fields can be produced by superposition. It is also advantageous at this time to introduce complex notation. The complex time-harmonic field, F is expressed as

$$\mathbf{F}(t) = \mathbf{F}_C e^{-i\omega t} \tag{1.10}$$

where

$$\mathbf{F}_C = \mathbf{F}_{Re} + i\mathbf{F}_{Im} \tag{1.11}$$

The partial derivative of the complex time-harmonic field is then:

$$\frac{\partial \mathbf{F}(t)}{\partial t} = \frac{\partial}{\partial t}\left(\mathbf{F}_{Re}e^{-i\omega t} + i\mathbf{F}_{Im}e^{-i\omega t}\right) = -i\omega\mathbf{F}_{Re}e^{-i\omega t} + \omega\mathbf{F}_{Im}e^{-i\omega t} = -i\omega\mathbf{F}(t) \tag{1.12}$$

Thus, evaluating the partial derivatives with respect to time, and inserting the constitutive relations 1.7-1.9, equations 1.1-1.4 can be re-written as:

$$\nabla \cdot \mathbf{E} = \frac{\rho}{\hat{\varepsilon}} \tag{1.13}$$

$$\nabla \cdot \mathbf{H} = 0 \tag{1.14}$$

$$\nabla \times \mathbf{H} - \sigma\mathbf{E} + i\omega\hat{\varepsilon}\mathbf{E} = 0 \tag{1.15}$$

$$\nabla \times \mathbf{E} - i\mu\omega\mathbf{H} = 0 \tag{1.16}$$

The permittivity can now be seen to be a complex number. Although the permeability will also in general be complex, the majority of this work focuses on the electric part, and the magnetic properties will not be treated. Factoring the electric field in equation 1.15, which is possible as the medium is assumed to be isotropic, yields:

$$\nabla \times \mathbf{H} = \mathbf{E}(\sigma - i\omega\widehat{\varepsilon}) = -i\omega\mathbf{E}\left(\frac{i\sigma}{\omega} + \widehat{\varepsilon}\right)$$

(1.17)

The complex permittivity is then:

$$\widehat{\varepsilon}_C = \widehat{\varepsilon} + \frac{i\sigma}{\omega}$$

(1.18)

Although the assumption of time-harmonic fields has been made, there is not yet any indication of how the electromagnetic fields extend in space. Only certain fields will satisfy Maxell's equations, 1.13-1.16. To form a solution, the curl of equations 1.17 and 1.16 is taken:

$$\nabla \times (\nabla \times \mathbf{H}) + i\widehat{\varepsilon}_C \omega \nabla \times \mathbf{E} = 0$$

(1.19)

$$\nabla \times (\nabla \times \mathbf{E}) - i\mu\omega(\nabla \times \mathbf{H}) = 0$$

(1.20)

Using the triple product

$$\nabla \times (\nabla \times a) = \nabla(\nabla \cdot a) - \nabla^2 a$$

(1.21)

and inserting equations 1.13 and 1.14:

$$-\nabla^2 \mathbf{H} + i\omega\widehat{\varepsilon}_C \nabla \times \mathbf{E} = 0$$

(1.22)

$$\nabla\left(\frac{\rho}{\widehat{\varepsilon}}\right) - \nabla^2 \mathbf{E} - i\mu\omega(\nabla \times \mathbf{H}) = 0$$

(1.23)

Equation 1.23 requires some comment at this point. Many texts assume that no free charges are present, giving divergence free equations. This is not completely necessary for this analysis, as the form of the permittivity used here comes with the assumptions of the medium being both homogeneous and isotropic. Therefore, both the free charge density and the permittivity of the system are divergence free, causing the first term in equation 1.23 to be zero. It is not required that no free charges exist: rather, only that they are divergence-free.

Substituting 1.16 and 1.17 back into 1.22 and 1.23, and simplifying gives

$$\nabla^2 \mathbf{H} + \mu\omega^2 \widehat{\varepsilon}_C \mathbf{H} = 0$$

(1.24)

$$\nabla^2 \mathbf{E} + \mu\omega^2 \widehat{\varepsilon}_C \mathbf{E} = 0$$

(1.25)

which are the wave equations.

A possible solution is a plane wave traveling in the x direction. Similar to time-harmonic fields, however, many complicated fields, including those such as pulsed fields, can be represented by a superposition of plane waves:

$$\mathbf{F}(t) = \mathbf{F}_C e^{(i\mathbf{k}\cdot\mathbf{x} - i\omega t)}$$

(1.26)

where k is the wavevector, and x is the direction of travel, and F represents either the electric or magnetic field. Inserting the general plane wave solution into equation 1.25 (the magnetic field equations will yield a symmetric result) gives:

$$-k^2\mathbf{E}(\mathbf{x},t) + \mu\omega^2\hat{\varepsilon}_C\mathbf{E}(\mathbf{x},t) = 0$$

(1.27)

Solving for k:

$$k = \sqrt{\mu\hat{\varepsilon}_C}\,\omega$$

(1.28)

It is clear that with a complex permittivity, the wavevector is also complex. The phase velocity of the wave is defined for non-magnetic materials as:[22]

$$v = \frac{\omega}{k} = \frac{1}{\sqrt{\mu\hat{\varepsilon}_c}} = \frac{c}{n}$$

$$n = \sqrt{\frac{\hat{\varepsilon}_c}{\varepsilon_0}}$$

(1.29)

where c is the speed of light, and n the index of refraction of material, which is also in generally complex. As well, it is common to see the dielectric function, often labelled the dielectric constant for regions where it is insensitive to frequency, defined as:

$$\varepsilon = n^2 = \frac{\hat{\varepsilon}_c}{\varepsilon_0}$$

(1.30)

The complex index of refraction and the dielectric function are referred to as the optical properties of the materials. Their definition comes from Maxwell's equations, and are thus considered macroscopic parameters to describe the objects in question. When using classical electrodynamics to solve a problem, however, these macroscopic values are quite appropriate.

So there are two sets of optical constants which are generally used side by side, although it is important to note that they are not independent. The complex forms of these optical constants are defined as

8

$$n = n'+ik$$
$$\varepsilon = \varepsilon'+i\varepsilon'' \tag{1.31}$$

where the complex dielectric function ε is related to the complex index of refraction n by

$$\varepsilon = n^2 = \left(n'\right)^2 + 2in'k - k^2 \tag{1.32}$$

and n can be recovered by taking the real and imaginary parts of the dielectric function, although care should be taken near the region of the branch cut of square root function, which lies along the line ε''=0 while ε'<0.

Understanding the dielectric function is best achieved through the use of a model, in this case a classical model of the dielectric function that is appropriate for both metals and molecules, the Lorentz model. This follows the damped and driven harmonic oscillator quite closely, although the model phrases the problem in terms of electrodynamics rather than classical mechanics. An oscillator of mass m, and charge q has three forces acting on it: a restoring spring force k**x**, where k is the spring constant, and **x** the displacement from equilibrium, a damping force γ**v**, where γ is the damping constant, and **v** the velocity, and a driving force produced by the local electric field **E**. The equation of motion is then

$$m\ddot{\mathbf{x}} + \gamma\dot{\mathbf{x}} + k\mathbf{x} = q\mathbf{E} , \tag{1.33}$$

There are two parts to the solution of equation 1.33, the first being a transient part which dies away quickly due to the damping. The oscillatory solution, which oscillates at the same frequency as **E** is similar to those derived in classical mechanics[23]

$$\mathbf{x} = \frac{\dfrac{q}{m}\mathbf{E}}{\omega_0^2 - \omega^2 - i\Gamma\omega}$$
$$\omega_0^2 = \frac{k}{m} \tag{1.34}$$
$$\Gamma = \frac{\gamma}{m}$$

Although the usual method is to derive the amplitude and phase angles in this case, it is more useful to use this solution to derive the macroscopic optical

constants[10]. The dipole moment that is induced by this oscillator is **p**=q**x**. If there are N oscillators per unit volume, the electric polarization **P,** the number of dipoles per unit volume, appearing in equation 1.5 is

$$\mathbf{P} = N\mathbf{p} = Nq\mathbf{x} = \frac{\omega_p^2}{\omega_0^2 - \omega^2 - i\Gamma\omega}\varepsilon_0\mathbf{E}$$
$$\omega_p^2 = \frac{Nq^2}{m\varepsilon_0}$$

(1.35)

This specific example of the polarization can be put into equation 1.5 to obtain

$$\mathbf{D} = \varepsilon_0\mathbf{E} + \frac{\omega_p^2}{\omega_0^2 - \omega^2 - i\Gamma\omega}\varepsilon_0\mathbf{E} = \left(1 + \frac{\omega_p^2}{\omega_0^2 - \omega^2 - i\Gamma\omega}\right)\varepsilon_0\mathbf{E}$$

(1.36)

When this is compared to equation 1.7, the permittivity is apparent, and thus the relative permittivity, or the dielectric function can be written as

$$\varepsilon = 1 + \frac{\omega_p^2}{\omega_0^2 - \omega^2 - i\Gamma\omega}$$

(1.37)

While the Lorentz model is an idealized model, it has utility from the generality. The charge carriers may be electrons or nuclei, or entire atoms, depending on what the physical system is.

The Drude model is a further approximation to the Lorentz model, by assuming that electrons in metals are near the Fermi level can be excited by very small amounts of energy, making them essentially free. The electrons are now the oscillators, and as they are free, the restoring force in the Lorentz oscillator is zero, causing the resonance frequency ω_0 also to be zero. In the Drude model the dielectric function is then

$$\varepsilon = 1 - \frac{\omega_p^2}{\omega^2 + i\Gamma\omega}$$

(1.38)

The Drude model demonstrates when bulk plasmon formation is possible, when the dielectric function goes to zero, which occurs when

$$\omega^2 + i\Gamma\omega - \omega_p^2 = 0$$
$$\omega = \frac{-i\Gamma \pm \sqrt{-\Gamma^2 + 4\omega_p^2}}{2}$$

(1.39)

Assuming that the damping is much smaller than the plasma frequency, the plasmon condition is $\omega = \omega_p + \dfrac{-i\Gamma}{2}$, where the sign uncertainty is dropped as the negative branch of the plasma frequency, will give a negative frequency. The bulk plasmon is thus a well defined entity, an oscillation of electrons with a lifetime defined by Γ. Localized surface plasmons are not quite so neatly captured, but an understanding of the Drude model is a valuable tool to understanding plasmonics.

Although it is possible to look up plasma frequencies ω_p and damping constants for most materials, and thus generate optical properties of metals from the Drude model, the model ignores many aspects, such as anisotropy, interband transitions, and differences between free and bound electrons. Tabulated values are available for many materials, and these give more realistic results than the Drude and Lorentz models.

With the complex definition of the optical constants, we have seen the generation of a new field in the study of optical properties of materials. As the permittivity is frequency dependent, it is important to remember that the square root of a complex number contains a branch cut along the negative part of the real axis, meaning that the principle square root will be discontinuous along the negative real axis. This is not usually a problem, as real materials will have a small positive imaginary value, representing attenuation in the medium. A new class of materials, however, referred to as metamaterials [24], or left-handed materials, have complex permittivity and permeability, where for both quantities the real part is negative, and the imaginary part positive. Explicitly defining these complex quantities

$$\widehat{\varepsilon}_C = \widehat{\varepsilon}_{\mathrm{Re}} + i\widehat{\varepsilon}_{\mathrm{Im}} \tag{1.40}$$

$$\mu_C = \mu_{\mathrm{Re}} + \mu_{\mathrm{Im}} \tag{1.41}$$

the product will be:

$$\widehat{\varepsilon}_C \mu_C = \widehat{\varepsilon}_{\mathrm{Re}}\mu_{\mathrm{Re}} - \widehat{\varepsilon}_{\mathrm{Im}}\mu_{\mathrm{Im}} + i\left(\widehat{\varepsilon}_{\mathrm{Re}}\mu_{\mathrm{Im}} + \widehat{\varepsilon}_{\mathrm{Im}}\mu_{\mathrm{Re}}\right) \tag{1.42}$$

As the imaginary parts are small, the real part of the product is dominated by the product of the real parts, giving a positive real part. The imaginary part, however, will be negative: however, as both terms are products of the negative real parts, and the positive imaginary parts. A positive imaginary part will be required after the square root, however, to represent that these materials are lossy. So the principle square root is multiplied through by a negative, giving a negative real part, and a positive imaginary part. The term left-handed material arises from the fact that, in this special case, the wave vector has a real part pointing in the opposite direction of propagation. This is of interest as many metals at optical frequencies posses a negative real permittivity in the bulk. It is through manipulation of the structure that this effect occurs.

C. Surface Enhanced Vibrational Spectroscopy

Surface enhanced spectroscopy is a complex field as it includes many different concepts of the surface, the enhancement, and the spectroscopy. For the purposes of this dissertation, the two main groups to be considered are 1) Surface Enhanced Vibrational Spectroscopy[25], including surface enhanced Raman scattering (SERS), surface enhanced resonance Raman scattering (SERRS), surface enhanced infrared absorption (SEIRA), and 2) Surface Enhanced Fluorescence (SEF). By far, SER(R)S has the most publications of the field, as the enhancement effect is quite dramatic.

Surface enhancement is defined here as enhancement of the intensity of the optical signal when is coupled to the localized surface plasmon excitation of metal nanostructures. Other aspects include the chemical effect, or chemical enhancement [26,27], which can arise from spectroscopic changes due to interactions with the surface (chemical adsorption), leading to changes in the electronic structure of the molecule, the breaking or creation of chemical bonds, or from charge transfer to and from the surface to the molecule. While all these factors certainly effect the observed spectroscopic result, it is the plasmon enhancement which provides the main contribution to the SERS effect[27]. Localized surface plasmons can be supported by nanorods, nanowires, and a plethora of nanoparticles of other different shapes (cubes, stars, cones, etc.), and, in particular, by metallic tips. The latter give rise to Tip Enhanced Raman Spectroscopy (TERS)[28,29].

A schematic of the energy levels involved in absorption, emission and scattering spectroscopies to be discussed is shown in Figure 1.2, for a simplified version of molecular energy levels: The two-state system, being the ground and the excited electronic states |g> and |e>. Each of these states has many vibrational states within it, labeled v, starting with v = 0, the fundamental vibrational state. Raman scattering in this context is excitation by a monochromatic source to a virtual state, and returning to a different vibrational state than the original. Since the virtual state is not a stationary state of the system, the molecule spends no time in it, and so the shape and energy of this

state are not important. The key point is the difference in energy between the incident photon and the Raman scattered photon. If there is no difference in energy, or the photon is elastically scattered, the effect is Rayleigh scattering. Infrared absorption is a transition within an electronic state, defined here as being a simple increase in vibrational state. As opposed to Raman, infrared spectroscopy uses a broad source and a photodetector, with the frequencies modulated by an interferometer, resulting in an interferogram leading to a Fourier transform infrared, or FT-IR spectrum. Infrared absorption and Raman scattering, although probing the same vibrational states, have intensity that depends on different quantities. In the case of the infrared, the absorption intensity is proportional to the derivative of the dipole moment with respect to the normal coordinate of the vibrational mode, whereas for Raman, the intensity is proportional to the derivative of the polarizability with respect to the normal coordinate. The use of the techniques together is a full complementary spectroscopic method, as vibrations which are weak in one technique may be very strong in the other.

Resonant Raman scattering is similar to Raman scattering, except that the energy of the incident light is matched to the energy difference between the ground and excited electronic states. This causes the molecule to be excited, and it has a possibility for a finite lifetime and movement on the excited state. As the photon returns to the ground state to a different vibrational state, it may have the character of the excited state, causing differences in relative intensities between RS and RRS.
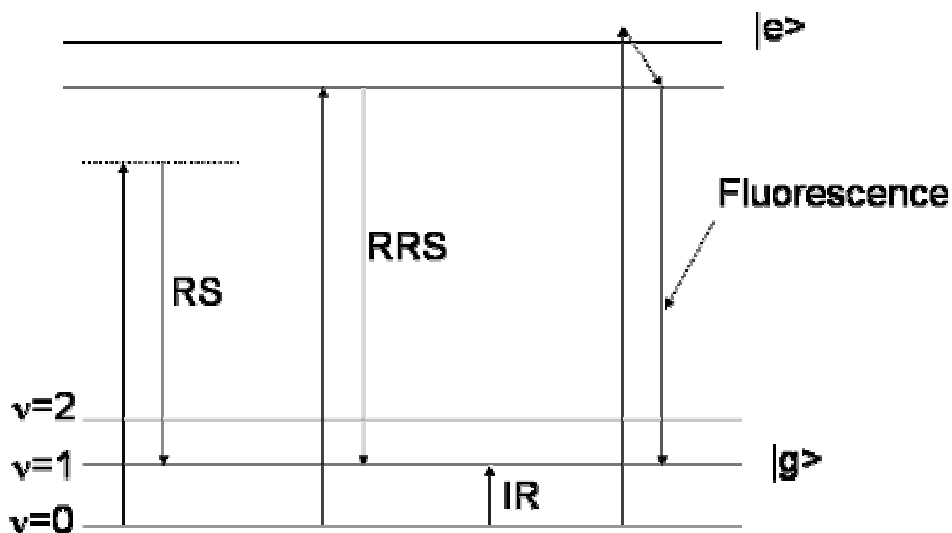
Figure 1.2. Schematic of Raman scattering (RS), resonant Raman scattering (RRS), Infrared Absorption (IR), and Fluorescence.

Fluorescence is a two part process, the first being absorption (annihilation) of a photon and formation of an excited state. The molecule may exist in the excited state for a period of time (lifetime), and may plummet down vibrational levels, or even back to the ground state by non-radiative processes, without emission of a photon. If the decay is radiative (photon creation), it may involve a variety of vibrational and rotational levels, causing a relatively large bandwidth that is generally not resolvable in room temperature experiments of liquids and solids.

Unlike the case for isolated molecules, surface enhanced spectroscopies rely on the total local field at the nanostructure location of the molecule, rather than the incident field of the light to provide the excitation. The local field enhancement, M can be defined as

$$|M| = \frac{|E_l + E_0|}{|E_0|}$$

(1.34)

where E_l is the local field due to the presence of the nanostructure, and E_0 the incident field. The concept of surface enhanced spectroscopy is that the metal nanoparticles create a local field considerably stronger than the incident field, causing a significant field enhancement.

The different surface enhanced spectroscopies follow different physical pathways, and thus, are enhanced in different ways. There is considerable evidence that both SERS[30] and SEF[31] are both enhanced to the fourth power of the field enhancement, meaning that a change in the order of magnitude of the electric field causes massive signal increases. In SEF, however, there is non-radiative decay near the metal surface[31,32] as well as enhancement of the field, and these competing mechanisms will determine the observed enhancement factor SEF.

Surface enhanced spectroscopy is coupling of light, the localized surface plasmon excitation of metal nanostructures, and a molecule. Classical electrodynamics is used to model the interaction of light with the nanoparticle through the use of macroscopic optical constants to calculate the local electromagnetic field. Although many different techniques have arisen from solutions to the different problems that the variety of possible nanoparticle shapes, they are most often treated through the framework of electrodynamics, the fundamentals of which are given above.

D. Bibliography

(1)   Ozbay, E. *Science* **2006**, *311*, 189-193.
(2)   Kittel, C. *Introduction to Solid State Physics*; 6th ed.; Wiley: New York, 1996.
(3)   Bohm, D.; Pines, D. *Physical Review* **1951**, *82*, 625.
(4)   Bohm, D.; Pines, D. *Physical Review* **1952**, *85*, 338.
(5)   Maier, S. A.; Brongersma, M. L.; Kik, P. G.; Meltzer, S.; Requicha, A. A. G.; Atwater, H. A. *Advanced Materials* **2001**, *13*, 1501.
(6)   Freestone, I.; Meeks, N.; Sax, M.; Higgitt, C. *Gold Bulletin* **2007**, *40*, 270.
(7)   Atwater, H. *Scientific American* **2007**, *296*, 56-63.
(8)   Mie, G. *Annalen der Physik* **1908**, *25*, 377-445.
(9)   Papavassiliou, G. C. *Progress in Solid State Chemistry* **1979**, *12*, 185-271.
(10)   Bohren, C. F.; Huffman, D. R. *Absorption and Scattering of Light by Small Particles.*; Wiley: New York, 1983.
(11)   Kerker, M. *The scattering of light and other electromagnetic radiation*; Academic Press, 1969.
(12)   Hao, E.; Li, S.; Bailey, R. C.; Zou, S.; Schatz, G. C.; Hupp, J. T. *Journal of Physical Chemistry B* **2004**, *108*, 1224-1229.
(13)   Sun, Y.; Xia, Y. *Analyst* **2003**, *128*, 686-691.
(14)   Sun, Y.; Xia, Y. *Analytical Chemistry* **2002**, *74*, 5297-5305.
(15)   Averitt, R. D.; Sarkar, D.; Halas, N. J. *Physical Review Letters* **1997**, *78*, 4217.
(16)   Grand, J.; Adam, P.-M.; Grimault, A.-S.; Vial, A.; Lamy de la Chapelle, M.; Bijeon, J.-L.; Kostcheev, S.; Royer, P. *Plasmonics* **2006**, *1*, 135.
(17)   Hao, E.; Schatz, G. C. *Journal of Chemical Physics* **2004**, *120*.
(18)   Sun, Y.; Xia, Y. *Science* **2002**, *298*, 2176.
(19)   Maillard, M.; Giorgio, S.; Pileni, M.-P. *Journal of Physical Chemistry* **2003**, *107*, 2466.
(20)   Nordlander, P.; Oubre, C.; Prodan, E.; Li, K.; Stockman, M. I. *Nano Letters* **2004**, *4*, 899-903.
(21)   Boisde, G.; Harmer, A. *Chemical and biochemical sensing with optical fibers and waveguides*; Arthech House: Boston, 1996.
(22)   Jackson, J. D. *Classical Electrodynamics*; 3rd ed.; John Wiley and Sons: New York, 1999.
(23)   Chow, T. L. *Classical Mechanics*; John Wiley and Sons: New York, 1995.
(24)   Pendry, J. B. *Contemporary Physics* **2004**, *45*, 191-202.
(25)   Aroca, R. *Surface-Enhanced Vibrational Spectroscopy*; John Wiley and Sons: Chichester, West Sussex, 2006.
(26)   Palonpon, A.; Ichimura, T.; Verma, P.; Inouye, Y.; Kawata, S. *Applied Physics Express* **2008**, *1*, 092401.
(27)   Otto, A. *Journal of Raman Spectroscopy* **2005**, *36*, 497-509.
(28)   Pettinger, B. In *Topics in Applied Physics*, 2006; Vol. 103.
(29)   Williams, C.; Roy, D. *Journal of Vacuum Science and Technology B* **2008**, *26*, 1761-1764.

(30) Le Ru, E. C.; Etchegoin, P. G. *Chemical Physics Letters* **2006**, *423*, 63-66.
(31) Johansson, P.; Xu, H.; Käll, M. *Physical Review B* **2005**, *72*, 035427.
(32) Gersten, J.; Nitzan, A. *Journal of Chemical Physics* **1981**, *75*, 1139-52.
(33) *Handbook of Mathematical Functions with Formulas, Graphs, and Mathematical Tables.*; 9 ed.; Abramowitz, M.; Stegun, I. A., Eds.; Dover Publications: New York, 1972.
(34) *Handbook of Optical Constants of Solids*; Palik, E. D., Ed.; Academic Press, 1985.
(35) Noguez, C. *Optical Materials* **2005**, *27*, 1204-1211.
(36) Noguez, C. *Journal of Physical Chemistry C* **2007**, *111*, 3806-3819.
(37) Griffiths, D. J. *Introduction to Electrodynamics*; 2nd ed.; Prentice Hall: Englewood Cliffs, New Jersey, 1989.

CHAPTER TWO

MIE THEORY

A. Solution to Maxwell's Equations for a Sphere

The exact solution of the scattering and absorption by a sphere, known as Mie theory[8], who explained the variation in colour of gold colloids suspended in water. Since that time, this method has been used numerous times in a wide variety of applications. Although the mathematics may be cumbersome, and certainly not trivial, they are quite amenable to computation. While obtaining extinction and scattering cross sections for arbitrary radius and optical properties is not too difficult, understanding and visualizing the results tends to be a more complex task. This is especially important for the case of field enhancement for the various surface enhanced spectroscopies, as it is the fields themselves, rather than the integrated results, which are of interest.

Although Mie theory, due to the exact nature, is correct for arbitrary size and index of refraction, two important details must be kept in mind when comparing it to experimental results. First, and most obvious, is that the treatment is for a sphere. Secondly, the particles are isolated. While these requirements are quite stringent, it is often the case that Mie results can provide a good first approximation for many systems, such as ellipsoids, or thin island films.

This derivation is similar in kind to that of Bohren and Huffman[10], although some of the notation and formalism is taken from Jackson.[22] While Bohren and Huffman present a well structured solution to the problem, the older notation, in terms of the associated Legendre polynomials, is less elegant that the spherical harmonic approach.

It has been shown previously that the time-harmonic fields in a linear, isotropic, homogeneous medium obey the following vector wave equations:

$$\nabla^2 \mathbf{H} + \mu \omega^2 \widehat{\varepsilon}_C \mathbf{H} = 0 \tag{2.1}$$

$$\nabla^2 \mathbf{E} + \mu \omega^2 \widehat{\varepsilon}_C \mathbf{E} = 0 \tag{2.2}$$

These fields are divergence free, and are not independent from one another. This can be summarized through Maxwell's equations.

$$\nabla \cdot \mathbf{E} = 0 \tag{2.3}$$

$$\nabla \cdot \mathbf{H} = 0 \tag{2.4}$$

$$\nabla \times \mathbf{H} + i\omega\varepsilon\mathbf{E} = 0 \tag{2.5}$$

$$\nabla \times \mathbf{E} - i\mu\omega\mathbf{H} = 0 \tag{2.6}$$

To solve the wave equations, suppose there is a vector function M, built from a scalar function ψ and some constant vector c, such that

$$\mathbf{M} = \nabla \times (\mathbf{c}\psi)$$
$$\nabla \cdot \mathbf{M} = \nabla \cdot (\nabla \times (\mathbf{c}\psi)) = 0 \tag{2.7}$$

M is used to try and solve the vector wave equations. Clearly it satisfies the divergence equations. The vector Laplacian of M is:

$$\nabla^2\mathbf{M} = \nabla(\nabla \cdot \mathbf{M}) - \nabla \times (\nabla \times \mathbf{M}) \tag{2.8}$$

The first term is clearly zero, from above. The curl of M is

$$\nabla \times \mathbf{M} = \nabla \times (\nabla \times (\mathbf{c}\psi)) = \nabla(\nabla \cdot (\mathbf{c}\psi)) - \nabla^2(\mathbf{c}\psi) \tag{2.9}$$

where the vector identity for the triple vector product was used. The curl of this result is required, or:

$$\nabla \times (\nabla \times \mathbf{M}) = \nabla \times [\nabla(\nabla \cdot (\mathbf{c}\psi))] - \nabla \times [\nabla^2(\mathbf{c}\psi)] \tag{2.10}$$

The first term here, however, can be recognized as the curl of a gradient, which is zero. Thus, the Laplacian of M is

$$\nabla^2\mathbf{M} = -\nabla \times (\nabla \times \mathbf{M}) = \nabla \times (\nabla^2(\mathbf{c}\psi)) \tag{2.11}$$

The vector Laplacian can be simplified

$$\nabla^2(\mathbf{c}\psi) = \nabla(\nabla \cdot (\mathbf{c}\psi)) - \nabla \times (\nabla \times (\mathbf{c}\psi))$$
$$= \nabla(\mathbf{c} \cdot \nabla\psi + \psi\nabla \cdot \mathbf{c}) - \nabla \times [\nabla\psi \times \mathbf{c} + \psi\nabla \times \mathbf{c}]$$
$$= \nabla(\mathbf{c} \cdot \nabla\psi) - \nabla \times (\nabla\psi \times \mathbf{c}) \tag{2.12}$$

To clean up the notation slightly, the gradient of the scalar function is called d. Thus

$$\nabla^2(\mathbf{c}\psi) = \nabla(\mathbf{c} \cdot \mathbf{d}) - \nabla \times (\mathbf{d} \times \mathbf{c}) \tag{2.13}$$

Applying the vector formulae

$$\nabla(\mathbf{c}\cdot\mathbf{d}) = (\mathbf{c}\cdot\nabla)\mathbf{d} + (\mathbf{d}\cdot\nabla)\mathbf{c} + \mathbf{c}\times(\nabla\times\mathbf{d}) + \mathbf{d}\times(\nabla\times\mathbf{c})$$

$$\nabla\times(\mathbf{d}\times\mathbf{c}) = \mathbf{d}(\nabla\cdot\mathbf{c}) - \mathbf{c}(\nabla\cdot\mathbf{d}) + (\mathbf{c}\cdot\nabla)\mathbf{d} - (\mathbf{d}\cdot\nabla)\mathbf{c} \qquad (2.14)$$

yields

$$\nabla^2(\mathbf{c}\psi) = \mathbf{c}\times(\nabla\times\mathbf{d}) + \mathbf{d}\times(\nabla\times\mathbf{c}) - \mathbf{d}(\nabla\cdot\mathbf{c}) + \mathbf{c}(\nabla\cdot\mathbf{d}) \qquad (2.15)$$

The curls of d and c are zero, as d is a gradient. Also, the divergence of c is zero. Finally, the result is recognized as the scalar Laplacian.

$$\nabla^2(\mathbf{c}\psi) = \mathbf{c}(\nabla\cdot\nabla\psi) = \mathbf{c}(\nabla^2\psi) \qquad (2.16)$$

So the Laplacian of the vector function is:

$$\nabla^2\mathbf{M} = \nabla\times(\mathbf{c}\nabla^2\psi) \qquad (2.17)$$

With the Laplacian derived, it is a trivial matter to use the vector function in the wave equation.

$$\nabla^2\mathbf{M} + k^2\mathbf{M} = \nabla\times(\mathbf{c}\nabla^2\psi) + k^2\nabla\times(\mathbf{c}\psi) = \nabla\times[\mathbf{c}(\nabla^2\psi + k^2\psi)] \qquad (2.18)$$

Therefore, M is a solution to the vector equation if ψ is a solution to the scalar wave equation. Another vector function can be constructed from M, N. If N is

$$\mathbf{N} = \frac{1}{k}\nabla\times\mathbf{M} \qquad (2.19)$$

then following the same development as M:

$$\nabla^2\mathbf{N} = -\nabla\times(\nabla\times\mathbf{N}) = -\nabla\times(\nabla\times\mathbf{N})$$

$$= -\frac{1}{k}\nabla\times(\nabla\times\{\nabla\times\mathbf{M}\}) = \frac{1}{k}\nabla\times(\nabla\times\nabla^2(\mathbf{c}\psi)) = \frac{1}{k}\nabla\times(\nabla\times\mathbf{c}\nabla^2\psi) \qquad (2.20)$$

Thus, N will also be a solution to the vector wave equation if is a solution to the scalar wave equation. The problem is now reduced to a fairly simple one, solving the scalar wave equation.

The derivation so far is general. The specific problem to be solved is that of a sphere, and thus the generating function ψ must satisfy the wave equation in spherical coordinates. Using the usual spherical coordinates choice of r,θ,φ, being the radius, zenith angle (from +z axis), and azimuthal angle (from +x), and the Laplacian definition from Jackson[22], the scalar wave equation is

$$\frac{1}{r^2}\frac{\partial}{\partial r}\left(r^2\frac{\partial\psi}{\partial r}\right) + \frac{1}{r^2\sin\theta}\frac{\partial}{\partial\theta}\left(\sin\theta\frac{\partial\psi}{\partial\theta}\right) + \frac{1}{r^2\sin^2\theta}\frac{\partial^2\psi}{\partial\phi^2} + k^2\psi = 0 \qquad (2.21)$$

Separating out radial and angular parts,

$$\psi = R(r)\Theta(\theta)\Phi(\phi) \tag{2.22}$$

Using the 'prime' notation to signify derivatives with respect to the argument (ie. R'(r)= ∂R(r)/∂r, then this is substituted in:

$$\frac{1}{r^2}\frac{\partial}{\partial r}\left(r^2 R'(r)\right)\Theta(\theta)\Phi(\phi) + \frac{R(r)\Phi(\phi)}{r^2\sin\theta}\frac{\partial}{\partial\theta}\left(\sin\theta\Theta'(\theta)\right) + \frac{R(r)\Theta(\theta)}{r^2\sin^2\theta}\Phi''(\phi) + k^2 R(r)\Theta(\theta)\Phi(\phi) = 0$$
(2.23)

If the equation is multiplied by $r^2\sin^2\theta/(R\Theta\Phi)$ then:

$$\frac{\sin^2\theta}{R(r)}\frac{\partial}{\partial r}\left(r^2 R'(r)\right) + \frac{\sin\theta}{\Theta(\theta)}\frac{\partial}{\partial\theta}\left(\sin\theta\Theta'(\theta)\right) + \frac{1}{\Phi(\phi)}\Phi''(\phi) + k^2 r^2\sin^2\theta = 0 \tag{2.24}$$

The third term depends on only φ, and no other term depends on φ. It is therefore isolated, and must yield a constant of separation, called m^2.

$$\Phi''(\phi) + m^2\Phi(\phi) = 0; \tag{2.25}$$

This has solutions

$$\Phi(\phi) = e^{\pm im\phi} \tag{2.26}$$

which is single valued for integer m. Dividing by $\sin^2\theta$ gives

$$\frac{1}{R(r)}\frac{\partial}{\partial r}\left(r^2 R'(r)\right) + \frac{1}{\sin\theta\Theta(\theta)}\frac{\partial}{\partial\theta}\left(\sin\theta\Theta'(\theta)\right) - \frac{m^2}{\sin^2\theta} + k^2 r^2 = 0 \tag{2.27}$$

Separating out the zenith angle terms, and setting x=cos θ gives

$$\Theta'(\theta) = \frac{\partial\Theta(\theta)}{\partial\theta} \rightarrow -\sin\theta\frac{\partial\Theta(x)}{\partial x} \tag{2.28}$$

Evaluating the equation to a constant C yields

$$\frac{\partial}{\partial x}\left((1-x^2)\frac{d\Theta(x)}{dx}\right) + \left(C - \frac{m^2}{1-x^2}\right)\Theta(x) = 0$$

$$\left((1-x^2)\frac{d^2\Theta(x)}{dx^2} - 2x\frac{d\Theta(x)}{dx}\right) + \left(C - \frac{m^2}{1-x^2}\right)\Theta(x) = 0 \tag{2.29}$$

This is Legendre's associated differential equation[33], and thus C is recognized as n(n+1). The solutions are then the associated Legendre polynomials, labeled $P^m{}_n(\cos\theta)$.

Similarly, the radial part can be separated out, and evaluated to a constant n(n+1):

$$\frac{\partial}{\partial r}\left(r^2 R'(r)\right) + \left(k^2 r^2 - n(n+1)\right)R(r) = 0$$

(2.30)

Due to the inclusion of k, this should be evaluated in dimensionless variables. Defining $\rho=kr$, referred to as the size parameter, and $Z=R(r)(\rho)^{1/2}$, gives

$$\frac{\partial R(r)}{\partial r} = \frac{\partial\left[Z\rho^{-1/2}\right]}{\partial\rho}\frac{\partial\rho}{\partial r} = k\left[\frac{\partial Z}{\partial\rho}\rho^{-1/2} - \frac{1}{2}Z\rho^{-3/2}\right]$$

$$\frac{\partial}{\partial\rho}\left(\rho^2\left[\frac{\partial Z}{\partial\rho}\rho^{-1/2} - \frac{1}{2}Z\rho^{-3/2}\right]\right) + \left(\rho^2 - n(n+1)\right)\left[Z\rho^{-1/2}\right] = 0$$

(2.31)

Evaluating the derivatives gives

$$\left(\frac{\partial^2 Z}{\partial\rho^2}\rho^{3/2} + \frac{3}{2}\frac{\partial Z}{\partial\rho}\rho^{1/2} - \frac{1}{2}\frac{\partial Z}{\partial\rho}\rho^{1/2} - \frac{1}{4}Z\rho^{-1/2}\right) + \left(\rho^2 - n(n+1)\right)\left[Z\rho^{-1/2}\right] = 0$$

$$\left(\frac{\partial^2 Z}{\partial\rho^2}\rho^{3/2} + \frac{\partial Z}{\partial\rho}\rho^{1/2}\right) + \left(\rho^2 - n(n+1) - \frac{1}{4}\right)\left[Z\rho^{-1/2}\right] = 0$$

(2.32)

Multiplying through by $(\rho)^{1/2}$ cleans the equation up slightly

$$\frac{\partial^2 Z}{\partial\rho^2}\rho^2 + \frac{\partial Z}{\partial\rho}\rho + \left(\rho^2 - \left(n^2 + n + \frac{1}{4}\right)\right)Z = 0$$

$$\frac{\partial^2 Z}{\partial\rho^2}\rho^2 + \frac{\partial Z}{\partial\rho}\rho + \left(\rho^2 - \left(n + \frac{1}{2}\right)^2\right)Z = 0$$

(2.33)

This is Bessel's differential equation[33], and the solutions are half integer order, n+1/2 is an integer. The solutions are then the spherical Bessel functions

$$j_n(\rho) = \sqrt{\frac{\pi}{2\rho}}J_{n+\frac{1}{2}}(\rho)$$

$$y_n(\rho) = \sqrt{\frac{\pi}{2\rho}}Y_{n+\frac{1}{2}}(\rho)$$

$$h_n^{(1)}(\rho) = j_n(\rho) + iy_n(\rho)$$

$$h_n^{(2)}(\rho) = j_n(\rho) - iy_n(\rho)$$

(2.34)

where j and y are the spherical Bessel functions of the first and second kind, J and Y the Bessel functions of the first and second kind, and $h^{(1)}$ and $h^{(2)}$ the spherical Hankel functions of the first and second kind, sometimes referred to as

23

spherical Bessel functions of the third kind. The index n is now an integer. Both j and y are solutions, so thus the Hankel functions are also solutions, being linear combinations of solutions. Thus, the full solution is

$$\psi_{mn} = z_n(kr)P_n^m(\cos\theta)e^{\pm im\phi}$$

(2.35)

where z_n is one of the four Bessel functions defined above. Although this result is similar to that derived by Bohren and Huffman, it is slightly more general, and avoids the use of trigonometric functions of azimuthal angle. Rather then split functions into even and odd categories, the real part of this result is even, and the imaginary part is odd. It is also possible to change to spherical harmonics at this point, which will help as the normalization and orthogonality conditions are well known. Bohren and Huffman's derivation requires splitting the scalar function into even and odd parts, due to the use of trigonometric functions, and also because they avoid the use of negative m. Spherical harmonics, however, form a complete set[22], and thus the sign uncertainty can be dropped. Without worrying about normalization, since it is the vector functions themselves that will be normalized, the scalar functions are thus written

$$\psi_{mn} = z_n(kr)Y_n^m(\theta,\phi)$$

(2.36)

as

$$Y_n^m(\theta,\phi) = \sqrt{\frac{2n+1}{4\pi}\frac{(n-m)!}{(n+m)!}}P_n^m(\cos\theta)e^{im\phi}$$

(2.37)

Where again, normalization will not yet be considered. The derivatives with respect to the angular are then:

$$\frac{\partial\psi_{mn}}{\partial\phi} = z_n(kr)\frac{\partial Y_n^m(\theta,\phi)}{\partial\phi} = imz_n(kr)Y_n^m(\theta,\phi)$$

$$\frac{\partial\psi_{mn}}{\partial\theta} = z_n(kr)\frac{\partial Y_n^m(\theta,\phi)}{\partial\theta} = z_n(kr)Y_n'^m(\theta,\phi)$$

(2.38)

Explicit forms of vector spherical harmonics, M and N, first require the choice of a pilot vector, c. Although this choice is arbitrary, a convenient choice is to make it the radius vector r. This defines M as being tangential to any sphere, or r*M=0. M can then be written

$$\mathbf{M}_{mn} = \nabla \times \mathbf{r}\psi_{mn} = \begin{pmatrix} 0 \\ \dfrac{1}{r\sin\theta}\dfrac{\partial}{\partial\phi}(r\psi_{mn}) \\ -\dfrac{1}{r}\dfrac{\partial}{\partial\theta}(r\psi_{mn}) \end{pmatrix} = z_n(kr)\begin{pmatrix} 0 \\ \dfrac{im}{\sin\theta}Y_n^m(\theta,\phi) \\ -Y_n'^m(\theta,\phi) \end{pmatrix}$$

(2.39)

The part of this vector which depends on Y_n^m bears a resemblance to the angular momentum operator, L. Defining L as

$$\mathbf{L} = -i\mathbf{r}\times\nabla$$

(2.40)

which differs from the usual quantum mechanical L by a factor of $\hbar$. Working LY_n^m out explicitly gives

$$\mathbf{L}Y_n^m = -i\mathbf{r}\times\nabla Y_n^m = -i\mathbf{r}\times\begin{pmatrix} 0 \\ \dfrac{1}{r}Y_n'^m \\ \dfrac{im}{r\sin\theta}Y_n^m \end{pmatrix} = -i\begin{vmatrix} \hat{r} & \hat{\theta} & \hat{\phi} \\ r & 0 & 0 \\ 0 & \dfrac{1}{r}Y_n'^m & \dfrac{im}{r\sin\theta}Y_n^m \end{vmatrix} = -i\begin{pmatrix} 0 \\ \dfrac{-im}{\sin\theta}Y_n^m \\ Y_n'^m \end{pmatrix} = \begin{pmatrix} 0 \\ \dfrac{-m}{\sin\theta}Y_n^m \\ -iY_n'^m \end{pmatrix}$$

(2.41)

which differs from the vector part of M by a factor of i. As the solution to the differential equation multiplied by a constant is still a solution, M can be written

$$\mathbf{M}_{mn} = z_n(kr)\begin{pmatrix} 0 \\ \dfrac{-m}{\sin\theta}Y_n^m(\theta,\phi) \\ -iY_n'^m(\theta,\phi) \end{pmatrix} = z_n(kr)\mathbf{L}Y_n^m$$

(2.42)

This helps in normalization, as the LY_n^m part is well studied. In fact, the normalized spherical harmonics used by Jackson are defined by[22]

$$\mathbf{X}_{mn} = \frac{1}{\sqrt{n(n+1)}}\mathbf{L}Y_n^m = \frac{1}{\sqrt{n(n+1)}}\begin{pmatrix} 0 \\ \dfrac{-m}{\sin\theta}Y_n^m(\theta,\phi) \\ -iY_n'^m(\theta,\phi) \end{pmatrix}$$

$$\int \mathbf{X}_{mn}^* \cdot \mathbf{X}_{mn}d\Omega = \delta_{nn'}\delta_{mm'}$$

(2.43)

An orthogonal M can now be written

$$\mathbf{M}_{mn} = z_n(kr)\mathbf{X}_{nm} = \frac{-z_n(kr)}{\sqrt{n(n+1)}}\begin{pmatrix} 0 \\ \dfrac{m}{\sin\theta}Y_n^m \\ iY_n'^m \end{pmatrix}$$

(2.44)

The equation for N requires derivatives with respect to r. A change of variables gives

$$\frac{1}{r}\frac{\partial}{\partial r}=\frac{k}{\rho}\frac{\partial}{\partial\rho}\frac{\partial\rho}{\partial r}=\frac{k^2}{\rho}\frac{\partial}{\partial\rho}$$

(2.46)

$$\mathbf{N}_{mn}=\frac{1}{k}\nabla\times\mathbf{M}_{mn}=\frac{1}{k\sqrt{n(n+1)}}\begin{pmatrix}\frac{-k}{\rho\sin\theta}\left[\frac{\partial}{\partial\theta}\left(-\sin\theta z_n(\rho)iY_n^{'m}\right)+\frac{z_n(\rho)im^2Y_n^m}{\sin\theta}\right]\\[2mm]\frac{k}{\rho}\frac{\partial}{\partial\rho}\left(\rho z_n(\rho)iY_n^{'m}\right)\\[2mm]\frac{-k}{\rho}\frac{\partial}{\partial\rho}\left(\frac{m\rho z_n(\rho)}{\sin\theta}Y_n^m\right)\end{pmatrix}$$

$$=\frac{1}{\sqrt{n(n+1)}}\begin{pmatrix}\frac{iz_n(\rho)}{\rho\sin\theta}\left[\frac{\partial}{\partial\theta}\left(\sin\theta\frac{\partial Y_n^m}{\partial\theta}\right)-\frac{m^2Y_n^m}{\sin\theta}\right]\\[2mm]\frac{iY_n^{'m}}{\rho}\frac{\partial}{\partial\rho}\left(\rho z_n(\rho)\right)\\[2mm]\frac{-mY_n^m}{\rho\sin\theta}\frac{\partial}{\partial\rho}\left(\rho z_n(\rho)\right)\end{pmatrix}$$

(2.47)

Recalling that the Legendre polynomials were obtained through the equation

$$\frac{\partial}{\partial\theta}\left(\sin\theta\Theta'(\theta)\right)+\Theta(\theta)\left(\frac{-m^2}{\sin\theta}+\sin\theta n(n+1)\right)=0$$

$$\frac{\partial}{\partial\theta}\left(\sin\theta\Theta'(\theta)\right)-\Theta(\theta)\frac{m^2}{\sin\theta}=-\sin\theta n(n+1)\Theta(\theta)$$

(2.48)

the radial part of N can be cleaned up, and N written explicitly:

$$\mathbf{N}_{mn}=\frac{1}{\sqrt{n(n+1)}}\begin{pmatrix}\frac{-iz_n(\rho)}{\rho}n(n+1)Y_n^m\\[2mm]\frac{iY_n^{'m}}{\rho}\frac{\partial}{\partial\rho}\left(\rho z_n(\rho)\right)\\[2mm]\frac{-mY_n^m}{\rho\sin\theta}\frac{\partial}{\partial\rho}\left(\rho z_n(\rho)\right)\end{pmatrix}$$

(2.49)

The orthogonality of N is given by[22]:

$$\int\mathbf{N}_{m'n'}^*\cdot\mathbf{N}_{mn}d\Omega=\frac{1}{k^2}\int\left(\nabla\times z_{n'}(r)\mathbf{X}_{m'n'}\right)^*\cdot\left(\nabla\times z_n(r)\mathbf{X}_{mn}\right)d\Omega=\delta_{n'n}\delta_{m'm}\left\{|z_n(r)|^2+\frac{1}{k^2r^2}\frac{\partial}{\partial r}\left[r(z_n(r))^*\frac{\partial}{\partial r}(rz_n(r))\right]\right\}$$

(2.50)

and finally

$$\int \mathbf{M}^*_{m'n'} \cdot \mathbf{N}_{mn} d\Omega = \frac{1}{k^2} \int \left(z_{n'}(r) \mathbf{X}_{m'n'} \right)^* \cdot \left(\nabla \times z_n(r) \mathbf{X}_{mn} \right) d\Omega = 0$$

(2.51)

With N and M firmly in hand, it is now possible to expand any wave as a function of these vector spherical harmonics, including, most importantly, the incident field and the scattered field by a sphere. The resulting fields are those important for SERS, and the origin of the enhanced field that is amplifying the scattering.

B. Expansion of Incident Field

If a circularly polarized plane wave that is incident from the z is on the sphere, the incident field can be written as

$$\mathbf{E}_i = \left(\hat{\mathbf{\varepsilon}}_1 \pm i\hat{\mathbf{\varepsilon}}_2\right)e^{ikz} \tag{2.52}$$

where the two possible helicities are shown. As it is only the spherical Bessel functions of the first kind that are finite at the origin, they are the function of choice in this problem. Any arbitrary field can be expanded into the vector spherical harmonics as:

$$\mathbf{E}_i = \sum_{n',m'}\left[A_{m'n'}\mathbf{M}_{m'n'} + B_{m'n'}\mathbf{N}_{m'n'}\right] \tag{2.53}$$

The coefficients A and B can be calculated by multiplying through from the right by X^*_{mn}, and integrating over the solid angle:

$$\int \mathbf{E}_i \cdot \mathbf{X}^*_{mn}d\Omega = \int \sum_{n',m'}\left[A_{m'n'}z_{n'}(kr)\mathbf{X}_{m'n'}\cdot\mathbf{X}^*_{mn} + \frac{1}{k}B_{m'n'}(\nabla\times[z_{n'}(kr)\mathbf{X}_{m'n'}])\cdot\mathbf{X}^*_{mn}\right]d\Omega \tag{2.54}$$

The second term is zero, by orthogonality, as given above. Also, the first term is zero for all m',n'≠m,n. This gives

$$\int \mathbf{E}_i \cdot \mathbf{X}^*_{mn}d\Omega = \int A_{mn}z_n(kr)\mathbf{X}_{mn}\cdot\mathbf{X}^*_{mn}d\Omega \tag{2.55}$$

The left hand side of the equation gives

$$\int \mathbf{E}_i \cdot \mathbf{X}^*_{mn}d\Omega = \int e^{ikz}\left(\mathbf{\varepsilon}_1 \pm i\mathbf{\varepsilon}_2\right)\cdot\mathbf{X}^*_{mn}d\Omega = \frac{1}{\sqrt{n(n+1)}}\int e^{ikz}\left(\mathbf{\varepsilon}_1 \pm i\mathbf{\varepsilon}_2\right)\cdot\begin{pmatrix}0\\ \dfrac{-i}{\sin\theta}\left(\dfrac{\partial}{\partial\phi}Y_n^m\right)^*\\ i\dfrac{\partial\left(Y_n^m\right)^*}{\partial\theta}\end{pmatrix}d\Omega \tag{2.56}$$

$$\hat{\mathbf{\varepsilon}}_1 \pm i\hat{\mathbf{\varepsilon}}_2 = (\sin\theta\cos\phi \pm i\sin\theta\sin\phi)\hat{\mathbf{r}} + (\cos\theta\cos\phi \pm i\cos\theta\sin\phi)\hat{\mathbf{\theta}} + (-\sin\phi \pm i\cos\phi)\hat{\mathbf{\phi}}$$
$$= \sin\theta e^{\pm i\phi}\hat{\mathbf{r}} + \cos\theta e^{\pm i\phi}\hat{\mathbf{\theta}} \pm i\left(e^{\pm i\phi}\right)\hat{\mathbf{\phi}} \tag{2.57}$$

$$(\varepsilon_1 \pm i\varepsilon_2)\cdot \begin{pmatrix} 0 \\ \dfrac{-i}{\sin\theta}\left(\dfrac{\partial}{\partial\phi}Y_n^m\right)^* \\ i\dfrac{\partial(Y_n^m)^*}{\partial\theta} \end{pmatrix} = e^{\pm i\phi}\left(-i\cot\theta\left(\dfrac{\partial}{\partial\phi}Y_n^m\right)^* \mp \dfrac{\partial(Y_n^m)^*}{\partial\theta}\right)$$

(2.58)

Using the definitions of the angular momentum raising and lowering operators, L_+ and L_-[22],

$$L_+ = e^{i\phi}\left(\dfrac{\partial}{\partial\theta} + i\cot\theta\,\dfrac{\partial}{\partial\phi}\right)$$

$$L_+ = e^{-i\phi}\left(-\dfrac{\partial}{\partial\theta} + i\cot\theta\,\dfrac{\partial}{\partial\phi}\right)$$

(2.59)

The above can be represented as

$$(\varepsilon_1 + i\varepsilon_2)\cdot \begin{pmatrix} 0 \\ \dfrac{-i}{\sin\theta}\left(\dfrac{\partial}{\partial\phi}Y_n^m\right)^* \\ i\dfrac{\partial(Y_n^m)^*}{\partial\theta} \end{pmatrix} = e^{i\phi}\left(-\dfrac{\partial}{\partial\theta} - i\cot\theta\,\dfrac{\partial}{\partial\phi}\right)(Y_n^m)^* = (L_-Y_n^m)^* = \sqrt{(n+m)(n-m+1)}(Y_n^{m-1})^*$$

$$(\varepsilon_1 - i\varepsilon_2)\cdot \begin{pmatrix} 0 \\ \dfrac{-i}{\sin\theta}\left(\dfrac{\partial}{\partial\phi}Y_n^m\right)^* \\ i\dfrac{\partial(Y_n^m)^*}{\partial\theta} \end{pmatrix} = e^{-i\phi}\left(\dfrac{\partial}{\partial\theta} - i\cot\theta\,\dfrac{\partial}{\partial\phi}\right)(Y_n^m)^* = (L_+Y_n^m)^* = \sqrt{(n-m)(n+m+1)}(Y_n^{m+1})^*$$

(2.60)

So therefore,

$$\int \mathbf{E}_i \cdot \mathbf{X}_{mn}^* d\Omega = \dfrac{1}{\sqrt{n(n+1)}}\int e^{ikz}(L_{\mp}Y_n^m)^* d\Omega = \dfrac{\sqrt{(n\pm m)(n\mp m+1)}}{\sqrt{n(n+1)}}\int e^{ikz}(Y_n^{m\mp 1})^* d\Omega$$

(2.61)

Representing the exponential using[22]

$$e^{i\mathbf{k}\cdot\mathbf{x}} = \sum_{n'=0}^{\infty} i^{n'}\sqrt{4\pi(2n'+1)}\,j_{n'}(kr)Y_{n'}^0(\gamma)$$

(2.62)

yields

$$\int \mathbf{E}_i \cdot \mathbf{X}^*_{mn} d\Omega = \frac{\sqrt{(n \pm m)(n \mp m + 1)}}{\sqrt{n(n+1)}} \int i^n \sqrt{4\pi(2n+1)} j_n(kr) Y_n^0 \left(Y_n^{m\mp1}\right)^* d\Omega$$

(2.63)

where the summation over n' is removed due to the orthogonality of the spherical harmonics[22]:

$$\int Y_{n'}^{m'} Y^{*m}_n d\Omega = \delta_{nn'} \delta_{mm'}$$

(2.64)

Use of the orthogonality relationship over m implies that m must be positive or negative 1. This finally gives:

$$\int \mathbf{E}_i \cdot \mathbf{X}^*_{mn} d\Omega = \frac{i^n \sqrt{4\pi(2n+1)} \sqrt{(n \pm m)(n \mp m + 1)}}{\sqrt{n(n+1)}} j_n(kr) \delta_{m,\pm1}$$

$$= \frac{i^n \sqrt{4\pi(2n+1)} \sqrt{n(n+1)}}{\sqrt{n(n+1)}} j_n(kr) \delta_{m,\pm1} = i^n \sqrt{4\pi(2n+1)} j_n(kr) \delta_{m,\pm1}$$

(2.65)

Recalling that

$$\int \mathbf{E}_i \cdot \mathbf{X}^*_{mn} d\Omega = A_{mn} j_n(kr)$$

(2.66)

yields

$$A_{mn}^{\pm} = i^n \sqrt{4\pi(2n+1)} j_n(kr) \delta_{m,\pm1}$$

(2.67)

Much of the work for finding B_{mn} is already done. The magnetic field can be represented as

$$\mathbf{H}_i = \hat{\boldsymbol{\varepsilon}}_3 \times \mathbf{E}_i = e^{ikz}\left(\hat{\boldsymbol{\varepsilon}}_3 \times (\hat{\boldsymbol{\varepsilon}}_1 \pm i\hat{\boldsymbol{\varepsilon}}_2)\right) = e^{ikz}\left(\hat{\boldsymbol{\varepsilon}}_3 \times \hat{\boldsymbol{\varepsilon}}_1 \pm i\hat{\boldsymbol{\varepsilon}}_3 \times \hat{\boldsymbol{\varepsilon}}_2\right) = e^{ikz}\left(\hat{\boldsymbol{\varepsilon}}_2 \mp i\hat{\boldsymbol{\varepsilon}}_1\right) = \pm i e^{ikz}\left(\hat{\boldsymbol{\varepsilon}}_1 \pm i\hat{\boldsymbol{\varepsilon}}_2\right) = \pm i\mathbf{E}_i$$

(2.68)

and it can be expanded as

$$\mathbf{H} = \sum_{n',m'} \left[A_{m'n'} \mathbf{N}_{m'n'} + B_{m'n'} \mathbf{M}_{m'n'} \right]$$

(2.69)

As before, multiplying through by the conjugate of $\mathbf{X}_{mn}$ and integrating over the solid angle gives

$$\int \mathbf{H}_i \cdot \mathbf{X}^*_{mn} d\Omega = \int B_{mn} j_n(kr) \mathbf{X}_{m'n'} \cdot \mathbf{X}^*_{mn} d\Omega = B_{mn} j_n(kr)$$

(2.70)

The left hand side can be put in terms of the incident electric field, and using the above result

$$\pm i \int \mathbf{E}_i \cdot \mathbf{X}^*_{mn} d\Omega = \pm i \left(i^n \sqrt{4\pi(2n+1)} j_n(kr) \delta_{m,\pm1} \right) = B_{mn} j_n(kr)$$

$$\therefore B^{\pm}_{mn} = \pm i \left(i^n \sqrt{4\pi(2n+1)} \delta_{m,\pm1} \right) = \pm i A_{mn}^{\pm}$$

(2.71)

The expansion of the plane wave electric field is finally

$$\mathbf{E}_i = \sum_{n,m} i^n \sqrt{4\pi(2n+1)} \big[\mathbf{M}_{mn} \pm i\mathbf{N}_{mn} \big] \delta_{m,\pm 1}$$

$$= \sum_n i^n \sqrt{4\pi(2n+1)} \big[\mathbf{M}_{\pm 1,n} \pm i\mathbf{N}_{\pm 1,n} \big]$$

(2.72)

and the magnetic field is

$$c\mathbf{H}_i = \sum_n i^n \sqrt{4\pi(2n+1)} \big[-i\mathbf{N}_{\pm 1,n} \mp i\mathbf{M}_{\pm 1,n} \big]$$

(2.73)

The electric field in explicit vector form, this is

$$\mathbf{E}_i = \sum_n i^n \frac{\sqrt{4\pi(2n+1)}}{\sqrt{n(n+1)}} \left[-j_n(kr) \begin{pmatrix} 0 \\ \pm Y_n^{\pm 1} \\ \sin\theta \\ iY_n^{\pm 1} \end{pmatrix} \pm i \begin{pmatrix} \dfrac{ij_n(kr)}{kr} n(n+1)Y_n^{\pm 1} \\ \dfrac{iY_n'^{\pm 1}}{kr} \dfrac{\partial}{\partial kr}(krj_n(kr)) \\ \dfrac{\mp Y_n^{\pm 1}}{kr\sin\theta} \dfrac{\partial}{\partial kr}(krj_n(kr)) \end{pmatrix} \right]$$

$$= \sum_n i^n \frac{\sqrt{4\pi(2n+1)}}{\sqrt{n(n+1)}} \left[\begin{pmatrix} \mp \dfrac{j_n(kr)}{kr} n(n+1)Y_n^{\pm 1} \\ \mp j_n(kr)Y_n^{\pm 1} \mp \dfrac{Y_n'^{\pm 1}}{kr} \dfrac{\partial}{\partial kr}(krj_n(kr)) \\ \sin\theta \\ i\left[-j_n(kr)Y_n'^{\pm 1} - \dfrac{Y_n^{\pm 1}}{kr\sin\theta} \dfrac{\partial}{\partial kr}(krj_n(kr)) \right] \end{pmatrix} \right]$$

(2.74)

Bohren and Huffman[10] use a different derivation, and comparing the functional forms of the plane wave is a useful exercise. The radial parts are

$$\mathbf{E}_i \cdot \hat{\mathbf{r}} = \mp \sum_n i^n \frac{\sqrt{4\pi(2n+1)}}{\sqrt{n(n+1)}} \frac{j_n(kr)}{kr} n(n+1)Y_n^{\pm 1}$$

$$\mathbf{E}_{iB\&H} \cdot \hat{\mathbf{r}} = E_0 \sum_n i^n \frac{2n+1}{n(n+1)} \left(-i\left[\frac{j_n(kr)}{kr} n(n+1)\sin\phi P_n^1(\cos\theta) \right] \right)$$

(2.75)

The first two radial terms from Bohren and Huffman are then

$$\mathbf{E}_{iB\&H}^1 \cdot \hat{\mathbf{r}} = E_0 i \frac{3}{2} \left(-i\left[\frac{2j_1(kr)}{kr} \sin\phi P_1^1(\cos\theta) \right] \right) = -3E_0 \frac{j_1(kr)}{kr} \sin\phi \sin\theta$$

$$\mathbf{E}_{iB\&H}^2 \cdot \hat{\mathbf{r}} = -E_0 \frac{5}{6} \left(-i\left[\frac{6j_2(kr)}{kr} \sin\phi P_2^1(\cos\theta) \right] \right) = -15iE_0 \left[\frac{j_2(kr)}{kr} \sin\phi \sin\theta \cos\theta \right]$$

(2.76)

whereas this work gives

$$\mathbf{E}^1_i \cdot \hat{\mathbf{r}} = \mp i \frac{\sqrt{4\pi 3}}{\sqrt{2}} \frac{j_1(kr)}{kr} 2Y_1^{\pm 1} = 3i \frac{j_1(kr)}{kr} \sin\theta e^{\pm i\phi}$$

$$\mathbf{E}^2_i \cdot \hat{\mathbf{r}} = \pm \frac{\sqrt{4\pi 5}}{\sqrt{6}} \frac{j_2(kr)}{kr} 6Y_2^{\pm 1} = -15 \frac{j_2(kr)}{kr} \sin\theta \cos\theta e^{\pm i\theta}$$

<div align="right">(2.77)</div>

where

$$Y_1^{\pm 1} = \mp \frac{1}{2}\sqrt{\frac{3}{2\pi}} \sin\theta e^{\pm i\phi}$$

$$Y_2^{\pm 1} = \mp \frac{1}{2}\sqrt{\frac{15}{2\pi}} \sin\theta \cos\theta e^{\pm i\phi}$$

<div align="right">(2.78)</div>

has been used. The two formulations differ by a factor of i, as well as the additional imaginary part introduced by the complex exponential. In the angular directions, the dipolar term involves the derivative with respect to θ

$$\frac{\partial}{\partial\theta} Y_1^{\pm 1} = \mp \frac{1}{2}\sqrt{\frac{3}{2\pi}} \cos\theta e^{\pm i\phi}$$

<div align="right">(2.79)</div>

and so

$$\mathbf{E}^1_i \cdot \hat{\boldsymbol{\theta}} = i\frac{3}{2} e^{\pm i\phi}\left(j_1(kr) + \cos\theta \frac{1}{kr}\frac{\partial}{\partial kr}(krj_1(kr)) \right)$$

$$\mathbf{E}^1_{iB\&H} \cdot \hat{\boldsymbol{\theta}} = E_0 i\frac{3}{2}\left(-\cos\phi j_1(kr) + i\cos\phi\cos\theta \frac{1}{kr}\frac{\partial}{\partial kr}(krj_1(kr)) \right)$$

<div align="right">(2.80)</div>

$$\mathbf{E}^1_i \cdot \hat{\boldsymbol{\phi}} = -\frac{3}{2} e^{\pm i\phi}\left(\pm j_n(kr)\cos\theta \mp \frac{1}{kr}\frac{\partial}{\partial kr}(krj_n(kr)) \right)$$

$$\mathbf{E}^1_{iB\&H} \cdot \hat{\boldsymbol{\phi}} = \frac{3i}{2} E_0\left(\sin\phi\cos\theta j_n(kr) - i\cos\phi \frac{1}{kr}\frac{\partial}{\partial kr}(krj_n(kr)) \right)$$

<div align="right">(2.81)</div>

So although the angular directions, like the radial contribution, also differ by a phase factor between these formulations, they still agree in terms of magnitude.

C. Scattered and Internal Fields

If the derived plane wave is incident on a homogeneous, isotropic sphere of radius a, at the surface of the sphere, the boundary conditions dictate that[10]

$$\left(\mathbf{E}_i + \mathbf{E}_{sc} - \mathbf{E}_{int}\right) \times \hat{\mathbf{r}} = \left(\mathbf{H}_i + \mathbf{H}_{sc} - \mathbf{H}_{int}\right) \times \hat{\mathbf{r}} = 0 \tag{2.82}$$

where E_i, E_{sca}, and E_{int} are the incident, scattered, and internal fields, respectively. Choosing the positive helicity for the polarization, which involves no loss of generality, the incident field is

$$\mathbf{E}_i = \sum_n C_n \left[\mathbf{M}^{(1)}{}_{1,n} + i\mathbf{N}^{(1)}{}_{1,n}\right] \tag{2.83}$$

$$\mathbf{H}_i = \frac{-k}{\omega\mu} \sum_n C_n \left[i\mathbf{N}^{(1)}{}_{1,n} + i\mathbf{M}^{(1)}{}_{1,n}\right] \tag{2.84}$$

where the superscript (1) refers to the use of spherical Bessel functions of the first kind (j_n), and

$$C_n = i^n \sqrt{4\pi(2n+1)} \tag{2.85}$$

Keeping a similar expansion for the internal and scattered fields, they can thus be written down as

$$\mathbf{E}_{sc} = -\sum_n C_n \left[ia_n \mathbf{N}^{(3)}{}_{1,n} + b_n \mathbf{M}^{(3)}{}_{1,n}\right]$$

$$\mathbf{H}_{sc} = \frac{k}{\omega\mu} \sum_n C_n \left[ib_n \mathbf{N}^{(3)}{}_{1,n} + ia_n \mathbf{M}^{(3)}{}_{1,n}\right]$$

$$\mathbf{E}_{int} = \sum_n C_n \left[id_n \mathbf{N}^{(1)}{}_{1,n} + c_n \mathbf{M}^{(1)}{}_{1,n}\right]$$

$$\mathbf{H}_{int} = \frac{-k_{int}}{\omega\mu_{int}} \sum_n C_n \left[ic_n \mathbf{N}^{(1)}{}_{1,n} + id_n \mathbf{M}^{(1)}{}_{1,n}\right] \tag{2.86}$$

where the superscript (1) and (3) refers to the use of spherical Bessel functions of the first kind (j_n) and third kind ($h^{(1)}{}_n$). The Hankel functions of the first kind refer to outgoing waves. While they are not well behaved at the origin, the scattered field only exists outside the sphere, so the singularity is not a problem. The problem is now reduced to finding a form for these scattering and internal field coefficients.

The boundary conditions above can be written in component form for any given n

33

$$E_{i\theta} + E_{sca\theta} = E_{\mathrm{int}\,\theta}$$
$$E_{i\phi} + E_{sca\phi} = E_{\mathrm{int}\,\phi}$$
$$H_{i\theta} + H_{sca\theta} = H_{\mathrm{int}\,\theta}$$
$$H_{i\phi} + H_{sca\phi} = H_{\mathrm{int}\,\phi}$$

$$(2.87)$$

The solution to these equations has been done in many texts: notably, in Kerker[11], and references therein. A simple form of the scattering coefficients may be obtained by introducing the Riccati-Bessel functions, defined as[33]:

$$\psi_n(\rho) = \rho j_n(\rho)$$
$$\xi_n(\rho) = \rho h_n^{(1)}(\rho)$$

$$(2.88)$$

where j_n and $h^{(1)}{}_n$ are the spherical Bessel functions of the first kind and spherical Hankel functions of the first kind. Assuming a nonmagnetic material, or at least that the magnetic permeability of the sphere is the same as the magnetic permeability of the surrounding medium, the scattering coefficients are[10]

$$a_n = \frac{m\psi_n(mx)\psi'_n(x) - \psi_n(x)\psi'_n(mx)}{m\psi_n(mx)\xi'_n(x) - \xi_n(x)\psi'_n(mx)}$$

$$b_n = \frac{\psi_n(mx)\psi'_n(x) - m\psi_n(x)\psi'_n(mx)}{\psi_n(mx)\xi'_n(x) - m\xi_n(x)\psi'_n(mx)}$$

$$(2.89)$$

where the size parameter x is x=kr, for brevity, and m the relative index of refraction, $m = n_{sphere}/n_{medium}$. The prime notation refers to differentiation with respect to the argument of the function in each case. The field coefficients for internal fields can be similarly written by taking equations 4.52 from Bohren and Huffman, equating µ and $µ_1$, and changing to Riccati-Bessel functions:

$$c_n = \frac{\dfrac{\psi_n(x)}{x}\xi'_n(x) - \dfrac{\xi_n(x)}{x}\psi'_n(x)}{\dfrac{\psi_n(mx)}{mx}\xi'_n(x) - \dfrac{\xi_n(x)}{x}\psi'_n(mx)} = \frac{m\psi_n(x)\xi'_n(x) - m\xi_n(x)\psi'_n(x)}{\psi_n(mx)\xi'_n(x) - m\xi_n(x)\psi'_n(mx)}$$

$$d_n = \frac{m\dfrac{\psi_n(x)}{x}\xi'_n(x) - m\dfrac{\xi_n(x)}{x}\psi'_n(x)}{m^2\dfrac{\psi_n(mx)}{mx}\xi'_n(x) - \dfrac{\xi_n(x)}{x}\psi'_n(mx)} = \frac{m\psi_n(x)\xi'_n(x) - m\xi_n(x)\psi'_n(x)}{m\psi_n(mx)\xi'_n(x) - \xi_n(x)\psi'_n(mx)}$$

$$(2.90)$$

An examination of these coefficients shows that the denominators of d_n and a_n are equal, and the same with c_n and b_n. Also, if the denominator of any particular coefficient goes to zero, it will dominate the scattered and internal fields. This dominance condition for the a_n and d_n modes is then

$$m\frac{\psi_n(mx)}{\psi'_n(mx)} = \frac{\xi_n(x)}{\xi'_n(x)}$$

while, similarly, the b_n and c_n modes dominate when:

$$\frac{\psi_n(mx)}{\psi'_n(mx)} = m\frac{\xi_n(x)}{\xi'_n(x)}$$

While these conditions can be used to determine optical properties, radii, or the incident wavelength necessary for the desired resonance, to generate field strengths or absorption and scattering cross sections, it is necessary to calculate the coefficients across a range of wavelengths in any case.

D. Extinction and Scattering Cross Sections

The extinction and scattering cross sections are derived by taking the integrals of the Poynting vector of the scattered field, and the integral of the dot product of the scattered field interacting with the incident field to find power loss by scattering and extinction, respectively. Then these powers are divided through by the incident intensity to obtain the cross sections. For the case of a sphere, these can be written succinctly as:

$$C_{sca} = \frac{2\pi}{k^2} \sum_{n=1}^{\infty} (2n+1)\left(|a_n|^2 + |b_n|^2\right)$$

$$C_{ext} = \frac{2\pi}{k^2} \sum_{n=1}^{\infty} (2n+1)\operatorname{Re}(a_n + b_n)$$

(2.93)

A Mie program written for Maple is included in Appendix 1. This program calculates extinction, scattering, and absorption cross sections as functions of incident wavelength. The program also calculates scattered field as a function of wavelength at an arbitrary point, and scattered field on a grid of points at a selected wavelength. For the wavelength dependent sections for sizes up to 100 nm, the program is extremely fast, while for points on a grid, for grid sizes up to 10000 points (100 nm x 100 nm, for example), the computation of course takes longer, depending on the size of the particle and the size of the grid. This mapping of the scattered field may be commented out, allowing execution of the entire program to obtain only the wavelength dependant results. The program uses Maple's internal definitions of the spherical Bessel functions of the first kind, and the closed form for the spherical Hankel functions, which is more efficient than using Maple's definitions. Higher order functions are obtained by upwards recursion. The program reads in dielectric function data for the material making up the sphere from a text file that is formatted into 2 columns, the data being the real and imaginary parts, with 1 nm resolution by default, although this is adjustable. The data is taken from Palik's Handbook of Optical Constants of Solids[34], with this tabulated data being interpolated by fitting to a quadratic equation. The radius of the sphere and the index of refraction of the host medium are also adjustable, although it is important to note that the index of

refraction of the medium should be real. Finally, the calculation limits in terms of wavelength are also adjustable. The resultant wavelength dependant electric field vectors are saved into memory for later analysis, although the program by default computes the magnitude. The program does not save the vectors at all points on the grid, as for large grids this would overwhelm the available memory. Rather, it saves the magnitude instead, corresponding to a 6 fold decrease in memory usage.

The computation of the scattered field on a grid of points defaults to a grid that is perpendicular to the incident wave, chosen as being in the $\hat{z}$ direction. The length of the grid is chosen as twice the radius of the sphere, resulting in 120x120 points for a 30 nm sphere, rather than 200x200 points if the full grid was utilized. This 50 nanometer sphere is calculated up to 5th order, corresponding to 70 different spherical harmonics. Even with this time saving measure, calculating the 1,000,800 vector spherical harmonics is not a suitable problem for a pocket calculator.

The vector spherical harmonics use the formal definition described in section A of this chapter. Similar to the spherical Bessel functions, the associated Legendre polynomials and scalar spherical harmonics are not really well defined. Both Legendre polynomials and the scalar spherical harmonics use a different phase, whereas these calculations always apply the Condon-Shortly phase[22], and as well, different branch cuts. To solve this problem, the associated Legendre polynomials are obtained by upwards recursion of the functions themselves, then multiplied through by the desired phase and an exponential factor in the case of the spherical harmonics, and called with the independent variables that they correspond with. The Hankel functions in the vector spherical harmonics use the same closed form described before.

The advantage of using Maple is due to the ability to do precision calculations for the spherical Bessel functions. Rather than using numerical recursion to calculate high orders, the ability to make functional definitions at each order means that there is no loss of precision due to floating point arithmetic. This ability allows us to avoid the problem which has plagued this sort

of calculation in the past[10]. Fortunately, this would be true even for extremely large particles, in the micrometer range, although this sort of calculation would take days using this program.

The plasmon response of a nanoparticle depends on 4 parameters: The size, the shape, the material of the nanoparticle, and the material of the host medium. With Mie scattering, the shape is chosen, as it is the solution for a sphere, and variation of the three remaining parameters will cause a change in the plasmon of the particle. Results will first be presented for varying size, then for varying the host medium, and finally, examples of different materials will be presented.

The most common metal used for surface enhancement is silver. The Mie scattering will demonstrate why it is the most efficacious material when used as a nanometric enhancer. The extinction, absorption, and scattering cross sections for a 30 nm silver sphere, in vacuum (n_{host}=1), are shown in Fgure 2.1.
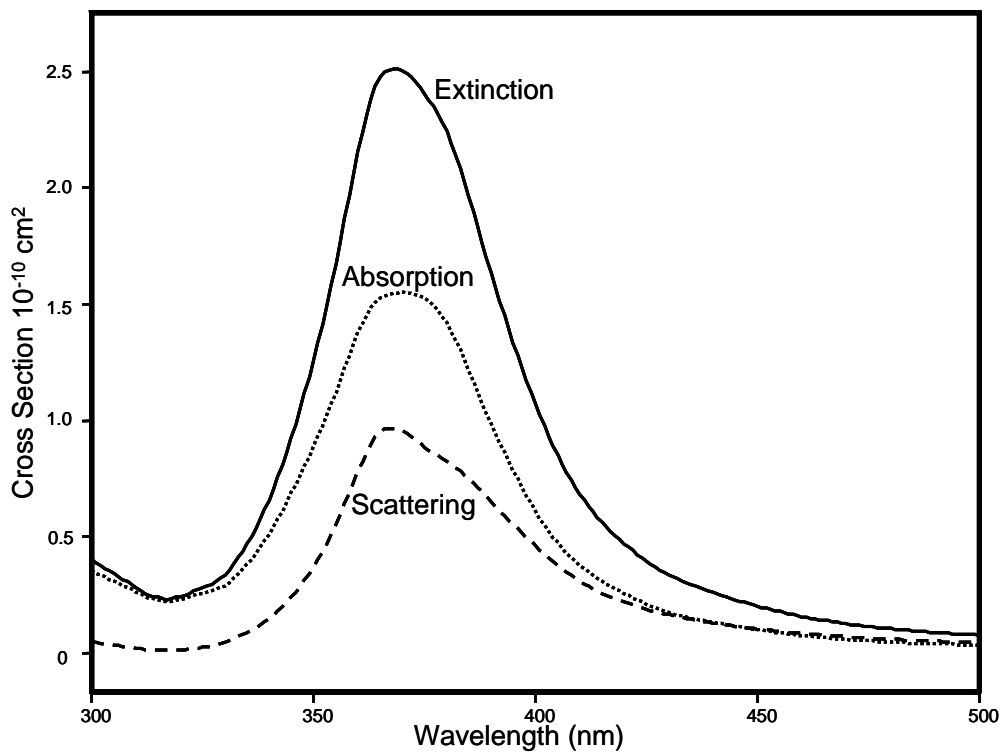
Figure 2.1. Extinction (solid), absorption (dotted), and scattering(dashed) cross sections as a function of wavelength for a 30nm silver sphere.

The extinction, absorption, and scattering cross sections peak at values of 368 nm, 370 nm, and 367 nm respectively.   For this size, the absorption is higher than the scattering, contributing 61.8 % of the extinction. This is a fairly typical example of colloidal results. While the absorption is a fairly symmetric, slightly truncated Lorentzian band, the scattering, and thus the extinction, are asymmetric. As the sphere radius increases, three things occur: (1) the cross sections increase, (2) the peaks shift to higher wavelengths, and (3) the peaks broaden. However, it is difficult to directly compare cross sections for particles of different sizes, because, while other factors contribute to the intensity, the particle itself has a direct effect. It is more useful to additionally calculate efficiencies (Q), defined as:

$$Q_{ext} = \frac{C_{ext}}{G}; Q_{sca} = \frac{C_{sca}}{G}; Q_{abs} = \frac{C_{abs}}{G}$$

(2.94)

Where C is the extinction, absorption, or scattering cross section, and G is the cross section area. In this case, the cross sectional area is easy to find, being πr^2. The changes in the spectra as a function of wavelength can be directly compared as efficiencies, as seen for 6 different radii in Figure 2.2
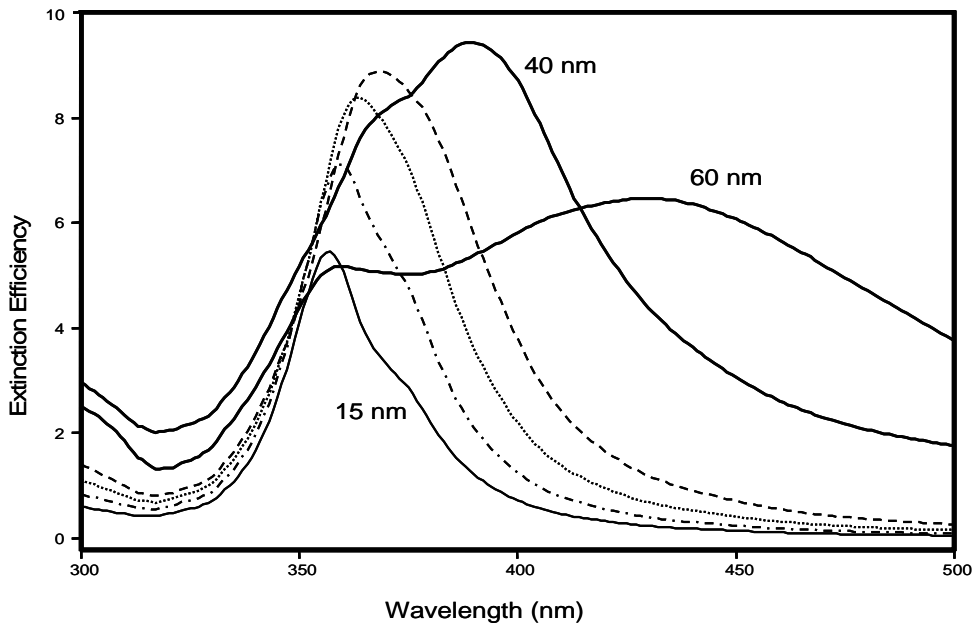
Figure 2.2. Extinction efficiency of 15 nm, 20 nm (dot-dash), 25 nm (dotted), 30 nm(dashed), 40 nm, and 60 nm silver spheres as a function of wavelength.

This trend towards increasing peak wavelength is clear, as well as a trend toward definite broadening of the peak. There are two other interesting details, namely, that as the extinction efficiency reaches a peak, it begins to drop off, and for the largest size shown, the shoulder that existed in smaller sizes resolves into a separate peak. The red-shift and damping of the main peak is due to radiation damping,[35,36] a feature which is included in the Mie calculation due to the dynamic nature of the calculation. When dipolar or dipolar and quadrupolar approximations are used, the radiation damping must be included in order to obtain results that agree with Mie theory, and thus experiment. The arrival, and subsequent splitting of the second peak is due to contribution of higher order moments. For smaller sizes, the higher order moments contribute, but not significantly, while for the larger sizes, the contribution approaches the same magnitude of the dipole moment.   The peak wavelength, intensity at the peak wavelength, full width at half maximum, peak area, extinction efficiency, and peak area divided by the cross sectional area, which are termed the area efficiency are given in table 2.1. The full width at half maximum (FWHM) is determined using Grams/AI 7.0 peak fitting routines, with a mixed Gaussian-Lorentzian band. These area efficiencies are normalized values of the total signal in each case.

Radius (nm)	Peak (nm)	Extinction Cross Section (10^{-11} cm^2)	FWHM (nm)	Peak Area (10^{-9} cm^{2}nm)	Efficiency	Area Efficiency (nm)
15	357	3.85	29.8	1.14	5.45	160.9
20	359	8.94	33.8	3.38	7.11	269.3
25	363	16.5	36.7	6.61	8.38	336.8
30	368	25.1	48.2	15.2	8.87	538.7
40	389	42.4	62.6	23.2	8.44	461.0
60	359	58.5	22.8	42.5	5.17	37.6
60	429	73.2	147.5	95.1	6.47	840.8

Table 2.1. Computed extinction results for silver spheres.

Peak Wavelength vs. Sphere Radius
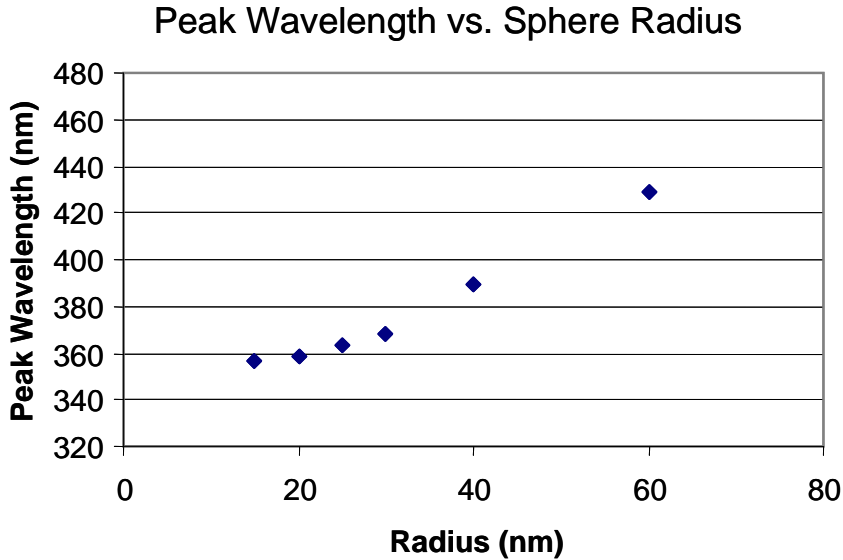
Figure 2.3. Peak wavelength of main peak vs. radius for silver spheres.

Although the efficiency peaks, the total normalized area of extinction in each case increases with size. And, as seen in the plot of peak wavelength vs. sphere radius, although the peak does red-shift to higher wavelengths, it does so at the cost of a much less well defined extinction.   It is worthwhile noting that the sphere response to a static field is given by

$$C_{ext} \propto \alpha = V \frac{\varepsilon - 1}{\varepsilon + 2}$$

(2.95)

for a sphere in vacuum, where α is the polarizability, V the volume, and ε is the dielectric function. This simple equation is a good predictor of peak location for very small particles, as resonance will occur when the dielectric function is equal to -2. For silver, this occurs at 354 nm, a value that is approached by for the smaller particles calculated with Mie theory. Unfortunately, this concept certainly does not apply for anything larger than 20 nm.

As surface enhanced phenomena depend on the scattered field, the scattering cross section is often a better indicator of the field enhancement than of the total extinction. The scattering efficiency for the same set of silver spheres is given in Figure 2.4, and numerical values in Table 2.2.
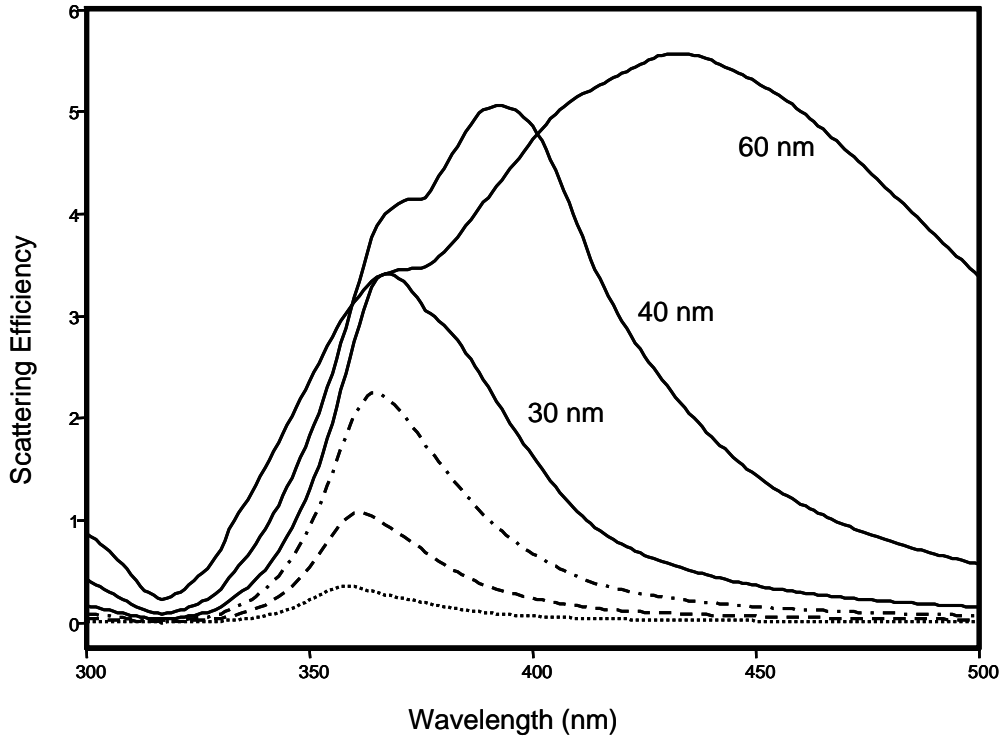
Figure 2.4. Scattering efficiency of silver spheres of 15 nm (dotted), 20 nm (dashed), 25 nm (dot-dash), 30 nm, 40 nm, and 60 nm.

Radius (nm)	Peak (nm)	Scattering Cross Section (10^{-11} cm^2)	FWHM (nm)	Area (10^{-9} cm^{2}nm)	Efficiency	Area Efficiency
15	358	0.255	29.0	0.791	0.361	11.2
20	361	1.34	33.4	0.642	1.070	51.1
25	365	4.41	37.8	2.37	2.248	120.8
30	367	9.63	41.6	3.92	3.405	138.7
40	364	18.9	21.8	1.46	3.764	29.1
40	393	25.4	63.4	21.0	5.057	416.9
60	359	34.9	23.6	2.28	3.083	20.2
60	433	63.0	128.1	81.4	5.567	719.9

Table 2.2. Computed scattering results for silver spheres.

The scattering efficiencies follow a different trend than the extinction. For the smallest particles calculated, the scattering is only a very small part of the extinction, while for larger particles, it becomes the dominant mode of dispersion. The basic trend is for the scattering efficiency to increase, the absorption

efficiency to decrease, and the extinction efficiency to make relatively small changes due to the summation of the scattering and absorption. Table 2.3 highlights this trend with the relevant cross sections and efficiencies for the six sizes computed.

So while it is true that the absorption efficiency decreases past 25 nm, it is also true that the absorption cross section begins to decrease after 40 nm, although these different sizes do have have the resolution necessary to make accurate determinations. The contribution by scattering to extinction increases monotonically, in conjunction with both the scattering cross section and scattering efficiency.

As stated previously, the host medium also effects the plasmon response of the particle. If the collective oscillations of the free electrons of the particle are considered to be harmonic oscillators, the dielectric medium surrounding the particle contributes to the damping, causing a red shift in peak frequency. The Mie extinction cross sections of a 30 nm particle in transparent solvents of vacuum (n_{vac}=1), water (n_{aqt}=1.33), ethanol (n_{eth}=1.36), carbon tetrachloride (n_{CCl4}=1.46) and benzene (n_{benz}=1.50) are shown in Figure 2.5. Figure 2.6 is a plot of peak wavelengths as a function of index of refraction of imbedding host.

Radius (nm)	Extinction Cross Section (10^{-11} cm^2)	Scattering Cross Section (10^{-11} cm^2)	Absorption Cross Section (10^{-11} cm^2)	Extinction Efficiency	Scattering Efficiency	Absorption Efficiency	% of Extinction due to Scattering
15	3.85	0.255	3.60	5.45	0.36	5.09	6.6
20	8.94	1.34	7.60	7.11	1.07	6.04	15.0
25	16.5	4.42	12.0	8.38	2.25	6.14	26.8
30	25.1	9.63	15.5	8.88	3.40	5.47	38.4
40	42.4	25.4	17.0	8.44	5.06	3.38	59.9
60	73.2	63.0	10.2	6.47	5.57	0.91	86.0

Table 2.3. Comparison of extinction, scattering, and absorption cross sections

and efficiencies for silver spheres.
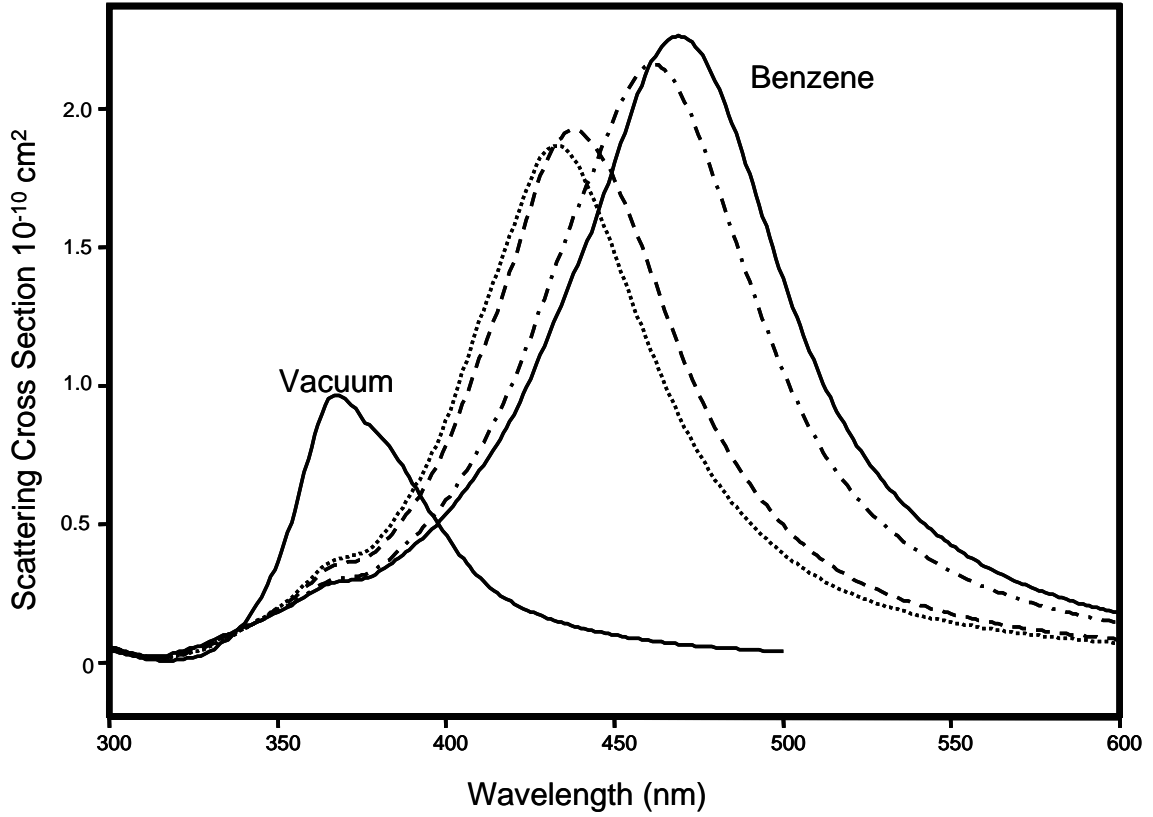
Figure 2.5. Mie Scattering cross sections of 30 nm silver particles in air, water (dotted), ethanol (dashed), carbon tetrachloride (dot-dash), and benzene.
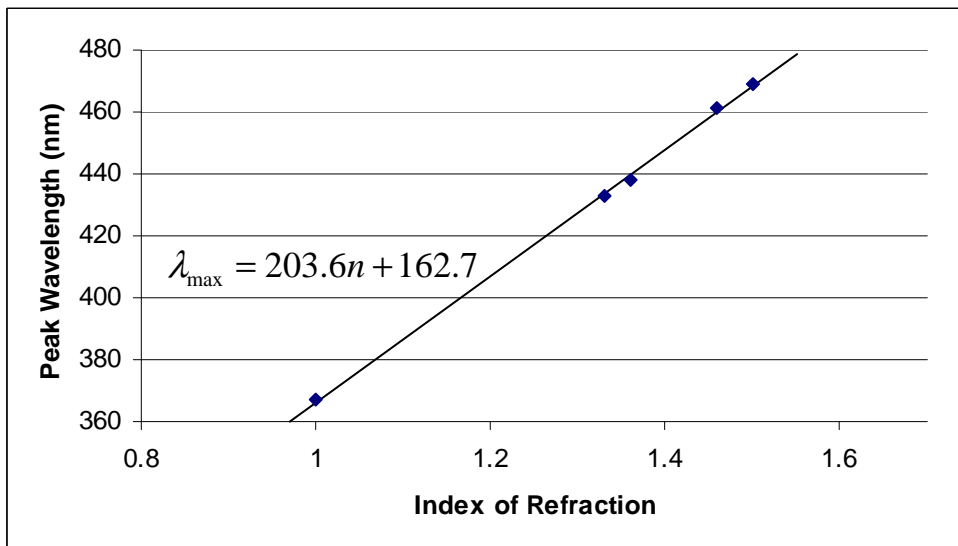
Figure 2.6. Plot of peak wavelength vs. Index of Refraction.

The relationship of peak wavelength with index of refraction is linear, with a regresion line of $\lambda_{max} = 203.6n + 162.7$, with a very acceptable R^2=0.9992. The line parameters will be both a function of particle size and material, and other variations of these physical features may not have a fit that is quite so clear.
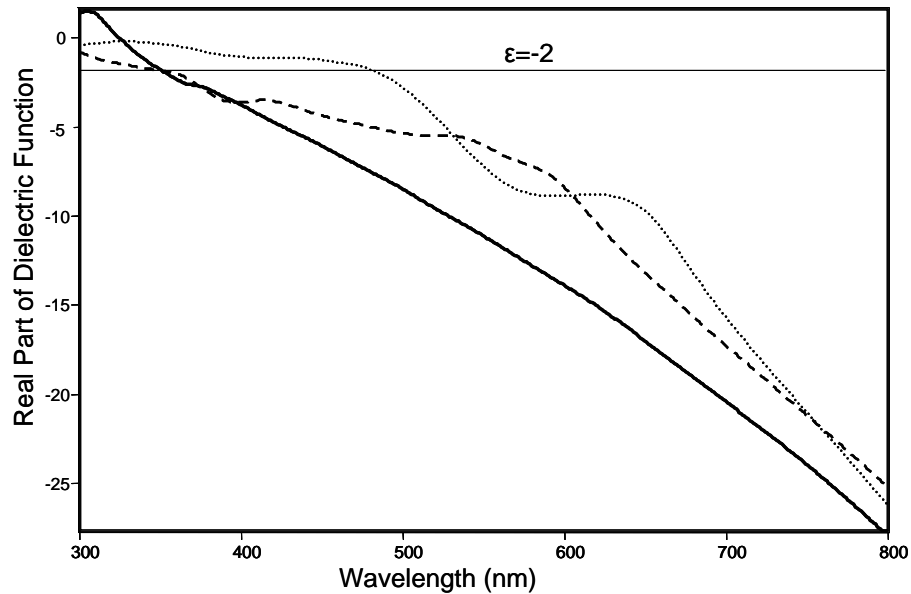
Figure 2.7. Real part of dielectric functions of Silver (solid), Gold (dotted) and Copper (dashed)
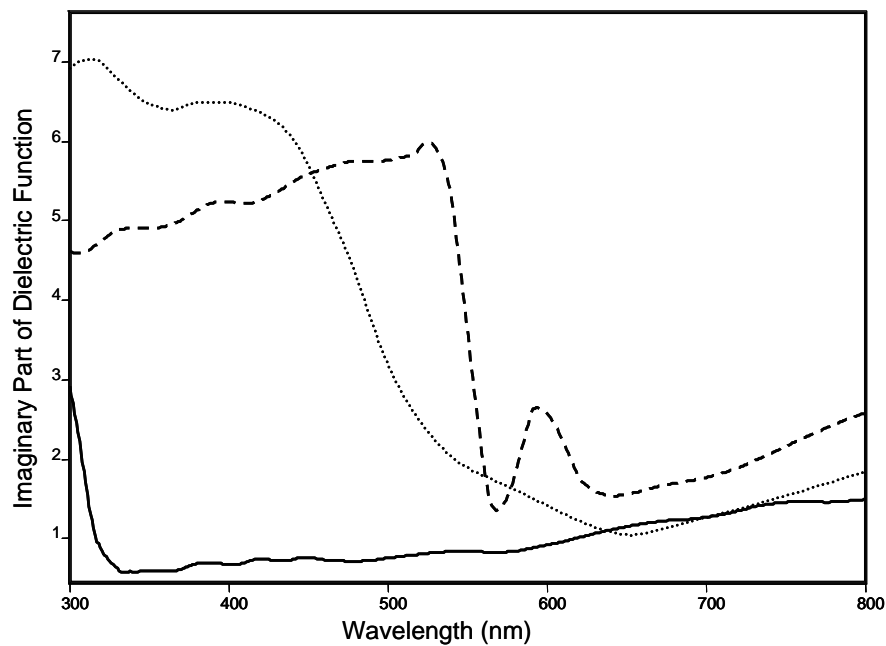
Figure 2.8. Real part of dielectric functions of Silver (solid), Gold (dotted) and Copper (dashed)

46

The final aspect of cross sections to consider is that of different materials. Three materials will be compared here, all noble metals: Silver, gold, and copper. Although the real part of the dielectric function is -2 in the visible range for each of them, at 354 nm, 486 nm, and 359 nm for silver, gold and copper respectively, the imaginary part of the dielectric function at these points are quite different, being 0.60, 3.96, 4.92 respectively. The real and imaginary parts of the dielectric function for these three materials is plotted in Figures 2.7 and 2.8, respectively. The imaginary part of the dielectric function corresponds to absorptive optical processes, and higher values will reduce the amount of scattering. Additionally, the higher imaginary value can also be thought of as contributing to damping, causing a decrease in peak quality. The low imaginary part of the dielectric function for silver is why it is used most often for plasmonics, as it has the clearest band strength, with little background. The extinction and scattering cross sections are shown in Figure 2.9 and 2.10, respectively, for 30 nm particles in vacuum.
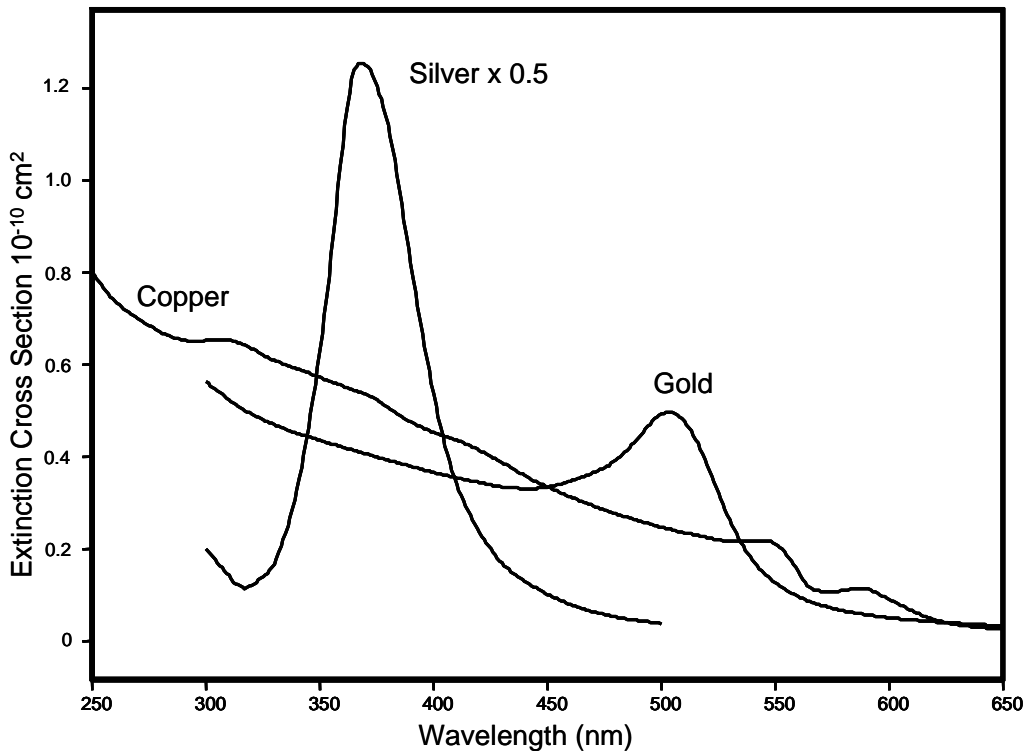
Figure 2.9: Extinction cross sections of Copper, Gold, and Silver. The intensity for silver is scaled by a factor of 0.5.
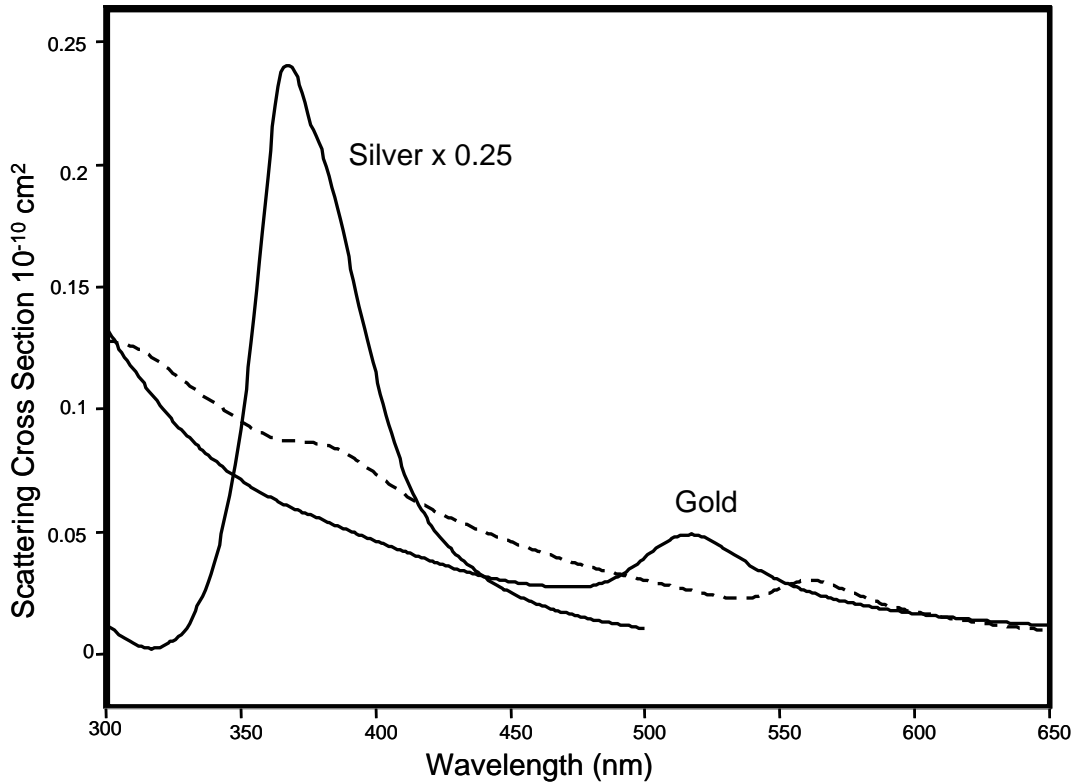
Figure 2.10: Scattering cross sections of Gold, Copper (dashed) and Silver. The intensity for silver is scaled by a factor of 0.25.

The extinction spectrum for 30 nm gold spheres shows a well defined, asymmetric peak located at 503 nm. It is noteworthy that this peak is approximately one sixth the intensity of that exhibited by silver for the same physical parameters, although these are both due to the dipolar resonance due to the dielectric function being -2, although it is slightly red-shifted due to the size of the particle. This difference is again due to the imaginary part of the dielectric function, as the denominator in the polarizability has a greater magnitude in the case of gold. The effect is even more pronounced in the case of copper, where there is no visible peak due to the very high damping. This is seen even more clearly in the scattering, although a small band centered at 562 nm is defined. This is in fact due to a decrease in the imaginary part of the dielectric function in this region of the spectrum, even though the real part is around -5.

The effect of the damping becomes clear when the polarizability equation is used. The imaginary parts of the dielectric function for silver, gold, and copper

at the wavelength where the real part of the dielectric function is -2 are 0.60, 3.96, 4.92, which yield

$$\alpha_{ag} = V\frac{\varepsilon-1}{\varepsilon+2} = V\frac{-3+i0.6}{i0.6}\cdot\frac{i0.6}{i0.6} = V\frac{i1.8+0.36}{0.36} = V(1+i5)$$

$$\alpha_{au} = V\frac{\varepsilon-1}{\varepsilon+2} = V(1+i0.7575) \qquad\qquad (2.96)$$

$$\alpha_{cu} = V\frac{\varepsilon-1}{\varepsilon+2} = V(1+i0.61)$$

Silver clearly has the greatest polarizability, and copper the least, causing the extinction and scattering to be considerably decreased in the case of gold and copper.

E. Calculation of the Near Field

The extinction and scattering cross sections are both derived from spatial integrals of the scattered field, whereas for surface enhanced spectroscopy, especially in the case of single molecule detection, the field at a specific point is more important. As surface enhanced Raman scattering, surface enhanced fluorescence, and surface enhanced infrared absorption all use detection of light over a spread of wavelengths to make spectroscopic characterization, it is important to be able to determine the field as a function of incident wavelength. The program included as Appendix B is able to calculate the scattered field as a function of frequency for an arbitrary point in space. The results presented here choose the point to be on the surface of the particle, along the axis of the incident electric field. Depending on the molecule that is used in surface enhancement, being at a point on the surface is highly probable, given that there may be molecule-metal chemical interactions that cause the molecule to chemically bond to the particle. The scattered field at this optimal point for field enhancement for 6 different sizes of silver spheres is presented in Figure 2.11.

The scattered field shows similar peaks to the scattering cross sections, although there they are slightly red shifted and broader. This because of the particular point chosen, whereas other points in space (for example, on the side of the sphere perpendicular to the incident field) will be blue-shifted, less intense, and narrower, giving the integrated response seen in the scattering cross section.
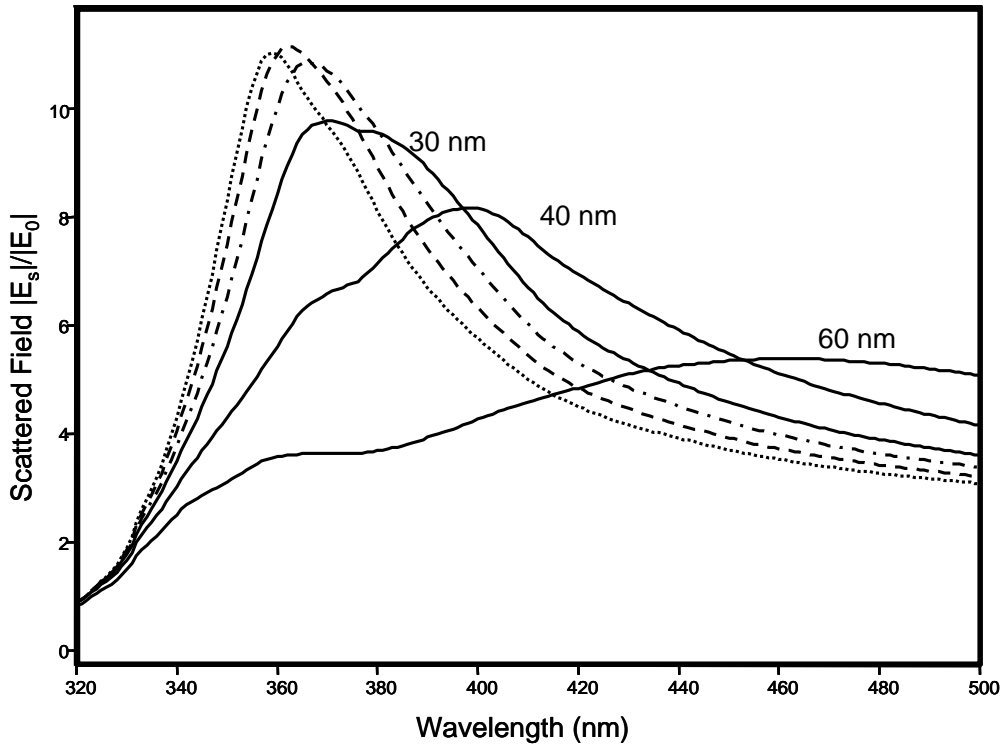
Figure 2.11: Scattered field by silver spheres of 15 nm(dotted), 20 nm (dashed), 25 nm(dot-dash), 30 nm, 40 nm, and 60 nm radii.

Although as the size increases, the scattering efficiency increases monotonically, the scattered field does not. There is clearly a peak value of the radius for which the field is strongest, which for the silver, is somewhere between 20 and 25 nm. This is because the scattering field exists at all points in space outside the particle. Considering the surface of the particle, where the scattered field is strongest, the larger particle clearly has a much larger surface area, so that even considering two particles of the same efficiency, the larger particle will have less field at any particular point, although the spatial normalized integrals (the efficiency) will be the same due to the larger integration area. Table 2.4 shows this trend, with an extra column where the efficiency is further divided by the cube of the radius. Because of the inherent asymmetry in the field peaks, due to the long tail at high wavelengths, they are curve fitted using a log-normal curve. For comparison, the scattering cross sections results for peak and FWHM are given in parenthesis. The scattered field intensity and volume normalized scattering efficiency are plotted in figure 2.12.

Radius (nm)	Peak (nm)	Relative Scattered Field Intensity	FWHM (nm)	Efficiency	Efficiency/R^3 (10^{-5} nm^{-3})
15	359 (358)	11.0	51.6 (29.0)	0.36	10.7
20	362 (361)	11.2	53.8 (33.4)	1.07	13.4
25	366 (365)	10.8	58.8 (37.8)	2.25	14.4
30	370 (367)	9.8	67.8 (41.6)	3.40	12.6
40	399 (393)	8.2	96.7 (63.4)	5.06	7.9
60	461 (433)	5.4	211.7 (128.1)	5.57	2.6

Table 2.4. Scattered field peak wavelength, relative intensity, FWHM, and scattering efficiency for silver spheres of 15, 20, 25, 30, 40, and 60 nm.
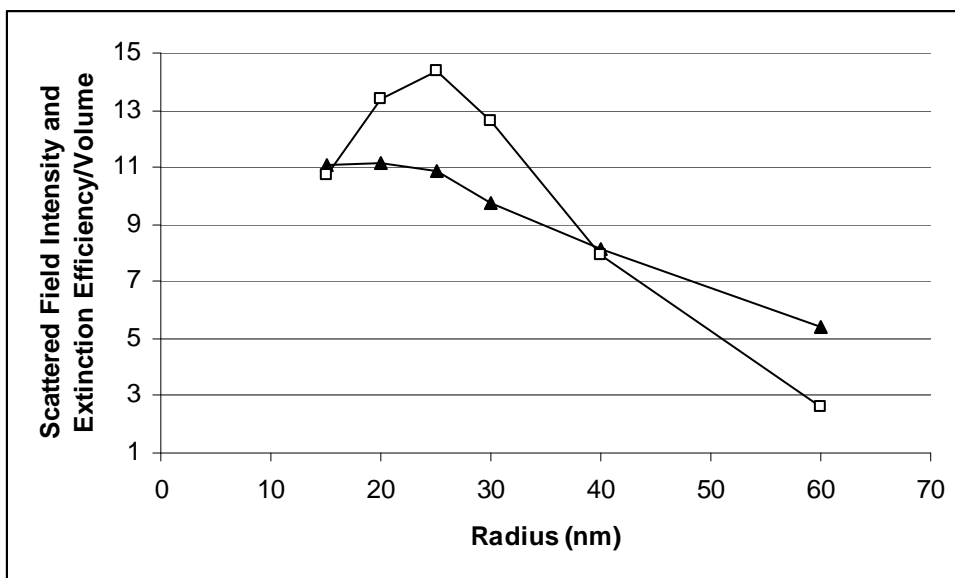
Figure 2.12 Plot of relative scattered field intensities (triangles) and extinction efficiencies divided by the cube of the radius (squares), as a function of radius.

Although the scattered field intensities and volume normalized extinction efficiencies are different quantities physically, they follow a similar trend. They each peak around the same wavelength (20-30nm), and decrease past that. The

relationship between them can be seen directly by plotting the field intensity, a microscopic quantity that is not directly observable against the volume normalized extinction efficiency, which can be calculated by extinction measurements. This is plotted in figure 2.13.
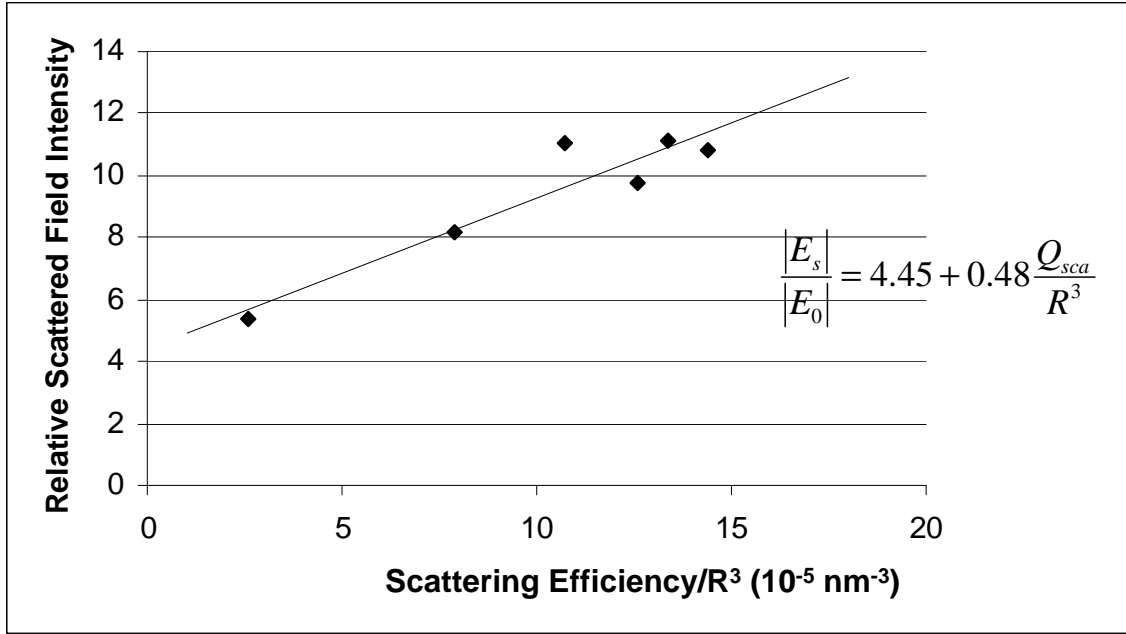
$$\frac{|E_s|}{|E_0|} = 4.45 + 0.48\frac{Q_{sca}}{R^3}$$

Figure 2.13 Plot of relative scattered field intensity against volume normalized scattering efficiency.

The regression line between these quantities is $\frac{|E_s|}{|E_0|} = 4.45 + 0.48\frac{Q_{sca}}{R^3}$, with an

R^2=0.88, which shows a linear trend. So although the peak size for enhancement may be determined for any material, it requires determination of the scattering for a variety of sizes. Any particle that is outside of the validity of the Rayleigh approximation requires Mie scattering, and there is no simple relationship for intensity as a function of size in this case.

Although larger particles may not be the best enhancers, other aspects of the plasmon response to light may be of great value to the experimentalist. The breadth of the peak, for example, means that the enhancement is well distributed for a variety of choices of laser lines, and a larger particle may be the best enhancer for high wavelength excitation.   An enhancing substrate that gives

moderate enhancement in both the visible and near infrared regions of the spectrum is an application for which large particles are very well suited.

Another variable to be considered is the field intensities at a point for different materials. As seen previously, the integrated results for copper and gold make them less ideal candidates for surface enhanced spectroscopy than silver. The near field calculation, however, also shows different trends than the integrated results, and so the field at a point on the surface is still the best indicator of enhancement results. The scattered field on the surface of 30 nm silver, gold, and copper particles in vacuum is shown in Figure 2.14.
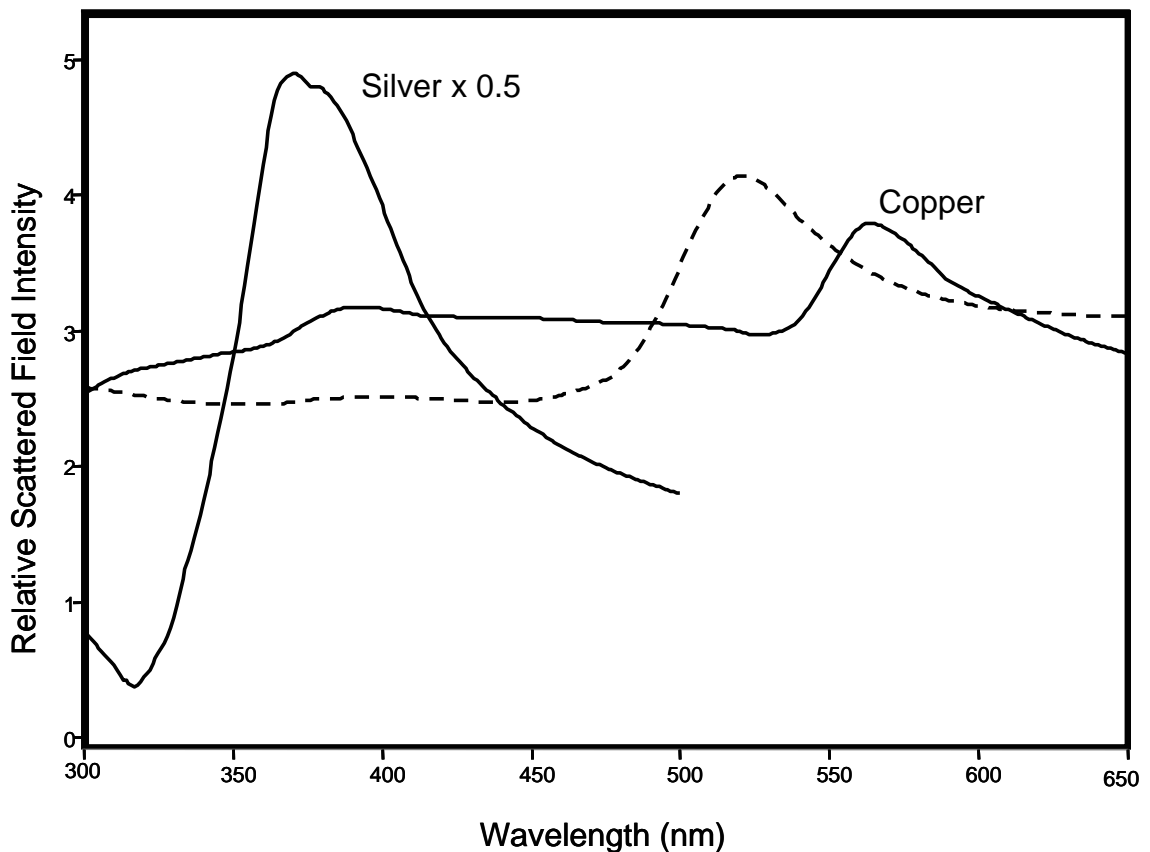
Figure 2.14 Relative scattered field intensity of silver, gold (dotted), and copper as a function of wavelength. The intensity of silver is scaled by 0.5.

At all wavelengths above 340 nm, silver has the strongest scattered field, although the tails in all three cases go asymptotically to ~2.5. Copper is a very consistent performer, being almost constant across the visible spectrum with a relative scattered field between 3 and 4 for the majority of wavelengths. The

peak noted in the scattering cross sections at 564 nm is present again, due to the drop in the imaginary part of the dielectric function, and as well, a small peak at 392 appears, corresponding to the dipolar resonance, which was not seen in the cross sections.

While scattered fields 10x higher than the incident field may not seem like much, the Raman signal goes as the 4th power of the total electric field[30]. The 30 nm silver particle discussed here will have a total field 11x higher than the incident, causing a surface enhanced Raman scattering (SERS) signal $1.4 \ 10^5$ times higher, a signal increase that is noteworthy indeed. As stated above, these three materials all have a relative scattered field around 2.5 as the near-infrared is approached, for a SERS enhancement of ~150.

The last variable to be considered in this section is the spatial distribution of the scattered field. The magnitude of relative scattered field is taken on points on a square grid that is perpendicular to the incident light, with twice the size of the radius along each axis. Results for 20 nm and 30 nm spheres are shown in Figure 2.15 with correct relative proportions, at 362 nm and 370 nm, respectively.
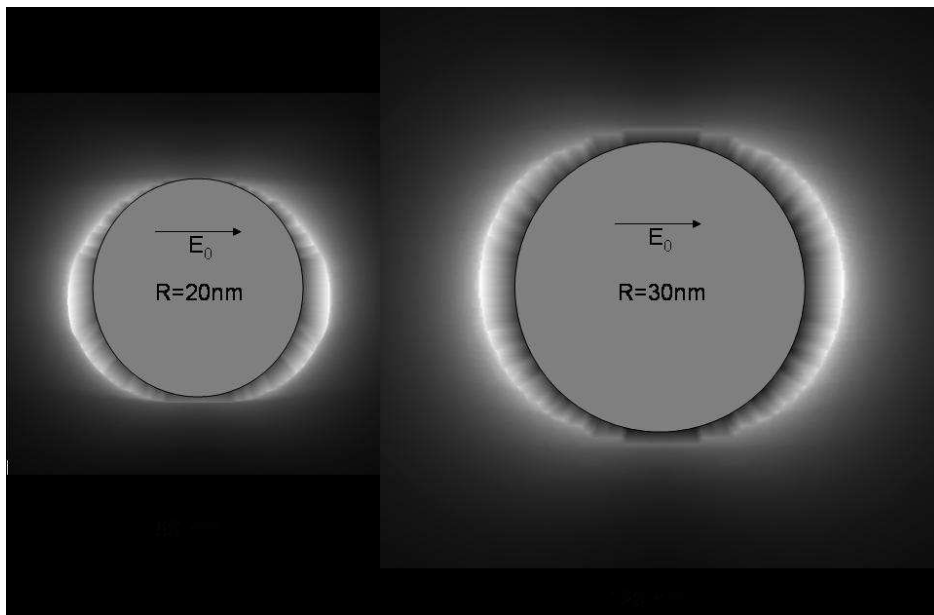
Figure 2.15 Scattered Field Intensities for 20 and 30 nm Silver Particles.

As seen in Figure 2.15   the regions of high intensity are in the direction of the incident field, with less intensity perpendicular to it. Also, for the 30 nm sphere,

the high intensity appears to reach out further away from the particle. The trend is shown in Figure 2.16.
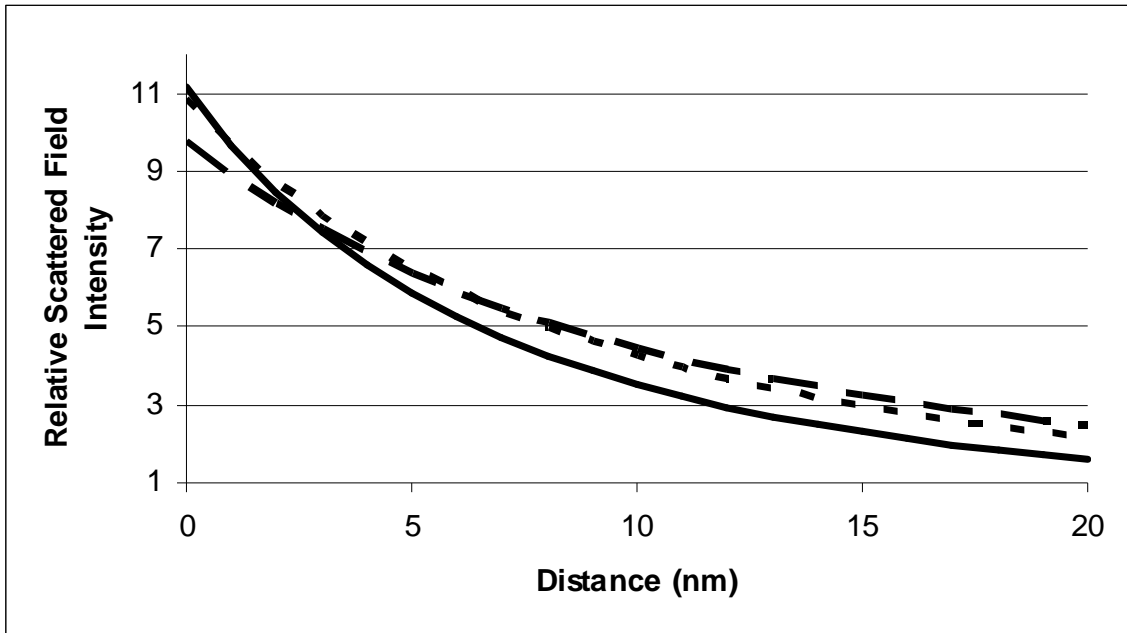
Figure 2.16 Relative scattered field intensity as a function of distance from surface for 20nm (solid), 25 nm (dotted), and 30 nm (dashed) silver spheres.

In materials, skin depth is defined as the distance it takes for the amplitude of a wave to drop by a factor of 1/e, where the intensity of the wave can be described by using an exponential[37]

$$E = E_0 e^{-kx}$$
(2.97)

where k in this case is the skin depth.   Since the plasmon is a wave bound to the metal, the scattered field should also decay exponentially away from the particle surface. This suggests taking the natural logarithm of the above data to obtain straight lines, as seen in Figure 2.17
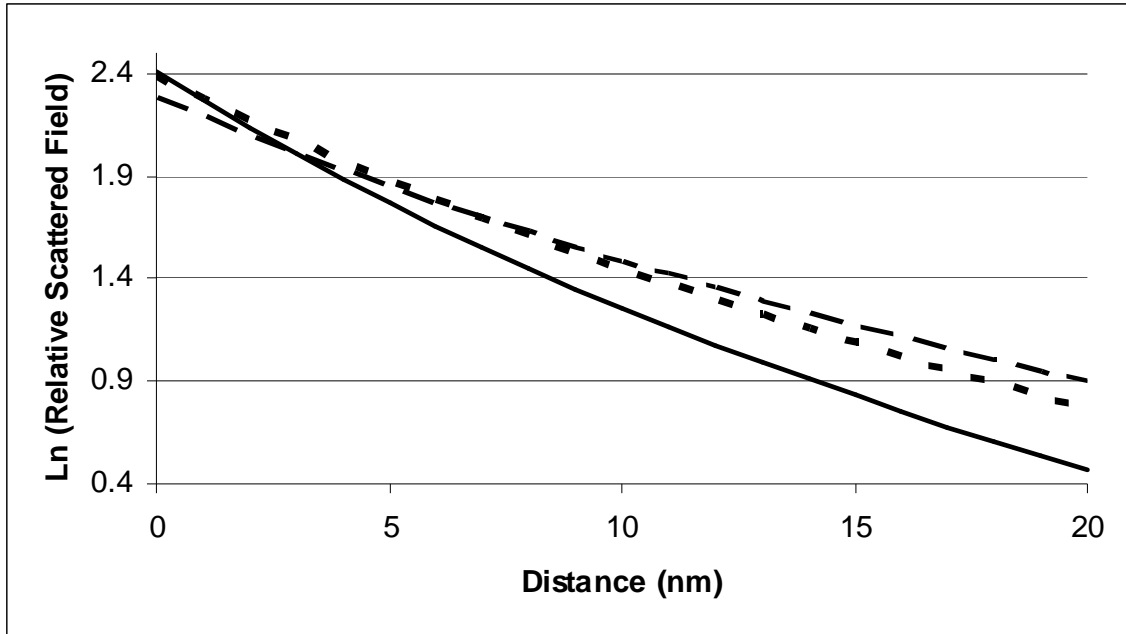
Figure 2.17 Natural logarithm of relative scattered field intensity as a function of distance from surface for 20nm (solid), 25 nm (dotted), and 30 nm (dashed) silver spheres.

Although the theory and computation for a single sphere has been a subject of scientific inquiry for slightly over a century, it is still a relevant model for plasmonics of dispersed particles, and also serves as an first order approximation for more complex or interacting structures. As well, the formalism that has been developed here has great utility for applications to more difficult problems, such as those seen in chapter 3, for nanoshells, and in chapter 5, for interacting spheres.

F. Bibliography

(1)   Mie, G. *Annalen der Physik* 1908, *25*, 377-445.
(2)   Bohren, C. F.; Huffman, D. R. *Absorption and Scattering of Light by Small Particles.*; Wiley: New York, 1983.
(3)   Jackson, J. D. *Classical Electrodynamics*; 3rd ed.; John Wiley and Sons: New York, 1999.
(4)   *Handbook of Mathematical Functions with Formulas, Graphs, and Mathematical Tables.*; 9 ed.; Abramowitz, M.; Stegun, I. A., Eds.; Dover Publications: New York, 1972.
(5)   Kerker, M. *The scattering of light and other electromagnetic radiation*; Academic Press, 1969.
(6)   *Handbook of Optical Constants of Solids*; Palik, E. D., Ed.; Academic Press, 1985.
(7)   Noguez, C. *Optical Materials* 2005, *27*, 1204-1211.
(8)   Noguez, C. *Journal of Physical Chemistry C* 2007, *111*, 3806-3819.
(9)   Le Ru, E. C.; Etchegoin, P. G. *Chemical Physics Letters* 2006, *423*, 63-66.
(10)   Griffiths, D. J. *Introduction to Electrodynamics*; 2nd ed.; Prentice Hall: Englewood Cliffs, New Jersey, 1989.

CHAPTER THREE
NANOSHELLS

A. Theoretical Background

Metal nanoshells occupy a prominent place in the field of metal nanostructures due to their remarkable optical properties. In particular, by tuning the relative core and shell dimensions, gold or silver nanoshells can be fabricated that absorb or scatter light at any wavelength across the entire visible and near-infrared regions of the electromagnetic spectrum[1-6].

Metal nanoparticles, in general, have surface plasmons that are sensitive to shape, size, and the dielectric properties of the surrounding medium, providing the variables that help to explain the particle's response to electromagnetic radiation. In addition, nanoshells have an additional unique degree of freedom provided by the thickness of the shell. The shell's thickness and size are shown to be the key variables in modeling and predicting the surface plasmon response to an electromagnetic field. However, it is often difficult determining the thickness of the shell.

There are a variety of applications for metal nanoshells, including biosensing[7] and drug delivery[8], optical waveguides, and spectroscopies which involve the near field, such as SNOM and surface-enhanced spectroscopies. Nanoshells of novel materials are also being fabricated for catalytic applications[9] or humidity sensing[10].

A great deal of the activity, especially with the optical properties of nanoshells, focuses on noble metal particles, especially gold.   The effect of the dielectric properties of the external environment has been well studied, both experimentally[11] and with Mie scattering[12], demonstrating that nanoshells are more sensitive to changes in external environments than collodial particles. It has also been well shown, computationally and experimentally, that there is a dramatic red-shift in the peak frequency with decreasing shell thickness[13]. The effects of rough and pinholed surfaces, as well as non-concentric sphere geometries, have been documented through FDTD[14] methods and DDA[15], and

work has also been done on the field densities on the surface and inside the core of nanoshells through modified Mie theory[16].

The following chapter examines the behaviour of surface plasmon resonances of metal nanoshells embedded with several different dielectric cores, using the full Mie formalism for extinction and scattering.   The further examination of surface plasmons of catalytic materials, such as platinum, rubidium, and maganese oxide may have important applications for future catalytic studies. Although the influence of the medium on single nanoparticles is well documented, there has been less work[17] done on the effects of the core, especially for conducting cores, such as those seen with Ag/Au core/shell systems.

Additionally, the use of novel core materials, such as dendrimers, which are well suited to the creation of uniform spherical structures, are discussed. Similar metal-organic hybrid materials may be generally characterized through techniques involving core/shell models such as those presented here.

Although the full Mie theory is the complete solution for computation of the optical properties of spherical particles[18], the physical interpretation of model systems is commonly found in the approximations, most notably, the static approximation. For example, for coated spheres the extinction cross section is given by[19] :

$$C_{ext} = 4R^2 k \, Im\left[\frac{(\varepsilon_{shell} - \varepsilon_m)(\varepsilon_{core} - 2\varepsilon_{shell}) + (1-g)(\varepsilon_{core} - \varepsilon_{shell})(\varepsilon_m + 2\varepsilon_{shell})}{(\varepsilon_{shell} + 2\varepsilon_m)(\varepsilon_{core} + 2\varepsilon_{shell}) + (1 - g)(2\varepsilon_{shell} - 2\varepsilon_m)(\varepsilon_{core} - \varepsilon_{shell})}\right]$$ (3.1)

Where R is the outer radius, k is the wavenumber, g is the volume fraction of the shell layer, and ε_{shell}, ε_{core}, and ε_m are the dielectric functions of the shell layer, core layer, and external medium, respectively.

Similar to the analysis by Templeton et $al.$ [20] on monolayer protected gold clusters, we are interested in maximizing the plasmon absorption. Since we are dealing with nanoshells, however, the shell thickness is a non-trivial quantity, and the approximation of the thickness going to zero would nullify the essential results. It is especially of interest to predict at what frequency or dielectric function value, the plasmon will be maximum, or, alternatively, for a chosen

material, what shell thickness is required to maximize the plasmon for a selected frequency. This allows for specific tailoring of the surface plasmon response of the nanoshell to whatever problem is at hand.

The surface plasmon modes are maximized in intensity when the real part of the denominator of equation 3.1 is zero, with the constraint that the imaginary part is also small. For clarity, the dielectric functions of the core and external medium are set to 1, although this is valid for any core and any non-absorbing external medium. For the moment assuming the dielectric function of the metal is real, and expressing this as a polynomial, we obtain:

$$(\varepsilon + 2)(1 + 2\varepsilon) + (1 - g)(2\varepsilon - 2)(1 - \varepsilon) = 0$$
$$2\varepsilon^2 + 5\varepsilon + 2 + (1 - g)(-2\varepsilon^2 + 4\varepsilon - 2) = 0$$
$$2g\varepsilon^2 + \varepsilon(9 - 4g) + 2g = 0 \tag{3.2}$$

where the dielectric function of the shell is expressed as ε for simplicity. This can be exactly true for a real ε, however, the materials of interest are absorbing, so we can express $\varepsilon = \varepsilon' + i\varepsilon''$, and take the real part to obtain::

$$2g\left(\varepsilon'^2 - \varepsilon''^2\right) + \varepsilon'(9 - 4g) + 2g = 0 \tag{3.3}$$

To obtain the thickness required for a specific material, g is solved for:

$$g = \frac{9\varepsilon'}{2(-\varepsilon'^2 + \varepsilon''^2 + 2\varepsilon' - 1)} = \frac{R_{shell}^3 - R_{core}^3}{R_{shell}^3} \tag{3.4}$$

Calculation of the dielectric function necessary for a given g is not quite as easy, as the real and imaginary parts may vary independently. Taking the negative root from the quadratic formula:

$$\varepsilon' = \frac{-9 + 4g - \sqrt{81 - 72g + 16g^2\varepsilon''^2}}{4g} \tag{3.5}$$

which admits a recursive solution. Use of tabulated values or a Lorentz type function for the dielectric function for the material of interest generates the frequency of the plasmon.

Although the static expression of the extinction cross section is useful for probing the basic underlying physics of the problem, the solution is not valid for particles unless they are significantly smaller than the wavelength of light.

Additionally, this form of solution is only valid in regions where the imaginary part of the index of refraction is small. For larger nanoshells, or in regions where the damping is high, the extended Mie equations must be used.

The Mie formalism extended to hollow particles is well detailed in a number of references[18,21], although a brief outline of the modified Mie coefficients for the sake of clarity is presented here. For a two layer sphere with inner radius a, and outer radius b, giving size parameters for x=ka and y=kb, and the indicies of refraction relative to the host medium of m_1 and m_2 for the core and shell, the scattering coefficients a_n and b_n are:

$$a_n = \frac{\psi_n(y)\left[\psi'_n(m_2 y) - A_n\varsigma'_n(m_2 y)\right] - m_2\psi'_n(y)\left[\psi_n(m_2 y) - A_n\varsigma_n(m_2 y)\right]}{\xi_n(y)\left[\psi'_n(m_2 y) - A_n\varsigma'_n(m_2 y)\right] - m_2\xi'_n(y)\left[\psi_n(m_2 y) - A_n\varsigma_n(m_2 y)\right]}$$

$$b_n = \frac{m_2\psi_n(y)\left[\psi'_n(m_2 y) - B_n\varsigma'_n(m_2 y)\right] - \psi'_n(y)\left[\psi_n(m_2 y) - B_n\varsigma_n(m_2 y)\right]}{m_2\xi_n(y)\left[\psi'_n(m_2 y) - A_n\varsigma'_n(m_2 y)\right] - \xi'_n(y)\left[\psi_n(m_2 y) - B_n\varsigma_n(m_2 y)\right]}$$

(3.6)

where ψ_n, ς_n, and ξ_n are the Riccati-Bessel functions of the first, second, and third kind, respectively, which are the spherical Bessel functions multiplied by the argument:

$$\psi_n(\rho) = \rho j_n(\rho)$$
$$\varsigma_n(\rho) = \rho y_n(\rho)$$
$$\xi_n(\rho) = \rho h_n^{(1)}(\rho)$$

(3.7)

and A_n and B_n are

$$A_n = \frac{m_2\psi_n(m_2 x)\psi'_n(m_1 x) - m_1\psi'_n(m_2 x)\psi_n(m_1 x)}{m_2\varsigma_n(m_2 x)\psi'_n(m_1 x) - m_1\varsigma'_n(m_2 x)\psi_n(m_1 x)}$$

$$B_n = \frac{m_2\psi_n(m_1 x)\psi'_n(m_2 x) - m_1\psi_n(m_2 x)\psi'_n(m_1 x)}{m_2\varsigma'_n(m_2 x)\psi_n(m_1 x) - m_1\psi'_n(m_1 x)\varsigma_n(m_2 x)}$$

(3.8)

if $m_2=m_1$, A_n and B_n are both zero, reducing the problem to that of a sphere, as expected. The extinction and scattering cross sections are the same as those of a sphere:

$$C_{sca} = \frac{2\pi}{k^2}\sum_{n=1}^{\infty}(2n+1)\left(|a_n|^2 + |b_n|^2\right)$$

$$C_{ext} = \frac{2\pi}{k^2}\sum_{n=1}^{\infty}(2n+1)\mathrm{Re}(a_n + b_n)$$

(3.9)

62

The convergence criterion given by Bohren and Huffman for spheres is applied. The calculations were done using Maple, and the optical properties of the metals were taken from Palik's Handbook[22]. The program results were checked against published data to ensure proper coding.

B. Results

Due to the unique properties of nanoshells, the plasmon is tunable across a wide range of electromagnetic frequencies, allowing electromagnetic interaction for materials in regions that were not previously accessible. The ability to predict the plasmon position in a systematic way opens possibilities to use existing, well known materials in novel ways. For example, as demonstrated with gold shells over polystyrene cores[23], the plasmon for gold is projected into the near infrared region for realistic geometries, allowing plasmon based phenomena, such as surface-enhanced spectroscopies, to be explored in regions which were not previously viable. The theory presented in the previous section gives accurate results for small particles of ideal materials. However, for practical applications, more rigorous methods must be used.

The surface plasmon of nanoshells of gold, silver, and iridium are studied through extended Mie theory. for a variety of dielectric cores (vacuum, aqueous, silica, polystyrene, and dendrimer), for a range of sizes, ranging from 20nm to 100 nm shell radii, with a variety of core radii. Gold core/silver shell and silver shell/ gold core systems are also calculated for the same size range.

The surface plasmon extinctions for silver particles of outer radius 20nm are shown in Figure 3.1. Both the core and external media are considered to be vacuum. A strong red-shifting of the peak wavelength is observed with decreasing shell thickness, accompanied by a modest increase in extinction cross-section. In order to compare the effects of changing the index of refraction of the core, the peak frequencies for the same shell sizes are calculated, and are seen to be linear, as shown in Figures 3.2 and 3.3 for vacuum, aqueous, silica, dendrimer cores for 60, 40, and 20 nm outer radii. Polystyrene and dendrimers have a similar indicies of refraction (1.57 for dendrimer, and 1.59 for polystyrene). Additionally, the peak position can be related to the index of refraction for the core, as also seen in Figures 3.2 and 3.3 for a silver nanoshell of constant volume ratios between inner and outer radii.
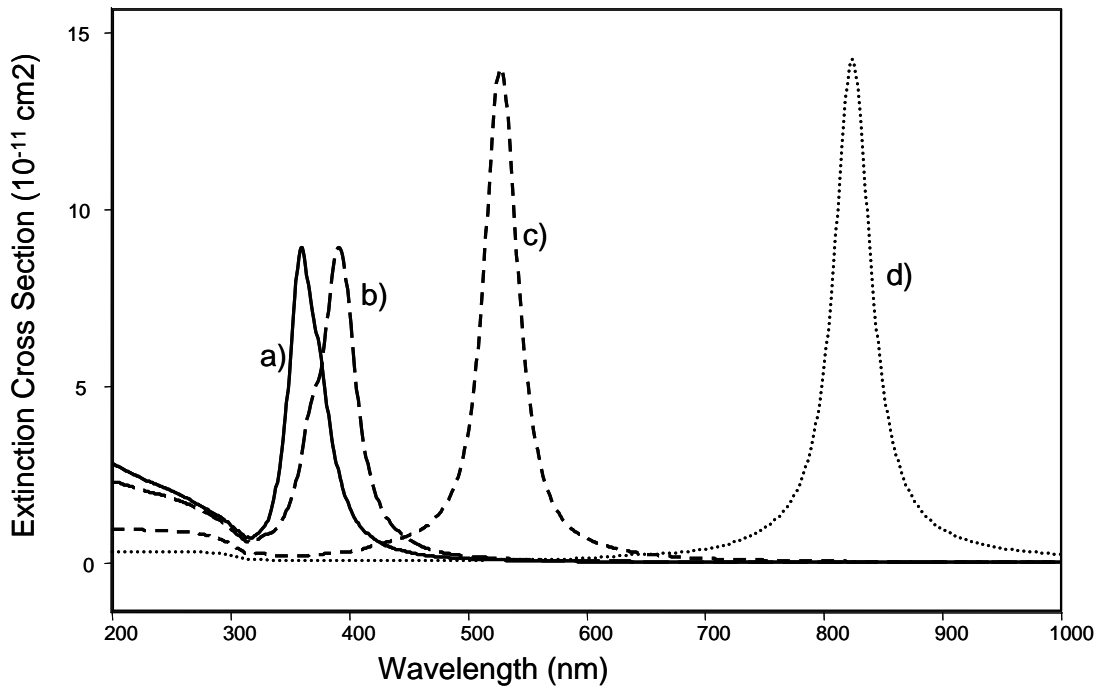
Figure 3.1. 20 nm outer radius of Ag: a) Solid line, sphere. b) Long dash, 11 nm inner radius. c) Short dash, 17 nm inner radius. d) dotted line, 19 nm inner radius.
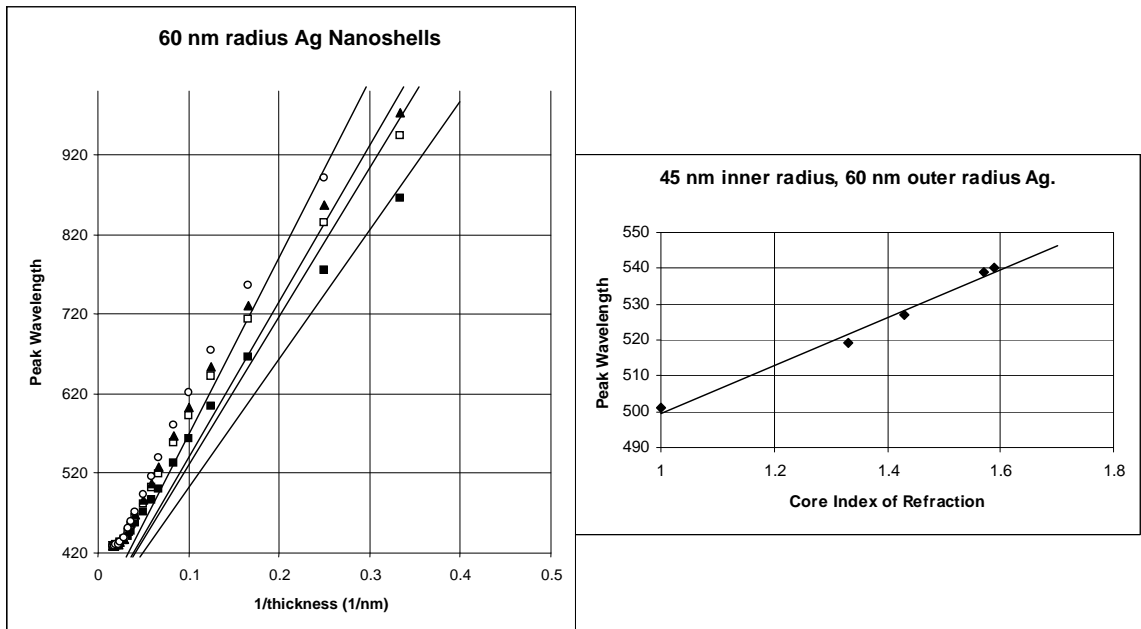
Figure 3.2: Peak wavelength vs. inverse shell thickness for Ag nanoshells of 60 nm outer radius, and peak wavelength vs. core index of refraction for 0.587 core/shell volume ratio for Ag nanoshells of 60nm outer radius.
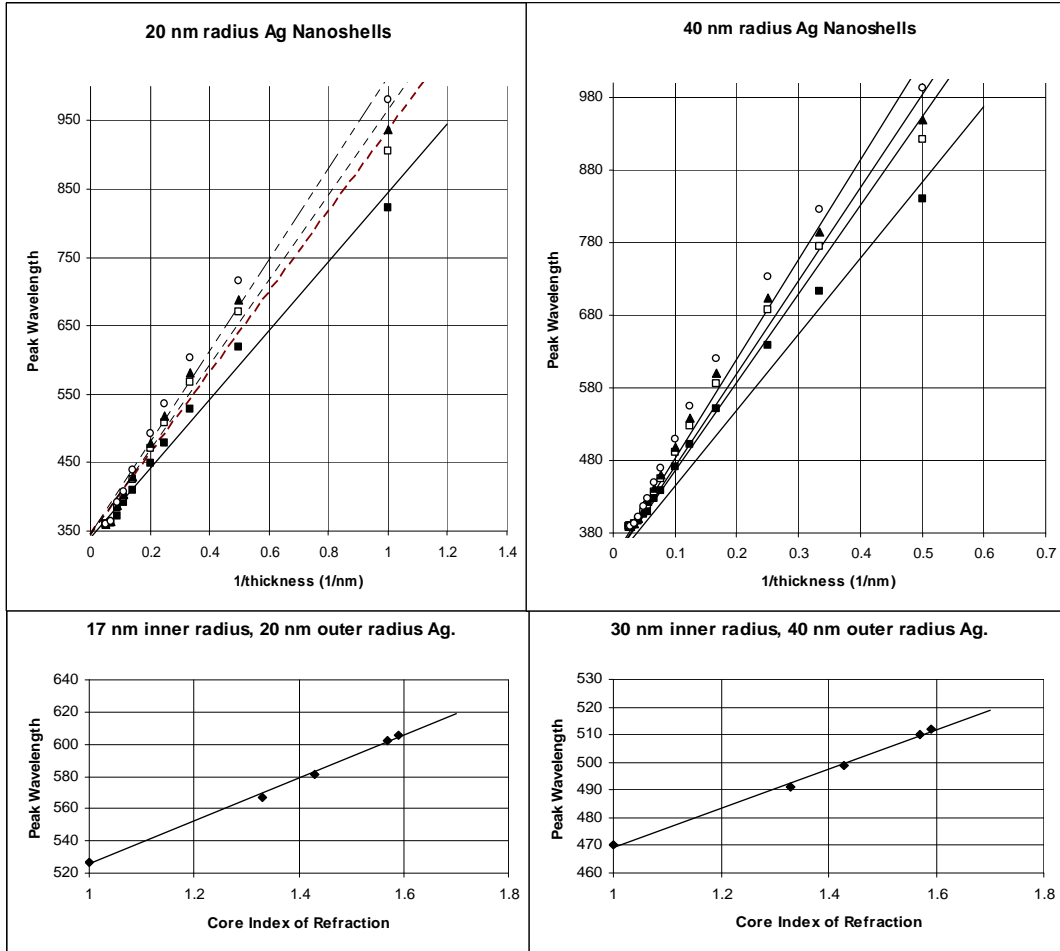
Figure 3.3: Peak wavelength vs. inverse shell thickness for Ag nanoshells of 20 and 40 nm outer radius, and peak wavelength vs. core index of refraction for 0.587 core/shell volume ratio for Ag nanoshells of 20 and 40nm outer radius.

Taking a least-square fit of the peak position vs. inverse thickness as a function of core index of refraction yields a linear expression of peak position as a function of both shell thickness and core index:

$$\lambda_{\max} = \frac{1}{t}\left(mn_{core} + b_2\right) + b_1$$

(3.7)

where t is the nanoshell thickness, b_1 is the wavelength at which the solid sphere peaks, b_2 is a constant based on how quickly the peak shifts only as a function of shell thickness. Similar results are shown for silver nanoshells of 40nm and 60 nm, with Figure 3.3 showing peak wavelength as a function of core index of refraction, with the same core/shell volume ratio. Table 3.1 gives these

phenomenological parameters for silver nanoshells up to 100nm in size. As it has been previously shown[12] that the peak position is also linearly dependant on external environment, this can also be included for any specific case.

Material and Size			
	m	b2	b1 (nm)
Ag, 20 nm	290.2	209.1	343.7
Ag, 40 nm	598.4	399.4	362.3
Ag, 60 nm	1137.9	275.3	396.1
Ag, 80 nm	1337.9	445.4	452.3
Ag, 100 nm	1463.9	440.9	535.2

Table 3.1. Calculated parameters for use in equation 3.7, from Mie calculations

It is no surprise that a dielectric core causes a red shift in the plasmon wavelength. As pointed out by Prodan et. al.[17], an interaction with a dielectric can be thought of as a reduction of the restoring force in the oscillation of the electrons due to polarization of the dielectric in response to the electric field. A corresponding reduction of extinction cross-section is also observed with higher index of refraction, pointing to a relative decrease in induced surface charge caused by the polarization of the medium.

The use of dendrimers as a dielectric core, as used here, involves idealizing the dielectric response to a static value. It has been shown[24] that the optical properties of dendrimers vary slowly as a function of frequency, as do many organic compounds in the optical region. The ability to make quantitative predictions for a range of dielectric cores, as above, allows not only for an accurate analysis of the plasmon response of the organic-metal hybrid for a specific value, but can take into account the frequency dependence of the core. Although dendritic materials are ideal for the creation of spherical metal shells, the analysis includes any organic-metal composites which have favorable

chemical, thermodynamic, or optical properties. The dendrimers considered here are fluorinated dendritic thermoset polymers, based on hyperbranched fluorinated polymers[25,26].

Due to the extreme red-shifting properties of the nanoshells, materials not previously studied with optical techniques may be observed, giving new opportunities for surface-enhancing substrates, optical waveguides, and optoelectronic materials. A recent study of nanoshells of MnO_2 is an example[9] of materials of great catalytic value.   For example, Ir nanoparticles absorb in the UV region, but due to red-shifting with decreasing shell thickness, the plasmon is broadened, and moved into the visible, as seen in Figure 3.4 for 20 nm radius Ir nanoshells in vacuum.
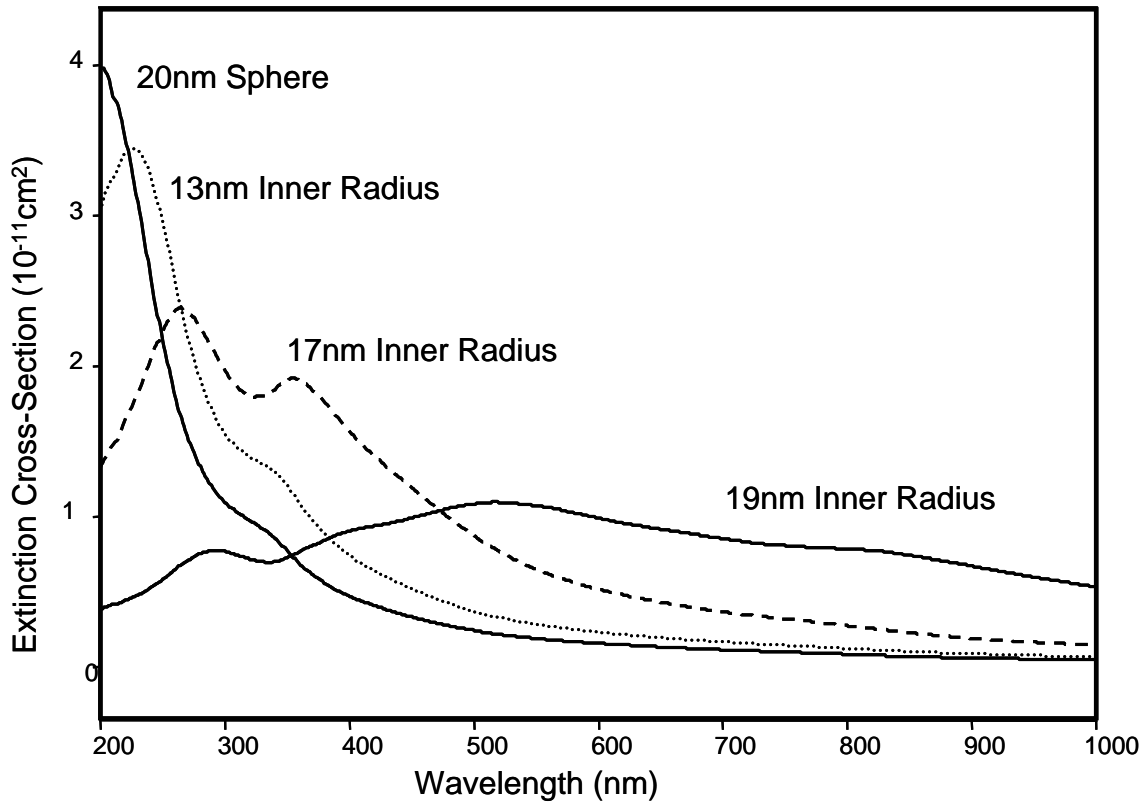
Figure 3.4. Extinction Cross Section of Ir nanoshells, outer radius 20nm, vacuum core.

The optical properties of silver, especially the low damping in the optical region, gives the ideal linear response of the peak wavelength, as a function of both shell thickness and core optical properties. For other materials, such as Au

and Ir, the imaginary part of the index of refraction is not negligible, and the dependence of the peak wavelength on shell thickness is not as well behaved. As seen in Figure 3.4, the peak frequency shifts discontinuously due to the increased damping in regions of longer wavelength, and new peaks form due to differing resonance conditions brought on by the frequency dependant optical properties. The use of Drude model dielectric functions will avoid these difficulties, and give idealized results, but are often not properly representative of the physical system being studied.

For any particular shell thickness, it is still possible to extract peak dependence as a function of the index of refraction of the core material. Figure 3.5 shows 40 nm external radius gold nanoshells, with a 34 nm inner radius, for vacuum, aqueous, silica, dendrimer, and polystyrene cores, with the inset showing the linear response of the peak frequency with respect to core material.
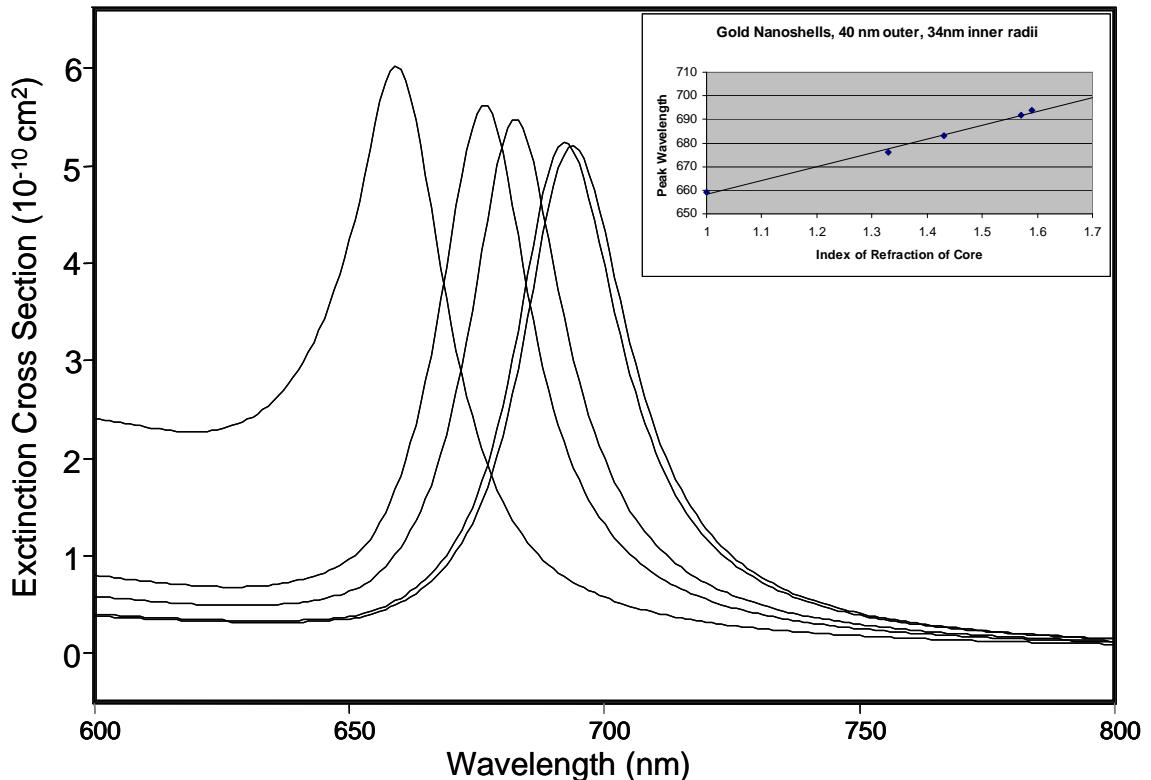
Figure 3.5. Plasmon response of Au nanoshells, 40 nm outer radius, 34 nm inner radius, for vacuum, aqueous, silica, dendrimer, and polystyrene cores.

An interesting case is when the optical properties of the core also change as a function of wavelength, as concentric shells of materials, such as silver/gold shell systems, or gold/silver[27]. The optical absorption of such composites can be a strong indicator of structure. As seen in Figure 3.6, for the same molar ratio between gold and silver, the optical absorption of the different core/coating configurations differ. As there is no dielectric response to the applied electromagnetic field, the characteristic red shift observed for hollow particles does not appear. For comparison, the optical extinction of binary composites with the same molar ratios is shown in Figure 3.7, with the optical properties of the mixture calculated through Maxwell-Garnet effective medium theory[28,29], and then the Mie extinction of the effective dielectric function taken.
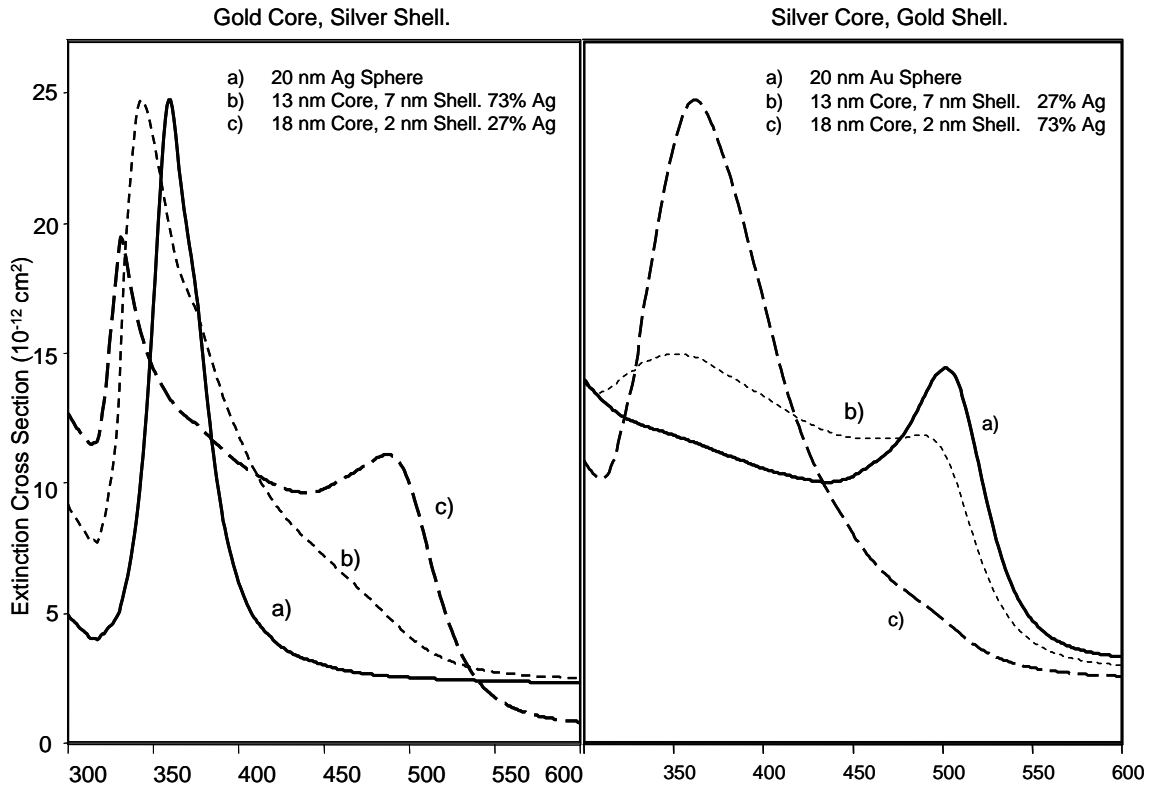
Figure 3.6. Plasmon response of silver/gold and gold/silver core/shell systems.
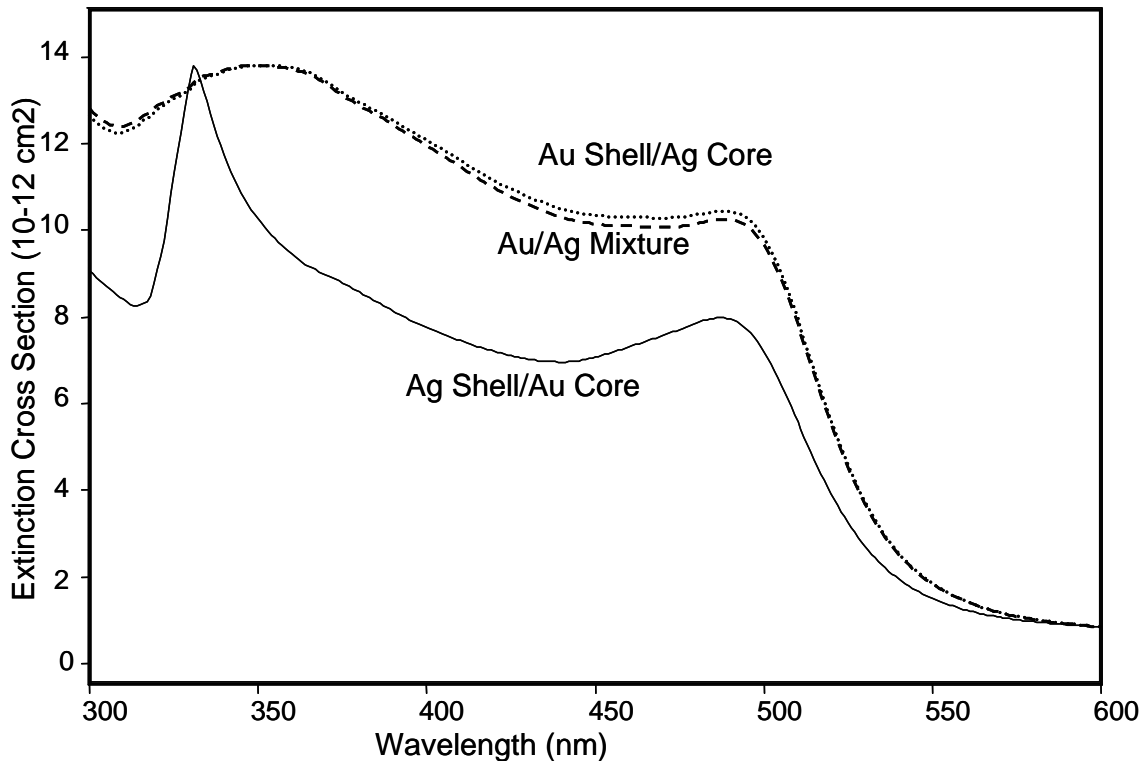
Figure 3.7. Plasmon response of silver/gold and gold/silver core/shell systems, contrasted with mixtures from effective medium theory, for 27% Ag by Volume.

Interestingly, the mixture of 27% silver gives very similar results to the silver/gold core/shell system. For this structured system, the silver has hardly any effect, as the light mostly interacts with the gold shell, although the silver core does play a role. If the silver is on the outer layer, however, the result is very different from the binary mixture, yielding a peak characteristic of a gold sphere, modulated by the larger gold core.

For ideal materials, the surface plasmon response of nanoshells can be treated linearly using extended Mie theory. Application of static results for coated spheres also allows for fast and accurate predictions, provided the materials have low damping and are small compared to the frequency of light. Computed Mie extinction for realistic systems of gold and silver compare well to published experimental results.

C. Bibliography

(1)   Jackson, J. B.; Halas, N. J. *Journal of Physical Chemistry B* **2001**, *105*, 2743-2746.

(2)   Oldenburg, S. J.; Jackson, J. B.; Westcott, S. L.; Halas, N. J. *Applied Physics Letters* **1999**, *75*, 2897.

(3)   Prodan, E.; Radloff, C.; Halas, N. J.; Nordlander, P. *Science* **2003**, *302*, 419.

(4)   Radloff, C.; Halas, N. J. *Nano Letters* **2004**, *4*, 1323.

(5)   Hirsch, L. R.; Stafford, R. J.; Bankson, J. A.; Sershen, S. R.; Rivera, B.; Price, R. E.; Hazle, J. D.; Halas, N. J.; West, J. L. *Proceedings of the National Academy of Science of the United States of America* **2003**, *100*, 13549.

(6)   Lal, S.; Grady, N. K.; Kundu, J.; Levin, C. S.; Lassiter, J. B.; Halas, N. J. *Chemical Society Reviews* **2008**, *37*, 898-911.

(7)   Wang, Y.; Xie, X.; Wang, X.; Ku, G.; Gill, K. L.; O'Neal, D. P.; Stoica, G.; Wang, L. V. *Nano Letters* **2004**, *4*, 1689-1692.

(8)   Svarovsky, S. A.; Szekely, Z.; Barchi, J. J. *Tetrahedron: Asymmetry* **2005**, *16*, 587-598.

(9)   Wang, L.; Ebina, Y.; Takada, K.; Sasaki, T. *Chemical Communications (Cambridge, United Kingdom)* **2004**, 1074-1075.

(10) Pal, B. N.; Basu, S.; Chakravorty, D. *Journal of Applied Physics* **2005**, *97*, 034311/1-034311/4.

(11) Sun, Y.; Xia, Y. *Analytical Chemistry* **2002**, *74*, 5297-5305.

(12) Tam, F.; Moran, C.; Halas, N. *Journal of Physical Chemistry B* **2004**, *108*, 17290-17294.

(13) Sun, Y.; Xia, Y. *Analyst*, *128*, 686-691.

(14) Oubre, C.; Nordlander, P. *Journal of Physical Chemistry B* **2004**, *108*, 17740-17747.

(15) Hao, E.; Li, S.; Bailey, R. C.; Zou, S.; Schatz, G. C.; Hupp, J. T. *Journal of Physical Chemistry B* **2004**, *108*, 1224-1229.

(16) Schelm, S.; Smith, G. B. *Journal of Physical Chemistry B* **2005**, *109*, 1689-1694.

(17) Prodan, E.; Lee, A.; Nordlander, P. *Chemical Physics Letters* **2002**, *360*, 325-332.

(18) Bohren, C. F.; Huffman, D. R. *Absorption and Scattering of Light by Small Particles.*; Wiley: New York, 1983.

(19) Mulvaney, P. *Langmuir* **1996**, *12*, 788.

(20) Templeton, A. C.; Pietron, J. J.; Murray, R. W.; Mulvaney, P. *Journal of Physical Chemistry B* **2000**, *104*, 564-570.

(21) Aragon, S. R.; Elwenspoek, M. *Journal of Chemical Physics* **1982**, *77*, 3406.

(22) *Handbook of Optical Constants of Solids*; Palik, E. D., Ed.; Academic Press, 1985.

(23) Shi, W.; Sahoo, Y.; Swihart, M. T.; Prasad, P. N. *Langmuir* **2005**, *21*, 1610-1617.

(24)   Pitois, C.; Vestberg, R.; Rodlert, M.; Malmstrom, E.; Hult, A.; Lindgren, M. *Optical Materials* **2002**, *21*, 499.
(25)   Pitois, C.; Vestberg, R.; Rodlert, M.; Malmstrom, E.; Hult, A.; Lindgren, M. *Optical Materials* **2002**, *21*, 499.
(26)   Ma, H.; Luo, J.; Kang, S. H.; Wong, S.; Kang, J. W.; Jen, A. K.-Y.; Barto, R.; Frank, C. W. *Macromolecular Rapid Communications* **2004**, *25*, 1667.
(27)   Zhu, J.; Wang, Y.; Lu, Y. *Colloids and Surfaces, A: Physicochemical and Engineering Aspects* **2004**, *232*, 155-161.
(28)   Bergman, D. J.; Stroud, D. In *Solid State Physics*, 1992; Vol. 46.
(29)   Maxwell-Garnet, J. C. *Philos. Trans. R. Soc. London, Ser. A.* **1906**, *205*, 1906.

CHAPTER FOUR

DIPOLE APPROXIMATION AND THE COUPLED DIPLOLE EQUATIONS

A. Non-Spherical Shapes Through the Dipolar Approximation

While the Mie solution to Maxwell's equations is the exact electrodynamic result, it only applies to spherical particles, which limits the theory's utility for many applications. Aside from spheres and concentric spheres, treated in chapter 2 and 3, respectively, exact models exist for both infinite cylinders[1] and ellipsoids of rotation[2]. The use of a treatment of infinite cylinders, however, does not have much application for the nanometric particle geometries considered in this work. The exact treatment for spheroids, on the other hand, is a far more difficult problem to solve, and outside the scope of this work. Ellipsoidal particles are often observed in thin films[3], however, and it is necessary to treat them in some fashion.

A fairly simple solution to this problem is to approximate the Mie equations for the case that x, the size parameter, is significantly smaller than unity: in other words, the particle size must be much smaller than the wavelength of the incident light. In practice, this corresponds to about 20 nm for applications using visible radiation. As seen in Chapter 2, the results for 15 and 20 nm spheres are very similar, excepting the increased cross-sections accounted for by the change in particle size. Beyond this size, however, significant changes in peak position and bandwidth occur.

The dipole approximation has various names, depending on the historical view that one takes of the field. The term dipole approximation comes from the fact that the equations can be derived by approximating the first term in the summation of the Mie solution, corresponding to the dipole moments[1]. It is also often called the quasi-static approximation, as it can be alternatively derived through finding the polarizability of a particle within a static field as a function of frequency[4,5]. It is also referred to as the Rayleigh approximation, or Rayleigh scattering, after Lord Rayleigh[6], who first described the inverse fourth power relationship of the scattering to the wavelength. The term Rayleigh scattering for

the phenomena is avoided here, as this is reserved for describing the elastic scattering from molecules, as opposed to Raman scattering.

For the case of a sphere much smaller than the wavelength of light, the extinction and scattering cross sections are derived in full by Bohren and Huffman[1] by taking power series approximations of the Bessel functions, to find

$$C_{ext} = \pi a^2 4x \operatorname{Im}\left\{\frac{\varepsilon - \varepsilon_m}{\varepsilon + 2\varepsilon_m}\right\}$$

$$C_{sca} = \pi a^2 \frac{8}{3} x^4 \left|\frac{\varepsilon - \varepsilon_m}{\varepsilon + 2\varepsilon_m}\right|^2$$

(4.1)

where x is the size parameter ka, a the radius, ε the dielectric function, and ε_m the dielectric function of the material in which the the particle is embedded. The scattering cross section has the inverse fourth power term as described by Rayleigh. The only other place where there is frequency dependence is in the polarizability term. The size dependence only enters through the cross sectional area and the size parameter, and the polarizability does not depend on size. This means that regardless of size, the shape of the curve will always be the same, with the intensity scaled up or down for larger or smaller radii.

The correction for the small size used in the dipole model is the surface damping or surface scattering term, which modifies the dielectric function. This term becomes important for sizes below 10 nm.[7,8] It is not used in this case, although future work will take advantage of this correction to bring computational results closer to experiment.

One advantage of the dipolar approximation is the ability to treat ellipsoids of rotation in a uniform way. An ellipsoid of rotation is an ellipsoid with two equal axes. If the two equal axes are the major axis, then the shape is referred to as an oblate ellipsoid (pancake shaped), and if the equal axes are the minor axis, then it is a prolate ellipsoid (cigar shaped). The polarizabilities in both cases are described by[1]

$$\alpha_{maj} = 4\pi abc \frac{\varepsilon - \varepsilon_m}{3\varepsilon_m + 3L_{maj}(\varepsilon - \varepsilon_m)}$$

$$\alpha_{min} = 4\pi abc \frac{\varepsilon - \varepsilon_m}{3\varepsilon_m + 3L_{min}(\varepsilon - \varepsilon_m)}$$

(4.2)

where a,b and c are the axes, and the L factors are the called geometrical factors here. The geometrical factors satisfy $L_a + L_b + L_c = 1$. The L's are often referred to as the depolarization factors[9], and depend upon geometry only, rather than the optical properties of the material. For the prolate ellipsoid, b and c are the minor axes, and are equal, and the geometrical factor is:

$$L_{maj}^{prolate} = \frac{1-e^2}{e^2}\left(-1 + \frac{1}{2e}\ln\frac{1+e}{1-e}\right)$$

$$e^2 = 1 - \frac{b^2}{a^2}$$

(4.3)

Where e is the eccentricity of the particle. For the oblate ellipsoid the geometrical factors may be determined by:

$$L_{maj}^{oblate} = \frac{g(e)}{2e^2}\left(\frac{\pi}{2} - \tan^{-1} g(e)\right) - \frac{g^2(e)}{2}$$

$$g(e) = \sqrt{\frac{(1-e^2)}{e^2}}$$

$$e^2 = 1 - \frac{c^2}{a^2}$$

(4.4)

where the other required geometrical factor may be inferred from the summation of geometrical factors is equal to one. The extinction cross section can be calculated by

$$C_{ext} = k\,\mathrm{Im}\{\alpha\}$$

(4.5)

An advantage of ellipsoids of rotation is the different possibilities of modeling a surface that arise due to the different axis possibilities. For prolate ellipsoids on a surface, for example, the light may "see" two different axis if the ellipsoid has the major axis perpendicular to the incident wave. The other possibility is that the major axis is parallel to the incident wave, so normally incident light with any polarization only has electric field components in the direction of one of the minor axes. Similar considerations for oblate ellipsoids are also possible.

Gold nanorods are a subject of investigation due to their plasmonic nature, biocompatibility, and desirable catalytic properties[10-12]. The above equations are used to describe short, prolate gold nanorods with the major axis parallel to the substrate. Figure 4.1 and Figure 4.2 represent the extinction cross section as a function of wavelength for the minor axis and major axis of a gold nanorod of major axis length 25 nm, and minor axis length 6.25, corresponding to a aspect ratio of 4.
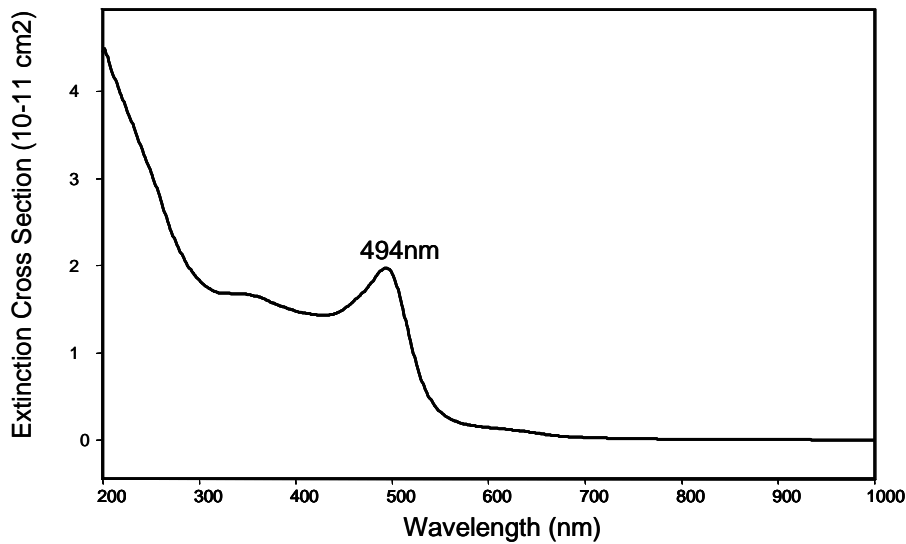
Figure 4.1: Extinction cross section of a gold nanorod of aspect ratio 4 considering only the minor axis.
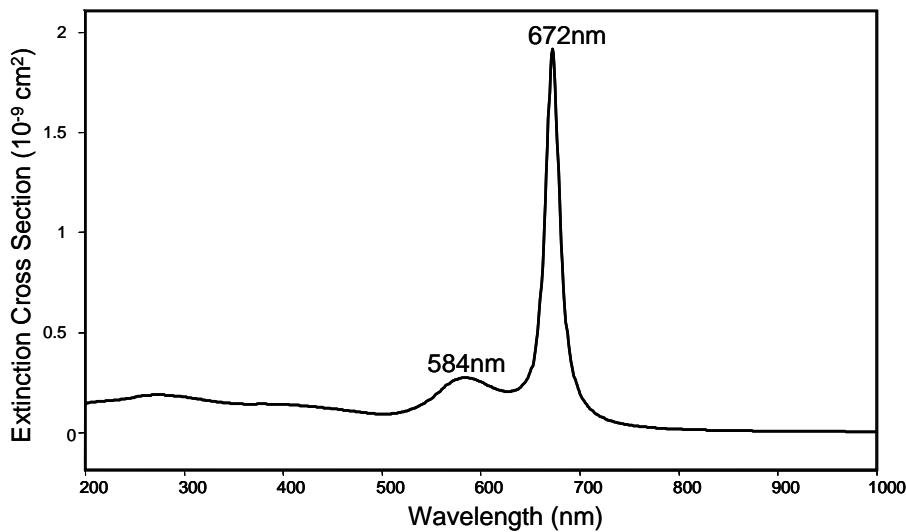
Figure 4.2 Extinction cross section of a gold nanorod of aspect ratio 4 considering only the major axis.

While there is a clear red shift of the major peak when comparing the major axis results to the minor axis, another important detail is the magnitude. The peak along the major axis is almost two orders of magnitude greater than the corresponding peak in the minor axis. Clearly the major axis will dominate the extinction when they are considered together, as shown in Figure 4.3.
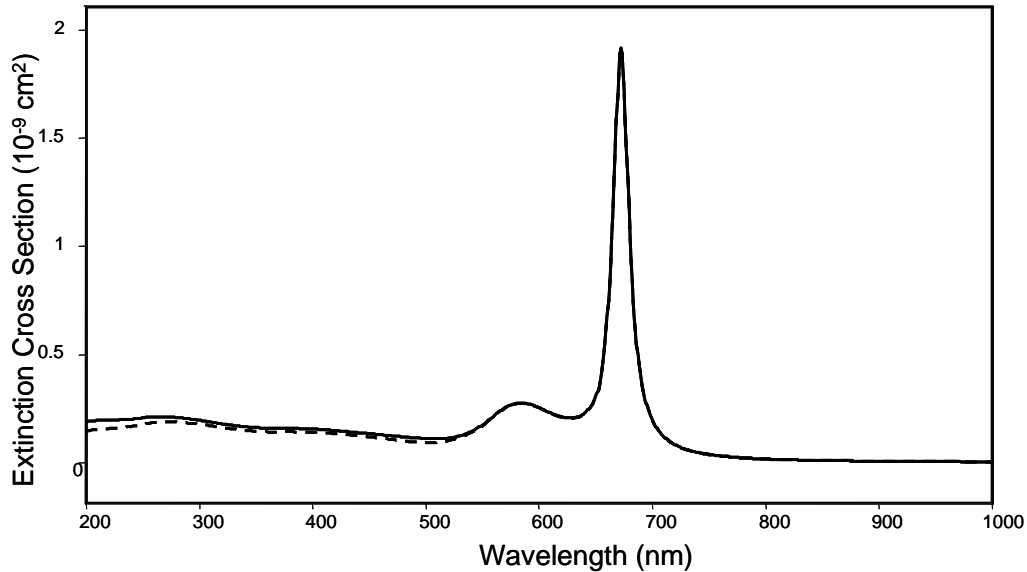
Figure 4.3. Extinction cross section of a gold nanorod of aspect ratio 4.

The physical origin of the two peaks in Figure 4.2 requires careful examination of both the optical properties of gold, and as well, the geometry in this situation. For an aspect ratio of 4, meaning that a/b=4, the square of the eccentricity is 15/16. This gives a geometrical parameter of L=0.07541. The resonance condition is:

$$\varepsilon_m + L_{maj}\left(\varepsilon - \varepsilon_m\right) = 0$$

$$\varepsilon = \frac{-1}{L_{maj}} + 1$$

(4.6)

For the calculated value of L, the real part of the dielectric function must be -12.26, which occurs at 672 nm, giving the main peak. The smaller peak at 584 is slightly different, and is due to the fact that in the extinction, it is the imaginary part of the polarizability that is taken. This peak originates from the absorption, rather than the scattering.

Also, as seen in Figure 4.4, a variety of solvents can be used to move the plasmon resonance to different wavelengths, following the same trend as seen for spheres in Chapter 2, and requires no more discussion here. Figure 4.5 shows the changes in the spectra as the aspect ratio is varied, which is a change that cannot be assayed in spherical particles. In particular, the second peak which arises as the aspect ratio is increased is due to absorptive processes.
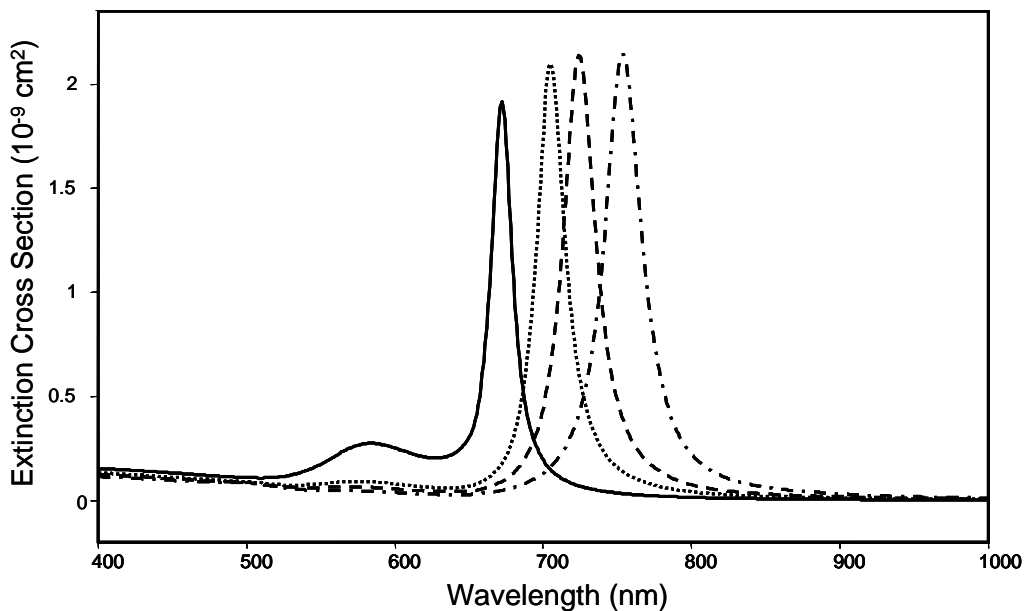
Figure 4.4. Extinction cross section of a gold nanorod of aspect ratio 4 in different media: Vacuum(ε_m=1), Water(ε_m=1.33) (dotted), Benzene(ε_m=1.5) (dashed), and ε_m=1.75 (dot-dash).
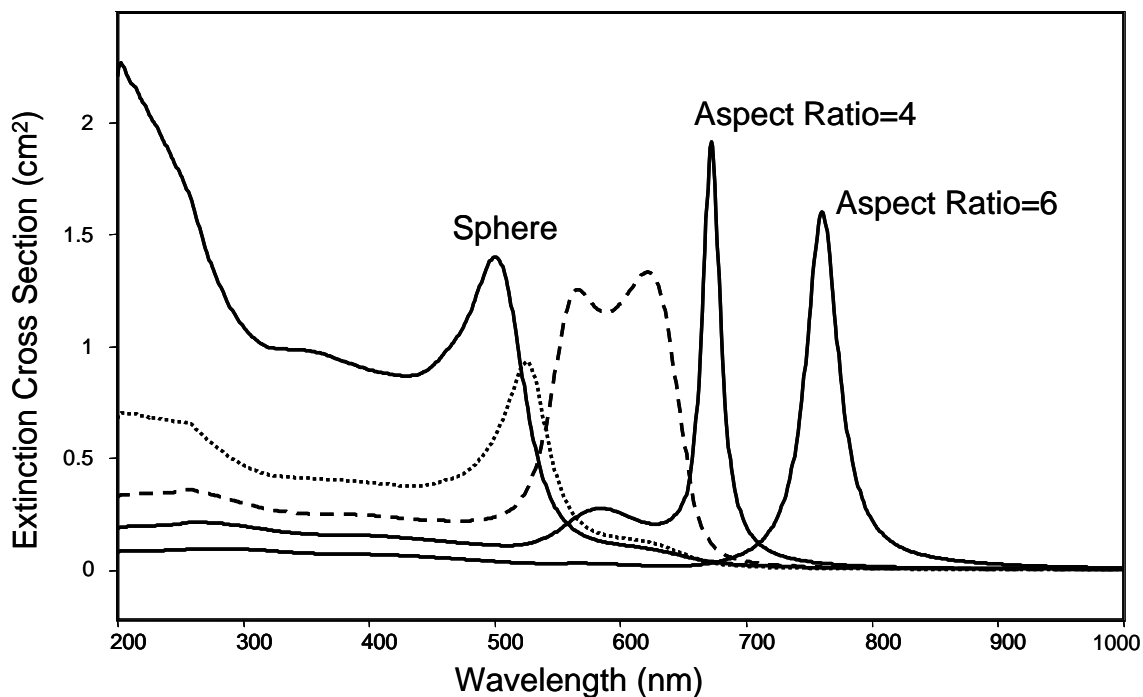
Figure 4.5: Extinction cross sections for gold spheres and nanorods, with major axis 25 nm, corresponding to sphere, aspect ratio of 2 (dotted), aspect ratio of 3 (dashed), aspect ratio of 4 and aspect ratio of 6.

B. Non-Spherical Shapes Through the Coupled Dipole Approximation

The coupled dipole equations (CDE) have been used in calculating the optical properties of composite media, including larger particles. In these larger particles, dipoles are arranged to mimic a more complicated system (such as those used in DDA [13],[14], as well as fractal structures[15]), which could be applied to model aggregation, surface composition, or percolation. The general nature of the solution allows for calculation of optical properties, as well as enhanced Raman and electric fields at any point in space.

Following the theoretical development by Markel, Shalaev, and coworkers[15], an arrangement of N monomers interacts with a plane wave of the form $\vec{E}(\vec{r},t) = \vec{E}_0 e^{i(\vec{k}\cdot\vec{r}-\omega t)}$. The local field induces a dipole moment for each monomer of $\vec{d}_i = \alpha_0 \vec{E}_l$, where α_0 is the isotropic polarizability, E_l the local field, and d_i the dipole moment of monomer i. Each monomer simultaneously interacts with all other monomers, as well as with the external field. The total dipole moment each monomer is:

$$d_{i\gamma} = \alpha_0 \left(E_{0\gamma} e^{i\vec{k}\cdot\vec{r}_i} + \sum_{j=1}^{N}{}' G_{\gamma\beta}\left(r_{ij}\right) d_{j\beta} \right)$$

(4.6)

where the greek indicies γ,β are the Cartesian coordinates, over which summation is implied. The primed summation indicates the j=i is excluded from the sum. Also, $r_{ij} = r_i - r_j$. G is a tensor defining the interaction between particles. The elements of this tensor are given by

$$G_{\gamma\beta}(\vec{r}) = k^3 \left(A(kr)\delta_{\gamma\beta} + B(kr)\frac{r_\gamma r_\beta}{r^2} \right)$$

$$A(kr) = \left(\frac{1}{kr} + \frac{i}{(kr)^2} - \frac{1}{(kr)^3} \right) e^{ikr}$$

$$B(kr) = \left(-\frac{1}{kr} - \frac{3i}{(kr)^2} + \frac{3}{(kr)^3} \right) e^{ikr}$$

(4.7)

This system of equations is easiest to solve in complex vector space of 3N dimensions, with basis vectors of |iγ >.   In this 3N space, the equation for the 3N dimensional dipole moment vector is

$$|d\rangle = \alpha_0 |E\rangle + \alpha_0 \hat{G}|d\rangle \qquad (4.8)$$

$\hat{G}$ is a 3N x 3N tensor with matrix elements given above, and the elements of E, the incident field, are given by

$$\langle i\gamma|E\rangle = E_{0\alpha} e^{i\vec{k}\cdot\vec{r}} \qquad (4.9)$$

Defining Z as the inverse of the polarizability, some rearrangement yields

$$Z\hat{1}|d\rangle - \hat{G}|d\rangle = |E\rangle \qquad (4.10)$$

These equations are a matrix equation of the form AX=Y, with complex elements where A is a known matrix, Y is a known vector. The unknown vector X is solved through the conjugate gradient method[13].

The polarizability of each particle is given by:

$$\alpha_0 = V\frac{\varepsilon - 1}{\varepsilon + 2} \qquad (4.11)$$

Where α is the polarizability, ε is the frequency dependent dielectric function[16], and V the volume of the dipole.   The radius of each sphere is calculated using a/R=1.612[17], where a is the spacing between the particles, 40 nm in this case, and R the radius. This value is less than the expected a/R=2, as the dipole response will not be homogeneous: rather, it will be stronger in the region where the particles are in contact. This value of a/R causes the dipoles to overlap, and interact more strongly. It is this overlap between the individual dipolar modes of each particle that causes the coupling.

The coupled dipole moment program used is presented in Appendix A. As a proof of principle, the program is first used to simulate something that is very well known, a sphere, basically using the coupled dipole program as a DDA program.   The sphere must first be discretized in some way, two examples being shown in Figure 4.6, where each miniature sphere represents a dipole.
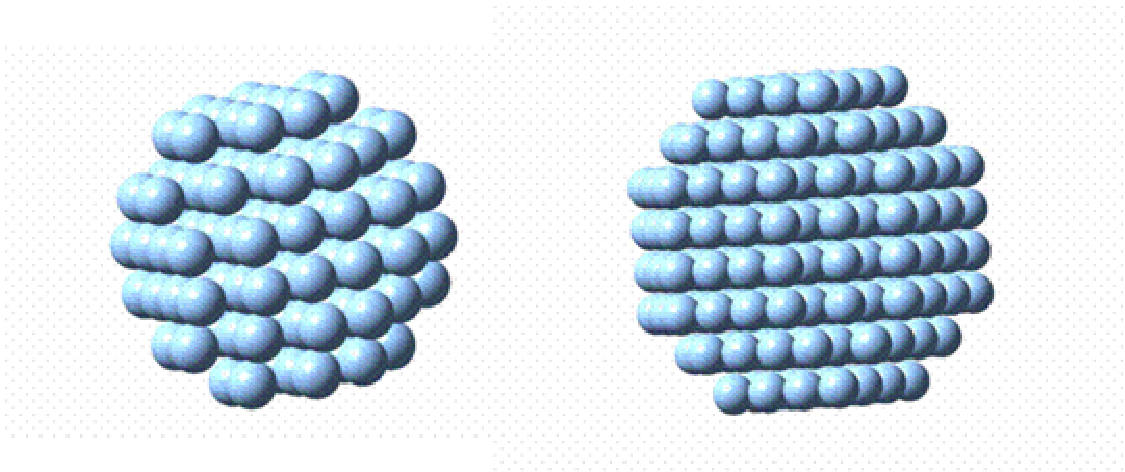
Figure 4.6: Spheres made up of 136 dipoles (left) and 304 dipoles (right).

The coupled dipole equations are used to simulate 10 nm silver spheres and 50 nm silver spheres, in order to ensure that the coupled dipole methodology is able to capture physical responses that are not explained within the dipolar model.   Since a 10 nm sphere can definitely be modeled with equation 4.1, while a 50 nm sphere, referring to Chapter 2, clearly can not be, this is a valid test for the coupled dipole model to be able to accurately simulate both cases. The proof of principle is demonstrated in Figures 4.7 and 4.8.
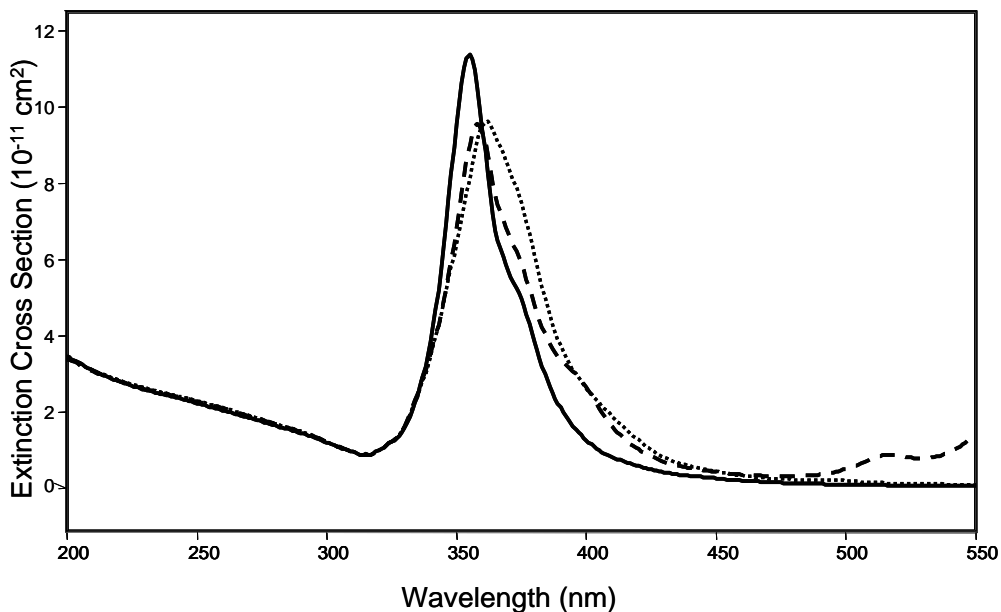
Figure 4.7: Extinction cross sections of 10 nm sphere using Mie (solid), CDE using 136 dipoles (dashed), CDE using 304 dipoles (dotted).
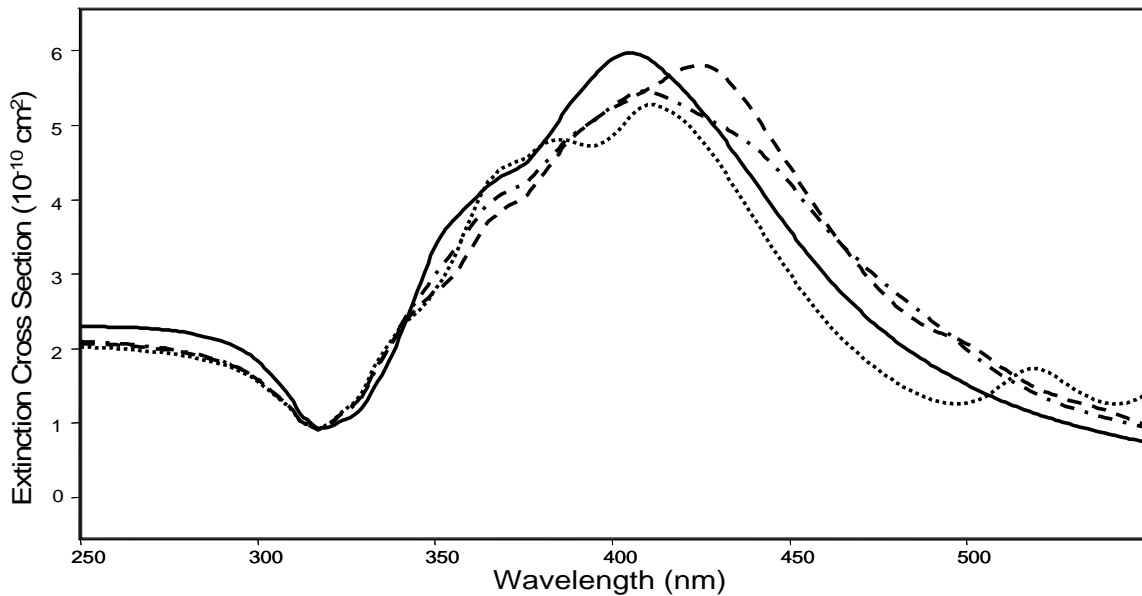
Figure 4.8 Extinction cross sections of 50 nm sphere using Mie (solid), CDE using 136 dipoles (dotted), CDE using 304 dipoles (dashed), CDE using 1024 dipoles (dot-dashed)

In both cases, the 136 dipole expression of a sphere fails fairly miserably, as there is an oscillating tail, which is indicative of poor discretization. In other words, the sphere isn't spherical enough, and is bumpy rather than smooth, causing the light to scatter off each particle individually. The 304 dipole model works much better in both cases, although the error in intensity is around 10%. The 1024 dipole model doesn't fare any better in terms of intensity for the case of the 50 nm sphere, but accurately predicts the peak wavelength, with the coupled dipole equations giving 409 nm as opposed to the 405 nm given in Mie theory, yielding an error of approximately 1%, small enough to be confident of the convergence.

With the principle of the use of CDE to create complex objects now in place, it can be used to calculate virtually any shape. Returning to the problem of gold nanorods, the dipolar model gave a good first order results, but failed to predict any changes in the spectra, besides intensity, as a function of size. Also, the dipolar model is only appropriate for the smallest particles that are considered, whereas the CDE have shown themselves to be able to model

84

particles outside of the dipole approximation. Figure 4.9 is an example of the discretization that can be done for a cylinder, breaking it up into 380 dipoles in this case, and Figure 4.10 shows the extinction of an aspect ratio 4 gold cylinder, with a major axis of 25 nm.
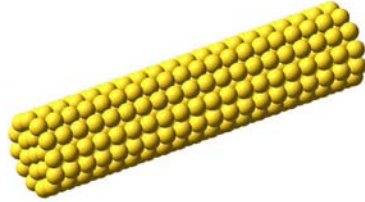
Figure 4.9: Discretization of a 380 dipole cylinder of aspect ratio 4.
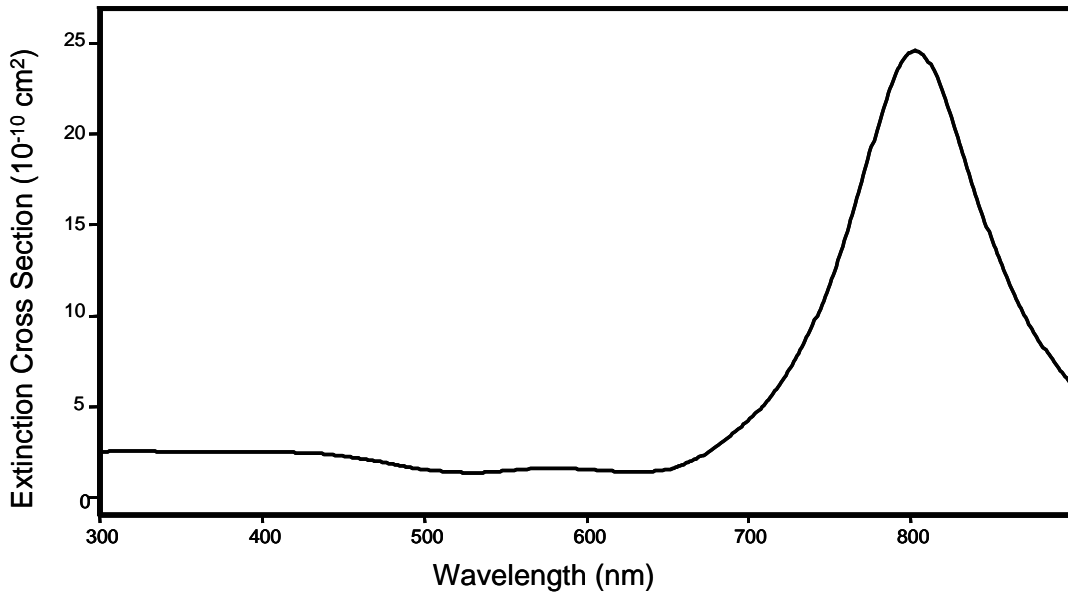
Figure 4.10: Extinction of a gold cylinder of major axis 25 nm, and minor axes 6.25 nm.

As opposed to the dipolar model, which displayed a very narrow, but intense peak at 674 nm, the coupled dipole equations applied to a similar

cylinder give a much broader peak, with peak extinction of 791 nm, although the intensity is similar. Although cylinders and ellipsoids have slightly different modes[18], the resulting spectra is fairly similar, due to the closely related structures.

C. Interacting Particles

While the single particle model has had success with experimental results, to gain a better understanding of the physical phenomenon, it is necessary to deal with nanostructure aggregates that support multiple surface plasmons. These aggregates produce spatial locations with extremely high local field (hot spots)[19]. It can be said that the basic parameters guiding plasmonic response are: (1) the response function to polarization (dielectric function) that confines the materials to a few metals (mainly silver and gold), (2) the shape (particles, shells, rings, etc.), (3) size and (4) the spatial geometry of nanostructure arrays or aggregates.[20,21]

In this work, the CDE are used to calculate the enhanced field between 2 particles using polarized light.   The addition of the field created by an oscillating dipole also allows for the calculation of enhancement in decay rate, a necessary component in the consideration of surface enhanced phenomena. For simplicity of calculation, and to avoid long computation times, each particle is treated as a separate dipole. While this certainly does not capture the full effect of a true interaction of realistic particles[22,23], it does provide a rough approximation to the real interaction, which will be dealt with in detail in Chapter 5.

The particles are arranged along the x axis, for simplicity. The light is incident from the z direction, with polarization chosen to be along the axis of the particles. This will excite only the coupled mode of the interacting particles, which will cause a shift in the resonance to lower energies compared to an isolated particle. The particles are chosen to have a radius of 20 nm. They are separated by a space of d, so that the center-to-center distance is 40nm+d. A schematic of this arrangement is shown in Figure 4.11.
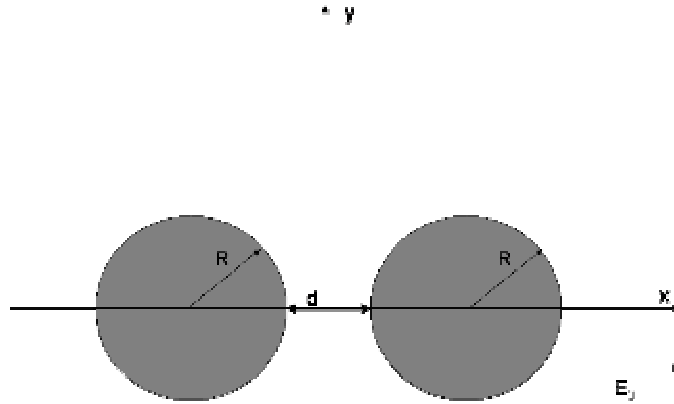
Figure 4.11 Schematic of particle arrangement for calculation of enhancement. The particles of radius R are separated by a distance d.

The electric field is calculated through the addition of a non-interacting particle at the desired position, and the sum of the dipole moment vectors divided by the polarizability of each particle is taken at this point. The enhancement of the electric field, M, is calculated by:

$$M = \left| \frac{\vec{E}_{inc} + \sum_i \vec{E}_i}{\vec{E}_{inc}} \right|$$

(4.12)

For the 2 particle model described above, the field at a point located symmetrically between the spheres (at a distance d/2 from each particle) is shown in Figure 4.12.
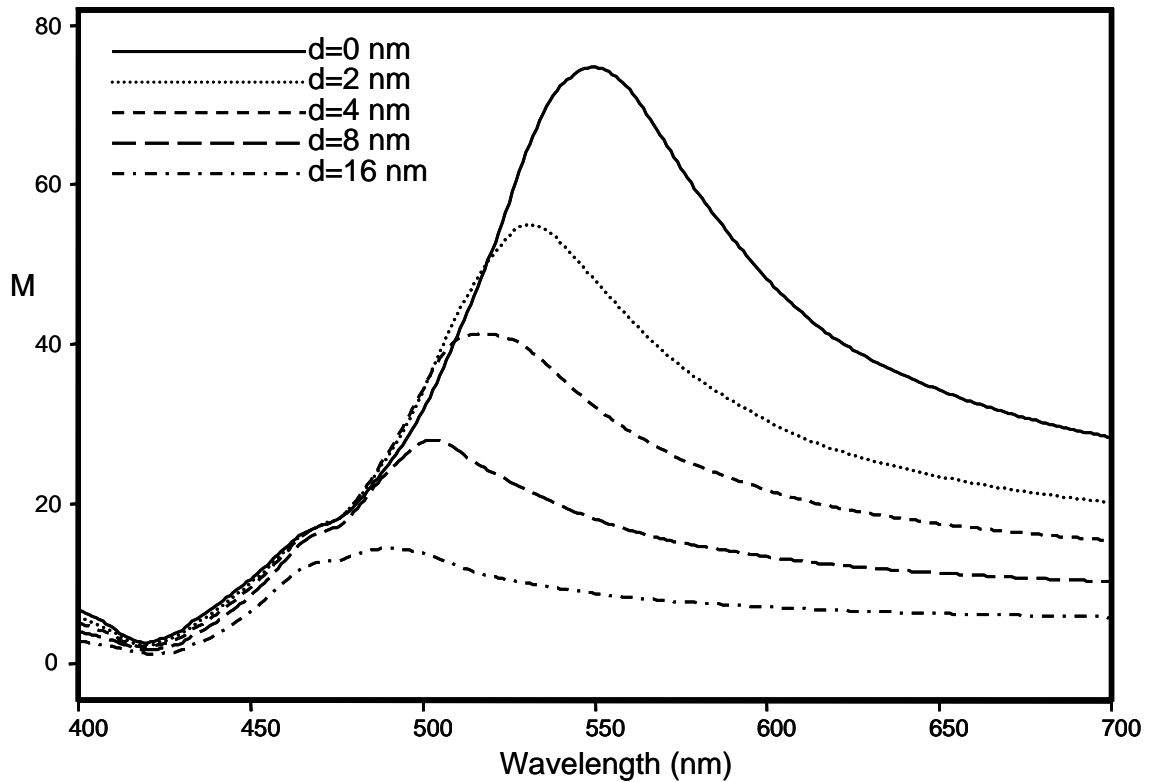
Figure 4.12: Field enhancement as a function of wavelength for 2 particle system.

These field enhancements show a clear trend. When the particles are well separated, the wavelength dependence is similar to that obtained for a single particle, with enhancement peaking at 490 nm. As the particles are moved closer together, the peak enhancement increases and red shifts, due to the increased coupling between the particles, as well as the decreased particle-molecule distance.

As an example of the changes in the spectra brought about by having more than two particles, different configurations of 3 particles are considered. The particles are arranged with no space between them, with a radius of 20 nm. The incident light is chosen to come from the z direction, and the electric field polarized in the x direction. For the case of 2 particles, they are arranged in a line along the x axis. For 3 particles, there are two different configurations used: 3a is with the third particle added in a triangular fashion, while 3b adds the particle to the right of particle 2. These configurations are as seen in Figure 4.13.
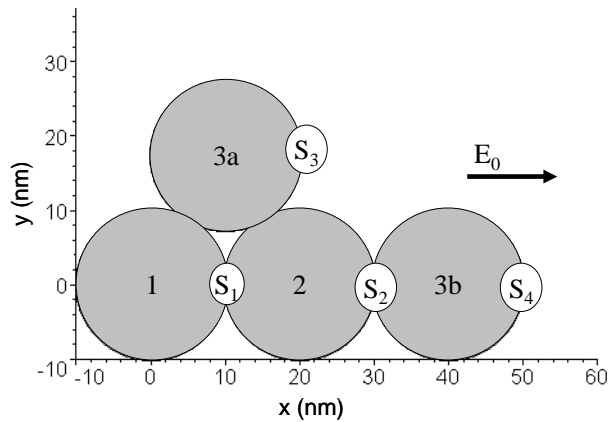
Figure 4.13 :   Arrangements of particles. 1 and 2 represent the positions of a single particle and dimer respectively, while 3a and 3b refer to the two different configurations of a 3 particle system.

The CDE, and equations for extinction and scattering cross sections as described by Markel et. al[17] are applied and solved through the conjugate gradient method[13]. The electric field is calculated through the addition of a non-interacting particle at the desired position, and the sum of the dipole moment vectors divided by the polarizability of each particle is taken at this point. The field enhancement M is also calculated.

M is used in two different ways: First, the dependence of the electric field at a variety of points is taken with respect to frequency. Secondly, contour maps of the electric field at peak frequencies are generated over the region of space surrounding the particles.

The extinction of 1, 2, and 3 particles, interacting as described above, is shown in Figure 4.14.
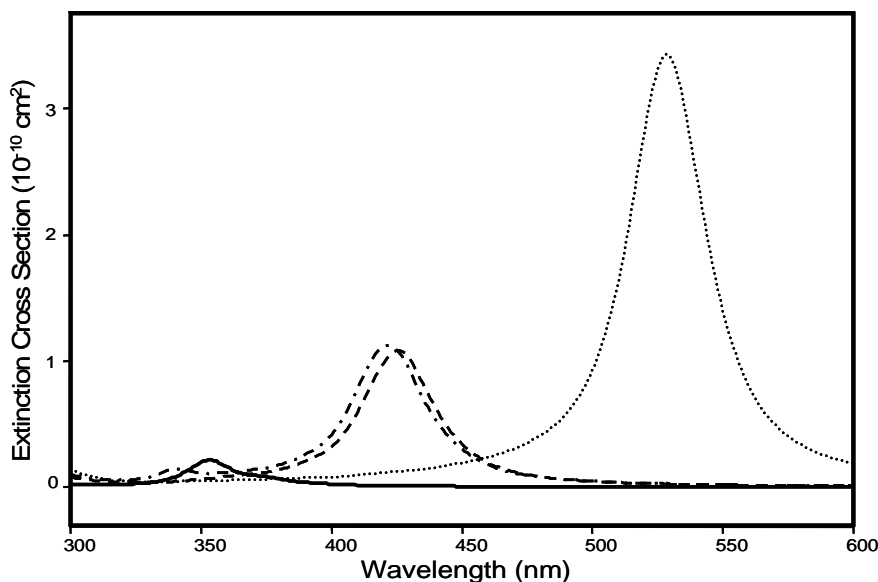
Figure 4.14: Extinction cross section vs. Incident Wavelength for 1 (solid), 2 (dashed), and 3 particles, in configuration 3a (dot-dash) and 3b (dotted).

The extinction for the single particle peaks at 354 nm, as expected for a 20 nm silver particle. Two particles along the line of the incident electric field polarization show strong coupling to both the electric field and each other, resulting in a much stronger extinction that is red shifted to 426 nm. Surprisingly, the addition of the third particle in configuration 3a causes a slight blue shift, to 422 nm, with a negligible increase in extinction. Examination of the dipole moment vectors in this case shows the creation of components in the y-direction, where in the 2 particle case, the response to the electric field is only in the x. Because these y components do not couple to the electric field, which is only in the x, they do not contribute to the extinction. In a sense, the 3rd particle causes a damping of the system by inducing dipole moments which do not couple to the incident field. In configuration 3b, the trend from the 2 particle system is continued, with a shift more to the red, to 528 nm, as well as a substantial increase in extinction. As 3a and 3b occupy the same volume, and have the same surface area, these very different spectra illustrate the sensitivity to geometry in nanoparticle extinction.

The scattering results follow a similar trend, with the scattering peaking at the same wavelength as the extinction for 1 and 2 particles. For configuration

91

3a, the scattering is strongest at 424 nm, and for 3b at 529 nm. The scattering contribution to the total extinction also demonstrates an interesting trend. For 1 particle, the scattering is only 3.7% of the extinction, while for 2 it contributes 12.7%. The scattering contributions for the two different configurations of 3 particles are 13.6% and 25.6% for 3a and 3b respectively, demonstrating that both extinction and scattering are strongly dependent on geometry.
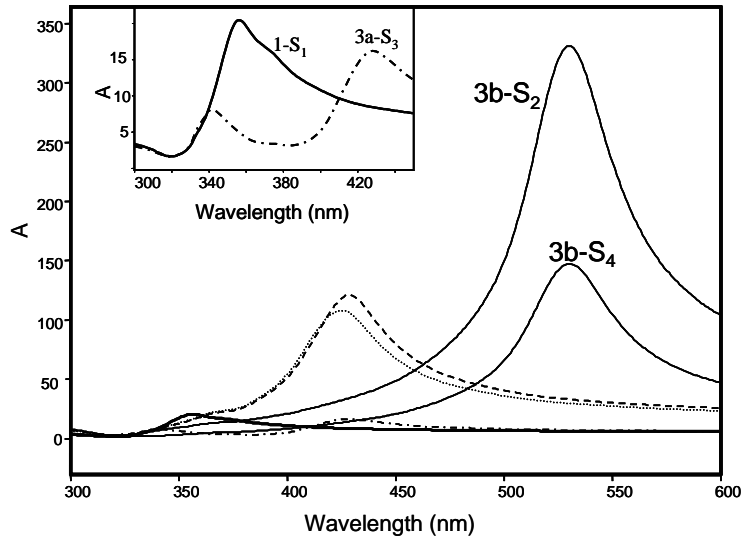
Figure 4.15. Electric field enhancement vs. Wavelength for 1 particle sampled at S_1 (solid), 2 particles sampled at S_1 (dashed), and 3 particles (dotted line), in configuration 3a sampled at S_1, and 3b sampled at S_2 and S_4. The inset shows detail of the single particle and configuration 3a from 300 to 450nm.

The electric field as a function of incident wavelength is shown in Figure 5. In general, the peak wavelengths are slightly red shifted compared to the extinction, and the tails to the red extend out much further. The single particle shows a peak at 356 nm. The maximum enhancement has a magnitude of 20.4. For two particles, the peak is at 428 nm both at the center (S_1), where the magnitude of the field enhancement is 121.1, and at the side (S_2), where A=63.1. The field is approximately three times as high to the right of both particles than for a single particle, due to the increased dipole moment from the interaction. In the center, the field is approximately doubled again relative to the outside, as the dipole moments of both particles are strongly felt. For 3 particles, in configuration 3a, due to the damping mentioned above, the peak is blue shifted

to 426 nm. The intensity drops slightly, compared to the enhancement for two particles, at the same positions. The field enhancement for the 3rd particle shows why: a peak at 342 nm appears, as seen in the inset of Figure 3, corresponding to a response that is not fully coupled to the other two particles. In this case, modes are created that correspond to both the single particle and the dimer. In configuration 3b, however, the strongest enhancement is observed at 530 nm, with a magnitude of 331.2 at one of the inside positions (S_2), and 147.4 to the right of all three particles (S_4). Again, there is a clear dependence on geometry for field strengths as well.

Figures 4.16, 4.17, and 4.18 show contour maps of the electric field enhancement over the region of space surrounding the particles, at the peak frequencies calculated in Figure 4.15. The color scale follows visible light, with violet and blue being the lowest enhancement, and red being the highest in each case. The particle radius as shown in the figures is slightly smaller than 10 nm, to allow visibility of the fields at the surface, and between the particles. The single particle shows the strongest enhancement in the direction of the field polarization, as expected. For two particles, the enhancement is strongest in the region between the particles, with an intermediate enhancement around the outside of the system in the direction of incident field polarization.
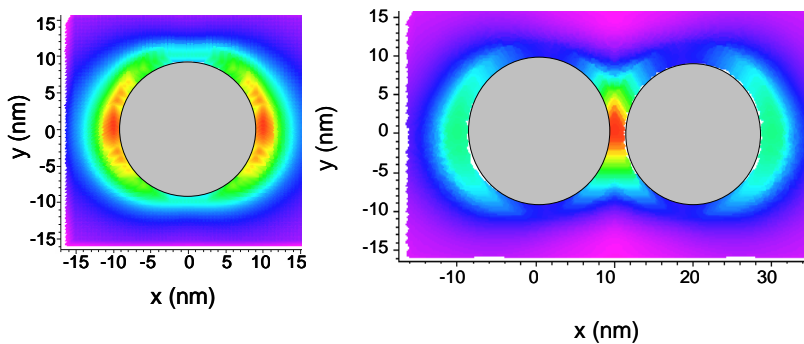
Figure 4.16: Electric field enhancement for 1 particle at 356 nm (left) and 2 particles at 428 nm (right). The scale is described in the text.
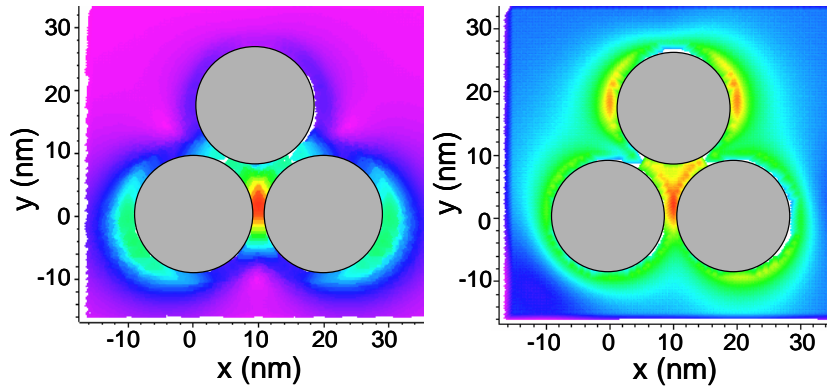
Figure 4.17: Electric field enhancement for 3 particles in configuration 3a at 426 nm (left) and 342 nm (right). The scale is described in the text.

For three particles, arranged as in 3a, there is a definite mode due to the dimer, as seen by the intense field between the bottom two particles. This mode follows the same pattern as observed in the two particle system, as seen in Figure 4.17. At 342 nm, while the strongest field is seen close to the geometric center of the 3 particle system, which is an off-resonance contribution from the 2 particle mode, there is also a strong field in the direction of the incident field from the top particle, corresponding to a single particle feature.
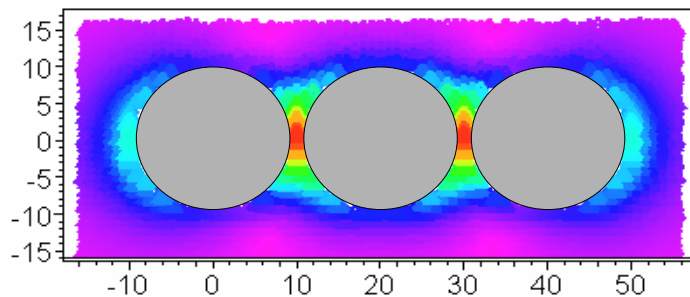
Figure 4.18: Electric field enhancement for 3 particles in configuration 3b at 530 nm. The scale is described in the text.

In configuration 3b, however, the strongest enhancement is localized between the particles. As these particles are fairly close together, the phase difference in the dipole response is negligible between the particles, creating an almost symmetric response.

Examination of the electric field patterns in both wavelength and space allows for an understanding of the distribution of the field, and different modes, corresponding to different degrees of coupling in a system that can be probed. Single particle models have the benefits of analytical solution, while coupled particles provide a model for the aggregated nanoparticles responsible for SERS enhancement. The CDE allow for computation optical properties as well as field strengths of these complex systems. For even simple systems such as 2 or 3 particles, field enhancements can increase by an order of magnitude from the increased interaction, relative to a single particle.

The same notion can be applied to fractal aggregations of particles, a common occurrence when colloids are dispersed on a surface[24]. Fractal patterns of colloids are created by self-avoiding random walks[25], samples of which are seen in Figure 4.19.
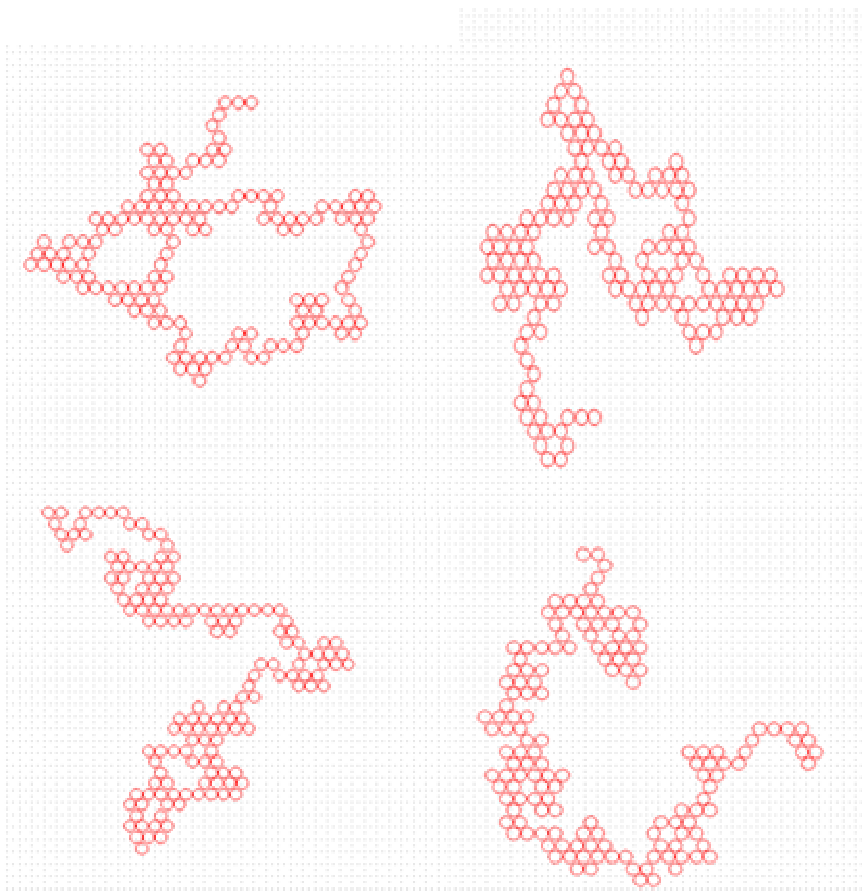
Figure 4.19: Self-avoiding random walks of 100 particles.

As long as each individual particle is smaller than the wavelength of light, the different self-avoiding random walks can be calculated using CDE. Extinction results for these four walks are shown in figure 4.19.
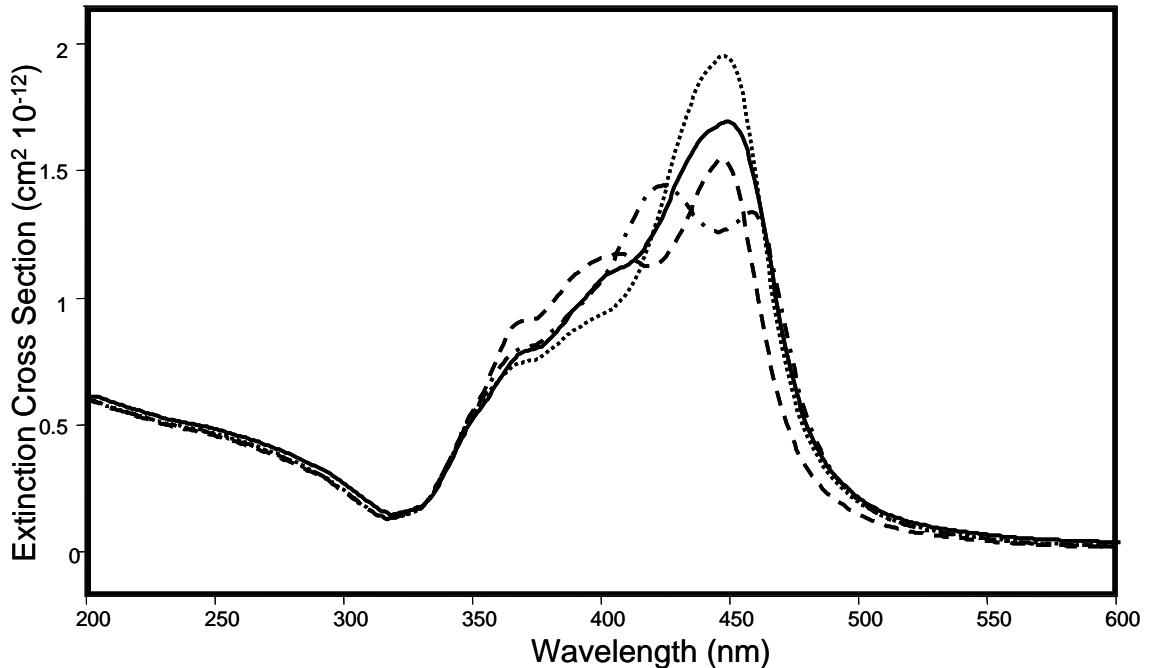
Figure 4.20: Extinction cross section of 20 nm silver particles for the configurations seen in Figure 4.19.

The use of the quasi-static or dipolar model allows examination of plasmonics from several avenues. First, it allows the use of approximate, closed form equations which have the virtues of being physically understandable as well as mathematically tractable. Secondly, ellipsoids of rotation are possible, a shape which causes spectral variations due to the eccentricity, as well as providing greater extinction cross sections and field intensities. Thirdly, by allowing a set of dipoles to interact gives rise to space discretization of complex particles, allowing virtually any imaginable shape to be calculated, as well as examination of the role of defects or protusions. Lastly, the each individual particle can be treated as a dipole, and the effect of the system of particles can be treated through the coupled dipole equations.

D. Bibliography

(1) Bohren, C. F.; Huffman, D. R. *Absorption and Scattering of Light by Small Particles.*; Wiley: New York, 1983.
(2) Asano, S.; Yamamoto, G. *Applied Optics* **1975**, *14*, 29.
(3) Granqvist, C. G.; Hunderi, O. *Phys. Rev. B* **1977**, *16*, 3513.
(4) Griffiths, D. J. *Introduction to Electrodynamics*; 2nd ed.; Prentice Hall: Englewood Cliffs, New Jersey, 1989.
(5) Jackson, J. D. *Classical Electrodynamics*; 3rd ed.; John Wiley and Sons: New York, 1999.
(6) Rayleigh, L. *Philos. Mag.* **1871**, *41*, 170-120.
(7) Noguez, C. *Optical Materials* **2005**, *27*, 1204-1211.
(8) Noguez, C. *Journal of Physical Chemistry C* **2007**, *111*, 3806-3819.
(9) Stoner, E. C. *Philos. Mag.* **1945**, *36*, 803.
(10) Link, S.; Mohamed, M. B.; El-Sayed, M. A. *Journal of Physical Chemistry B* **1999**, *103*, 3073-3077.
(11) Yu, Y.-Y.; Chang, S.-S.; Lee, C.-L.; Wang, C. R. C. *Journal of Physical Chemistry B* **1997**, *101*, 6661-6664.
(12) Jana, N. R.; Gearheart, L.; Murphy, C. J. *Journal of Physical Chemistry B* **2001**, *105*, 4065-4067.
(13) Draine, T. *Astropyhys. J.* **1988**, *333*, 848.
(14) Podolski, V. A.; Sarychev, A. K.; Narimanov, E. E.; Shalaev, V. M. *Opt. A: Pure Appl. Opt.* **2005**, *7*, S32-S37.
(15) Markel, V. A.; Shalaev, V. M.; Stechel, E. B.; Kim, W.; Armstrong, R. L. *Physical Review B* **1996**, *53*, 2425-2436.
(16) *Handbook of Optical Constants of Solids*; Palik, E. D., Ed.; Academic Press, 1985.
(17) Markel, V. A.; Shalaev, V. M. In *Computational Studies of New Materials*; Jelski, D. A., George, T. F., Eds.; World Scientific Publishing: Singapore, 1999.
(18) Sosa, I. O.; Noguez, C.; Barrera, G. *Journal of Physical Chemistry B* **2003**, *107*, 6269.
(19) Stockman, M. I.; Faleev, S. V.; Bergman, D. J. *Physical Review Letters* **2001**, *87*, 167401-4.
(20) Eustis, S.; El-Sayed, M. A. *Chemical Society Reviews* **2006**, *35*, 209-217.
(21) Willets, K. A.; Van Duyne, R. P. *Annual Review of Physical Chemistry* **2007**, *58*, 267-297.
(22) Claro, F. *Physical Review B* **1984**, *30*, 4989.
(23) Noguez, C.; Barrera, G. *Physical Review B* **1998**, *57*, 302.
(24) Lindsay, H. M.; Lin, M. Y.; Weitz, D. A.; Sheng, P.; Chen, Z.; Klein, R.; Meakin, P. *Faraday Discussions of the Chemical Society* **1987**, *83*, 153-165.
(25) Binder, K.; Heermann, D. W. *Monte Carlo Simulation in Statistical Physics*; Springer-Verlag: New York, 1988.

CHAPTER FIVE

EXTENDED MIE THEORY

A. Theory of Cooperative Scattering

The problem of scattering by multiple particles has an extensive history. Indeed, it is a topic still under investigation, creating a wide variety of notation and methods. As there is no universal agreement as to a formalism, it is important to clearly define how the problem is to be approached in this case.

Although for this work, the desired outcome is field enhancements for surface enhanced Raman scattering, as well as extinction and scattering cross sections to aid in surface characterization, the outcomes from scattering by multiple particles have a wide variety of applications. The desire to understand the interactions of nanometric particles has been motivated by recent developments in a number of areas, including surface enhanced Raman scattering, including single molecule detection[1,2], subwavelength microscopy techniques, such as atomic force microscopy[3] and scanning near-field optical microscopy[4]. The latter is specifically of interest, as it has the ability to obtain absorption and scattering information with resolution in the nanometer range, and nanotechnology based on plasmonics[5]. With the recent growth in computing power, it has become possible to approach problems that were not previously calculable within any reasonable time frame. While these areas began as the study of simple scatterers with analytical solutions such as spheres and cylinders, the application of classical electromagnetism has moved on to more complicated particles. While complex monomers are quite interesting in their response to an electromagnetic field, an important extension that should be made is to that of aggregation of simple scatterers. While the calculation of the near field is a difficult and tedious process in any case, it is the simplest. It remains an important theoretical problem in the field of plasmonics.

When the simple scatterer can be treated as a sphere, the result is Mie theory, as seen previously. When there is an aggregation of spheres, the treatment is referred to as extended Mie theory. The idea of extended Mie theory

is similar to that of any multiple particle scattering, wherein the scattering is calculated for each particle individually, and the solution expanded out using a complete basis (in this case the vector spherical harmonics) where the expansion coefficients are determined using the appropriate boundary conditions. This expansion gives calculable equations *only* if the basis function symmetry is identical to the symmetry of the scatterer. This is why this particular technique works only with a limited group of particles, which are spheres, cylinders, and ellipsoids[6]. For multiple particles, it is then necessary to transform the basis of one particle to another. This problem has already been solved for spheres, with the necessary transformation being the addition coefficients for the vector spherical harmonics[7].

   While the basis of the theory for the scattering of multiple spheres has been available for slightly over a century, since the time of Mie, its realization has been much slower due to the inherent complexity of the task. Fuller[6] gives an excellent review of the problem, but a few of the historical highlights bear repeating here. The addition coefficients, sometimes referred to as translation coefficients, for the spherical vector harmonics are grounded in the theory of the addition of angular momenta, of which much of the pioneering work was done by Clebsch[8]. Although early attempts used the dipolar approximation to approach the problem of two spheres[9], the exact solution could not be assayed until the development of the addition theorem for the spherical harmonics. This was first done for the scalar spherical harmonics in 1954 by Friedman and Russek[10], and then the vector spherical harmonics by Stein[11] in 1961, and Cruzan[7] in 1962. Cruzan's work is of note, and is used here, as the addition coefficients have vector addition terms that are explicitly linked to the Clebsch-Gordon coefficients. Modern applications use the Wigner-3j symbol to represent the Clebsch-Gordon coefficients, and Cruzan was the first to make that connection. It was only in work of Bruning and Lo[12-14] that exact calculations for the special case of two and three particles along a single axis were comprehensively studied, along with experimental verification through backscattering measurements. These authors

used matrix inversion to solve the set of linear equations that arise from this special case.

Although there have been many papers published on the subject, the majority of the work on cooperative scattering of particles has been within limits of the Rayleigh, or dipolar approximation[6], although there are certainly exceptions focussing specifically on plasmonics[15,16]. This is largely because these equations can be written in a closed form, and computation can be quickly done. Many of these use the term 'Mie theory' to describe it, although care should be taken, as they are not Mie's exact solution. This is also true to near field calculations applied to SERS. Initial work to apply extended Mie to surface enhanced Raman scattering was undertaken by Inoue and Ohtaka[17], who successfully applied an integral approach to the problem using retarded Green's functions for chains of spheres along a common axis. Although elegant, this work was not developed further, and it remains to be seen whether this formalism could be extended to arbitrary configurations.

Aside from Inoue's work, there are basically two methods of solution. One is similar to the T-matrix approach from classical electromagnetism. This approach is seen where all the boundary conditions are solved simultaneously to obtain a large matrix, which is inverted to solve the system. This is the method used by Bruning and Lo[13]. The difficulty with this approach is that for more than two spheres, or for the strongly interacting spheres, a great many terms are required, leading to matricies with literally tens of thousands of elements to be inverted. The second method is referred to as the order of scattering, which was formalized by Fuller and Kattawar[18,19], and Fuller[6,20]. This method makes intuitive sense, as it is more or less an iterative scheme. In this calculation, the scattering is first calculated for each isolated sphere, and the scattered field of each particle is felt by all the other spheres, which is then re-scattered, and so on. Although Fuller and Kattawar's work initially called it "the consummate solution"[18,19], later work by Fuller revealed that the iterative scheme is unstable in the vicinity of a single sphere resonance, termed a progenitor resonance. This progenitor resonance may span a rather large frequency range, and so the use

of the term "consummate" was deemed "ill-advised"[6].   Despite this problem, and other issues of convergence, the order of scattering method makes physical sense. Recently, Hongxing Xu[21,22], and Hongxing Xu and Li[23] developed a new algorithm that is a combination of matrix inversion and order of scattering that appears to circumvent both problems: that of large matricies in a pure matrix inversion, and also convergence problems in order of scattering methods. The methodology presented here is based on that of Xu and Li. Although this hybrid method is successful in calculation of near field intensities, the calculation of extinction and scattering cross sections remains an outstanding problem.

The problem can be broken into 4 basic parts: scattering by isolated spheres, calculation of the vector spherical harmonics, expanding the plane wave onto the vector spherical harmonics, and calculation of the vector addition coefficients for the vector spherical harmonics. The most time consuming and problematic part of extended Mie theory is the vector addition coefficients, partly because it is the newest, and thus, most complicated: the other three sections exist in a simpler form for the isolated particle. The vector addition coefficients, as well as being dependant on both frequency as well as spatial coordinates, require the integral of the product of three associated Legendre functions, a problem solved by Gaunt[24] for application to the helium atom, although again, the solution is extremely time consuming. One of the many contributions to this field by Bruning and Lo[13] was to devise a three term recurrence relation for the Gaunt integrals for the case of particles along a common z axis. In the 1990's, Yu-Lin Xu[25-27] derived a recursion method for calculation of the Gaunt integrals for arbitrary configuration that compares well numerically to Gaunt's solution, as well as taking less time computationally.

Following both the previous development of Mie theory in this work, as well as fitting in the new elements according to the formalism of Hongxing Xu[22], the incident and scattered field for a set of L particles can be expanded into the vector spherical harmonics

$$^i\mathbf{E}_l = \sum_{n=1}^{\infty} \sum_{m=-n}^{n} \sum_{p=1}^{2} {}^iC_{mnp}^l \big| mn1p \big\rangle$$

$$^s\mathbf{E}_l = \sum_{n=1}^{\infty} \sum_{m=-n}^{n} \sum_{p=1}^{2} {}^sC_{mnp}^l \big| mn3p \big\rangle$$

(5.1)

where the superscripts s and i stand for scattered and incident, respectively, n and m are the angular momenta, and l the index over the sphere number up to L. The vector spherical harmonics |mnjp> are represented by basis kets, where p=1 stands for $\mathbf{M}_{mn}^j$ and p=2 for $\mathbf{N}_{mn}^j$, as derived in the previous section. The j index denotes the kind of spherical Bessel function used, being j=1 for the regular spherical Bessel function $j_n(x)$, j=2 for the spherical Bessel function of the second kind $y_n(x)$, j=3 for the spherical Hankel function of the first kind, $h_n(x)= j_n(x)+i\ y_n(x)$, and finally, j=4 for the spherical Hankel function of the second kind, which is the complex conjugate of the j=3 case. In any event, only the j=1 and j=3 are used, representing the Bessel functions required for the incident and scattered wave. The last elements are the expansion coefficients $^iC_{mnp}^l$ and $^sC_{mnp}^l$ for the vector spherical harmonics |mnjp> centered at the l'th sphere.

As the vector spherical harmonics are well known at this point, the problem is reduced to finding the expansion coefficients $^sC_{mnp}^l$, which is indeed the most difficult aspect of this calcuation. The scattered field expansion coefficients may be determined by summation of single scattering events using the order of scattering approach, and are functions of the incident coefficients $^iC_{mnp}^l$, the Mie coefficients a_n^l and b_n^l, as shown previously, and lastly, the vector addition coefficients $^{lh}A_{mn}^{\mu\nu}$ and $^{lh}B_{mn}^{\mu\nu}$. The function is called T_l. To summarize,

$$^sC_{mnp}^l = {}^LT_l\left({}^iC_{\mu\nu q}^h, a_\nu^h, b_\nu^h, {}^{lh}A_{mn}^{\mu\nu}, B_{mn}^{\mu\nu} \right)$$

(5.2)

where ν and μ designate angular momentum, analogous to n and m, respectively. The variable q plays the same role as p. Although the magnetic fields can also be written using the same sort of relations, the discussion will be limited to the electric field.

The vector spherical harmonics themselves, in spherical coordinates r, θ, φ, where r is the radius, θ the zenith angle measured from the positive z-axis, and φ the azimuthal angle, measured in the xy plane, are:[13]

102

$$\mathbf{M}_{mn}^{j} = |mnj1\rangle = \begin{bmatrix} 0 \\ \dfrac{1}{\sin\theta}\dfrac{\partial}{\partial\phi} \\ \dfrac{\partial}{\partial\theta} \end{bmatrix} z_n^{(j)}(kr)Y_n^m(\theta,\phi)$$

$$\mathbf{N}_{mn}^{j} = |mnj2\rangle = \begin{bmatrix} n(n+1)z_n^{(j)}(kr) \\ -\dfrac{\partial}{\partial r}\{rz_n^{(j)}(kr)\}\dfrac{\partial}{\partial\theta} \\ \dfrac{\partial}{\partial r}\{rz_n^{(j)}(kr)\}\dfrac{1}{\sin\theta}\dfrac{\partial}{\partial\phi} \end{bmatrix} \dfrac{1}{kr}Y_n^m(\theta,\phi)$$

(5.3)

Where j controls the type of Bessel function used in the equation. These vectors can be simplified by recalling

$$\frac{\partial}{\partial\phi}Y_n^m(\theta,\phi) = imY_n^m(\theta,\phi)$$

$$\frac{\partial}{\partial r}\{rz_n^j(kr)\} = \frac{\partial}{\partial kr}\frac{\partial kr}{\partial r}\{rz_n^j(kr)\} = \frac{\partial}{\partial kr}\{krz_n^j(kr)\}$$

(5.4)

which yields

$$\mathbf{M}_{mn}^{j} = |mnj1\rangle = \begin{bmatrix} 0 \\ \dfrac{im}{\sin\theta} \\ \dfrac{\partial}{\partial\theta} \end{bmatrix} z_n^{(j)}(kr)Y_n^m(\theta,\phi)$$

$$\mathbf{N}_{mn}^{j} = |mnj2\rangle = \begin{bmatrix} n(n+1)z_n^{(j)}(kr) \\ -\dfrac{\partial}{\partial kr}\{krz_n^{(j)}(kr)\}\dfrac{\partial}{\partial\theta} \\ \dfrac{\partial}{\partial kr}\{krz_n^{(j)}(kr)\}\dfrac{im}{\sin\theta} \end{bmatrix} \dfrac{1}{kr}Y_n^m(\theta,\phi)$$

(5.5)

which gives them a form explicitly the same as those derived previously, aside from a difference in normalization. The normalization is taken care of by the expansion coefficients of the incident field. As seen previously, the incident

electric field is expanded into the vector spherical harmonics. The expansion coefficients can be inferred from

$$^{i}C_{mnp}^{l} = \frac{\langle mnjp \| ^{i}\mathbf{E}_{l} \rangle}{\langle mnjp | mnjp \rangle}$$

(5.6)

These coefficients were first written explicitly by Inoue and Ohtaka[17], although they have been reproduced elsewhere with differing phase[21].

$$^{i}C_{mn1}^{l} = \frac{2\pi i^{n}}{n(n+1)} \left\{ \begin{array}{l} -(iE_{x} - E_{y})\sqrt{(n+m+1)(n-m)}\left(Y_{n}^{m+1}(\hat{k})\right)^{*} \\ -(iE_{x} + E_{y})\sqrt{(n-m+1)(n+m)}\left(Y_{n}^{m-1}(\hat{k})\right)^{*} \\ +2imE_{z}\left(Y_{n}^{m}(\hat{k})\right)^{*} \end{array} \right\}$$

$$^{i}C_{mn2}^{l} = \frac{2\pi i^{n}}{n(n+1)} \left\{ \begin{array}{l} n\sqrt{\dfrac{(n+m+1)(n+m+2)}{(2n+1)(2n+3)}}(iE_{x} - E_{y})\left(Y_{n+1}^{m+1}(\hat{k})\right)^{*} \\ -n\sqrt{\dfrac{(n-m+1)(n-m+2)}{(2n+1)(2n+3)}}(iE_{x} + E_{y})\left(Y_{n+1}^{m-1}(\hat{k})\right)^{*} \\ -(n+1)\sqrt{\dfrac{(n-m-1)(n-m)}{(2n-1)(2n+1)}}(-iE_{x} + E_{y})\left(Y_{n-1}^{m+1}(\hat{k})\right)^{*} \\ -(n+1)\sqrt{\dfrac{(n+m-1)(n+m)}{(2n-1)(2n+1)}}(iE_{x} + E_{y})\left(Y_{n-1}^{m-1}(\hat{k})\right)^{*} \\ +\left[\begin{array}{l} 2in\sqrt{\dfrac{(n+m+1)(n-m+1)}{(2n+1)(2n+3)}}\left(Y_{n+1}^{m}(\hat{k})\right)^{*} \\ -2i(n+1)\sqrt{\dfrac{(n+m)(n-m)}{(2n-1)(2n+1)}}\left(Y_{n-1}^{m}(\hat{k})\right)^{*} \end{array} \right]E_{z} \end{array} \right\}$$

(5.7)

While this explicit form of the expansion coefficients is certainly unwieldy, a choice of **k**, the wavevector of the incident light, and the polarization of the incident electric field will make many of the terms collapse.

Of the 3 parts that go into the calculation of the expansion coefficients of the scattered field, 2 are explicitly realized: the Mie coefficients from the previous

section, and the expansion coefficients of the incident field, which have also been written explicitly. All that remains is to understand the vector addition coefficients for the vector spherical harmonics.

B. Addition Coefficients for the Vector Spherical Harmonics

The $^{lh}A^{\mu\nu}_{mn}$ and $^{lh}B^{\mu\nu}_{mn}$ terms used are those given by Cruzan[7], as rewritten by Yu-Lin Xu[25], defined as being the coefficients for translation from the l'th to the h'th coordinate system. The purpose of the addition coefficients is to translate the vector spherical harmonics from one coordinate system to another.

$$^{l}\mathbf{M}^{j}_{\mu\nu} = \sum_{n=1}^{\infty}\sum_{m=-n}^{n}\left(^{lh}A^{\mu\nu\,h}_{mn}\mathbf{M}^{j}_{mn} + {}^{lh}B^{\mu\nu\,h}_{mn}\mathbf{N}^{j}_{mn}\right)$$

$$^{l}\mathbf{N}^{j}_{\mu\nu} = \sum_{n=1}^{\infty}\sum_{m=-n}^{n}\left(^{lh}A^{\mu\nu\,h}_{mn}\mathbf{N}^{j}_{mn} + {}^{lh}B^{\mu\nu\,h}_{mn}\mathbf{M}^{j}_{mn}\right)$$

(5.8)

This is the addition theorem for the vector spherical harmonics. To calculate the scattered field expansion coefficients, it is necessary to calculate the vector addition coefficients. They are:

$$^{lh}A^{\mu\nu}_{mn} = (-1)^{m}i^{n-\nu}\frac{2n+1}{2n(n+1)}\sum_{p=|n-\nu|}^{n+\nu}\left\{ \begin{array}{l} i^{p}\left[n(n+1)+\nu(\nu+1)-p(p+1)\right]\times \\ a(-m,n,\mu,\nu,p)h^{(1)}_{p}(kr_{l,h})P^{\mu-m}_{p}(\cos\theta_{l,h})e^{i(\mu-m)\phi_{l,h}} \end{array} \right\}$$

$$^{lh}B^{\mu\nu}_{mn} = (-1)^{m+1}i^{n-\nu}\frac{2n+1}{2n(n+1)}\sum_{p=|n-\nu|}^{n+\nu}\left\{ i^{p}b(-m,n,\mu,\nu,p,p-1)h^{(1)}_{p}(kr_{l,h})P^{\mu-m}_{p}(\cos\theta_{l,h})e^{i(\mu-m)\phi_{l,h}} \right\}$$

(5.9)

Where $r_{l,h}$, $\theta_{l,h}$, and $\phi_{l,h}$ are the coordinates of the l'th sphere in the h'th coordinate system, and b(-m,n,μ,v,p,p-1) is:

$$b(-m,n,\mu,\nu,p,p-1) = \frac{2p+1}{2p-1}\left[\begin{array}{l} (n-m)(n+m+1)a(-m-1,n,\mu,\nu,p-1) \\ -(p+m-\mu)(p+m-\mu-1)a(-m+1,n,\mu,\mu,\nu,p-1) \\ +2m(p+m-\mu)a(-m,n,\mu,\nu,p-1) \end{array} \right]$$

(5.10)

In these equations, a(m,n,μ,v,p) is the Gaunt coefficient, defined using the Wigner-3j symbol as

$$a(m,n,\mu,\nu,p) = (-1)^{m+\mu}(2p+1)\left[\frac{(n+m)!(\nu+\mu)!(p-m-\mu)!}{(n-m)!(\nu-\mu)!(p+m+\mu)!}\right]\begin{pmatrix} n & \nu & p \\ 0 & 0 & 0 \end{pmatrix}\begin{pmatrix} n & \nu & p \\ m & \mu & -m-\mu \end{pmatrix}$$

(5.11)

The Gaunt coefficients vanish when n+v+p is odd, due to the triangular inequalities for the first symbol. Also, p cannot be less than the absolute value of

m+μ. If these conditions are not fulfilled, the Gaunt coefficient is zero. The Wigner 3j symbols in this case are calculated using Maple 10, with a additional package written by Cooke[28], which uses Racah's formula to do the calculation exactly.

While these are not as time consuming to calculate when compared to other elements of the program, it can be difficult to make sure that they are free of error.

C. Calculation of the Near Field

The calculation uses a matrix formalism, which is to help the bookkeeping of the many indices required, although first, it is important to determine the dimensionality of the problem. For every n, there are 2n+1 possible m states. While summation of n to infinity gives the exact result, the higher orders of n contribute less, and so the summation can be terminated at some finite n. Of course, a problem is knowing *when* how many modes are necessary, as each n requires many more m values, with more complex calculations, leading to much longer computation times. The dimensions of the required tensors initially go as $\sum_{n=1}^{N} 2n+1$, where N is the final n value. Including the different 'p' indices gives double that. So the final matrix dimensions are 6 for a dipolar calculation, 16 for dipolar and quadrupolar, 30 for including up to octapolar, and so on. The initial definitions are:

$$
\begin{aligned}
X_p^l &= \begin{bmatrix} {}^iC_{-11p}^l & {}^iC_{01p}^l & {}^iC_{11p}^l & {}^iC_{-22p}^l & \dots & {}^iC_{MNp}^l \end{bmatrix} \\
Y_p^l &= \begin{bmatrix} \left|-11jp\right\rangle^l & \left|01jp\right\rangle^l & \left|11jp\right\rangle^l & \left|-22jp\right\rangle^l & \dots & \left|MNjp\right\rangle^l \end{bmatrix} \\
Z_1^l &= \begin{bmatrix} b_1^l & b_1^l & b_1^l & b_2^l & \dots & b_N^l \end{bmatrix}^D \\
Z_2^l &= \begin{bmatrix} a_1^l & a_1^l & a_1^l & a_2^l & \dots & a_N^l \end{bmatrix}^D
\end{aligned}
\qquad (5.12)
$$

where N in this case is the final n value, and M the final m. The Z vectors hold the Mie coefficients, which do not depend on m, although the coefficients are repeated for each possible m value to give the Z vectors the same dimensions as X and Y. The superscript D means that a matrix is actually formed from this vector, using the vector elements on the diagonal. The matrices of the addition coefficients are

$$
{}^{lh}\overline{A} = \begin{bmatrix}
{}^{lh}A_{-11}^{-11} & {}^{lh}A_{01}^{-11} & {}^{lh}A_{11}^{-11} & {}^{lh}A_{-22}^{-11} & \cdots & {}^{lh}A_{MN}^{-11} \\
{}^{lh}A_{-11}^{01} & {}^{lh}A_{01}^{01} & {}^{lh}A_{11}^{01} & {}^{lh}A_{-22}^{01} & \cdots & {}^{lh}A_{MN}^{01} \\
{}^{lh}A_{-11}^{11} & {}^{lh}A_{01}^{11} & {}^{lh}A_{11}^{11} & {}^{lh}A_{-22}^{11} & \cdots & {}^{lh}A_{MN}^{11} \\
{}^{lh}A_{-11}^{-22} & {}^{lh}A_{01}^{-22} & {}^{lh}A_{11}^{-22} & {}^{lh}A_{-22}^{-22} & \cdots & {}^{lh}A_{MN}^{-22} \\
\cdots & \cdots & \cdots & \cdots & \cdots & \cdots \\
{}^{lh}A_{-11}^{MN} & {}^{lh}A_{01}^{MN} & {}^{lh}A_{11}^{MN} & {}^{lh}A_{-22}^{MN} & \cdots & {}^{lh}A_{MN}^{MN}
\end{bmatrix}
$$

$$
{}^{lh}\overline{B} = \begin{bmatrix}
{}^{lh}B_{-11}^{-11} & {}^{lh}B_{01}^{-11} & {}^{lh}B_{11}^{-11} & {}^{lh}B_{-22}^{-11} & \cdots & {}^{lh}B_{MN}^{-11} \\
{}^{lh}B_{-11}^{01} & {}^{lh}B_{01}^{01} & {}^{lh}B_{11}^{01} & {}^{lh}B_{-22}^{01} & \cdots & {}^{lh}B_{MN}^{01} \\
{}^{lh}B_{-11}^{11} & {}^{lh}B_{01}^{11} & {}^{lh}B_{11}^{11} & {}^{lh}B_{-22}^{11} & \cdots & {}^{lh}B_{MN}^{11} \\
{}^{lh}B_{-11}^{-22} & {}^{lh}B_{01}^{-22} & {}^{lh}B_{11}^{-22} & {}^{lh}B_{-22}^{-22} & \cdots & {}^{lh}B_{MN}^{-22} \\
\cdots & \cdots & \cdots & \cdots & \cdots & \cdots \\
{}^{lh}B_{-11}^{MN} & {}^{lh}B_{01}^{MN} & {}^{lh}B_{11}^{MN} & {}^{lh}B_{-22}^{MN} & \cdots & {}^{lh}B_{MN}^{MN}
\end{bmatrix}
\tag{5.13}
$$

So these matrices and vectors have $\sum_{n=1}^{N} 2n+1$ dimensions, and contain all the

necessary information: Mie coefficients, translation coefficients, expansion

coefficients, and vector spherical harmonics. We next write a set of matrices and

vectors that include the two different 'p' possibilities, and therefore have

$2\sum_{n=1}^{N} 2n+1$ dimensions, which are slightly more succinct due to the initial

definitions

$$
\begin{aligned}
G_l &= \begin{bmatrix} X_1^l & X_2^l \end{bmatrix} \\
{}^lW_1^E &= \begin{bmatrix} Y_{11}^l & Y_{12}^l \end{bmatrix}^T \\
{}^lW_3^E &= \begin{bmatrix} Y_{31}^l & Y_{32}^l \end{bmatrix}^T \\
S_l &= \begin{bmatrix} Z_1^l & 0 \\ 0 & Z_2^l \end{bmatrix} \\
\Omega_{lh} &= \begin{bmatrix} {}^{lh}\overline{A} & {}^{lh}\overline{B} \\ {}^{lh}\overline{B} & {}^{lh}\overline{A} \end{bmatrix}
\end{aligned}
\tag{5.14}
$$

All the remaining work is done using these 5 terms, all with

$2\sum_{n=1}^{N} 2n+1$ dimensions. There is G, a row vector containing the incident

expansion coefficients, W^E_1, a column vector containing the vector spherical harmonics with spherical Bessel functions of the first kind, W^E_3, of the same type as W^E_1, except using spherical Hankel functions of the first kind, and two matrices. The first is S, a diagonal matrix containing all the Mie coefficients, and Ω_{lh}, containing all the vector addition coefficients. As the problem is limited to the electric field scattered by the spheres, vectors and matricies concerned with the field inside the spheres, as well as terms containing the magnetic field, are ignored.

The use of these terms becomes clear for the case of a single particle. As it is the only scatterer, the scattered field coefficients are the incident field expansion coefficients mediated by the Mie terms, or

$$^1T = GS \tag{5.15}$$

which is a row vector. The scattered field is

$$^1\mathbf{E}_s = {}^1TW^E_3 \tag{5.16}$$

which is a 3 dimensional vector, as the row vector ^1T acts on the column vector W^E_3. In W^E_3, however, each element is a 3 dimensional vector, yielding a sum of electric field vectors, corresponding to the different n,m, and p possibilities. In other words, this is a matrix representation of

$$^1\mathbf{E}_s = \sum_{n}^{N} \sum_{m=-n}^{n} b_n{}^i C_{mn1} |mn31\rangle + a_n{}^i C_{mn2} |mn32\rangle \tag{5.17}$$

which are the Mie results for a single sphere. For two spheres, the situation becomes more complicated, and requires the use of the Ω_{lh} matrices. Using the concept of order of scattering, the scattering matrix T of one of the spheres is representative of the outgoing wave, and is the sum of the different orders of scattering as a result of its own scattering, and the scattering of the other sphere. The following picture should make the notion of order of scattering clear,

considering first the scattering by sphere 1.

Figure 5.1: Ray diagram of the scattering events considered in order of scattering method.

There are 3 separate scattering events depicted in the above figure. The first is the scattering of the incident light off the sphere, designated T_1. The second scattering event has 2 parts. First, the light scatters off of sphere 2, called T_2, some of which impinges on sphere 1, which is re-scattered. This re-scattering process is represented by $\Omega_{21}S_1$, where Ω_{21} is the translation matrix for the basis functions of sphere 2 in sphere 1's coordinate system, and S_1 are the Mie coefficients for sphere 1. Multiplying matrices to the right gives the entire process the $T_2\Omega_{21}S_1$. The third scattering event is a three-part process, starting with the light scattered by the first sphere, T_1. Although some of it escapes detection, some of it impinges on sphere 2, which is then re-scattered. Using the same idea as the second scattering event, the result is $T_1\Omega_{12}S_2$. The third step in the third scattering event is that this light is scattered again by sphere 1, yielding $T_1\Omega_{12}S_2\Omega_{21}S_1$.

The 0th order of scattering for the two spheres can therefore be written

$$^{2}T_{1}=^{1}T_{1}+^{1}T_{2}\Omega_{21}S_{1}$$
$$^{2}T_{2}=^{1}T_{2}+^{1}T_{1}\Omega_{12}S_{2}$$
(5.18)

which includes the first two scattering events described. The 1st order of scattering includes the 3rd event, and a fourth event, which is not pictured, but can be inferred. The total sum of the 0th and 1st order of scattering is

$$^{2}T_{1}=^{1}T_{1}+^{1}T_{2}\Omega_{21}S_{1}+\left(^{1}T_{1}+^{1}T_{2}\Omega_{21}S_{1}\right)\Omega_{12}S_{2}\Omega_{21}S_{1}$$
$$^{2}T_{2}=^{1}T_{2}+^{1}T_{1}\Omega_{12}S_{2}+\left(^{1}T_{2}+^{1}T_{1}\Omega_{12}S_{2}\right)\Omega_{21}S_{1}\Omega_{12}S_{2}$$
(5.19)

Designating the number of orders of scattering to be considered as N_{os}, the summation to arbitrary N_{os} is

$$^{2}T_{1}=\left(^{1}T_{1}+^{1}T_{2}\Omega_{21}S_{1}\right)\sum_{i=0}^{N_{os}}\left(\Omega_{12}S_{2}\Omega_{21}S_{1}\right)^{i}$$

$$^{2}T_{2}=\left(^{1}T_{2}+^{1}T_{1}\Omega_{12}S_{2}\right)\sum_{i=0}^{N_{os}}\left(\Omega_{21}S_{1}\Omega_{12}S_{2}\right)^{i}$$
(5.20)

Although this uses different notation, it is the same concept as the order of scattering described by Fuller[6,18-20], with all the difficulties in convergence. The hybrid matrix inversion-order of scattering formalism conceived by Xu[21,22] makes a small change to the summation over the scattering orders. The summation

$$\sum_{i=0}^{N_{os}}\left(\Omega_{12}S_{2}\Omega_{21}S_{1}\right)^{i}=\sum_{i=0}^{N_{os}}A^{i}$$
(5.21)

has a closed form for the case of $|A|<1$

$$\sum_{i=0}^{N_{os}}A^{i}=1+A+A^{2}+...+A^{N_{os}}$$

$$A\sum_{i=0}^{N_{os}}A^{i}=A+A^{2}+...+A^{N_{os}}+A^{N_{os}+1}$$

$$\sum_{i=0}^{N_{os}}A^{i}-A\sum_{i=0}^{N_{os}}A^{i}=1-A^{N_{os}+1}$$
(5.22)

$$\sum_{i=0}^{N_{os}}A^{i}\left(1-A\right)=1-A^{N_{os}+1}$$

$$\sum_{i=0}^{N_{os}}A^{i}=\frac{1-A^{N_{os}+1}}{1-A}$$

If we allow consideration of an infinite number of orders of scattering, this gives

$$\sum_{i=0}^{N_{os}} A^i = \frac{1}{1-A} \tag{5.23}$$

which is a closed form for the summation over the orders of scattering:

$$\sum_{i=0}^{N_{os}} \left(\Omega_{12}S_2\Omega_{21}S_1\right)^i = \frac{1}{1-\Omega_{12}S_2\Omega_{21}S_1} \tag{5.23}$$

So while this involves a matrix inversion for each case, it is an inversion of a matrix of only dimensions $2\sum_{n=1}^{N} 2n+1$, no matter how many particles are considered. Naturally, more particles will mean more matrix inversions, but they are always of the constant size. This also sidesteps the convergence issues, as repeated matrix multiplications are no longer necessary. An additional advantage is that an infinite order of scattering is considered, giving accuracy is that regard.

The T matrix for each particle is then

$$^2T_1 = \left(^1T_1 + {}^1T_2\Omega_{21}S_1\right)\frac{1}{1-\Omega_{12}S_2\Omega_{21}S_1}$$
$$^2T_2 = \left(^1T_2 + {}^1T_1\Omega_{12}S_2\right)\frac{1}{1-\Omega_{21}S_1\Omega_{12}S_2} \tag{5.24}$$

The total electric field is given by the sum of the electric fields scattered by the two particles:

$$^2\mathbf{E}_s = {}^2T_1\,{}^1W_3^E + {}^2T_2\,{}^2W_3^E \tag{5.25}$$

Li and Xu[23] improved the formalism more, which creates a clearer way to do the calculation for 3 particles. For the sake of brevity, matrices of double the size already considered are used, although the matrix inversion remains of the same dimension. The two particle case considered can be written as

$$\left(^2T_1, {}^2T_2\right) = \left(G_1, G_2\right)\Psi^{(2)}$$

$$\Psi^{(2)} = \begin{pmatrix} S_1\dfrac{1}{1-\Omega_{12}S_2\Omega_{21}S_1} & S_1\Omega_{12}S_2\dfrac{1}{1-\Omega_{21}S_1\Omega_{12}S_2} \\[2ex] S_2\Omega_{21}S_1\dfrac{1}{1-\Omega_{12}S_2\Omega_{21}S_1} & S_2\dfrac{1}{1-\Omega_{21}S_1\Omega_{12}S_2} \end{pmatrix} \tag{5.25}$$

The scattering by a third particle must consider the scattering by light scattered from it, the re-scattering of light scattered by particle 1 and 2, and all subsequent

orders which is scattered back and forth. The scattering matrix of the third sphere is

$$
{}^3T_3 = \left((G_1, G_2) \Psi^{(2)} \begin{pmatrix} \Omega_{1,3} \\ \Omega_{2,3} \end{pmatrix} S_3 + G_3 S_3 \right) \frac{1}{1 - (\Omega_{3,1}, \Omega_{3,2}) \Psi^{(2)} \begin{pmatrix} \Omega_{1,3} \\ \Omega_{2,3} \end{pmatrix} S_3} \tag{5.26}
$$

Although the term to be inverted looks like it has twice the dimensions previously, it can be expressed as

$$
\begin{aligned}
(\Omega_{31} \quad \Omega_{32}) \Psi^{(2)} \begin{pmatrix} \Omega_{13} \\ \Omega_{23} \end{pmatrix} &= (\Omega_{31} \quad \Omega_{32}) \begin{pmatrix} S_1 \dfrac{1}{1 - \Omega_{12} S_2 \Omega_{21} S_1} & S_1 \Omega_{12} S_2 \dfrac{1}{1 - \Omega_{21} S_1 \Omega_{12} S_2} \\ S_2 \Omega_{21} S_1 \dfrac{1}{1 - \Omega_{12} S_2 \Omega_{21} S_1} & S_2 \dfrac{1}{1 - \Omega_{21} S_1 \Omega_{12} S_2} \end{pmatrix} \begin{pmatrix} \Omega_{13} \\ \Omega_{23} \end{pmatrix} \\
&= (\Omega_{31} \quad \Omega_{32}) \begin{pmatrix} S_1 \dfrac{1}{1 - \Omega_{12} S_2 \Omega_{21} S_1} \Omega_{13} + S_1 \Omega_{12} S_2 \dfrac{1}{1 - \Omega_{21} S_1 \Omega_{12} S_2} \Omega_{23} \\ S_2 \Omega_{21} S_1 \dfrac{1}{1 - \Omega_{12} S_2 \Omega_{21} S_1} \Omega_{13} + S_2 \dfrac{1}{1 - \Omega_{21} S_1 \Omega_{12} S_2} \Omega_{23} \end{pmatrix} \\
&= \Omega_{31} S_1 \dfrac{1}{1 - \Omega_{12} S_2 \Omega_{21} S_1} \Omega_{13} + \Omega_{31} S_1 \Omega_{12} S_2 \dfrac{1}{1 - \Omega_{21} S_1 \Omega_{12} S_2} \Omega_{23} \\
&\quad + \Omega_{32} S_2 \Omega_{21} S_1 \dfrac{1}{1 - \Omega_{12} S_2 \Omega_{21} S_1} \Omega_{13} + \Omega_{32} S_2 \dfrac{1}{1 - \Omega_{21} S_1 \Omega_{12} S_2} \Omega_{23}
\end{aligned} \tag{5.27}
$$

So, while the shorthand of the equation looks like it implies extra dimensions to invert, it only collapses the sums of terms. Once ${}^3T_3$ is calculated, it is used to calculate the three particle scattering for the other two particles ${}^3T_1$ and ${}^3T_2$ by

$$
\left({}^2T_1, {}^2T_2 \right) = \left[(G_1, G_2) + {}^3T_3 (\Omega_{31}, \Omega_{32}) \right] \Psi^{(2)} \tag{5.28}
$$

While Li and Xu generalize this approach for any number of particles, three is enough to generate the sort of hot spot required for surface enhanced Raman experiments. The rest of this section is devoted to special cases of the above theory, which eases computation while being a suitable model for field enhancement.

D. Normal Incidence

For normal incidence, where the light is impinging from the -z axis, for example, the expansion coefficients simplify somewhat. This is a common situation for surface enhancement, where the nanoparticles lie on a plane, forming a substrate, and the incident light approaches perpendicular to that plane. The expansion coefficients for the incident light simplify for two reasons: First, the wavevector **k** is now defined to be in the $+\hat{z}$ direction. Also, no component of the electric field will be in the z direction, or $E_z=0$. Applying this condition first simplifies the expansion coefficients to

$$
{}^{i}C^{l}_{mn1} = \frac{2\pi i^n}{n(n+1)}\left\{\begin{array}{l} -(iE_x - E_y)\sqrt{(n+m+1)(n-m)}\left(Y_n^{m+1}(\hat{k})\right)^* \\ -(iE_x + E_y)\sqrt{(n-m+1)(n+m)}\left(Y_n^{m-1}(\hat{k})\right)^* \end{array}\right\}
$$

$$
{}^{i}C^{l}_{mn2} = \frac{2\pi i^n}{n(n+1)}\left\{\begin{array}{l} n\sqrt{\dfrac{(n+m+1)(n+m+2)}{(2n+1)(2n+3)}}(iE_x - E_y)\left(Y_{n+1}^{m+1}(\hat{k})\right)^* \\ -n\sqrt{\dfrac{(n-m+1)(n-m+2)}{(2n+1)(2n+3)}}(iE_x + E_y)\left(Y_{n+1}^{m-1}(\hat{k})\right)^* \\ -(n+1)\sqrt{\dfrac{(n-m-1)(n-m)}{(2n-1)(2n+1)}}(-iE_x + E_y)\left(Y_{n-1}^{m+1}(\hat{k})\right)^* \\ -(n+1)\sqrt{\dfrac{(n+m-1)(n+m)}{(2n-1)(2n+1)}}(iE_x + E_y)\left(Y_{n-1}^{m-1}(\hat{k})\right)^* \end{array}\right\}
$$

(5.29)

The second condition, that the light is incident from the $+\hat{z}$ direction implies that θ in the spherical harmonics is identically zero. Using the definition[29]

$$
Y_n^m(\theta,\phi) = \sqrt{\frac{2n+1}{4\pi}\frac{(n-m)!}{(n+m)!}}P_n^m(\cos\theta)e^{im\phi}
$$

$$
\left(Y_n^m(\theta,\phi)\right)^* = (-1)^m Y_n^{-m}(\theta,\phi)
$$

(5.30)

it is clear from this definition that complex conjugation has no effect on the associated Legendre polynomial $P^m_n(\cos\theta)$. The associated Legendre polynomials reparameterized in terms of angle have a generating function of

$$
P_n^m(\cos\theta) = (-1)^m(\sin\theta)^m\frac{d^m}{d(\cos\theta)^m}(P_n(\cos\theta))
$$

(5.31)

which is valid only for positive m. Taking the first $P_n(x)=\cos\theta$, the possible associated Legendre polynomials are

$$P_1^0(\cos\theta)=(-1)^0(\sin\theta)^0\frac{d^0}{d(\cos\theta)^0}(\cos\theta)=\cos\theta$$

$$P_1^1(\cos\theta)=-\sin\theta\frac{d}{d(\cos\theta)}(\cos\theta)=-\sin\theta$$

(5.32)

Due to the presence of the sin function, $P^1_1(\cos\theta)=0$. The associated Legendre polynomial for m=0 will not be zero, as it is the Legendre polynomial $P_n(\cos\theta)$ in that case. However, for any m not equal zero, the $P^1_n(\cos\theta)=0$, as can be seen for the m=1 case obtained by recursion:

$$P_{n+1}^m(\cos\theta)=\frac{(2n+1)\cos\theta P_n^m(\cos\theta)-(n+m)P_{n-1}^m(\cos\theta)}{n-m+1}$$

$$P_{n+1}^1(\cos\theta)=\frac{(2n+1)\cos\theta P_n^1(\cos\theta)-(n+1)P_{n-1}^1(\cos\theta)}{n}$$

$$P_2^1(\cos\theta)=-3\cos\theta\sin\theta\big|_{\theta=0}=0$$

$$P_3^1(\cos\theta)=\frac{-15\cos^2\theta\sin\theta+3\sin\theta}{2}\bigg|_{\theta=0}=0$$

(5.33)

The sin function in the generating function of the associated Legendre polynomials controls the exponent of the sin function in the result. Unless m=0, a sin function will always be present, making the function 0 for θ=0. The incident coefficients are zero for any case except m=-1 and m=1. Although the azimuthal angle is undetermined in this case, it no longer has an effect in the equations, since the non-zero elements will always pass an m=0 into the spherical harmonic, making the complex exponent unity. In other words, the required spherical harmonics in the incident field expansion coefficients now appear as

$$Y_n^m(0,\phi)=\sqrt{\frac{2n+1}{4\pi}}P_n(\cos\theta)=\left(Y_n^m(0,\phi)\right)^*$$

(5.34)

With the use of the Kronecker delta, this gives the coefficients as:

$$^{i}C_{mn1}^{l} = \frac{-\sqrt{\pi}i^{n}}{\sqrt{n(n+1)}}\sqrt{2n+1}P_{n}(\cos\theta)\left\{(iE_{x}-E_{y})\delta_{m,-1}+(iE_{x}+E_{y})\delta_{m,1}\right\}$$

$$^{i}C_{mn2}^{l} = \frac{\sqrt{\pi}i^{n}}{\sqrt{n(n+1)}}\frac{1}{\sqrt{2n+1}}\left\{\begin{array}{l}nP_{n+1}(\cos\theta)[(iE_{x}-E_{y})\delta_{m,-1}-(iE_{x}+E_{y})\delta_{m,1}]\\-(n+1)\sqrt{\frac{1}{4\pi}}P_{n-1}(\cos\theta)[(-iE_{x}+E_{y})\delta_{m,-1}+(iE_{x}+E_{y})\delta_{m,1}]\end{array}\right\}$$

(5.35)

While not quite elegant yet, they are certainly in a much more tractable form with a very physical assumption. An additional aid from this simplification is that there is no angular difference in the **k** for any of the particles, so that the G vector is the same for each particle. Thus, for two particles, the T matrix is

$$^{2}T_{1} = (GS_{1}+GS_{2}\Omega_{21}S_{1})\frac{1}{1-\Omega_{12}S_{2}\Omega_{21}S_{1}} = G(S_{1}+S_{2}\Omega_{21}S_{1})\frac{1}{1-\Omega_{12}S_{2}\Omega_{21}S_{1}}$$

$$^{2}T_{2} = (GS_{2}+GS_{1}\Omega_{12}S_{2})\frac{1}{1-\Omega_{21}S_{1}\Omega_{12}S_{2}} = G(S_{2}+S_{1}\Omega_{12}S_{2})\frac{1}{1-\Omega_{21}S_{1}\Omega_{12}S_{2}}$$

(5.36)

Although many zeros will appear in the G vector, it does not necessarily reduce the number of terms in the T matrix. For example, due to the matrices of addition coefficients, the term being multiplied by G is a matrix with no elements that are necessarily zero. As such, the resulting T will also have no elements that are necessarily zero. Note that this choice of coordinates makes the situation analogous to the single particle case, where m=±1 were the only choices. It is not so simple here, of course, due to the multiple particle scattering.

A different choice of axis may elongate the calculation somewhat, but is often more useful, as different terms can simplify for a different choice of **k**. For a different set-up consider the case where the light impinges from the $-\hat{x}$, making the wavevector point in the $+\hat{x}$ direction. This is a reasonable choice, as the azimuthal angle will be identically zero, and the zenith angle π/2. Also, no component of the electric field will point in the $\hat{x}$ direction. The restriction on the azimuthal angle will cause the spherical harmonics to be wholly real, removing the need for complex conjugation.

$$
{}^{i}C_{mn1}^{l} = \frac{2\pi i^{n}}{n(n+1)} \left\{ \begin{array}{l} E_{y}\left(\sqrt{(n+m+1)(n-m)}Y_{n}^{m+1}(\hat{x}) - E_{y}\sqrt{(n-m+1)(n+m)}Y_{n}^{m-1}(\hat{x})\right) \\ + 2imE_{z}Y_{n}^{m}(\hat{x}) \end{array} \right\}
$$

$$
{}^{i}C_{mn2}^{l} = \frac{2\pi i^{n}}{n(n+1)} \left\{ \begin{array}{l} -E_{y}\left(\begin{array}{l} n\sqrt{\dfrac{(n+m+1)(n+m+2)}{(2n+1)(2n+3)}}Y_{n+1}^{m+1}(\hat{x}) + n\sqrt{\dfrac{(n-m+1)(n-m+2)}{(2n+1)(2n+3)}}E_{y}Y_{n+1}^{m-1}(\hat{x}) + \\ (n+1)\sqrt{\dfrac{(n-m-1)(n-m)}{(2n-1)(2n+1)}}E_{y}Y_{n-1}^{m+1}(\hat{x}) + (n+1)\sqrt{\dfrac{(n+m-1)(n+m)}{(2n-1)(2n+1)}}E_{y}Y_{n-1}^{m-1}(\hat{x}) \end{array} \right) \\[2em] + \left[2in\sqrt{\dfrac{(n+m+1)(n-m+1)}{(2n+1)(2n+3)}}Y_{n+1}^{m}(\hat{x}) - 2i(n+1)\sqrt{\dfrac{(n+m)(n-m)}{(2n-1)(2n+1)}}Y_{n-1}^{m}(\hat{x}) \right]E_{z} \end{array} \right\}
$$

(5.37)

Unfortunately, while there are a number of zeros for the Legendre polynomials for θ= π/2, it is not really worth pursuing.

E. Particles Along a Common Z-Axis

For the case of two or more particles along a single axis there is substantial improvement in the form of the addition coefficients. As seen previously, the associated Legendre polynomials for the case of θ=0 are zero for any m except m=0. This causes zeros for many terms in the addition coefficients. For the case of two particles, it can therefore mean substantial improvements in computational time. For the coefficients presented here,

$$
^{lh}A_{mn}^{\mu\nu} = (-1)^m i^{n-\nu}\frac{2n+1}{2n(n+1)}\sum_{p=|n-\nu|}^{n+\nu}\left\{\begin{array}{l}i^p\left[n(n+1)+\nu(\nu+1)-p(p+1)\right]\times\\ a(-m,n,\mu,\nu,p)h_p^{(1)}(kr_{l,h})P_p^{\mu-m}(\cos\theta_{l,h})e^{i(\mu-m)\phi_{l,h}}\end{array}\right\}
$$

$$
^{lh}B_{mn}^{\mu\nu} = (-1)^{m+1} i^{n-\nu}\frac{2n+1}{2n(n+1)}\sum_{p=|n-\nu|}^{n+\nu}\left\{i^p b(-m,n,\mu,\nu,p,p-1)h_p^{(1)}(kr_{l,h})P_p^{\mu-m}(\cos\theta_{l,h})e^{i(\mu-m)\phi_{l,h}}\right\}
$$

(5.38)

this implies that μ=m. These terms can then be rewritten:

$$
^{lh}A_{mn}^{m\nu} = (-1)^m i^{n-\nu}\frac{2n+1}{2n(n+1)}\sum_{p=|n-\nu|}^{n+\nu}\left\{\begin{array}{l}i^p\left[n(n+1)+\nu(\nu+1)-p(p+1)\right]\times\\ a(-m,n,m,\nu,p)h_p^{(1)}(kr_{l,h})P_p(\cos\theta_{l,h})\end{array}\right\}
$$

$$
^{lh}B_{mn}^{m\nu} = (-1)^{m+1} i^{n-\nu}\frac{2n+1}{2n(n+1)}\sum_{p=|n-\nu|}^{n+\nu}\left\{i^p b(-m,n,m,\nu,p,p-1)h_p^{(1)}(kr_{l,h})P_p(\cos\theta_{l,h})\right\}
$$

(5.39)

where

$$
b(-m,n,\mu,\nu,p,p-1)=\frac{2p+1}{2p-1}\left[\begin{array}{l}(n-m)(n+m+1)a(-m-1,n,\mu,\nu,p-1)\\ -(p+m-\mu)(p+m-\mu-1)a(-m+1,n,\mu,\mu,\nu,p-1)\\ +2m(p+m-\mu)a(-m,n,\mu,\nu,p-1)\end{array}\right]
$$

(5.40)

now becomes:

$$
b(-m,n,m,\nu,p,p-1)=\frac{2p+1}{2p-1}\left[\begin{array}{l}(n-m)(n+m+1)a(-m-1,n,m,\nu,p-1)\\ -p(p-1)a(-m+1,n,m,\mu,\nu,p-1)\\ +2mpa(-m,n,m,\nu,p-1)\end{array}\right]
$$

(5.41)

In the equation for $A^{m\nu}_{mn}$ the a(-m,n,m,v,p) is

$$
a(-m,n,m,\nu,p)=(2p+1)\left[\frac{(n-m)!(\nu+m)!}{(n+m)!(\nu-m)!}\right]\begin{pmatrix}n & \nu & p\\ 0 & 0 & 0\end{pmatrix}\begin{pmatrix}n & \nu & p\\ -m & m & 0\end{pmatrix}
$$

(5.42)

and the terms in $B^{m\nu}_{mn}$ are

$$a(-m-1,n,m,\nu,p-1) = -(2p-1)\left[\frac{(n-m-1)!(\nu+m)!\,p!}{(n+m+1)!(\nu-m)!(p-2)!}\right]\begin{pmatrix} n & \nu & p-1 \\ 0 & 0 & 0 \end{pmatrix}\begin{pmatrix} n & \nu & p-1 \\ -m-1 & m & 1 \end{pmatrix}$$

$$a(-m+1,n,\mu,\nu,p-1) = -(2p-1)\left[\frac{(n-m+1)!(\nu+m)!(p-2)!}{(n+m-1)!(\nu-m)!\,p!}\right]\begin{pmatrix} n & \nu & p-1 \\ 0 & 0 & 0 \end{pmatrix}\begin{pmatrix} n & \nu & p-1 \\ -m+1 & m & -1 \end{pmatrix}$$

$$a(-m,n,\mu,\nu,p-1) = (2p-1)\left[\frac{(n-m)!(\nu+m)!}{(n+m)!(\nu-m)!}\right]\begin{pmatrix} n & \nu & p-1 \\ 0 & 0 & 0 \end{pmatrix}\begin{pmatrix} n & \nu & p-1 \\ -m & m & 0 \end{pmatrix}$$

(5.43)

Using the recursion relations, Bruning and Lo[12] showed that this is equivalent to:

$$^{lh}A^{m\nu}_{mn} = (-1)^m i^{n-\nu}\frac{2n+1}{2n(n+1)}\sum_{p=|n-\nu|}^{n+\nu}\begin{Bmatrix} i^p[n(n+1)+\nu(\nu+1)-p(p+1)]\times \\ a(-m,n,m,\nu,p)h^{(1)}_p(kr_{l,h})P_p(\cos\theta_{l,h}) \end{Bmatrix}$$

$$^{lh}B^{m\nu}_{mn} = (-1)^m i^{n-\nu}\frac{2n+1}{2n(n+1)}\sum_{p=|n-\nu|}^{n+\nu}\{i^p(-2imkd)a(-m,n,m,\nu,p)h^{(1)}_p(kr_{l,h})P_p(\cos\theta_{l,h})\}$$

(5.44)

which is a great simplification of $B^{m\nu}_{mn}$. Further, the Legendre polynomials are 1 for all p at θ=0, and have a value of $(-1)^p$ at θ=π. Thus, switching the particle index is only a difference in sign. So for θ=0 the coefficients are:

$$^{lh}A^{m\nu}_{mn} = (-1)^m i^{n-\nu}\frac{2n+1}{2n(n+1)}\sum_{p=|n-\nu|}^{n+\nu}\begin{Bmatrix} i^p[n(n+1)+\nu(\nu+1)-p(p+1)]\times \\ a(-m,n,m,\nu,p)h^{(1)}_p(kr_{l,h}) \end{Bmatrix}$$

$$^{lh}B^{m\nu}_{mn} = (-1)^m i^{n-\nu}\frac{2n+1}{2n(n+1)}\sum_{p=|n-\nu|}^{n+\nu}\{i^p(-2imkd)a(-m,n,m,\nu,p)h^{(1)}_p(kr_{l,h})\}$$

(5.45)

Thus, the only geometrical term of importance is the distance between the particles, as expected.

F. Field on a Point on the Z-axis

For the case considered previously, that of particles along a common axis, the addition coefficients for the spherical harmonics are simplified significantly. The highest field in many cases will be at the junction between the two particles, which is a point on the z-axis. It is worthwhile simplifying the vector spherical harmonics to speed calculation for this point. The vector spherical harmonics, using the Hankel functions are

$$|mn31\rangle = \begin{bmatrix} 0 \\ \dfrac{im}{\sin\theta} \\ \dfrac{\partial}{\partial\theta} \end{bmatrix} h_n^{(1)}(kr)Y_n^m(\theta,\phi)$$

$$|mn32\rangle = \begin{bmatrix} n(n+1)h_n^{(j)}(kr) \\ -\dfrac{\partial}{\partial kr}\left\{krh_n^{(j)}(kr)\right\}\dfrac{\partial}{\partial\theta} \\ \dfrac{\partial}{\partial kr}\left\{krh_n^{(j)}(kr)\right\}\dfrac{im}{\sin\theta} \end{bmatrix} \dfrac{1}{kr}Y_n^m(\theta,\phi)$$

(5.46)

We can assume without loss of generality in this case that one particle is at the origin, labelled particle 1, and the second on the positive z axis, labelled particle 2. The distance between the sphere surfaces is labelled d, and so the distance between particle centers, assuming identical particles, is 2r+d. The zenith angle from particle 1 to the middle of the distance between them is identically zero, while the zenith angle for particle 2 to the same point is π. Once again, the azimuthal angle is indeterminate.

As seen before, the associated Legendre polynomials are zero for θ=0 except in the case of m=0. The vector spherical harmonics, however, have additional terms that may affect this. The argument opens by considering the first 2 (scalar) spherical harmonics[29]

$$Y_1^0(\theta,\phi) = \sqrt{\frac{3}{4\pi}} \cos\theta$$

$$Y_1^1(\theta,\phi) = -\sqrt{\frac{3}{8\pi}} \sin\theta e^{i\phi}$$

<div align="right">(5.47)</div>

Although the m=1 case is zero for θ=(0, π), there is a Y^m_n term divided by sin θ which will not be zero. When multiplied by m and divided by sin θ, this second type of term is

$$\frac{mY_1^0(0,\phi)}{\sin\theta} = 0$$

$$\frac{mY_1^1(0,\phi)}{\sin\theta} = -\sqrt{\frac{3}{8\pi}} e^{-i\phi}$$

<div align="right">(5.48)</div>

There is a further third type of term, the derivative of the spherical harmonic with respect to θ. These functions go as

$$\frac{\partial}{\partial\theta} Y_1^0(0,\phi) = 0$$

$$\frac{\partial}{\partial\theta} Y_1^1(0,\phi) = -\sqrt{\frac{3}{8\pi}} e^{-i\phi}$$

<div align="right">(5.49)</div>

And so, once again, these terms do not drop out so easily. For n=2 there are 3 m possibilities

$$Y_2^0(\theta,\phi) = \sqrt{\frac{5}{16\pi}} (3\cos^2\theta - 1)\Big|_{\theta=0} = \sqrt{\frac{5}{4\pi}}$$

$$Y_2^1(\theta,\phi) = -\sqrt{\frac{15}{8\pi}} \sin\theta\cos\theta e^{i\phi}\Big|_{\theta=0} = 0$$

$$Y_2^2(\theta,\phi) = \sqrt{\frac{15}{32\pi}} \sin^2\theta e^{2i\phi}\Big|_{\theta=0} = 0$$

<div align="right">(5.50)</div>

Taking the second case, multiplied by m and divided by sin θ

$$\frac{mY_2^0(\theta,\phi)}{\sin\theta} = 0$$

$$\frac{mY_2^1(\theta,\phi)}{\sin\theta} = -\sqrt{\frac{15}{8\pi}}\cos\theta e^{i\phi}\bigg|_{\theta=0} = -\sqrt{\frac{15}{8\pi}}e^{i\phi} \qquad (5.51)$$

$$\frac{mY_2^2(\theta,\phi)}{\sin\theta} = 2\sqrt{\frac{15}{32\pi}}\sin\theta e^{2i\phi}\bigg|_{\theta=0} = 0$$

And lastly, the differentiated terms are:

$$\frac{\partial}{\partial\theta}Y_2^0(\theta,\phi) = -\sqrt{\frac{5}{16\pi}}(6\cos\theta\sin\theta)\bigg|_{\theta=0} = 0$$

$$\frac{\partial}{\partial\theta}Y_2^1(\theta,\phi) = -\sqrt{\frac{15}{8\pi}}(\cos^2\theta - \sin^2\theta)e^{i\phi}\bigg|_{\theta=0} = -\sqrt{\frac{15}{8\pi}}e^{i\phi} \quad (5.52)$$

$$\frac{\partial}{\partial\theta}Y_2^2(\theta,\phi) = \sqrt{\frac{15}{32\pi}}(2\cos\theta\sin\theta)\theta e^{2i\phi}\bigg|_{\theta=0} = 0$$

Lastly, for n=3 there are 4 m possibilities.

$$Y_3^0(\theta,\phi) = \sqrt{\frac{7}{16\pi}}\cos\theta(5\cos^2\theta - 3)\bigg|_{\theta=0} = \sqrt{\frac{7}{\pi}}$$

$$Y_3^1(\theta,\phi) = -\frac{1}{8}\sqrt{\frac{21}{\pi}}\sin\theta(5\cos^2\theta - 1)e^{i\phi}\bigg|_{\theta=0} = 0$$

$$Y_3^2(\theta,\phi) = \sqrt{\frac{15}{32\pi}}\sin^2\theta\cos\theta e^{2i\phi}\bigg|_{\theta=0} = 0 \qquad (5.53)$$

$$Y_3^3(\theta,\phi) = \sqrt{\frac{15}{32\pi}}\sin^3\theta e^{3i\phi}\bigg|_{\theta=0} = 0$$

Considering the other two forms of the spherical harmonics as before:

$$\frac{mY_3^0(\theta,\phi)}{\sin\theta} = 0$$

$$\frac{mY_3^1(\theta,\phi)}{\sin\theta} = -\frac{1}{8}\sqrt{\frac{21}{\pi}}(5\cos^2\theta - 1)e^{i\phi}\bigg|_{\theta=0} = -\frac{1}{2}\sqrt{\frac{21}{\pi}}e^{i\phi}$$

$$\frac{mY_3^2(\theta,\phi)}{\sin\theta} = 2\sqrt{\frac{15}{32\pi}}\sin\theta\cos\theta e^{2i\phi}\bigg|_{\theta=0} = 0 \qquad (5.54)$$

$$\frac{mY_3^3(\theta,\phi)}{\sin\theta} = 3\sqrt{\frac{15}{32\pi}}\sin^2\theta e^{3i\phi}\bigg|_{\theta=0} = 0$$

$$\frac{\partial}{\partial\theta}Y_3^0(\theta,\phi) = -\sqrt{\frac{7}{16\pi}}\sin\theta(15\cos^2\theta - 3)\bigg|_{\theta=0} = 0$$

$$\frac{\partial}{\partial\theta}Y_3^1(\theta,\phi) = -\frac{1}{8}\sqrt{\frac{21}{\pi}}\cos\theta(5\cos^2\theta - 10\sin^2\theta - 1)e^{i\phi}\bigg|_{\theta=0} = -\frac{1}{2}\sqrt{\frac{21}{\pi}}e^{i\phi}$$

$$\frac{\partial}{\partial\theta}Y_3^2(\theta,\phi) = \sqrt{\frac{15}{32\pi}}\sin\theta(2\cos^2\theta - \sin^2\theta)e^{2i\phi}\bigg|_{\theta=0} = 0 \qquad (5.55)$$

$$\frac{\partial}{\partial\theta}Y_3^3(\theta,\phi) = \sqrt{\frac{15}{32\pi}}3\sin^2\theta\cos\theta e^{3i\phi}\bigg|_{\theta=0} = 0$$

The point of going through these first 9 spherical harmonics is to show that there are only results at m=0 and m=1, and therefore, for m=-1. Higher orders of m follow the same trend, as the generating function explicitly has a sinθ term which controls the order of sinθ in each associated function. Since dividing by sinθ and differentiation with respect to θ each reduce the order of sinθ by one, no matter what n value, the associated Legendre polynomial in the spherical harmonics for m greater than 2 will always be zero.

G. Asymptotic Expansion for Large Separation

If the particles are situated far from each other, a simple form of the translation coefficients can be derived. An asymptotic result would not only be useful to form approximate results quickly, but is also useful in verifying the validity of the numerical results for the translation coefficients. Since the translation coefficients are both critical to the solution of the problem, and also require detailed calculation which may be prone to error, some method of verification would be highly desirable.

The spherical Hankel functions, $h_n^{(1)}(x)$ of the first kind, sometimes called the spherical Bessel functions of the third kind, can be written as[30]

$$h_n^{(1)}(x) = \frac{(i)^{-n-1}e^{ix}}{x} \sum_0^n \left(n+\frac{1}{2},k\right) \frac{1}{(-2ix)^k}$$

$$\left(n+\frac{1}{2},k\right) = \frac{(n+k)!}{k!\Gamma(n-k+1)}$$

(5.56)

where k is an integer that is implicitly summed to n, and Γ is the gamma function. Since the argument of the gamma function is always a positive integer, this is simplified to $\Gamma(n-k+1)=(n-k)!$ For arbitrary n, this yields

$$h_n^{(1)}(x) = \frac{(i)^{-n-1}e^{ix}}{x}\left(1 + \frac{(n+1)!}{(n-1)!}\frac{i}{2x} - \frac{(n+2)!}{2!(n-2)!}\frac{1}{4x^2} + ...\right)$$

(5.57)

The second term, which is proportional to the inverse of the argument, can be simplified by examination of the ratio of factorial terms:

$$\frac{(n+1)!}{(n-1)!} = \frac{(n+1)n(n-1)(n-2)(...)(1)}{(n-1)(n-2)(...)(1)} = n(n+1)$$

(5.58)

And similarly for the third and higher order terms. Thus, the Hankel function goes as

$$h_n^{(1)}(x) = \frac{(i)^{-n-1}e^{ix}}{x}\left(1 + \frac{in(n+1)}{2x} - \frac{(n+2)(n+1)n(n-1)}{2!}\frac{1}{4x^2} + ...\right)$$

(5.59)

For large x, this function can be truncated. Keeping only the constant term, this becomes

$$h_n^{(1)}(x) = \frac{(i)^{-n-1}e^{ix}}{x}\left(1 + O\left(\frac{n^2}{x}\right)\right)$$

(5.60)

This asymptotic form is thus appropriate when x>>n². As x=kd, when d is the centre to centre distance between the spheres, this corresponds to

$$\frac{2\pi d}{\lambda} >> n^2 \rightarrow d >> \frac{n^2\lambda}{2\pi}$$

(5.61)

The Hankel functions appears in the translation coefficients, where they are of maximum order p=n+v.

$$h_p^{(1)}(kd) = \frac{i^{-p-1}e^{ikd}}{kd}$$

(5.62)

The translation coefficients are

$$A_{mv}^{mn} = (-1)^m i^{v-n}\frac{2v+1}{2v(v+1)}\sum_p i^{-p}\left[n(n+1)+v(v+1-p(p+1)\right]a(m,n,-m,v,p)h_p^{(1)}(kd)$$

$$B_{mv}^{mn} = -(-1)^m i^{v-n}\frac{2v+1}{2v(v+1)}\sum_p i^{-p}2imkda(m,n,-m,v,p)h_p^{(1)}(kd)$$

(5.63)

Putting the asymptotic form in gives:

$$A_{mv}^{mn} = (-1)^m i^{v-n}\frac{2v+1}{2v(v+1)}\frac{e^{ikd}}{kd}\sum_p i^{-p}i^{-p-1}\left[n(n+1)+v(v+1)-p(p+1)\right]a(m,n,-m,v,p)$$

$$B_{mv}^{mn} = -(-1)^m i^{v-n}\frac{2v+1}{2v(v+1)}e^{ikd}\sum_p i^{-p}i^{-p-1}2ima(m,n,-m,v,p)$$

(5.64)

The exponents of i can be simplified to give:

$$i^{-p}i^{-p-1} = i^{-2p}i^{-1} = \left(\pm\sqrt{-1}\right)^{2p}i^{-1} = (-1)^p i^{-1}$$

(5.65)

$$A_{mv}^{mn} = (-1)^m i^{v-n-1}\frac{2v+1}{2v(v+1)}\frac{e^{ikd}}{kd}\sum_p (-1)^p\left[n(n+1)+v(v+1)-p(p+1)\right]a(m,n,-m,v,p)$$

$$B_{mv}^{mn} = -(-1)^m i^{v-n}\frac{2v+1}{2v(v+1)}e^{ikd}\sum_p (-1)^p 2ma(m,n,-m,v,p)$$

(5.66)

Due to the nature of the $a(m,n,-m,v,p)$ terms, which are zero if $n+v+p$ is an odd number, p will uniformly be even or odd, as $p = n+v$, $n+v-2,...,| n-v|$. We can pull out the $(-1)^p$ factor, and represent it as $(-1)^{v-n}$ which will be positive for $n+v$ even, and negative for $n+v$ odd, as required. We also can insert a Legendre polynomial, $P_p(\cos\theta)$, into the sum, as it will be unity for all p for $\theta=0$.

$$A_{mv}^{mn} = -i(-1)^{m+v-n}i^{v-n}\frac{2v+1}{2v(v+1)}\frac{e^{ikd}}{kd}\sum_p[n(n+1)+v(v+1)-p(p+1)]a(m,n,-m,v,p)P_p(\cos\theta)$$

$$B_{mv}^{mn} = -(-1)^{m+v-n}i^{v-n}2m\frac{2v+1}{2v(v+1)}e^{ikd}\sum_p a(m,n,-m,v,p)P_p(\cos\theta)$$

(5.67)

And again, cleaning up the exponentials involving i and (-1):

$$(-1)^{m+v-n}i^{v-n} = (-1)^{m+v-n}i^{-(n-v)} = (-1)^{m+v-n}(-1)^{n-v}i^{(n-v)} = (-1)^m i^{(n-v)} \qquad (5.68)$$

$$A_{mv}^{mn} = (-1)^m i^{n-v-1}\frac{2v+1}{2v(v+1)}\frac{e^{ikd}}{kd}\sum_p[n(n+1)+v(v+1)-p(p+1)]a(m,n,-m,v,p)P_p(\cos\theta)$$

$$B_{mv}^{mn} = (-1)^{m+1}i^{n-v}2m\frac{2v+1}{2v(v+1)}e^{ikd}\sum_p a(m,n,-m,v,p)P_p(\cos\theta)$$

(5.69)

The B^{mn}_{mv} is slightly easier, and the procedure is clearer starting there. A secondary definition will also make things simpler:

$$B_{mv}^{mn} = i^{n-v}(-1)^{m+1}2m\frac{2v+1}{2v(v+1)}e^{ikd}B1$$

$$B1 = \sum_p a(m,n,-m,v,p)P_p(\cos\theta)$$

(5.70)

The Gaunt coefficient is defined by the linearization

$$P_n^m(x)P_v^{-m}(x) = \sum_p a(m,n,-m,v,p)P_p(x) \qquad (5.71)$$

Thus, the B1 is:

$$B1 = P_n^m(\cos\theta)P_v^{-m}(\cos\theta) \qquad (5.72)$$

The associated Legendre polynomials obey[29]

$$P_l^{-m}(x) = (-1)^m \frac{(l-m)!}{(l+m)!} P_l^m(x) \tag{5.73}$$

This yields

$$B1 = (-1)^m \frac{(\nu-m)!}{(\nu+m)!} P_n^m(\cos\theta) P_\nu^m(\cos\theta) \tag{5.74}$$

Examining the definition of the Legendre polynomial for positive m, [29]

$$P_l^m(x) = (-1)^m (1-x^2)^{\frac{m}{2}} \frac{d^m}{dx^m} P_l(x) \tag{5.75}$$

it can be seen that for θ=0 or π, B1, and thus, the $B^{mn}{}_{m\nu}$ term will be zero for all m, as all the $P^m{}_l(1)$ for m≠0 involve a $(1-x)^{m/2}$, yielding zero. Of course, in the case of m=0, the $B^{mn}{}_{m\nu}$ term is also zero. So for all m, $B^{mn}{}_{m\nu}$ goes asymptotically to zero for the case of large separation. A similar analysis of $A^{mn}{}_{m\nu}$ gives:

$$A_{m\nu}^{mn} = i^{n-\nu-1}(-1)^m \frac{2\nu+1}{2\nu(\nu+1)} \frac{e^{ikd}}{kd} \left[\begin{array}{l} \sum_p \{n(n+1)+\nu(\nu+1)\}a(m,n,-m,\nu,p)P_p(\cos\theta) \\ -\sum_p p(p+1)a(m,n,-m,\nu,p)P_p(\cos\theta) \end{array} \right]$$

$$A_{m\nu}^{mn} = i^{n-\nu-1}(-1)^m \frac{2\nu+1}{2\nu(\nu+1)} \frac{e^{ikd}}{kd} [\{n(n+1)+\nu(\nu+1)\}B1 - A1]$$

$$A1 = \sum_p p(p+1)a(m,n,-m,\nu,p)P_p(\cos\theta)$$

(5.76)

In this case, B1 has a simple form, as the Legendre polynomials are unity for cosθ=1:

$$B1 = (-1)^m \frac{(\nu-m)!}{(\nu+m)!} \delta_{m,0} = \delta_{m,0} \tag{5.77}$$

The presence of the p(p+1) in the A1 factor causes problems with the summation. However, in the recurrence relations[7] for a(m,n,-m,v,p) there are 2 relations that can help:

$$a(m,n,-m,\nu,p) = a(m+1,n,-m,\nu,p) + a(m,n,-m+1,\nu,p)$$
$$p(p+1)a(m,n,-m,\nu,p) = (\nu-m)(\nu+m+1)a(m,n,-m-1,\nu,p)$$
$$+ (n+m)(n-m+1)a(m-1,n,-m,\nu,p)$$
(5.78)

Putting the second equation into A1 gives:

$$A1 = \sum_p \left[(v-m)(v+m+1)a(m,n,-m-1,v,p) + (n+m)(n-m+1)a(m-1,n,-m,v,p)\right]P_p(\cos$$

(5.79)

This can be simplified by using the first recursion relation:

$$a(m,n,-m-1,v,p) = a(m+1,n,-m-1,v,p) + a(m,n,-m,v,p)$$
$$a(m-1,n,-m,v,p) = a(m,n,-m,v,p) + a(m-1,n,-m+1,v,p)$$
$$\therefore (v-m)(v+m+1)a(m,n,-m-1,v,p) + (n+m)(n-m+1)a(m-1,n,-m,v,p)$$
$$= (v-m)(v+m+1)\left[a(m+1,n,-m-1,v,p) + a(m,n,-m,v,p)\right]$$
$$+ (n+m)(n-m+1)\left[a(m,n,-m,v,p) + a(m-1,n,-m+1,v,p)\right]$$
$$= a(m,n,-m,v,p)\left[(n+m)(n-m+1) + (v-m)(v+m+1)\right]$$
$$+ (v-m)(v+m+1)a(m+1,n,-m-1,v,p) + (n+m)(n-m+1)a(m-1,n,-m+1,v,p)$$

(5.80)

Although this is becoming quite cumbersome, the goal of summation over magnetic angular momentum is zero is now achieved. Using the linearization equation on first of these three terms gives

$$\left[(n+m)(n-m+1) + (v-m)(v+m+1)\right]\sum_p a(m,n,-m,v,p)P_p(\cos\theta)$$

$$= \left[(n+m)(n-m+1) + (v-m)(v+m+1)\right]B1$$

$$= \left[n(n+1) + v(v+1)\right]\delta_{m,0}$$

(5.81)

for the first term. Note that this will cause a cancellation in the equation for $A^{mn}{}_{mv}$. For the second and third term:

$$(v-m)(v+m+1)\sum_p a(m+1,n,-m-1,v,p)P_p(\cos\theta) = (v-m)(v+m+1)P_n^{m+1}(\cos\theta)P_v^{-m-1}(\cos\theta)$$

$$(n+m)(n-m+1)\sum_p a(m-1,n,-m+1,v,p)P_p(\cos\theta) = (n+m)(n-m+1)P_n^{m-1}(\cos\theta)P_v^{-m+1}(\cos\theta)$$

(5.82)

The magnetic angular momentum on the second term can be flipped again

$$(v-m)(v+m+1)P_n^{m+1}(\cos\theta)P_v^{-m-1}(\cos\theta) = (-1)^{m+1}\frac{(v-m-1)!}{(v+m+1)!}(v-m)(v+m+1)P_n^{m+1}(\cos\theta)P_v^{m+1}(\cos$$

$$(n+m)(n-m+1)P_n^{m-1}(\cos\theta)P_v^{-m+1}(\cos\theta) = (-1)^{m-1}\frac{(v-m+1)!}{(v+m-1)!}(n+m)(n-m+1)P_n^{m-1}(\cos\theta)P_v^{m-1}(\cos$$

(5.83)

Finally, these can be expressed as with Kronecker delta in both cases, and the resulting expressions simplified.

$$(-1)^{m+1}\frac{(v-m-1)!}{(v+m+1)!}(v-m)(v+m+1)P_n^{m+1}(\cos\theta)P_v^{m+1}(\cos\theta)=v(v+1)\delta_{m,-1}$$

$$(-1)^{m-1}\frac{(v-m+1)!}{(v+m-1)!}(n+m)(n-m+1)P_n^{m-1}(\cos\theta)P_v^{m-1}(\cos\theta)=n(n+1)\delta_{m,1}$$

(5.84)

A1 can thus be summarized as

$$A1=[v(v+1)+n(n+1)]\delta_{m,0}+v(v+1)\delta_{m,-1}+n(n+1)\delta_{m,1}$$

(5.85)

This gives an elegant equation for A^{mn}_{mv}

$$A^{mn}_{mv}=i^{n-v-1}(-1)^m\frac{2v+1}{2v(v+1)}\frac{e^{ikd}}{kd}\begin{bmatrix}\{n(n+1)+v(v+1)\}\delta_{m,0}-\{n(n+1)+v(v+1)\}\delta_{m,0}\\-v(v+1)\delta_{m,-1}-n(n+1)\delta_{m,1}\end{bmatrix}$$

$$A^{mn}_{mv}=-i^{n-v-1}(-1)^m\frac{2v+1}{2v(v+1)}\frac{e^{ikd}}{kd}\left[v(v+1)\delta_{m,-1}+n(n+1)\delta_{m,1}\right]$$

(5.86)

It is clear that m must be odd, so this can be re-written as

$$A^{mn}_{mv}=i^{n-v-1}\frac{2v+1}{2v(v+1)}\frac{e^{ikd}}{kd}\left(v(v+1)\delta_{m,-1}+n(n+1)\delta_{m,1}\right)$$

(5.87)

While it is true that B^{mn}_{mv} does go asymptotically to zero, it does so rather slowly, and it would be useful to obtain a more accurate form. Retaining the second order term in the asymptotic expansion above gives:

$$h_p^{(1)}(kd)\sim\frac{i^{-p-1}e^{ikd}}{kd}\left(1+\frac{ip(p+1)}{2kd}\right)$$

(5.88)

This gives a starting point of

$$B^{mn}_{mv}=(-1)^{m+1}i^{n-v}2m\frac{2v+1}{2v(v+1)}e^{ikd}\sum_p\begin{pmatrix}a(m,n,-m,v,p)P_p(\cos\theta)\\+\dfrac{ip(p+1)}{2kd}a(m,n,-m,v,p)P_p(\cos\theta)\end{pmatrix}$$

(5.89)

Which can be easily recognized as:

$$B^{mn}_{mv}=(-1)^{m+1}i^{n-v}2m\frac{2v+1}{2v(v+1)}e^{ikd}\left(B1+\frac{i}{2kd}A1\right)$$

(5.90)

130

As seen above, due to the combination of m and $\delta_{m,0}$, the B1 term does not contribute, and inserting the above result for A1 yields

$$B_{m\nu}^{mn} = (-1)^{m+1} i^{n-\nu} 2m \frac{2\nu+1}{2\nu(\nu+1)} e^{ikd} \left(\frac{i}{2kd} \left(\nu(\nu+1)\delta_{m,-1} + n(n+1)\delta_{m,1} \right) \right)$$

$$B_{m\nu}^{mn} = (-1)^{m} i^{n-\nu-1} 2m \frac{2\nu+1}{2\nu(\nu+1)} \frac{e^{ikd}}{kd} \left(\left(\nu(\nu+1)\delta_{m,-1} + n(n+1)\delta_{m,1} \right) \right)$$

(5.91)

Which is a result of the same order as $A^{mn}{}_{m\nu}$, but will differ by a factor of m.

H. Rayleigh Regime for Identical Particles

The Rayleigh regime, sometimes referred to as the static or dipolar approximation allows n=1 terms only. This can be thought of as the first order scattering by two coupled particles. With the other special cases considered above, this problem is almost calculable by hand, allowing verification of a computer program with a simple case. A further assumption is identical particles, which again increases simplicity. A schematic of this ideal case is shown below (Figure 5.2):
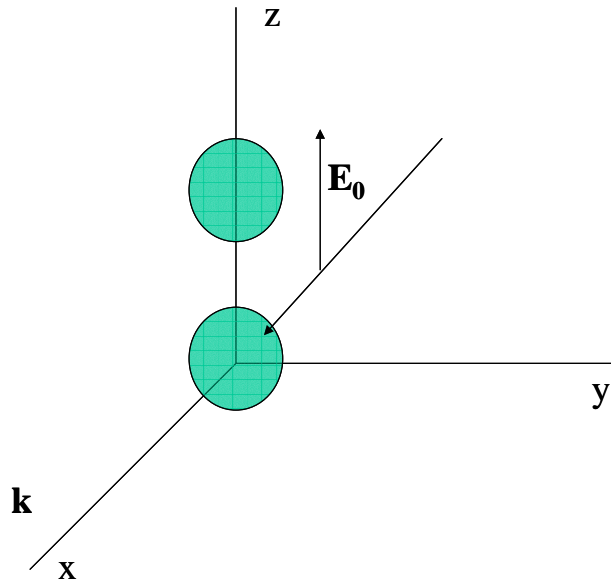
Figure 5.2. Schematic of two particles along z axis.

For the case of particles along the z axis, with light impinging from the x direction, and further, linearly polarized so that electric field components are only along the z axis (along the particle axis, in other words), the expansion coefficients for the incident wave are:

$$^{i}C_{mn1}^{l} = \frac{2\pi i^{n}}{n(n+1)} 2imE_{z}Y_{n}^{m}(\hat{x})$$

$$^{i}C_{mn2}^{l} = \frac{2\pi i^{n}}{n(n+1)}\left[2in\sqrt{\frac{(n+m+1)(n-m+1)}{(2n+1)(2n+3)}}Y_{n+1}^{m}(\hat{x}) - 2i(n+1)\sqrt{\frac{(n+m)(n-m)}{(2n-1)(2n+1)}}Y_{n-1}^{m}(\hat{x})\right]E_{z}$$

(5.92)

In the Rayleigh approximation, n=1.

$$^iC_{m11}^l = -2\pi mE_z Y_1^m\left(\frac{\pi}{2},0\right)$$

$$^iC_{m12}^l = -2\pi E_z\left[\sqrt{\frac{(2+m)(2-m)}{15}}Y_2^m\left(\frac{\pi}{2},0\right) - 2\sqrt{\frac{(1+m)(1-m)}{3}}Y_0^m\left(\frac{\pi}{2},0\right)\right]$$

(5.93)

The total 6 terms (m=-1, m=0, and m=1) are:

$$^iC_{-111}^l = 2\pi E_z Y_1^{-1}\left(\frac{\pi}{2},0\right)$$

$$^iC_{-112}^l = -2\pi E_z\sqrt{\frac{1}{5}}Y_2^{-1}\left(\frac{\pi}{2},0\right)$$

$$^iC_{011}^l = 0$$

$$^iC_{012}^l = -2\pi E_z\left[\sqrt{\frac{4}{15}}Y_2^0\left(\frac{\pi}{2},0\right) - 2\sqrt{\frac{1}{3}}Y_0^0\left(\frac{\pi}{2},0\right)\right]$$

(5.94)

$$^iC_{111}^l = -2\pi E_z Y_1^1\left(\frac{\pi}{2},0\right)$$

$$^iC_{112}^l = -2\pi E_z\sqrt{\frac{1}{5}}Y_2^1\left(\frac{\pi}{2},0\right)$$

The 6 required spherical harmonics are all low order, and can be found in Jackson[29]

$$Y_0^0(\theta,\phi) = \frac{1}{\sqrt{4\pi}} \rightarrow Y_0^0\left(\frac{\pi}{2},0\right) = \frac{1}{\sqrt{4\pi}}$$

$$Y_1^1(\theta,\phi) = -\sqrt{\frac{3}{8\pi}}\sin\theta e^{i\phi} \rightarrow Y_1^1\left(\frac{\pi}{2},0\right) = -\sqrt{\frac{3}{8\pi}}$$

$$Y_1^{-1}(\theta,\phi) = \sqrt{\frac{3}{8\pi}}\sin\theta e^{-i\phi} \rightarrow Y_1^{-1}\left(\frac{\pi}{2},0\right) = \sqrt{\frac{3}{8\pi}}$$

$$Y_2^0(\theta,\phi) = \sqrt{\frac{5}{4\pi}}\left(\frac{3}{2}\cos^2\theta - \frac{1}{2}\right) \rightarrow Y_2^0\left(\frac{\pi}{2},0\right) = -\frac{1}{2}\sqrt{\frac{5}{4\pi}}$$

(5.95)

$$Y_2^1(\theta,\phi) = -\sqrt{\frac{15}{8\pi}}\sin\theta\cos\theta e^{i\phi} \rightarrow Y_2^1\left(\frac{\pi}{2},0\right) = 0$$

$$Y_2^{-1}(\theta,\phi) = \sqrt{\frac{15}{8\pi}}\sin\theta\cos\theta e^{-i\phi} \rightarrow Y_2^{01}\left(\frac{\pi}{2},0\right) = 0$$

which yields

$$^iC^l_{-111} = \sqrt{\frac{3\pi}{2}}E_z$$

$$^iC^l_{-112} = 0$$

$$^iC^l_{011} = 0$$

$$^iC^l_{012} = -2\pi E_z\left[-\sqrt{\frac{4}{15}}\frac{1}{2}\sqrt{\frac{5}{4\pi}} - 2\sqrt{\frac{1}{3}}\sqrt{\frac{1}{4\pi}}\right] = \sqrt{3\pi}E_z \tag{5.96}$$

$$^iC^l_{111} = \sqrt{\frac{3\pi}{2}}E_z$$

$$^iC^l_{112} = 0$$

For θ=0, the addition coefficients for the vector spherical harmonics are

$$^{lh}A^{m1}_{m1} = (-1)^m\frac{3}{4}\sum_{p=0}^{2}\left\{i^p[4-p(p+1)]\times a(-m,1,m,1,p)h^{(1)}_p(kr_{l,h})\right\}$$

$$^{lh}B^{m1}_{m1} = (-1)^m\frac{3}{4}\sum_{p=0}^{2}\left\{i^p(-2imkd)a(-m,1,m,1,p)h^{(1)}_p(kr_{l,h})\right\} \tag{5.97}$$

The Gaunt coefficients will be zero when n+v+p is an odd number, so only p=0 and p=2 must be considered in the summation.

$$^{lh}A^{m1}_{m1} = (-1)^m\frac{3}{4}\left\{\begin{array}{l}4a(-m,1,m,1,0)h^{(1)}_0(kr_{l,h})\\+2a(-m,1,m,1,2)h^{(1)}_2(kr_{l,h})\end{array}\right\}$$

$$^{lh}B^{m1}_{m1} = (-1)^m\frac{3}{4}\left\{\begin{array}{l}-(2imkd)a(-m,1,m,1,0)h^{(1)}_0(kr_{l,h})\\+(2imkd)a(-m,1,m,1,2)h^{(1)}_2(kr_{l,h})\end{array}\right\} \tag{5.98}$$

So there are only 3 possibilities, m=-1, m=0, and m=1. These are explicitly

$$^{lh}A^{-11}_{-11} = -\frac{3}{4}\left\{\begin{array}{l}4a(1,1,-1,1,0)h^{(1)}_0(kr_{l,h})\\+2a(1,1,-1,1,2)h^{(1)}_2(kr_{l,h})\end{array}\right\}$$

$$^{lh}A^{01}_{01} = \frac{3}{4}\left\{\begin{array}{l}4a(0,1,0,1,0)h^{(1)}_0(kr_{l,h})\\+2a(0,1,,1,2)h^{(1)}_2(kr_{l,h})\end{array}\right\} \tag{5.99}$$

$$^{lh}A^{11}_{11} = -\frac{3}{4}\left\{\begin{array}{l}4a(-1,1,1,1,0)h^{(1)}_0(kr_{l,h})\\+2a(-1,1,1,1,2)h^{(1)}_2(kr_{l,h})\end{array}\right\}$$

The Gaunt integrals in the Wigner 3j formalism are

$$a(-m,1,m,1,p) = (2p+1)\left[\frac{(1-m)!(1+m)!}{(1+m)!(1-m)!}\right]\begin{pmatrix} 1 & 1 & p \\ 0 & 0 & 0 \end{pmatrix}\begin{pmatrix} 1 & 1 & p \\ -m & m & 0 \end{pmatrix}$$

$$a(-m,1,m,1,p) = (2p+1)\begin{pmatrix} 1 & 1 & p \\ 0 & 0 & 0 \end{pmatrix}\begin{pmatrix} 1 & 1 & p \\ -m & m & 0 \end{pmatrix}$$

(5.100)

First evaluate for the two different p cases.

$$a(-m,1,m,1,0) = \begin{pmatrix} 1 & 1 & 0 \\ 0 & 0 & 0 \end{pmatrix}\begin{pmatrix} 1 & 1 & 0 \\ -m & m & 0 \end{pmatrix} = -\frac{1}{\sqrt{3}}\begin{pmatrix} 1 & 1 & 0 \\ -m & m & 0 \end{pmatrix}$$

$$a(-m,1,m,1,2) = 5\begin{pmatrix} 1 & 1 & 2 \\ 0 & 0 & 0 \end{pmatrix}\begin{pmatrix} 1 & 1 & 2 \\ -m & m & 0 \end{pmatrix} = \sqrt{\frac{10}{3}}\begin{pmatrix} 1 & 1 & 2 \\ -m & m & 0 \end{pmatrix}$$

(5.101)

And then evaluate for the 3 different m possibilities, giving the six total required Gaunt integrals.

$$a(1,1,-1,1,0) = -\frac{1}{\sqrt{3}}\begin{pmatrix} 1 & 1 & 0 \\ 1 & -1 & 0 \end{pmatrix} = \sqrt{\frac{1}{3}} = -\frac{1}{3}$$

$$a(0,1,0,1,0) = -\frac{1}{\sqrt{3}}\begin{pmatrix} 1 & 1 & 0 \\ 0 & 0 & 0 \end{pmatrix} = -\frac{1}{\sqrt{3}}\left(-\frac{1}{\sqrt{3}}\right) = \frac{1}{3}$$

$$a(-1,1,1,1,0) = -\frac{1}{\sqrt{3}}\begin{pmatrix} 1 & 1 & 0 \\ -1 & 1 & 0 \end{pmatrix} = -\frac{1}{3}$$

$$a(1,1,-1,1,2) = \sqrt{\frac{10}{3}}\begin{pmatrix} 1 & 1 & 2 \\ 1 & -1 & 0 \end{pmatrix} = \sqrt{\frac{10}{3}}\sqrt{\frac{1}{30}} = \frac{1}{3}$$

(5.102)

$$a(0,1,0,1,2) = \sqrt{\frac{10}{3}}\begin{pmatrix} 1 & 1 & 2 \\ -m & m & 0 \end{pmatrix} = \sqrt{\frac{10}{3}}\sqrt{\frac{30}{15}} = \frac{2}{3}$$

$$a(-1,1,1,1,2) = \sqrt{\frac{10}{3}}\begin{pmatrix} 1 & 1 & 2 \\ -1 & 1 & 0 \end{pmatrix} = \frac{1}{3}$$

To give for the A's

$$^{lh}A_{-11}^{-11} = \frac{1}{2}\left(2h_0^{(1)}(kr_{l,h}) - h_2^{(1)}(kr_{l,h})\right)$$

$$^{lh}A_{01}^{01} = h_0^{(1)}(kr_{l,h}) + h_2^{(1)}(kr_{l,h})$$

(5.103)

$$^{lh}A_{11}^{11} = \frac{1}{2}\left(2h_0^{(1)}(kr_{l,h}) - h_2^{(1)}(kr_{l,h})\right)$$

Note that the −m and m give equivalent results. And for the B's the results are:

$$^{lh}B_{-11}^{-11} = \frac{ikd}{2}\left\{h_0^{(1)}(kr_{l,h}) + h_2^{(1)}(kr_{l,h})\right\}$$

$$^{lh}B_{01}^{01} = 0 \tag{5.104}$$

$$^{lh}B_{11}^{11} = -\frac{ikd}{2}\left\{h_0^{(1)}(kr_{l,h}) + h_2^{(1)}(kr_{l,h})\right\}$$

The m=1 and m=-1 case give results that differ by a factor of -1.

As the spherical Hankel functions have a closed form, it is worthwhile simplifying these terms. They are defined as[30]

$$h_n^{(1)}(z) = (-i)^{n+1}\frac{e^{iz}}{z}\sum_{m=0}^{n}\frac{i^m}{m!(2z)^m}\frac{(n+m)!}{(n-m)!}$$

$$h_0^{(1)}(z) = \frac{-ie^{iz}}{z} \tag{5.105}$$

$$h_2^{(1)}(z) = \frac{ie^{iz}}{z}\left(1 + \frac{3i}{z} - \frac{3}{z^2}\right)$$

For the two different combinations:

$$h_0^{(1)}(z) + h_2^{(1)}(z) = \frac{-ie^{iz}}{z} + \frac{ie^{iz}}{z}\left(1 + \frac{3i}{z} - \frac{3}{z^2}\right) = \frac{3ie^{iz}}{z^3}(iz - 1)$$

$$2h_0^{(1)}(z) - h_2^{(1)}(z) = \frac{-2ie^{iz}}{z} - \frac{ie^{iz}}{z}\left(1 + \frac{3i}{z} - \frac{3}{z^2}\right) = -\frac{3ie^{iz}}{z}\left(1 + \frac{i}{z} - \frac{1}{z^2}\right) \tag{5.106}$$

With the following adjustments to the notation, this gives

$$A_{-11}^{-11} = A_{11}$$

$$A_{01}^{01} = A_{01}$$

$$A_{11}^{11} = A_{11} \tag{5.107}$$

$$B_{-11}^{-11} = -B_{11}$$

$$B_{11}^{11} = B_{11}$$

$$A_{01} = \frac{-3e^{iz}}{z^3}(z + i)$$

$$A_{11} = \frac{3e^{iz}}{2z^2}\left(-iz^2 + z + i\right) \tag{5.108}$$

$$B_{11} = \frac{3e^{iz}}{2z^2}(iz - 1)$$

The matrices can now be built. The hybrid order of scattering/matrix inversion method still gives an improvement in time, as, rather than a 12x12 matrix to be inverted, two 6x6 matrices are inverted instead. also, Along the z-axis, the vector addition coefficients transform as[13]

$$
\begin{aligned}
{}^{lh}A_{m1}^{m1} &\to (-1)^{n+\nu} \times {}^{hl}A_{m1}^{m1} \\
{}^{lh}B_{m1}^{m1} &\to (-1)^{n+\nu+1} \times {}^{hl}B_{m1}^{m1}
\end{aligned}
\tag{5.109}
$$

meaning in this case, the A's are the same, and the B's change sign. The matrices holding the vector translation coefficients are then:

$$
{}^{21}\overline{A} = \begin{bmatrix} A_{11} & 0 & 0 \\ 0 & A_{01} & 0 \\ 0 & 0 & A_{11} \end{bmatrix} = {}^{12}\overline{A}
$$

$$
{}^{21}\overline{B} = \begin{bmatrix} -B_{11} & 0 & 0 \\ 0 & 0 & 0 \\ 0 & 0 & B_{11} \end{bmatrix}; {}^{12}\overline{B} = \begin{bmatrix} B_{11} & 0 & 0 \\ 0 & 0 & 0 \\ 0 & 0 & -B_{11} \end{bmatrix}
$$

$$
\Omega_{21} = \begin{bmatrix} A_{11} & 0 & 0 & -B_{11} & 0 & 0 \\ 0 & A_{01} & 0 & 0 & 0 & 0 \\ 0 & 0 & A_{11} & 0 & 0 & B_{11} \\ -B_{11} & 0 & 0 & A_{11} & 0 & 0 \\ 0 & 0 & 0 & 0 & A_{01} & 0 \\ 0 & 0 & B_{11} & 0 & 0 & A_{11} \end{bmatrix}; \Omega_{12} = \begin{bmatrix} A_{11} & 0 & 0 & B_{11} & 0 & 0 \\ 0 & A_{01} & 0 & 0 & 0 & 0 \\ 0 & 0 & A_{11} & 0 & 0 & -B_{11} \\ B_{11} & 0 & 0 & A_{11} & 0 & 0 \\ 0 & 0 & 0 & 0 & A_{01} & 0 \\ 0 & 0 & -B_{11} & 0 & 0 & A_{11} \end{bmatrix}
$$

(5.110)

The S matrix, which is the same if the particles are identical, is diagonal

$$
S = \begin{bmatrix} b & 0 & 0 & 0 & 0 & 0 \\ 0 & b & 0 & 0 & 0 & 0 \\ 0 & 0 & b & 0 & 0 & 0 \\ 0 & 0 & 0 & a & 0 & 0 \\ 0 & 0 & 0 & 0 & a & 0 \\ 0 & 0 & 0 & 0 & 0 & a \end{bmatrix}
\tag{5.111}
$$

So while the Rayleigh case in this formalism is still difficult, it is a far easier problem to begin with. It also provides a valuable opportunity to check later

results, providing a starting point for the rather mathematically ornate general case.

In order to test the program, calculation of values for a special case through calculation by hand is a valuable tool for determination of mathematical or programming errors. Choosing as an exemplar the case of 30nm silver spheres in contact, in the Rayleigh regime is as good a place to start as any other. The scattered field on the surface of an isolated sphere peaks at a wavelength of 370 nm. While slightly off resonance, evaluating numerically at 377 nm is slightly easier, as kR and 2kR are both round numbers. Silver has a complex index of refraction of 0.188+i1.64 at this point. The wavenumber and Mie coefficients at this wavelength are:

$$
\begin{aligned}
k &= 1.666 \cdot 10^{-2} \, nm^{-1} \\
kR &= 0.5 \\
a_1 &= 0.3443 - i0.0875 \\
b_1 &= 0.000381 + i0.00232
\end{aligned}
$$
(5.112)

Choosing the incident field to lie in the +z with a magnitude of unity, the expansion coefficients for the scattered field are:

$$
\begin{aligned}
{}^iC^l_{-111} &= \sqrt{\frac{3\pi}{2}} \\
{}^iC^l_{-112} &= 0 \\
{}^iC^l_{011} &= 0 \\
{}^iC^l_{012} &= \sqrt{3\pi} \\
{}^iC^l_{111} &= \sqrt{\frac{3\pi}{2}} \\
{}^iC^l_{112} &= 0
\end{aligned}
$$
(5.113)

The vector spherical harmonics for particle 1 are:

$$|m131\rangle = \begin{bmatrix} 0 \\ \dfrac{im}{\sin\theta} \\ \dfrac{\partial}{\partial\theta} \end{bmatrix} h_1^{(1)}(kr)Y_1^m(\theta,\phi)$$

$$|m132\rangle = \begin{bmatrix} 2h_1^{(j)}(kr) \\ -\dfrac{\partial}{\partial kr}\{krh_1^{(j)}(kr)\}\dfrac{\partial}{\partial\theta} \\ \dfrac{\partial}{\partial kr}\{krh_1^{(j)}(kr)\}\dfrac{im}{\sin\theta} \end{bmatrix} \dfrac{1}{kr}Y_1^m(\theta,\phi)$$

(5.114)

The required Hankel functions are:

$$h_1^{(1)}(z) = -\frac{e^{iz}}{z^2}(z+i)$$

$$\frac{h_1^{(1)}(z)}{z} = -\frac{e^{iz}}{z}(z+i)$$

$$\frac{\dfrac{\partial}{\partial z}zh_1^{(1)}(z)}{z} = -\frac{e^{iz}}{z^2}\left(iz-1-\frac{i}{z}\right)$$

(5.115)

which for z=kr, give values of

$$h_1^{(1)}(kR) = 0.1625 - i4.469$$

$$\frac{h_1^{(1)}(kR)}{kR} = 0.3251 - i8.939$$

$$\frac{\dfrac{\partial}{\partial z}\left[kRh_1^{(1)}(kR)\right]}{kR} = 0.6338 + i7.184$$

(5.116)

and the required spherical harmonics

$$Y_1^0(\theta,\phi) = \sqrt{\frac{3}{4\pi}}\cos\theta; \frac{mY_1^0(\theta,\phi)}{\sin\theta} = 0; \frac{\partial}{\partial\theta}Y_1^0(\theta,\phi) = -\sqrt{\frac{3}{4\pi}}\sin\theta$$

$$Y_1^1(\theta,\phi) = -\sqrt{\frac{3}{8\pi}}\sin\theta e^{i\phi}; \frac{mY_1^1(\theta,\phi)}{\sin\theta} = -\sqrt{\frac{3}{8\pi}}e^{i\phi}; \frac{\partial}{\partial\theta}Y_1^1(\theta,\phi) = -\sqrt{\frac{3}{8\pi}}\cos\theta e^{i\phi}$$

$$Y_1^{-1}(\theta,\phi) = \sqrt{\frac{3}{8\pi}}\sin\theta e^{-i\phi}; \frac{mY_1^{-1}(\theta,\phi)}{\sin\theta} = \sqrt{\frac{3}{8\pi}}e^{-i\phi}; \frac{\partial}{\partial\theta}Y_1^{-1}(\theta,\phi) = -\sqrt{\frac{3}{8\pi}}\cos\theta e^{i\phi}$$

(5.117)

and at θ=0

$$Y_1^0(0,\phi) = \sqrt{\frac{3}{4\pi}}; \frac{mY_1^0(0,\phi)}{\sin\theta} = 0; \frac{\partial}{\partial\theta}Y_1^0(0,\phi) = 0$$

$$Y_1^1(0,\phi) = 0; \frac{mY_1^1(0,\phi)}{\sin\theta} = -\sqrt{\frac{3}{8\pi}}e^{i\phi}; \frac{\partial}{\partial\theta}Y_1^1(0,\phi) = -\sqrt{\frac{3}{8\pi}}e^{i\phi} \quad (5.118)$$

$$Y_1^{-1}(0,\phi) = 0; \frac{mY_1^{-1}(0,\phi)}{\sin\theta} = \sqrt{\frac{3}{8\pi}}e^{-i\phi}; \frac{\partial}{\partial\theta}Y_1^{-1}(0,\phi) = \sqrt{\frac{3}{8\pi}}e^{-i\phi}$$

The vector spherical harmonics at z=30nm, which is on the surface of the sphere, numerically are

$$|-1131\rangle = \begin{bmatrix} 0 \\ -1.544 - i0.05615 \\ 0.05615 - i1.544 \end{bmatrix}e^{i\phi}; |-1132\rangle = \begin{bmatrix} 0 \\ -0.2190 - i2.482 \\ 2.482 - i0.2190 \end{bmatrix}e^{i\phi}$$

$$|0131\rangle = \begin{bmatrix} 0 \\ 0 \\ 0 \end{bmatrix}; |0132\rangle = \begin{bmatrix} 0.3177 - i8.7352 \\ 0 \\ 0 \end{bmatrix} \quad (5.119)$$

$$|1131\rangle = \begin{bmatrix} 0 \\ -1.544 - i0.05615 \\ -0.05615 + i1.544 \end{bmatrix}e^{-i\phi}; |1132\rangle = \begin{bmatrix} 0 \\ 0.2190 + i2.482 \\ 2.482 - i0.2190 \end{bmatrix}e^{-i\phi}$$

The isolated sphere scattering matrix T is

$$^1T = GS = \sqrt{3\pi}\begin{bmatrix} \sqrt{\frac{1}{2}} & 0 & \sqrt{\frac{1}{2}} & 0 & 1 & 0 \end{bmatrix}\begin{bmatrix} b_1 & 0 & 0 & 0 & 0 & 0 \\ 0 & b_1 & 0 & 0 & 0 & 0 \\ 0 & 0 & b_1 & 0 & 0 & 0 \\ 0 & 0 & 0 & a_1 & 0 & 0 \\ 0 & 0 & 0 & 0 & a_1 & 0 \\ 0 & 0 & 0 & 0 & 0 & a_1 \end{bmatrix}$$

$$= \sqrt{3\pi}\begin{bmatrix} \sqrt{\frac{1}{2}}b_1 & 0 & \sqrt{\frac{1}{2}}b_1 & 0 & a_1 & 0 \end{bmatrix}$$

(5.120)

and the electric field is therefore:

$$^1E_S = {}^1TW_3^E = \sqrt{3\pi}\left[\sqrt{\frac{1}{2}}b_1 \quad 0 \quad \sqrt{\frac{1}{2}}b_1 \quad 0 \quad a_1 \quad 0\right]\begin{bmatrix} |-1131\rangle \\ |0131\rangle \\ |1131\rangle \\ |-1132\rangle \\ |0132\rangle \\ |1132\rangle \end{bmatrix}$$

(5.121)

$$= \sqrt{3\pi}\left(\sqrt{\frac{1}{2}}b_1\left(|-1131\rangle + |1131\rangle\right) + a_1|0132\rangle\right)$$

$$^1E_s = \sqrt{3\pi}\left(\sqrt{\frac{1}{2}}b_1\left(\begin{bmatrix} 0 \\ -1.544 - i0.05615 \\ 0.05615 - i1.544 \end{bmatrix}e^{i\phi} + \begin{bmatrix} 0 \\ -1.544 - i0.05615 \\ -0.05615 + i1.544 \end{bmatrix}e^{-i\phi}\right) + a_1\begin{bmatrix} 0.3177 - i8.7352 \\ 0 \\ 0 \end{bmatrix}\right)$$

$$^1E_s = \sqrt{3\pi}\left(\sqrt{\frac{1}{2}}b_1 e^{i\phi}\begin{bmatrix} 0 \\ -3.088 - i0.1123 \\ 0 \end{bmatrix} + a_1\begin{bmatrix} 0.3177 - i8.7352 \\ 0 \\ 0 \end{bmatrix}\right)$$

$$^1E_s = \begin{bmatrix} -2.0114 - i9.3189 \\ (-0.002 - i0.0156)e^{i\phi} \\ 0 \end{bmatrix}$$

(5.122)

The majority of the scattered field is in the radial direction. However, there is a small component in the θ direction as well, representing a small amount of scattering perpendicular to z. The actual direction depends on our definition of φ. The transformation from spherical to Cartesian coordinates for θ=0 makes this explicit:

$$^1E^{\oplus}{}_s = \begin{bmatrix} 0 & \cos\phi & -\sin\phi \\ 0 & \sin\phi & \cos\phi \\ 1 & 0 & 0 \end{bmatrix}\begin{bmatrix} -2.0114 - i9.3189 \\ (-0.002 - i0.0156)e^{i\phi} \\ 0 \end{bmatrix} = \begin{bmatrix} (-0.002 - i0.0156)e^{i\phi}\cos\phi \\ (-0.002 - i0.0156)e^{i\phi}\sin\phi \\ -2.0114 - i9.3189 \end{bmatrix}$$

(5.123)

Although the values of the scattered field are not determined due to the axis choice, they are correct up to a phase $e^{i\phi}$. We are generally interested in the magnitude of the field in any case, however. This is

$$\left|{}^{1}E_{s}\right|^{2} = \begin{bmatrix} -2.0114+i9.3189 & (-0.002+i0.0156)e^{-i\phi} & 0 \end{bmatrix} \begin{bmatrix} -2.0114-i9.3189 \\ (-0.002-i0.0156)e^{i\phi} \\ 0 \end{bmatrix}$$

$$\left|{}^{1}E_{s}\right| = 9.533$$

(5.124)

If the incident field direction is switched to the y, the magnitude is 3.84, the contribution coming from the $\hat{\phi}$ direction.

For two interacting particles, the situation is more complicated, but much of the work is already done. The A and B terms are:

$$A_{01} = \frac{-3e^{iz}}{z^3}(z+i)$$

$$A_{11} = \frac{3e^{iz}}{2z^2}\left(-iz^2+z+i\right)$$

$$B_{11} = \frac{3e^{iz}}{2z^2}(iz-1)$$

(5.125)

As these terms have Hankel functions that are a function of the center to center distance, z=1 rather than 0.5, this makes them even easier to calculate.

$$A_{01} = 0.9035 - i4.1453$$
$$A_{11} = 0.8104 + i1.2622$$
$$B_{11} = -2.0726 - i0.4518$$

(5.126)

Having Maple do the matrix multiplication and matrix inversion detailed previously, the scattering matrices for the two particle system, in column format for easier comparison are:

$$^{2}T_{1} = \begin{bmatrix} 0.0008259+i0.005019 \\ 0 \\ 0.0008259+i0.005019 \\ 0.001169+i0.002399 \\ 0.2094-i0.5554 \\ -0.001169-i0.002399 \end{bmatrix} ; {}^{2}T_{1} = \begin{bmatrix} 0.0008259+i0.005019 \\ 0 \\ 0.0008259+i0.005019 \\ -0.001169-i0.002399 \\ 0.2094-i0.5554 \\ 0.001169+i0.002399 \end{bmatrix}$$

(5.127)

Examining these results, the largest contributor will be the m=0, p=2 case, which corresponds to the radial mode. However, if we naively apply the vector

142

spherical harmonics at the corresponding θ=0 and θ=π, the latter giving a -1 in the associated Legendre polynomial, this term will cancel completely. That is because the vector spherical harmonics are derived relative to the position of their particular sphere, rather than to a fixed coordinate system. For example, if the radial part of the field for particle 1 points in the positive direction in its own reference frame (toward $+\hat{z}$) at the desired point, then particle 2's radial component will be pointing in the negative direction in its own reference frame. However, the unit vector $\hat{r}$ in these for particle 2 points in the $-\hat{z}$ direction. So it is best to do the field addition in the Cartesian frame.

Supressing the arbitrary phase factor to φ=0 gives the spherical to Cartesian coordinate matrix as for θ=0

$$\begin{bmatrix} \hat{x} \\ \hat{y} \\ \hat{z} \end{bmatrix} = \begin{bmatrix} 0 & 1 & 0 \\ 0 & 0 & 1 \\ 1 & 0 & 0 \end{bmatrix} \begin{bmatrix} \hat{r} \\ \hat{\theta} \\ \hat{\phi} \end{bmatrix}$$

(5.128)

while for θ=π it is

$$\begin{bmatrix} \hat{x} \\ \hat{y} \\ \hat{z} \end{bmatrix} = \begin{bmatrix} 0 & -1 & 0 \\ 0 & 0 & 1 \\ -1 & 0 & 0 \end{bmatrix} \begin{bmatrix} \hat{r} \\ \hat{\theta} \\ \hat{\phi} \end{bmatrix}$$

(5.129)

We can now put the vector spherical harmonics for the two particles into Cartesian space. For the first particle:

$$\left| -1131 \right\rangle_{1}^{\oplus} = \begin{bmatrix} -1.544 - i0.05615 \\ 0.05615 - i1.544 \\ 0 \end{bmatrix}; \left| -1132 \right\rangle_{1}^{\oplus} = \begin{bmatrix} -0.2190 - i2.482 \\ 2.482 - i0.2190 \\ 0 \end{bmatrix}$$

$$\left| 0132 \right\rangle_{1}^{\oplus} = \begin{bmatrix} 0 \\ 0 \\ 0.3177 - i8.7352 \end{bmatrix}$$

$$\left| 1131 \right\rangle_{1}^{\oplus} = \begin{bmatrix} -1.544 - i0.05615 \\ -0.05615 + i1.544 \\ 0 \end{bmatrix}; \left| 1132 \right\rangle_{1}^{\oplus} = \begin{bmatrix} 0.2190 + i2.482 \\ 2.482 - i0.2190 \\ 0 \end{bmatrix}$$

(5.130)

For the θ=π we first add in the extra negative due to the

$$\left|-1131\right\rangle_{\frac{1}{2}}^{\oplus} = \begin{bmatrix} 1.544 + i0.05615 \\ -0.05615 + i1.544 \\ 0 \end{bmatrix}; \left|-1132\right\rangle_{\frac{1}{2}}^{\oplus} = \begin{bmatrix} -0.2190 - i2.482 \\ 2.482 - i0.2190 \\ 0 \end{bmatrix}$$

$$\left|0132\right\rangle_{\frac{1}{2}}^{\oplus} = \begin{bmatrix} 0 \\ 0 \\ 0.3177 - i8.7352 \end{bmatrix}$$

$$\left|1131\right\rangle_{\frac{1}{2}}^{\oplus} = \begin{bmatrix} 1.544 + i0.05615 \\ 0.05615 - i1.544 \\ 0 \end{bmatrix}; \left|1132\right\rangle_{\frac{1}{2}}^{\oplus} = \begin{bmatrix} 0.2190 + i2.482 \\ 2.482 - i0.2190 \\ 0 \end{bmatrix}$$

(5.131)

As the mathematical details were covered before, where in this case the only difference is that the scattered field of the two particles must be added, the magnitude of the scattered field is:

$$\left|^2 E_s\right| = 10.38$$

(5.132)

Although this is not significantly larger, remember that due to the interaction between the particles, the peak value shifts. As well, higher order moments for particles near each other contribute far more than that of the isolated particle.

I. Extinction Cross Sections and Field Calculations

Extinction cross sections may be obtained by letting the scattered field E_s interact with the incident field. This is accomplished by the dot product of the incident field expansion coefficients with the scattering matrix T, or

$$C_{ext} = GT$$

Using the methodology described above for a system of two spheres along a common z axis, the extinction cross sections for two 30 nm silver spheres is presented in Figure 5.3, and the extinction cross sections for 20 nm spheres is given in Figure 5.4.
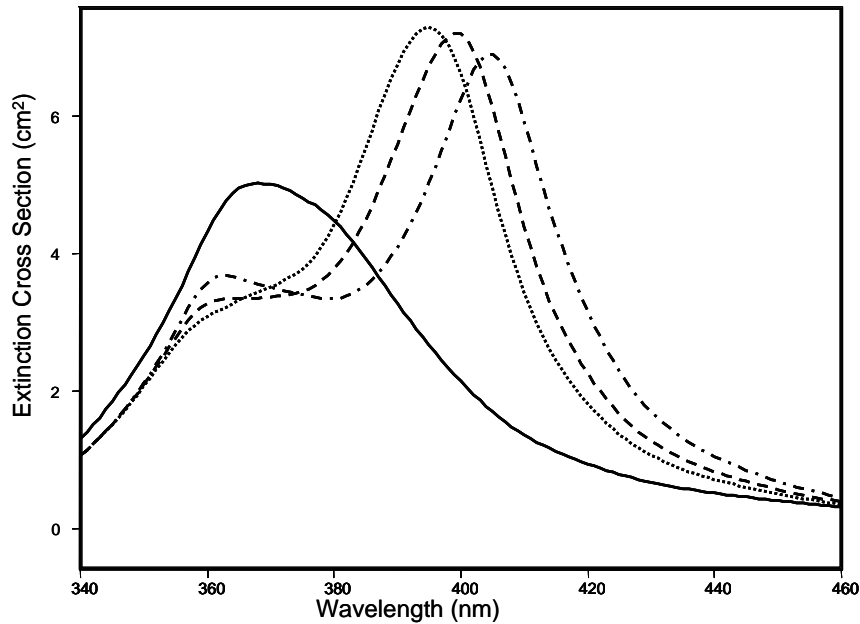
Figure 5.3: Extinction cross section of two interacting 30 nm silver spheres, with surface separation of infinity (solid), 2 nm (dotted), 1 nm (dashed), and in contact (dot-dash)
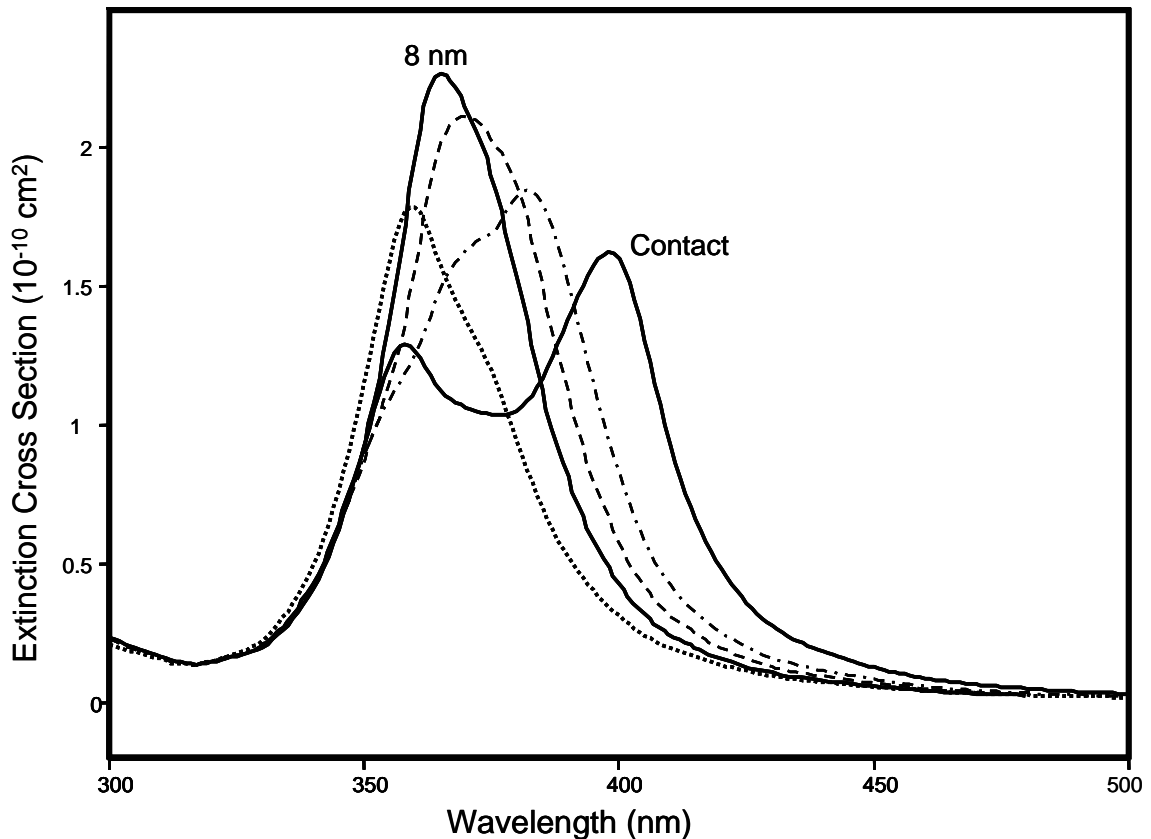
Figure 5.4: Extinction cross section of two 20nm particles at a distance of infinity (dotted), 8 nm, 4 nm (dashed), 2 nm (dot-dash), and in contact.

For application to surface enhanced spectroscopy, the enhanced field is needed to estimate enhancement factors. These are taken in two ways: 1) The enhancement factor of the field is calculated at a point for a variety of wavelengths, and 2) the enhanced field is calculated at a variety of points on a grid for a single wavelength. Both of these calculations have different tradeoffs. If the wavelength is varied, all of the addition coefficients for the vector spherical harmonics must be recalculated, as the Hankel functions contained therein must be recalculated, meaning that at every wavelength to be considered, the matrix inversion must be redone. In both cases, the spherical harmonics themselves must be calculated for each individual desired point. However, in the case of the spatial variation, to achieve sufficient resolution, a large number of points must be calculated.

146

Considering first variation with the frequency, the same conditions seen in Figure 5.4 are used, that of 20 nm spheres, which is presented in Figure 5.5. Unlike the extinction cross sections, in which the intensities were reasonably insensitive to changes in distance, the field enhancement is strongly dependant on particle separation. In terms of field intensity, the optimal position is for particles in contact.
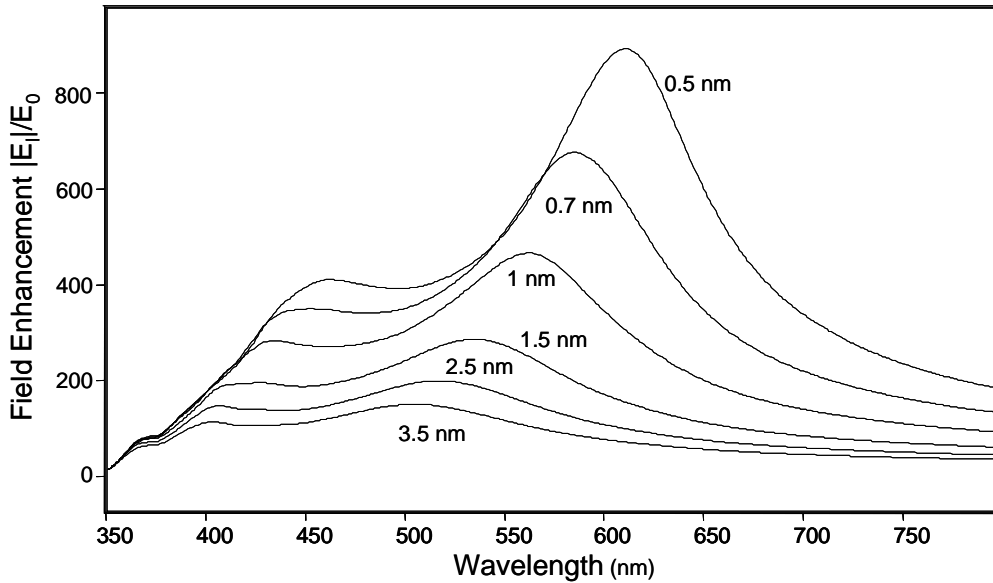
Figure 5.5: Field enhancements for 40nm particles with varying surface separation.

Comparing these results to those obtained for a two particle model in chapter 5, it is clear that the calculated enhancement of the local field is far stronger, and as well, red-shifted further. New spectra details also arise, such as a quadrupolar band, and as well, smaller contributions from higher order moments. While the dipolar model captures illustrates the trend, the full calculation using extended Mie theory clearly gives a full description of the full interaction.

For applications in quantum optics, the enhanced damping of a radiating dipole is also calculated, as is fully described in Chapter 6. The damping of an oscillating dipole located in the point equidistant from each particle is shown in Figure 5.6, along with the field enhancements.
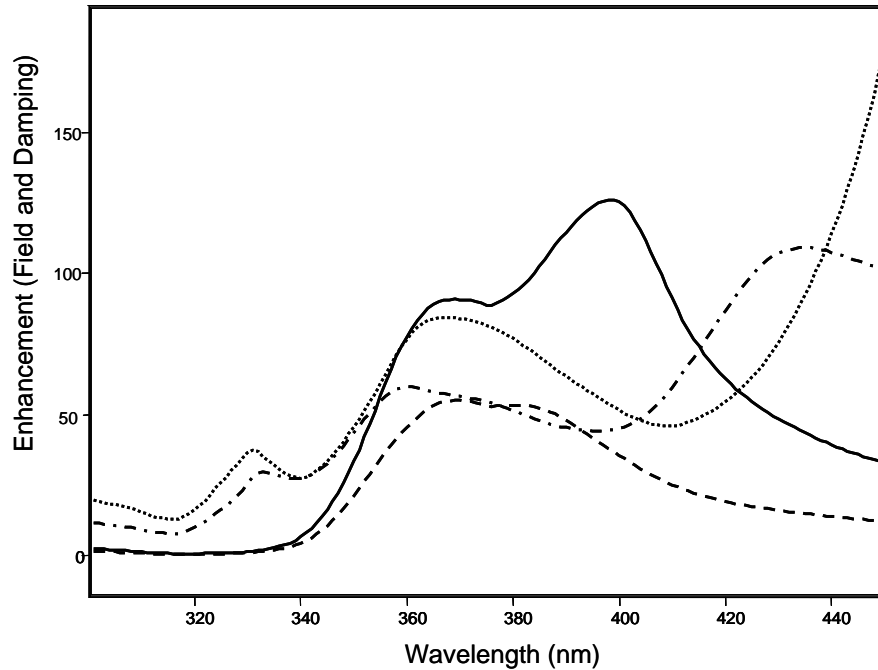
Figure 5.6: Enhancement for two 20 nm silver particles. In contact, field enhancement (solid) and damping enhancement (dotted), at 2 nm surface separation, field enhancement (dashed) and damping enhancement (dot-dash)

The formalism described above is first applied in the general case to obtain field intensities at points on a grid. The calculations are up to and including 5th order terms for light that is normally incident from the +z direction. The particles are placed in the xy plane, so that $\theta = \pi/2$. For two 20 nm silver particles with surfaces 2 nm apart, the magnitude of the enhanced electric field appears as Figure 5.7.
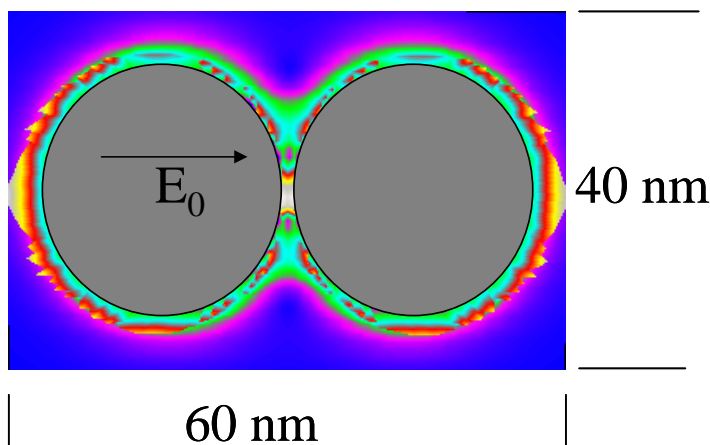
Figure 5.7: Electric field enhancement for 2 20nm silver particles.

The field is greatest in between the particles, and on the outside of the particles in the direction of the incident field. It is significantly reduced perpendicular to the direction of polarization.

Arrangements of three particles can be seen in Figure 5.8 and Figure 5.9, where in Figure 5.8 they are in a triangular formation so that all particles have a surface distance of 2 nm, while in Figure 5.9 they are in a line. The direction of the electric field is the same in both cases.
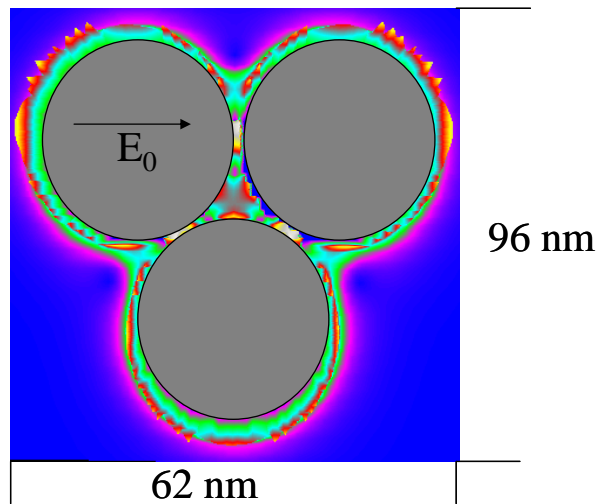
Figure 5.8: Electric field enhancement for 3 20nm silver particles in a triangular formation.
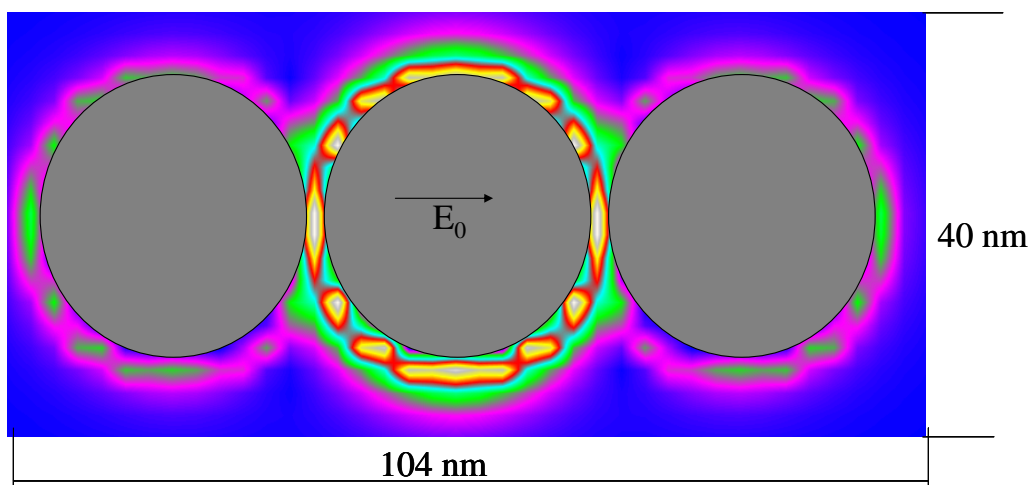
Figure 5.9: Electric field enhancement for 3 20nm silver particles in a straight line.

The arrangements of three particles, in the first, triangular case, does not differ much from that of two particles, except that there are now 3 areas of high intensity, at the closest junction between the particles in each case. For three particles, however, there is a significant difference: The magnitude around the central particle is almost an order of magnitude higher than around the outer particles.

These three particle results show the importance of aggregation and particle separation for surface enhanced spectroscopy, and as well, the extended Mie results show the need for the calculation of the near field directly, as the variations in intensity are not necessarily correlated with the far field extinction.

Extended Mie theory for interacting particles is mathematically ornate, and the calculation is computationally expensive. However, the results are not dependent on issues such as grid size, a common problem when dealing with curved surfaces in a space descritization scheme. The particles themselves are limited to spheres, although of arbitrary size. The ability to compute spectral cross sections as well as scattered, and thus enhanced fields with arbitrary precision is a valuable tool for the study of interacting particles, an important component of surface enhanced phenomena.

J. Bibliography

(1)   Goulet, P.; Pieczonka, N.; Aroca, R. *Journal of Raman Spectroscopy* **2005**, *36*, 574-580.
(2)   Kneipp, K.; Kneipp, H.; Itzkan, I.; Dasari, R. R.; Feld, M. S. *Chemical Reviews* **1999**, *99*, 2957-2975.
(3)   Binnig, G.; Rohrer, H. *Reviews of Modern Physics* **1999**, *71*, S324.
(4)   Pohl, D. W.; Deck, W.; Lanz, M. *Applied Physics Letters* **1984**, *44*, 651.
(5)   Novotny, L.; Bian, R. X.; Xie, X. S. *Physical Review Letters* **1997**, *79*, 645-648.
(6)   Fuller, K. A. *Applied Optics* **1991**, *30*, 4716.
(7)   Cruzan, O. R. *Quarterly of Applied Mathematics* **1962**, *20*, 33.
(8)   Clebsch, R. F. A. *Crelle's Journal* **1863**, *61*, 195-251.
(9)   Germogenova, O. A. *Izv. Akad. Nauk SSR Ser. Geofiz* **1963**, *XX*, 648-653.
(10)   Friedman, B.; Russek, J. *Quarterly of Applied Mathematics* **1954**, *12*, 13-23.
(11)   Stein, S. *Quarterly of Applied Mathematics* **1961**, *19*, 15-24.
(12)   Bruning, J. H.; Lo, Y. T. *Antenna Laboratory Report, Technical Reports* **1969**, *69-5*.
(13)   Bruning, J. H.; Lo, Y. T. *IEEE Transactions on Antennas and Propagation* **1971**, *AP-19*, 378.
(14)   Bruning, J. H.; Lo, Y. T. *IEEE Transactions on Antennas and Propagation* **1971**, *AP-19*, 391.
(15)   Claro, F. *Physical Review B* **1984**, *30*, 4989.
(16)   Noguez, C.; Barrera, G. *Physical Review B* **1998**, *57*, 302.
(17)   Inoue, M.; Ohtaka, K. *Journal of the Physical Society of Japan* **1983**, *52*, 3853-3864.
(18)   Fuller, K. A.; Kattawar, G. W. *Optics Letters* **1988**, *13*, 1063.
(19)   Fuller, K. A.; Kattawar, G. W. *Optics Letters* **1988**, *13*, 90.
(20)   Fuller, K. A. *Journal of the Optical Society of America A* **1994**, *11*, 3251.
(21)   Xu, H. *Physics Letters A* **2003**, *312*, 411-419.
(22)   Xu, H. *Journal of the Optical Society of America A* **2004**, *21*, 804.
(23)   Li, Z.; Xu, H. *Journal of Quantitative Spectroscopy & Radiative Transfer* **2007**, *103*, 394–401.
(24)   Gaunt, J. A. *Philosophical Transactions of the Royal Society of London Series A* **1929**, *228*, 151-196.
(25)   Xu, Y.-L. *Journal of Computational Physics* **1996**, *127*, 285-298.
(26)   Xu, Y.-L. *Journal of Computational Physics* **1998**, *139*, 137-165.
(27)   Xu, Y.-L. *Journal of Computational Physics* **1997**, *134*, 200.
(28)   Cooke, D.; 1.0 ed.; GNU Public Licence: Hamilton, Ontario, 2006.
(29)   Jackson, J. D. *Classical Electrodynamics*; 3rd ed.; John Wiley and Sons: New York, 1999.
(30)   *Handbook of Mathematical Functions with Formulas, Graphs, and Mathematical Tables.*; 9 ed.; Abramowitz, M.; Stegun, I. A., Eds.; Dover Publications: New York, 1972.

CHAPTER SIX

QUANTUM OPTICAL MODEL OF SURFACE ENHANCED SPECTROSCOPY

A. Unified Surface Enhanced Spectroscopy Through Quantum Optics

Most models for SEF focus on the plasmonics, and treat the molecule as a classical dipole. While the plasmonics models increasingly give more realistic results for the plasmon observed in the system, the treatment of the molecule, and thus the molecule-metal system, is not always as well developed. In their 2005 paper, Johansson, Xu, and Kall[1] present a unified model of enhanced Raman scattering and enhanced fluorescence within the context of quantum optics. This model is easily modified to include the field enhancement (M) and decay enhancement (M_d), which may be calculated through plasmonics methodology.

This model assumes only 2 electronic states, with the ground, |g>, and excited, |e>, states having energies $\hbar\omega_g$ and $\hbar\omega_e$ respectively. Also, a dipole moment is defined, where $p_0 = l_{dip}e$, where e is the elementary charge, and l_{dip} the dipole length. The energies and the dipole moment are all that are required to characterize the electronic states in this model. Finally, there is assumed to be a single vibrational mode of energy $\hbar\omega_{vib}$, which has N_{vib} states in each of the electronic states. Thus there is a total of N=2 N_{vib} states, |g,n=1..N_{vib}> and |e,m=1..N_{vib}>. The equation of motion of the NxN density matrix ρ is:

$$i\frac{d\rho}{dt} = \frac{1}{\hbar}\left[H_{mol} + H', \rho\right] + L_{tr}\rho + L_{ph}\rho \qquad (6.1)$$

The Hamiltonian is made up of 2 terms, the molecular (H_{mol}) and the molecule-field interaction (H'). $L_{tr}\rho$ is a damping term in the density matrix due to transitions spontaneous emission of photons[2], but also includes non-radiative processes and vibrational damping. $L_{ph}\rho$ represents damping due to phase relaxation. This parameter allows broadening of the bands, which may be experimentally due to either other vibrational states or temperature broadening.

The diagonal molecular Hamiltonian is a sum of electronic and vibrational energies:

$$H_{mol} = \sum_{n=0}^{N_{vib}-1} \sum_{l=ge} |l;n\rangle (\hbar\omega_l + n\hbar\omega_{vib}) \langle l;n| \qquad (6.2)$$

The interaction Hamiltonian, H', is off diagonal.

$$H' = -\left(\frac{pE_0 M(\omega_L)}{2}\right) \sum_{n,m=0}^{N_{vib}-1} \left(|e;m\rangle e^{-i\omega_L t} f(n,m)\langle g;n| + |g;n\rangle e^{i\omega_L t} f(n,m)\langle e;m|\right) \qquad (6.3)$$

Where p_0 is the dipole moment, E_0 the incident electric field, and $M(\omega_L)$ the field enhancement at the frequency of the laser line. f(n,m) is the Frank-Condon factor, defined as:

$$f(n,m) = \sqrt{n!m!} e^{-\alpha^2/2} \sum_{k=0}^{\min(n,m)} \frac{(-1)^{(m+k)} \alpha^{n+m-2k}}{k!(n-k!)(m-k)!} \qquad (6.4)$$

Where α is the dimensionless displacement between states.

The $L_{tr}\rho$ and $L_{ph}\rho$ terms are evaluated using an NxN operator σ_{ij}, in which all matrix elements are zero except the ij element. The $L_{tr}\rho$ term is then[2]:

$$L_{tr}\rho = -\sum_{jk} \frac{i\Gamma_{kj}}{2} \left[\sigma_{jk}\sigma_{kj}\rho + \rho\sigma_{jk}\sigma_{kj} - 2\sigma_{kj}\rho\sigma_{jk}\right] \qquad (6.5)$$

Γ_{kj} is the damping rate due to spontaneous transitions from state j to state k. This is calculated using Fermi's golden rule:

$$\Gamma_{kj} = \frac{|M_d(\omega)|^2 \omega^3}{3\pi\hbar\varepsilon_0 c^3} |p_0|^2 |f(n,m)|^2 \qquad (6.6)$$

where ω is the frequency of the transition, $\omega = \omega_{ge} + (m-n)\omega_{vib}$, defining $\omega_{ge} = \omega_e - \omega_g$, and M_d the enhancement of the decay rate due to interaction between the molecule and the metal particle. It should be noted that $L_{tr}\rho$ as written does not include any temperature effects, such as thermal excitation, and is therefore a zero temperature case.

Lastly, $L_{ph}\rho$ is:

$$L_{ph}\rho = -i\gamma_{ph} \sum_{i\in g}^{j\in e} \left[\sigma_{ij}\rho_{ij} + \sigma_{ji}\rho_{ji}\right] \qquad (6.7)$$

This problem is made more amenable by representing the density matrix as a vector of N^2 dimensions, such as

$$\vec{\rho} = (\rho_{11}, \rho_{21}, ..., \rho_{N1}, \rho_{12}, \rho_{22}, ..\rho_{NN})$$ (6.8)

Equation 6.1, once solved, can be expressed as:

$$i\hbar \frac{d\vec{\rho}}{dt} = \ddot{L}\vec{\rho}$$ (6.9)

where $\ddot{L}$ is an N^2x N^2 tensor that couples the time evolution of a matrix element with all the matrix elements at time t. The time independent form of $\ddot{L}$ is:

$$\ddot{L}' = e^{i\ddot{\Omega}t} \ddot{L} e^{-i\ddot{\Omega}t}$$ (6.10)

where $\ddot{\Omega}$ is a diagonal tensor with elements referring to populations or intraband coherences are zero. Upwards coherences have a value of Ω_L, while downwards coherences are $-\Omega_L$.

The differential cross section is given by

$$\frac{d^2\sigma}{d\Omega d(\hbar\omega)} = \frac{\omega^4 |M(\omega,\theta)|^2}{I_{in} 8\pi^3 c^3 \varepsilon_0 \hbar} |p_0|^2 \sum_{b,k\in g}^{a,j\in e} f(b,a)f(k,j)\sum_r \text{Re}[\rho_{0,ra} G_{0jk,rb}(\omega - \Omega_L)]$$ (6.11)

where:

$$I_{in} = \frac{c\varepsilon_0 E_0^2}{2}$$ (6.12)

G_0 and ρ_0 represent a stationary Green's tensor and initial density matrix, respectively. The initial density matrix can be obtained by solving the system of N equations given by:

$$(\ddot{L}' - \ddot{\Omega})\rho_0 = 0$$ (6.13)

It is also required that the trace of the initial density matrix is unity.

The Green's tensor is defined as

$$\rho_{jk} = \sum_{rs} G_{jk,rs}\rho(0)_{rs}$$ (6.14)

While each matrix element is given by:

$$\hat{G}_0(\omega) = i[(\omega + i\delta)\hat{I} + \hat{\Omega} - \hat{L}']^{-1}$$ (6.15)

The combination of plasmonics calculations to model the enhancing particles, and rigorous molecular treatment allow for a comprehensive model. The

quantum optic model of Kall and colleagues[1,3] gives a unified treatment of a model molecule with two electronic states, and an arbitrary number of vibrational levels. Although more complete methods are possible, (e.g., by adding different vibrational bands), this method includes the most important elements, and allows coupling to calculated plasmonic results.

As this treatment differs from the standard resonance fluorescence treatments in standard quantum optics[2,4,5], it is worthwhile demonstrating the solution for a system with 2 vibrational levels, or 4 states in all. The molecular Hamiltonian is:

$$H_{mol} = \sum_{n=0}^{1} \sum_{l=g,e} |l;n\rangle(\hbar\omega_l + n\hbar\omega_{vib})\langle l;n|$$

$$H_{mol} = |g;0\rangle\hbar\omega_g\langle g;0| + |e;0\rangle(\hbar\omega_e)\langle e;0|$$

$$+ |g;1\rangle(\hbar\omega_g + \hbar\omega_{vib})\langle g;1| + |e;1\rangle(\hbar\omega_e + \hbar\omega_{vib})\langle e;1| \qquad (6.16)$$

Setting the ground state energy to zero, and considering the basis kets to be

$$|g;0\rangle = \begin{pmatrix} 1 \\ 0 \\ 0 \\ 0 \end{pmatrix} ; |g;1\rangle = \begin{pmatrix} 0 \\ 1 \\ 0 \\ 0 \end{pmatrix} ; |e;0\rangle = \begin{pmatrix} 0 \\ 0 \\ 1 \\ 0 \end{pmatrix} ; |e;2\rangle = \begin{pmatrix} 0 \\ 0 \\ 0 \\ 1 \end{pmatrix} \qquad (6.17)$$

gives for the molecular Hamiltonian a form of:

$$H_{mol} = \begin{pmatrix} 0 & 0 & 0 & 0 \\ 0 & \hbar\omega_{vib} & 0 & 0 \\ 0 & 0 & \hbar\omega_e & 0 \\ 0 & 0 & 0 & \hbar\omega_e + \hbar\omega_{vib} \end{pmatrix} \qquad (6.18)$$

The interaction Hamiltonian is more difficult, but still tractable.

$$H' = -\left(\frac{pE_0 M(\omega_L)}{2}\right) \sum_{n,m=0}^{1} \left(|e;m\rangle e^{-i\omega_L t} f(n,m)\langle g;n| + |g;n\rangle e^{i\omega_L t} f(n,m)\langle e;m|\right)$$

$$H' = -\left(\frac{pE_0 M(\omega_L)}{2}\right) \begin{bmatrix} \left(|e;0\rangle e^{-i\omega_L t} f(0,0)\langle g;0| + |g;0\rangle e^{i\omega_L t} f(0,0)\langle e;0|\right) + \\ \left(|e;0\rangle e^{-i\omega_L t} f(1,0)\langle g;1| + |g;1\rangle e^{i\omega_L t} f(1,0)\langle e;0|\right) + \\ \left(|e;1\rangle e^{-i\omega_L t} f(0,1)\langle g;0| + |g;0\rangle e^{i\omega_L t} f(0,1)\langle e;1|\right) + \\ \left(|e;1\rangle e^{-i\omega_L t} f(1,1)\langle g;1| + |g;1\rangle e^{i\omega_L t} f(1,1)\langle e;1|\right) \end{bmatrix} \qquad (6.19)$$

155

$$H' = -\left(\frac{pE_0 M(\omega_L)}{2}\right)\begin{pmatrix} 0 & 0 & e^{i\omega_L t}f(0,0) & e^{i\omega_L t}f(0,1) \\ 0 & 0 & e^{i\omega_L t}f(1,0) & e^{i\omega_L t}f(1,1) \\ e^{-i\omega_L t}f(0,0) & e^{-i\omega_L t}f(1,0) & 0 & 0 \\ e^{-i\omega_L t}f(0,1) & e^{-i\omega_L t}f(1,1) & 0 & 0 \end{pmatrix} \quad (6.20)$$

The third term in the Hamiltonian uses operators σ_{ab}, which in this case is a 4x4 matrix with all elements zero except for ab. A useful relation for these operators is

$$\sigma_{ab}\sigma_{cd} = \sigma_{ad}\delta_{bc} \quad (6.21)$$

This allows for reasonably fast evaluation of these operators without writing out the matricies. This equation controls the spontaneous transitions from state j to state k, due to vibrational damping and radiative damping. Due to the use of the zero temperature limit, upwards transitions are not allowed. Thus, j>k in the summations. Writing these summations explicitly gives:

$$L_{tr}\rho = -\sum_{j=k+1}^{4}\sum_{k=1}^{4}\frac{i\Gamma_{kj}}{2}\left[\sigma_{jk}\sigma_{kj}\rho + \rho\sigma_{jk}\sigma_{kj} - 2\sigma_{kj}\rho\sigma_{jk}\right]$$

$$L_{tr}\rho = -\sum_{j=k+1}^{4}\begin{pmatrix} \dfrac{i\Gamma_{1j}}{2}\left[\sigma_{j1}\sigma_{1j}\rho + \rho\sigma_{j1}\sigma_{1j} - 2\sigma_{1j}\rho\sigma_{j1}\right]+ \\[2mm] \dfrac{i\Gamma_{2j}}{2}\left[\sigma_{j2}\sigma_{2j}\rho + \rho\sigma_{j2}\sigma_{2j} - 2\sigma_{2j}\rho\sigma_{j2}\right]+ \\[2mm] \dfrac{i\Gamma_{3j}}{2}\left[\sigma_{j3}\sigma_{3j}\rho + \rho\sigma_{j3}\sigma_{3j} - 2\sigma_{3j}\rho\sigma_{j3}\right]+ \\[2mm] \dfrac{i\Gamma_{4j}}{2}\left[\sigma_{j4}\sigma_{4j}\rho + \rho\sigma_{j4}\sigma_{4j} - 2\sigma_{4j}\rho\sigma_{j4}\right] \end{pmatrix} \quad (6.22)$$

$$
L_{tr}\rho = -\begin{pmatrix}
\dfrac{i\Gamma_{12}}{2}\left[\sigma_{21}\sigma_{12}\rho + \rho\sigma_{21}\sigma_{12} - 2\sigma_{12}\rho\sigma_{21}\right]+ \\[6pt]
\dfrac{i\Gamma_{13}}{2}\left[\sigma_{31}\sigma_{13}\rho + \rho\sigma_{31}\sigma_{13} - 2\sigma_{13}\rho\sigma_{31}\right]+ \\[6pt]
\dfrac{i\Gamma_{14}}{2}\left[\sigma_{41}\sigma_{14}\rho + \rho\sigma_{41}\sigma_{14} - 2\sigma_{14}\rho\sigma_{41}\right]+ \\[6pt]
\dfrac{i\Gamma_{2j}}{2}\left[\sigma_{32}\sigma_{23}\rho + \rho\sigma_{32}\sigma_{23} - 2\sigma_{23}\rho\sigma_{32}\right]+ \\[6pt]
\dfrac{i\Gamma_{2j}}{2}\left[\sigma_{42}\sigma_{24}\rho + \rho\sigma_{42}\sigma_{24} - 2\sigma_{24}\rho\sigma_{42}\right]+ \\[6pt]
\dfrac{i\Gamma_{34}}{2}\left[\sigma_{43}\sigma_{34}\rho + \rho\sigma_{43}\sigma_{34} - 2\sigma_{34}\rho\sigma_{43}\right]
\end{pmatrix}
\tag{6.23}
$$

The first two terms are simplified using the expression above

$$
L_{tr}\rho = -\begin{pmatrix}
\dfrac{i\Gamma_{12}}{2}\left[\sigma_{22}\rho + \rho\sigma_{22} - 2\sigma_{12}\rho\sigma_{21}\right]+ \\[6pt]
\dfrac{i\Gamma_{13}}{2}\left[\sigma_{33}\rho + \rho\sigma_{33} - 2\sigma_{13}\rho\sigma_{31}\right]+ \\[6pt]
\dfrac{i\Gamma_{14}}{2}\left[\sigma_{44}\rho + \rho\sigma_{44} - 2\sigma_{14}\rho\sigma_{41}\right]+ \\[6pt]
\dfrac{i\Gamma_{23}}{2}\left[\sigma_{33}\rho + \rho\sigma_{33} - 2\sigma_{23}\rho\sigma_{32}\right]+ \\[6pt]
\dfrac{i\Gamma_{24}}{2}\left[\sigma_{44}\rho + \rho\sigma_{44} - 2\sigma_{24}\rho\sigma_{42}\right]+ \\[6pt]
\dfrac{i\Gamma_{34}}{2}\left[\sigma_{44}\rho + \rho\sigma_{44} - 2\sigma_{34}\rho\sigma_{43}\right]
\end{pmatrix}
\tag{6.24}
$$

While this calculation yields a 4x4 matrix with all non-zero elements, and cannot nothing useful can be extracted from the full form, it is worthwhile examining what each term means. The second summand is the k=1, j=3 term which controls the spontaneous transition from the excited electronic state to the ground electronic state.

$$
-\frac{i\Gamma_{13}}{2}\left[\sigma_{33}\rho + \rho\sigma_{33} - 2\sigma_{13}\rho\sigma_{31}\right]
$$

$$
= -\frac{i\Gamma_{13}}{2}\left[\begin{pmatrix}
0 & 0 & 0 & 0 \\
0 & 0 & 0 & 0 \\
\rho_{3,1} & \rho_{3,2} & \rho_{3,3} & \rho_{3,4} \\
0 & 0 & 0 & 0
\end{pmatrix} + \begin{pmatrix}
0 & 0 & \rho_{1,3} & 0 \\
0 & 0 & \rho_{2,3} & 0 \\
0 & 0 & \rho_{3,3} & 0 \\
0 & 0 & \rho_{4,3} & 0
\end{pmatrix} - 2\begin{pmatrix}
\rho_{3,3} & 0 & 0 & 0 \\
0 & 0 & 0 & 0 \\
0 & 0 & 0 & 0 \\
0 & 0 & 0 & 0
\end{pmatrix}\right]
\tag{6.25}
$$

157

The first two terms cause a loss of population of state 3, as well as a loss of coherence between state 3 and all other states. The third term, on the other hand, increases the population of state 1, without an increase any coherence. It is worthwhile pointing out that the population gained by state 1 is the same as the loss of population of state 3.

The last term introduces phenomenological dephasing. These are simpler to calculate, involving only one operator and one density matrix element. This term is

$$
L_{ph}\rho = -i\gamma_{ph}\sum_{i\in g}^{j\in e}\left[\sigma_{ij}\rho_{ij} + \sigma_{ji}\rho_{ji}\right] = -i\gamma_{ph}\sum_{i=1}^{2}\sum_{j=3}^{4}\left[\sigma_{ij}\rho_{ij} + \sigma_{ji}\rho_{ji}\right]
$$

$$
= -i\gamma_{ph}\sum_{i=1}^{2}\left[\sigma_{i3}\rho_{i3} + \sigma_{3i}\rho_{3i} + \sigma_{i4}\rho_{i4} + \sigma_{4i}\rho_{4i}\right]
$$

$$
= -i\gamma_{ph}\begin{bmatrix}\sigma_{13}\rho_{13} + \sigma_{31}\rho_{31} + \sigma_{14}\rho_{14} + \sigma_{41}\rho_{41} + \\ \sigma_{23}\rho_{23} + \sigma_{32}\rho_{32} + \sigma_{24}\rho_{24} + \sigma_{42}\rho_{42}\end{bmatrix} \qquad (6.26)
$$

$$
= -i\gamma_{ph}\begin{pmatrix} 0 & 0 & \rho_{13} & \rho_{14} \\ 0 & 0 & \rho_{23} & \rho_{24} \\ \rho_{31} & \rho_{32} & 0 & 0 \\ \rho_{41} & \rho_{42} & 0 & 0 \end{pmatrix}
$$

So while this term is a decay in the coherence between the electronic states, it does not effect the populations directly.

In order to calculate the energy transfer to the spheres by the molecule, or what can be considered the enhancement in the damping, the electromagnetic field impinging on the spheres is given by an oscillating dipole, rather than a plane wave. We will consider a dipole on the z axis, for the case of 2 spheres also on the z axis. For an oscillating dipole of the form $\hat{z}p_0 e^{-i\omega t}$ the oscillating dipole wave expansion coefficients are[1]

$$
C_{mnp}^{dip} = \frac{p_0 k^3}{4\pi\varepsilon_0}\sqrt{\frac{8\pi}{3}}c_{2,1,0,p,n,m}(\vec{r}_i)
$$

(6.27)

which puts the expansion coefficient into the same notation as the extended Mie treatment, although the coupling coefficient c requires some arithmetic. The c term is given as

$$c_{2,1,0,1,n,m}(\vec{r}_i) = \frac{2n+1}{i\sqrt{n(n+1)}} \sum_{j=-1}^{1} R_{-j} F_{10}^j \tilde{A}_{1,j,n-1,m+j}(\vec{r}_i) C_{n,m,n-1,m+j}^{1,-j}$$

$$c_{2,1,0,2,n,m}(\vec{r}_i) = \sum_{j=-1}^{1} F_{10}^j F_{nm}^j \tilde{A}_{1,j,n,m+j}(\vec{r}_i)$$

(6.28)

Although the notation is different in this work, the $\tilde{A}$ terms are in fact the translation coefficients for the vector spherical harmonics, as the authors define them as

$$\tilde{A}_{n,m,\nu,\mu}(\vec{R}) = 4\pi \sum_{p=|n-\nu|}^{n+\nu} (-i)^{n-p-\nu} h_p(kr) Y_p^{m-\mu} C_{n,m,\nu,\mu}^{p,m-\mu}$$

(6.29)

where C in this case is the Gaunt coefficient. As before, this term will be zero for all m≠μ for θ=0,π, due to the associated Legendre polynomial in the spherical harmonic term. Expanding out the summations over j gives

$$c_{2,1,0,2,n,m}(\vec{r}_i) = F_{10}^j F_{nm}^j \tilde{A}_{1,-1,n,m-1}(\vec{r}_i) + F_{10}^j F_{nm}^j \tilde{A}_{1,0,n,m}(\vec{r}_i) + F_{10}^j F_{nm}^j \tilde{A}_{1,1,n,m+1}(\vec{r}_i)$$

(6.30)

$$c_{2,1,0,1,n,m}(\vec{r}_i) = \frac{2n+1}{i\sqrt{n(n+1)}} \left(\begin{array}{l} R_{-j} F_{10}^{-1} \tilde{A}_{1,-1,n-1,m-1}(\vec{r}_i) C_{n,m,n-1,m-1}^{1,1} + \\ R_{-j} F_{10}^j \tilde{A}_{1,0,n-1,m}(\vec{r}_i) C_{n,m,n-1,m}^{1,0} + R_{-j} F_{10}^j \tilde{A}_{1,1,n-1,m+1}(\vec{r}_i) C_{n,m,n-1,m+1}^{1,-1} \end{array} \right)$$

(6.31)

both of which require m=0. The remaining two terms for m=0 are

$$F_{n0}^0 = 0$$

$$F_{n0}^{\pm 1} = \frac{1}{\sqrt{2}}$$

$$R_1 = -\sqrt{\frac{4\pi}{3}}$$

$$R_0 = R_{-1} = \sqrt{\frac{4\pi}{3}}$$

(6.32)

For a result of

$$c_{2,1,0,1,n,m}(\vec{r}_i) = \frac{2n+1}{i\sqrt{2n(n+1)}}\sqrt{\frac{4\pi}{3}}\left(\tilde{A}_{1,-1,n-1,-1}(\vec{r}_i)C^{1,1}_{n,0,n-1,-1} - \tilde{A}_{1,1,n-1,1}(\vec{r}_i)C^{1,-1}_{n,0,n-1,1}\right)$$

$$c_{2,1,0,2,n,0}(\vec{r}_i) = \frac{1}{2}\left(\tilde{A}_{1,-1,n,-1}(\vec{r}_i) + \tilde{A}_{1,1,n,1}(\vec{r}_i)\right)$$

(6.33)

The Gaunt integrals are slightly differently defined, and as they appear in differently than before, they are worth defining.

$$C^{LM}_{l,m,l',m'} = \int d\Omega \left(Y_l^m(\Omega)\right)^* Y_L^M(\Omega)Y_{l'}^{m'}(\Omega) = (-1)^m \int d\Omega Y_l^{-m}(\Omega)Y_L^M(\Omega)Y_{l'}^{m'}(\Omega)$$

$$C^{LM}_{l,m,l',m'} = \sqrt{\frac{(2l+1)(2L+1)(2l'+1)}{4\pi}}\begin{pmatrix} l & l' & L \\ 0 & 0 & 0 \end{pmatrix}\begin{pmatrix} l & l' & L \\ -m & m' & M \end{pmatrix}$$

(6.34)

So using these expansion coefficients, the field is re-calculated at the point where the molecule is located, and the Poynting vector is calculated using the square of the scattered field. As a free oscillating dipole emits power as

$$P_{free} = \frac{\omega^4 p^2}{12\pi\varepsilon_0 c^3}$$

(6.35)

the enhancement of the damping is

$$|M_d|^2 = \frac{P_{Mie}}{P_{free}}$$

(6.36)

where P_{Mie} is the spatial integral of the Poynting vector. Because the constants in front of the expansion coefficient are multiplicative factors for the vector spherical harmonics, we can clean up some of the constants by considering the square of the constants in the expansion coefficients

$$|M_d|^2 = \frac{\dfrac{p^2 k^6}{16\varepsilon_0^2\pi^2}\dfrac{8\pi}{3}}{\dfrac{\omega^4 p^2}{12\pi\varepsilon_0 c^3}}\frac{\varepsilon_0 c}{2}E^2 = k^6\frac{c^4}{\omega^4}E^2 = k^2 E^2$$

(6.37)

where the expansion coefficients are now $c_{2,1,0,p,n,m}$. This implies that to calculate the damping, the same formalism as usual is used as usual, except that the damping expansion coefficients only act on the m=0 component of the results, which contribute to the radial part of the vector spherical harmonics.

B. Quantum Optical Results from Coupled Particles

To obtain spectra, equation 6.11 is used, with the elements of the Green's tensor obtained from equation 6.15 and 6.9, and the initial density matrix elements from equation 6.13.   Enhanced spectra are calculated using the results from CDE, as shown in the Chapter 4. The results are seen in figure 6.1.
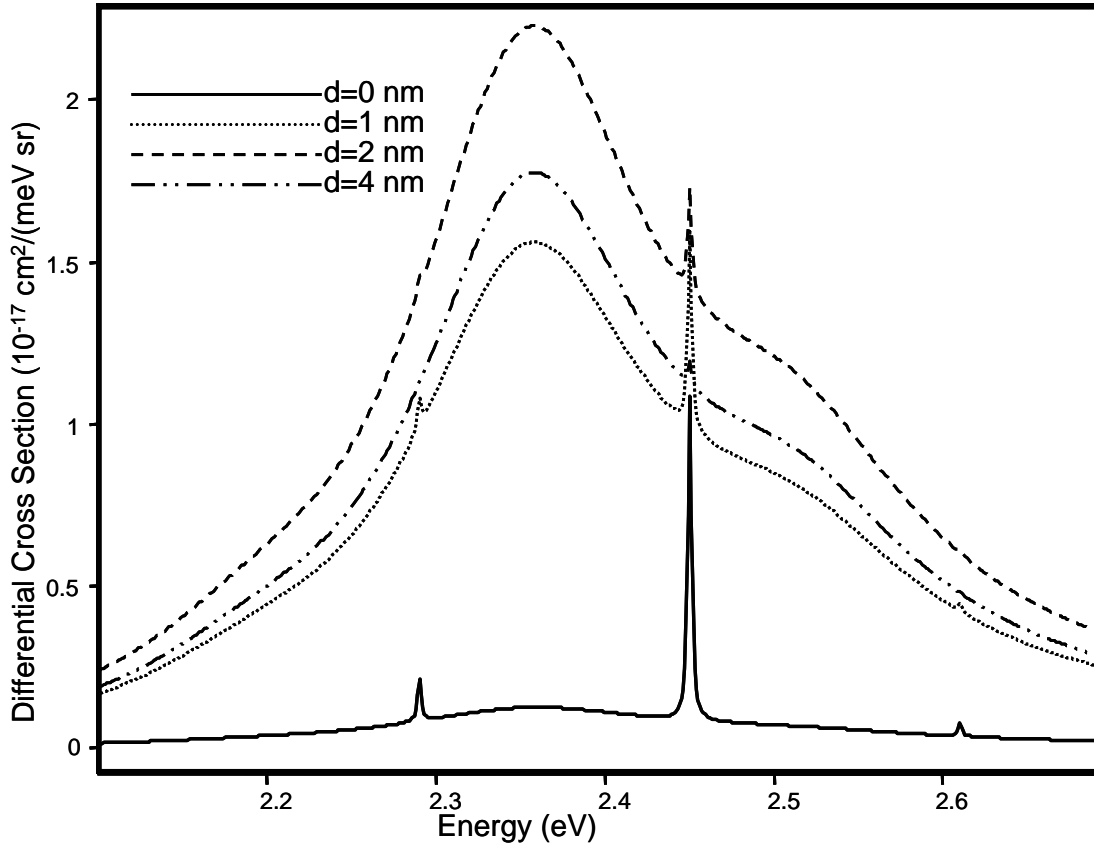
Figure 6.1. Scattering and Fluorescence cross sections for d=0, 1, 2, and 4 nm. The parameters used are: $\hbar\omega_L$=2.45 eV, : $\hbar\omega_{ge}$=2.35 eV, $\hbar\omega_{vib}$=0.16 eV, γ_{ph}=1x10^{14} Hz, α=0.5, and E_0=1x10^4 N/C.

There are 4 elements that appear in the spectra. First, there is a Rayleigh scattered band at the laser line, in this case 2.45 eV, and two smaller bands shifted by 0.16eV. The small band at 2.29 eV represents a Stokes process in Raman scattering, while the band at 2.61 is from an anti-Stokes process. Finally, there is a broad fluorescence centred at the ground-electronic band gap, at 2.35 eV. All of these bands are expected, as these are the parameters that were put into the program. Interestingly, there is a shoulder to the fluorescence, centered

at 2.51 eV.   This represents fluorescence to the upper vibrational state in the ground electronic state. Tabulated values of these intensities are given in table 6.1.

d	Fluorescence	Rayleigh	Stokes	Anti-Stokes
0	1.25	9.880	1.260	0.420
1	14.20	6.040	0.712	0.192
2	20.20	2.790	0.395	0.111
4	16.10	0.609	0.079	0.009

Table 6.1: Differential cross section results. Intensities are in units of 10^{-18} cm^2/(meV sr).

The enhanced Raman scattering and fluorescence at close particle-molecule distances show an almost complete quenching of the fluorescence, with a strong Raman enhancement. The fluorescence reaches a maximum around d=2 nm, while at intermediate distances the quenching effect is reduced, resulting in fairly strong fluorescence with moderate Raman. Past the optimal distance, both the fluorescence and Raman enhancement decay.

This quantum optical approach gives the proper treatment to the molecule by treating it as a quantum object. Serious drawbacks at this time include the assumption that there is only one vibrational mode, and that eventually, electron transfer effects from the particle to the molecule need to be included. Even this initial work, however, shows results that follow the same trend as experiment.

Bibliography

(1) Johansson, P.; Xu, H.; Käll, M. *Physical Review B* **2005**, *72*, 035427.
(2) Scully, M. O.; Zubaire, M. S. *Quantum Optics*; Cambridge University Press: New York, 1997.
(3) Xu, H. *Journal of the Optical Society of America A* **2004**, *21*, 804.
(4) Loudon, R. *The Quantum Theory of Light*; 3rd ed.; Oxford University Press: Norfolk, 2004.
(5) Meystre, P.; Sargent, M. I. *Elements of Quantum Optics*; 2nd ed.; Springer-Verlag: New York, 1990.

CHAPTER SEVEN

SURFACE ENHANCED INFRARED ABSORPTION (SEIRA)

A. Introduction to Surface Enhanced Infrared Absorption

Although the majority of this dissertation is focused on plasmonics applied to the visible region of the spectrum, the same models can be applied to obtain results in the infrared region. The approximate models described previously apply better in the infrared, due to the long wavelength. This chapter is mostly from Aroca, R. F.; Ross, D. J.; Domingo, C. *Applied Spectroscopy* **2004**, *58*, 324A-338A. [1], and used with permission, although that paper contains an extensive discussion of applications that does not appear here.

The discovery of surface-enhanced Raman scattering (SERS)[2-4] opened the field of surface-enhanced spectroscopy, including linear and non-linear optical phenomena[5,6]. In particular, the realization of surface-enhanced infrared absorption (SEIRA)[7] permitted one to speak of a unified field of surface-enhanced vibrational spectroscopy (SEVS), supported by the enhanced Raman and infrared techniques. Since the enhancement factor in the absorption seems modest when compared with those of SERS, the SEIRA effect has not received the attention of SERS.

The initial sporadic activity on the subject of SEIRA was largely concentrated in Japan and a look at the early work can be found in Osawa's review[8]. In the 90's SEIRA received its share of attention, and there were several reports for both the practical and theoretical aspects of the phenomena[9-12]. Since the bulk of SEIRA work is recent, there is still value in demonstrating the effect itself. In particular, it is helpful to examine the SEIRA spectra that can be obtained for the same system on different enhancing surfaces. The effect has been observed on island films of the coinage metals and a few other surfaces, most notably, Pt[12], Sn[13], Pd and Ru[14,15]. Recently, infrared enhanced absorption was demonstrated for anthracene coating polar dielectric nanoparticles of silicon carbide and aluminum oxide with 100 fold enhancement[16]. In the latter experiments, SEIRA is explained as being the result of the enhanced optical fields at the surface of the particles when illuminated at the surface plasmon

(phonon) resonance frequencies. It is pointed out that this phonon resonance effect is analogous to plasmon resonance that is the basis for surface enhanced Raman scattering and SEIRA in metals.

The role of surface plasmons has been well documented and there is abundant literature on the subject. A review of the plasmon literature directly related to SEIRA and SERS is available[17]. Recently, the first study was reported on metal films with architectures designed to produce surface plasmons in the infrared region, permitting a comparison of SEIRA results for these films and those where plasmons are not detected[18]. The authors observed SEIRA in the region of a surface plasmon using engineered surfaces. When these results were compared to SEIRA on evaporated metal films, equivalent results were obtained.

The experiments have always been tailored to attain enhanced optical fields and thereby the explanation is given in terms of electromagnetic (EM) models. In his broad review on SEIRA, Osawa[8] discusses these models, which can quantitatively explain both the effect, and its applications to the study of electrochemical reactions. Following, and by analogy with, the interpretation accepted for SERS, it has been suggested that electromagnetic and chemical contributions are responsible for the observed infrared enhancement. One cannot stretch this analogy too far, because the hypothetical chemical contributions to SERS includes additional multiplicative effects. These effects include charge transfer, which leads to resonance Raman scattering[19,20].

Computations of the EM enhancement using effective medium theories have been reviewed[21] and there is no question that there is a key contribution from enhanced local fields to SEIRA. There is an increase in the rate of absorption per unit volume that is proportional to the energy density of the field at the appropriate frequency. The enhanced local field augments this energy density at the surface of particles where the adsorbed molecule resides. This local field varies according to several factors, size, shape and the dielectric function, among others[22,23]. The enhancement varies from point to point and the average value is expected to match the observations.

There are further consequences for the observed infrared spectrum from molecules adsorbed at these local fields. The local field may be highly polarized. Moscovits[5] has illustrated the implications of having a perpendicular polarized field, or a tangentially polarized field, in determining the surface selection rules. The latter is discussed, separately, below, using a physisorbed molecule as a study case. In addition, the local field changes the dipole moment of the adsorbed molecule (that one can call chemical effect) in a fashion similar to what is seen in electrochemistry[24], producing a variation in the dipole moment derivatives and hence in the infrared intensity.

Griffiths and coworkers[12] reported a peculiar property in the symmetry of the SEIRA band shape of the CO on platinum. The band asymmetry has been studied in Griffiths' group, and has been observed in both Ag and Au island films. The effect can be simulated using the dielectric function of the metal and the substrate. However, the "Fano band" shape has attracted attention due to a possible link of the observations with the dynamic interaction of the adsorbate vibrations with electron-hole pair excitations[25]. Expressions for an isolated vibrational mode, for a molecule adsorbed on a metallic surface in the presence of electron-hole damping producing asymmetric line shape, have been derived by Landgreth[26].

The enhancement factors found in SEIRA can range up to 10^3, but are usually found to be in the 10 − 100 region at best. Compared to the very large enhancements observed in SERS up to 10^{10}, this effect is not nearly as dramatic, and has attracted less interest. However, even this small enhancement can be used to detect monolayers of films[10]. Although SEIRA does not yield the enhancement necessary for single-molecule detection as SERS does[27,28], SEIRA is a viable means of enhancing the infrared signal from adsorbed molecules on a variety of metals, semimetals, semiconductors and polar dielectric nanostructures.

The electromagnetic enhancement on rough metal surfaces has been extensively discussed for radiation in both the visible and near infrared regions of the spectrum[29], while there has been less work done for middle and far infrared

regions. Computational approaches for SERS electromagnetic enhancement (EM)[30,31] are often applicable to SEIRA, and these can be roughly divided into three types: isolated particle models, finite numbers of particle models, and surface and film models.

A simple model for a rough surface is that of a collection of non-interacting spheroids (See reviews and references therein)[5,32,33]. For a spheroidal particle, the induced field is uniform, but not necessarily parallel to an arbitrarily applied field, excepting the case of a sphere. The sense of depolarization is that the field inside the particle is less than the applied field, and the term is applied to the induced field, which points in the direction opposite the applied field. In surface enhanced spectroscopy, however, the internal field is greater than the applied field. Previous research has attempted to explain the SEIRA effect in terms of surface plasmons in the infrared spectral region[18]. The study used tuned surfaces to give large islands, which have a plasmon resonance in the near to middle infrared. Calculations of field enhancement using the modified long wavelength approximation gave good agreement with observed plasmons on a variety of substrates[18].

A successful electromagnetic study of enhancement factors in the ultraviolet, visible and near infrared, for a variety of materials, showed very weak field enhancement in the near infrared compared to the visible[34]. This technique can be extended to the full infrared region, although the result should be similar to the static case due to the long wavelengths.   We have adapted this method to calculate the field enhancement for silver and tin in the fingerprint region of the infrared and the results are shown in Figure 7.1. The model consists of spheroids embedded in a medium of unity dielectric constant, with lengths of 90 and 30 nm for major and minor axes respectively. The dielectric functions of the metals are taken from the Handbook of Optical Constants[35]. These values for Ag and Sn are plotted in Figure 7.2.
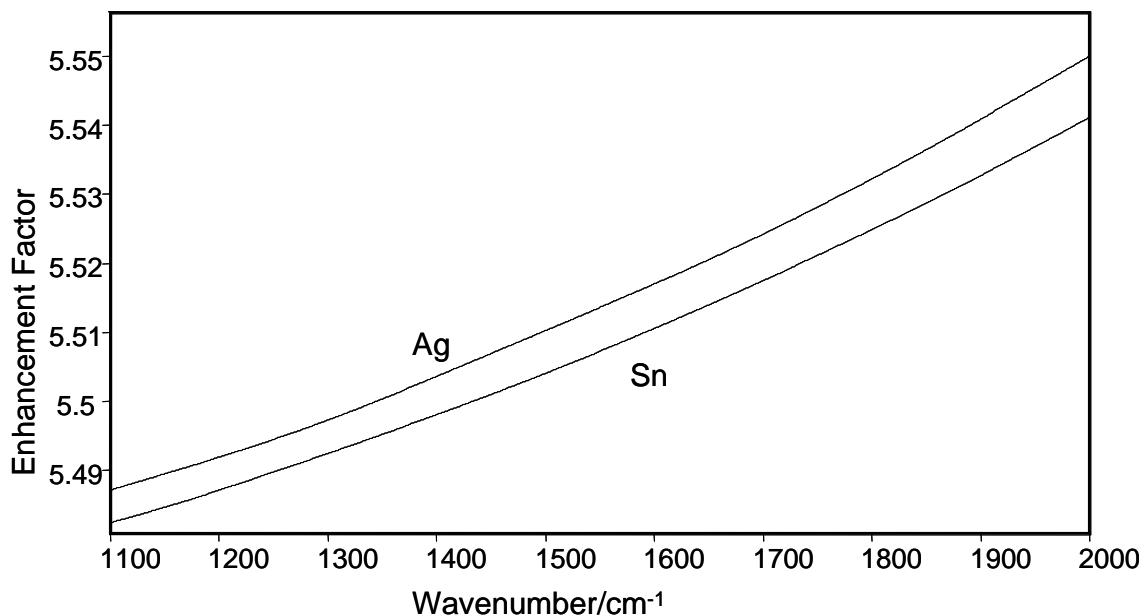
Figure 7.1. Enhancement factor of the electromagnetic field for spheroids in vacuum, with lengths of 90 and 30 nm for major and minor axes respectively.
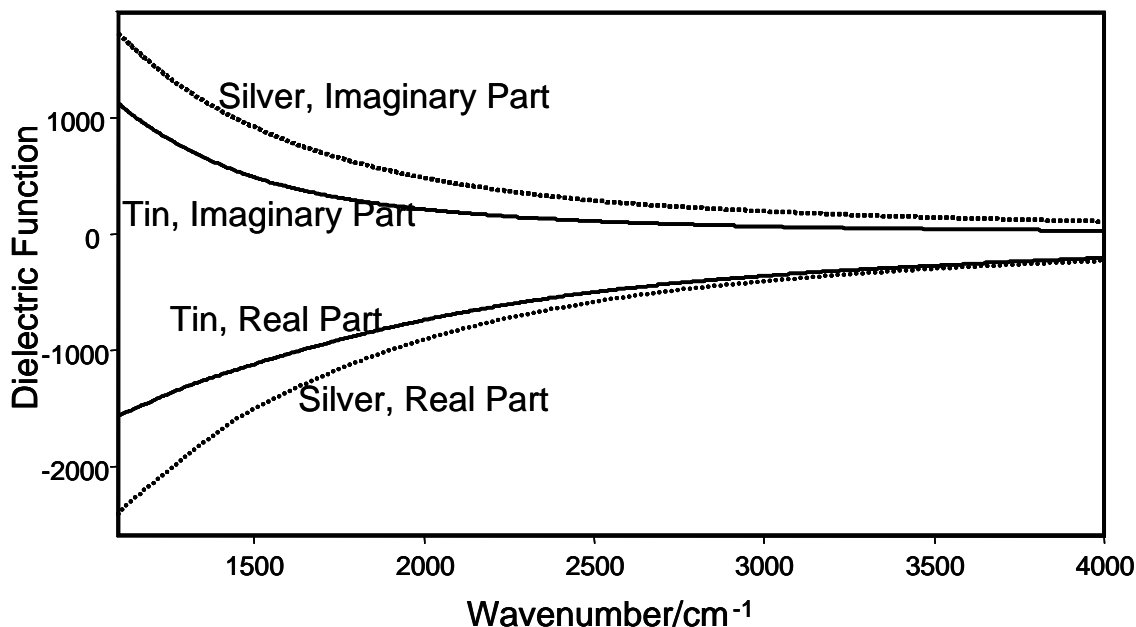
Figure 7.2. Real and Imaginary parts of the dielectric function for Silver and Tin.

Recently, an experimental study of the enhanced infrared absorption of anthracene on dielectric particles, namely SiC and Al_2O_3, reports enhancements on the order of one hundredfold[16]. The author argues that this enhancement can be explained on the basis of the surface field enhancements due to phonon resonance. The field enhancements on the surface for these systems can also

168

be calculated. Figure 4.3 shows the enhancement factor for SiC averaged over the surface of a particle with the same computational parameters as above. The sharpness of the resonance agrees with the argument of phonon contributions, as phonons, compared to plasmons, have much less damping[36].
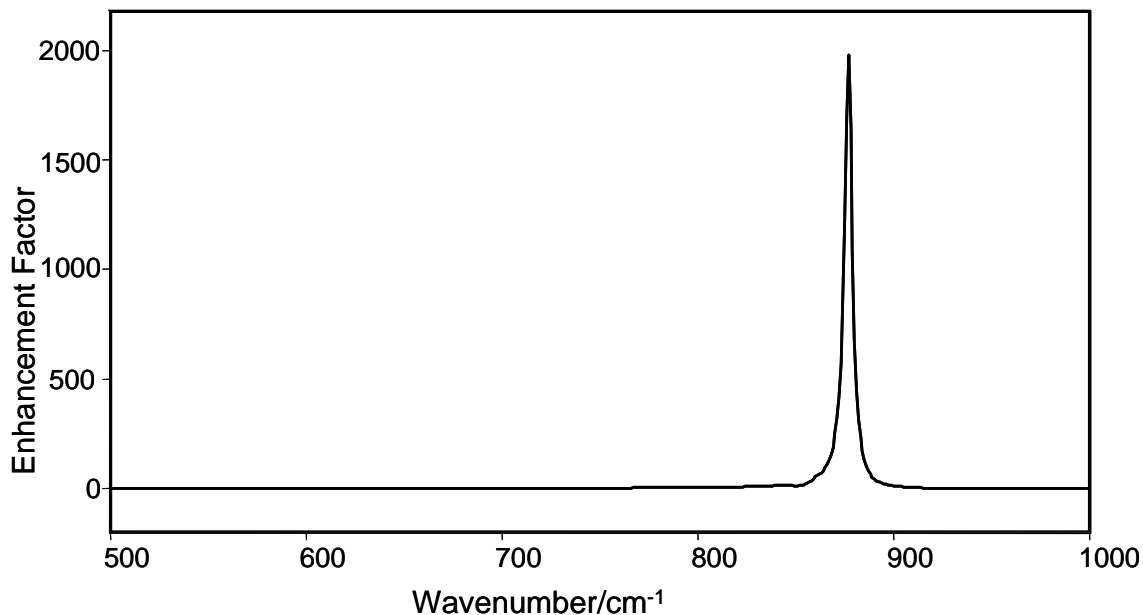
7.3. Enhancement factor for SiC averaged over the surface of a particle with the same computational parameters as those in Figure 7.1

Although this model is very useful for giving a prediction of enhancement factors, it neglects the inhomogeneous nature of a film or colloids, and as well does not account for any chemical contributions to the enhancement. A full discussion of the problems in any electromagnetic calculation in surface enhanced vibrational spectroscopy can be found in the review by Moskovits[5].

A more advanced model than that of the isolated particle is a finite number of particles interacting in a well-defined way. Due to the complexity of these calculations, however, their use has not been popular for SERS enhancement calculations, and has not been applied to SEIRA.

B. Effective Medium Theory

The electromagnetic SEIRA enhancement may be calculated using effective medium theories (EMT), which uses the effective optical property of a heterogeneous material. The substrates used in SEIRA are usually metal island films, or granular materials (such as semi-metals or semiconductors). Effective medium theory is a formalism used to model these discontinuous surfaces so that they may be characterized by a set of effective electrical properties, such as conductivity or dielectric function[9,10,21,37]. In the case of SEIRA the effective property represents an average for the metal films, the substrate and the organic coat. Finding the dielectric function for the surface enhanced sample involves finding the effective optical properties of the mixture of these components. The spatial average of the dielectric function of the sample comprised of substrate, metal islands, and analyte is achieved using one of effective medium formalism[38-42]. A general review, including electrical properties, has been written by Bergman and Stroud[43].

Two of the most used formalisms for effective medium calculations are the Maxwell-Garnet and the Bruggeman methods. The general form of the Maxwell-Garnet model can be given as[40]:

$$\overline{\varepsilon} = \varepsilon_h \frac{3 + 2\sum_i f_i \alpha_i}{3 - \sum_i f_i \alpha_i}$$

Where α is the polarizability of the inclusions, and i is the index over different particles. This allows for the distribution of particle shapes and sizes to be included in the calculation, as opposed to simple spheres. $\overline{\varepsilon}$ is the effective dielectric function, and ε_h is the dielectric function of the host material, in which the particles are embedded, while f represents the volume fraction of the inclusions.

The Bruggeman model is a self-consistent theory which includes a greater amount of interaction between inclusions[44]. The self-consistency enters through the use of the Bruggeman condition, $\varepsilon_h \rightarrow \overline{\varepsilon}$, which requires that the solution be

a dielectric function of a host that has the same optical properties as the effective medium. This formalism can be expressed in general as:

$$\bar{\varepsilon} = \varepsilon_h \frac{3(1-f) + f\alpha'}{3(1-f) - 2f\alpha'}$$

where α' is the polarizability of the inclusions with the "Bruggeman" condition applied.

There are several reports where EMT's have been used to model SEIRA experiments[10,12,37]. Osawa[8] models island films as a set of ellipsoids of rotation, where the symmetry axis is normal to the substrate. In the present calculations, the polarizability of a coated ellipsoid is used, with depolarisation factors derived by Stoner[45]. Since the inhomogeneities in the layer are much smaller than the wavelength of the incident light, it is assumed the mixed film is a continuous layer, with parallel sides, so Fresnel's equations may be used to calculate the reflectance and transmittance[46]. In general, discontinuous metal films consist of islands, which may be modeled as ellipsoids of revolution or spheroids of uniform shape and size[41]. There are 2 different types of ellipsoids of revolution: oblate, where the 2 larger axes are equal, and prolate, where the 2 smaller axes are equal. Normann and coworkers[40] claim that prolate spheroids with the rotation axis parallel to the plane provide the best description of electron micrographs as well as the best fit between measured and computed spectra.

The dielectric function, denoted ε_m, for the bulk metals, was taken from the Handbook of Optical Constants of Solids[35]. Islands have a major axis of length a, minor axis b, and an aspect ratio defined as $\eta = a/b$. A geometry for the metal islands can be found by fitting computed UV-Visible plasmon spectra to measured data in the same region. The characteristic plasmon resonances for metals in this region lead to strong absorption bands for most noble metals, and these spectral features are strongly dependent on the shape and size of the metal particles.

Additional considerations of the inhomogeniety of the size and shape of the particles can be taken into account by using a distribution. Since real films are not made up of surfaces with particles of only one size and aspect ratio, a

distribution of the axis of particles which make up a film makes a better model for the surface[40]. It has been found that a log-normal distribution provides the best fit for electron microscopy data[47]. The log-normal distribution is given by:

$$f_{LN}(x_s) = \frac{1}{(2\pi)^{1/2}\ln(\sigma_s)}\exp\left(-\frac{1}{2}\left[\frac{\ln\left(\frac{x_s}{\bar{x}_s}\right)}{\ln(\sigma_s)}\right]^2\right)$$

Where σ_s is the standard deviation of the length of the minor axis, x_s the length of the minor axis, and $\bar{x}_s$ the average length of the minor axis. In general, a larger deviation will result in a broader plasmon, since contributions from many different shapes will form the spectra. The use of a distribution over aspect ratios in this way provides a better fit to experimental data, although does not change the physical interpretation.

The introduction of the organic layer to the metal surface can be represented in two ways. The first is to assume that the molecule forms a thin layer uniformly coating the surface. The net dipole moment *p* may be given by[46,48]:

$$p = \alpha V E_{loc}$$

where α is the polarizability, V is the volume of the inclusion, and E_{loc} is the local field, made up of the incident field and the enhanced field from the particle. For a coated spheroid with one axis parallel to the incident electric field, the polarizability is given by [48,49].

$$\alpha = \sum_i \frac{1}{2}\frac{(\varepsilon_d - \varepsilon_h)(\varepsilon_m L1_i + \varepsilon_d(1 - L1_i)) + Q(\varepsilon_m - \varepsilon_d)(\varepsilon_d(1 - L2_i) + e_h L2_i)}{(\varepsilon_d L2_i + \varepsilon_h(1 - L2_i))(\varepsilon_m L1_i + \varepsilon_d(1 - L1_i)) + Q(\varepsilon_m - \varepsilon_d)(\varepsilon_d - \varepsilon_h)L2_i(1 - L2_i)}$$

Where ε_m is the dielectric function of the metal, ε_d the dielectric function of the organic layer, ε_h the dielectric function of the host medium. Q is the volume ratio of the ellipsoid, defined by $Q = \frac{V core}{V coat}$, *i* is the index over the axes of the inclusion,

and $L1_i$ and $L2_i$ are the geometrical factors corresponding to the core ellipsoid and the coated ellipsoid, respectively.

Basic to the definition of ellipsoids is the geometrical factor. The geometrical factor is a measure of the curvature perpendicular to a specific axis of the ellipsoid, and has a value $0<L<1$. The geometrical factors for the major axis of an oblate are[41]:

$$L_1 = \frac{g(e)}{2e^2}\left[\frac{\pi}{2} - \tan^{-1} g(e)\right] - \frac{g^2(e)}{2}, \, g(e) = \left(\frac{1-e^2}{e^2}\right)^{1/2}$$

and for the major axis of a prolate:

$$L_1 = \frac{1-e^2}{e^2}(-1 + \frac{1}{2e}\ln\frac{1+e}{1-e})$$

where e is the eccentricity of the spheroid.

The second method of introducing organic molecules to the metal surface is to model the inclusions directly embedded in the organic matrix. This model is better suited to thicker layers of organic, since a coating around a particle poorly describes this case. In this model the polarizability is given by:

$$\alpha = \sum_i \frac{1}{2}\frac{\varepsilon_m - \varepsilon_d}{\varepsilon_d + L_i(\varepsilon_m - \varepsilon_d)}$$

with the same notation as above, excepting that only one geometrical factor is needed.

For the Bruggeman EMT, the Bruggeman condition is also applied to obtain α' [8]. The reaction field equations for both the Maxwell-Garnet and the Bruggeman theory with coated ellipsoid polarizability as outlined above for application to SEIRA calculations.

The Bruggeman EMT tends to give higher enhancements, and has often been used to explain some of the larger experimentally observed enhancements. This is due to the higher degree of interaction involved in Bruggeman EMT as compared to Maxwell-Garnet, although Maxwell-Garnet seems to give results that are more in-line with isolated particle results and most experiments. Bruggeman EMT has been used to verify some experimental results, however,

173

these experiments also used molecules which chemisorbed, and so some of the observed enhancement may be due to the chemisorption of the molecule onto the surface[42].

Effective medium theory is popular for SEIRA as enhancement factors can be calculated without any difficulties regarding the nature of the enhancement. Although useful, effective medium theory does not give any insight as to the mechanism of the phenomenon. As an example of effective medium calculations in use, Figure 7.4 shows the Maxwell-Garnet calculation for a collection of prolate ellipsoids, with a major axis of 90 nm and a minor axis of 30 nm, and uniformly coated with a 1 nm thick layer of the analyte. The analyte in these model calculations is 3,4,9,10-perylene-tetracarboxylic-dianhydride, or PTCDA, a well-known organic dye[50], presented fully in appendix B. The dielectric function for the organic is taken from the absorption by means of a Lorentz model using the 1300 cm⁻1 band of PTCDA, and applied as a constant across the whole range of the calculation. This gives the effect of the metal. The result is very similar to those of the field calculations from a single particle, increasing towards the visible range of the spectrum, but the enhancement for tin is slightly higher than for silver in this case.
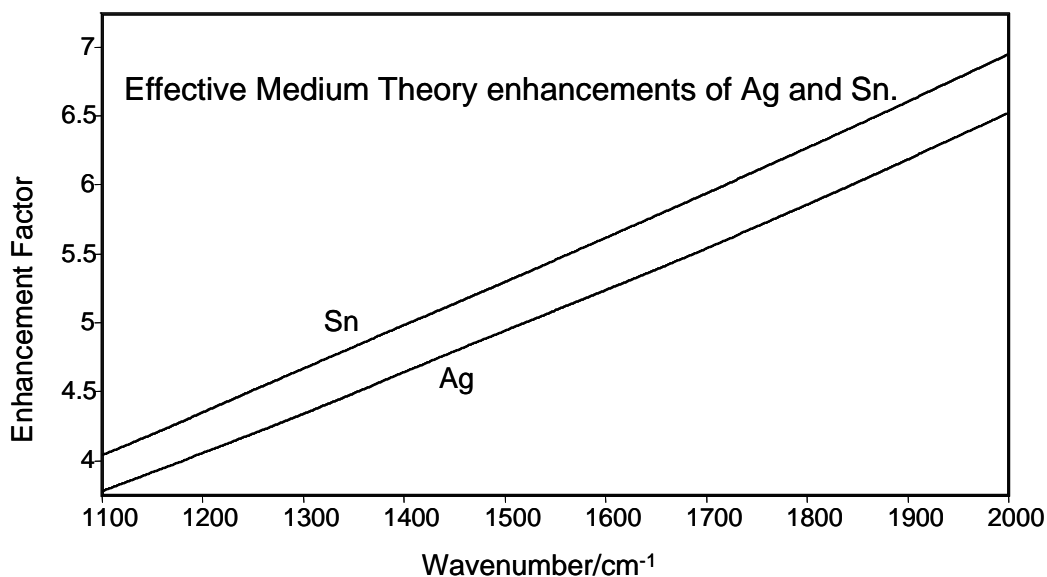
Figure 7. 4. Maxwell-Garnet computation for a collection of prolate ellipsoids, with a major axis of 90 nm and a minor axis of 30 nm, coated with a 1 nm thick layer of PTCDA.

174

C. SEIRA of PTCDA

As a study case to illustrate the application of the selection rules in the spectral interpretation of the FTIR transmission, reflection-absorption infrared spectroscopy (RAIRS) and SEIRA, we have selected the 3,4,9,10-perylene-tetracarboxylic-dianhydride (PTCDA) dye, a molecule with 38 atoms ($C_{24}H_8O_6$), 108 vibrational degrees of freedom and 46 infrared active fundamental vibrations[51] distributed in 10 $b_{3u}(x)$ + 18 $b_{2u}(y)$ + 18 $b_{1u}(z)$ symmetry species. The molecule is a flat rectangle of 14.2 Å for the long axis (z) and 9.2 Å on the short axis (y) as shown in Figure 7.5.
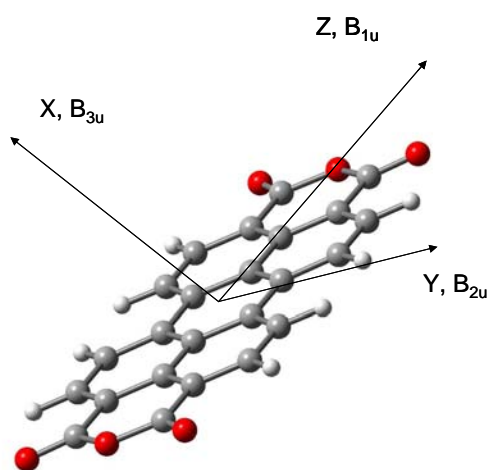
Figure 7.5: Planar, D_{2h} PTCDA molecule.

Since the molecule has a centre of symmetry (D_{2h} group), the mutual exclusion rule applies. RAIRS is an infrared technique that takes advantage of the large E_0 component at the reflecting surface. In the present study case the samples for RAIRS were prepared by evaporating first 100 nm of Ag onto a Corning 7059 glass slide, held at 200 ^{o}C under high vacuum. Fifty nanometers of perylene tetracarboxylic anhydride (PTCDA) were then evaporated onto this smooth silver surface[52]. The RAIRS spectra were obtained by using a Spectra-Tech variable angle reflectance accessory set such that the incident beam impacted the surface at 80^0 from the normal.

The reference is the transmission spectrum of the solid dispersed in a KBr pellet that is equivalent to a random distribution of the PTCDA molecules, i.e. a

random molecular orientation. To help the vibrational analysis a calculation of the vibrational frequencies and intensities is carried out. To illustrate the agreement between the experiment and DFT computations, the transmission FTIR of a PTCDA pellet and the B3LYP/6-31g(d) results obtained using Gaussian 98[53], where a scaling factor of 0.9614[54] was used, are shown in Figure 7.6. It can be seen that there is a good agreement between the calculated and observed vibrational intensities. The latter is in spite of the condensed matter effects on the observed infrared spectra, and that the computations are performed within the harmonic approximation. The spectrum of the KBr pellet can be now compared with the RAIRS spectrum of a 50 nm PTCDA film deposited onto smooth reflecting silver mirror. The RAIRS results are shown in Figure 7.7, where the calculated vibrational intensities for the b_{3u} species are also included to facilitate the assignment. According to the surface selection rules, only the vibrational modes having nonzero dipole moment derivative components perpendicular to the surface should be active in RAIRS. Hence, from the RAIRS spectrum of the PTCDA molecule it can be extracted that it is preferentially oriented with its x-axis (out-of-molecular plane) perpendicular to the metal surface, a flat-on molecular orientation. Similar results were obtained for PTCDA films of 20 nm mass thickness[52]. The fact that the in-plane vibrations are still seen, is an indication that in this relatively thick film (50 nm mass thickness) there is a certain degree of randomness.
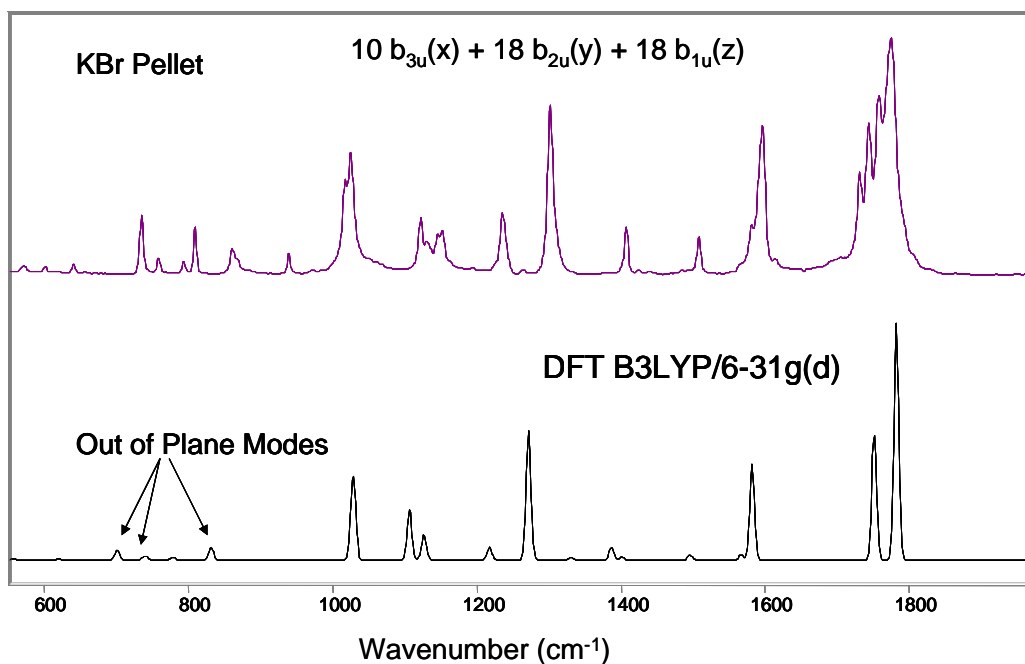
Figure 7.6: DFT B3LYP/6-31g(d) computation results, and the transmission FTIR spectrum of PTCDA in a KBr pellet.
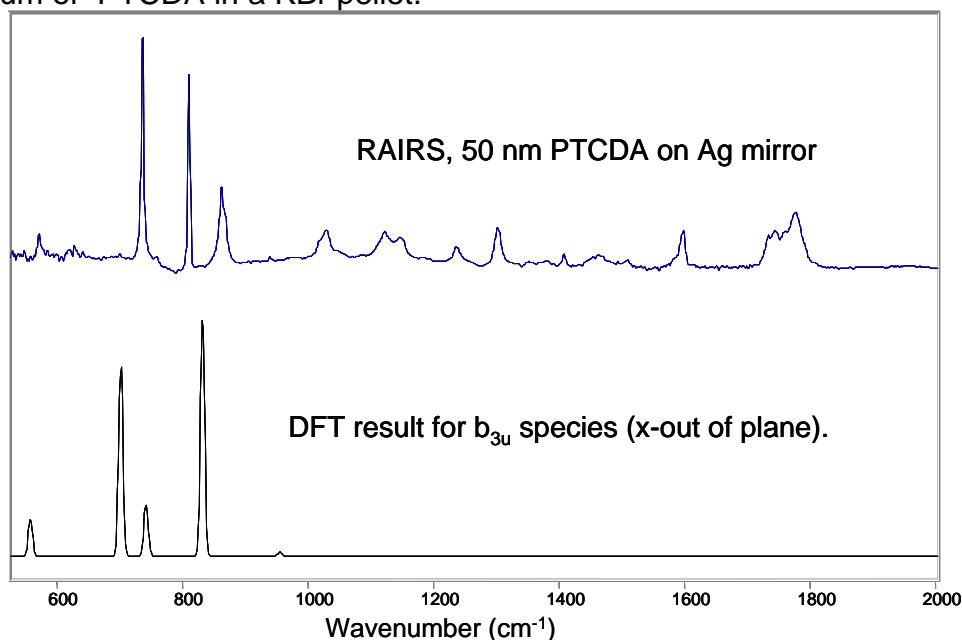
Figure 7.7: RAIRS spectrum of a 50 nm PTCDA film deposited onto smooth reflecting silver mirror and calculated vibrational intensities for the b_{3u} species.

The experimental conditions for the deposition of the SEIRA metal surface are the same as for the RAIRS experiment, except, of course, for the mass thickness. The spectroscopic results for a 50 nm mass thickness PTCDA film

deposited on silver islands and on a KBr crystal are shown in Figure 7.8. For comparison, the spectrum of the KBr pellet is included as a reference. If one assumes the same molecular orientation in the PTCDA films deposited onto smooth silver film and KBr crystal, the transmission spectrum of the film on KBr, where the electric field is polarized parallel to the surface, should give a strong absorption for the in-plane mode and a weak signal for the out-of-plane modes (b_{3u}). Since the latter is observed (Figure 7.8), the transmission spectrum of the PTCDA film on the KBr crystal is in agreement with the RAIRS results pointing to a preferential flat-on molecular orientation in the evaporated films. The SEIRA spectrum shown in Figure 7.8 is strikingly different from the RAIRS spectrum and clearly does not show the same selection rules. Since in the infrared spectral region, one would also expect that the local optical field on the surface of the silver island film is perpendicular to the surface (as in RAIRS), the simplest explanation would be to assume that the PTCDA molecules are not oriented flat-on the metal island. Instead, there is a random distribution of orientations and the vibrational intensities are much closer to that of the free molecule (or KBr spectrum).
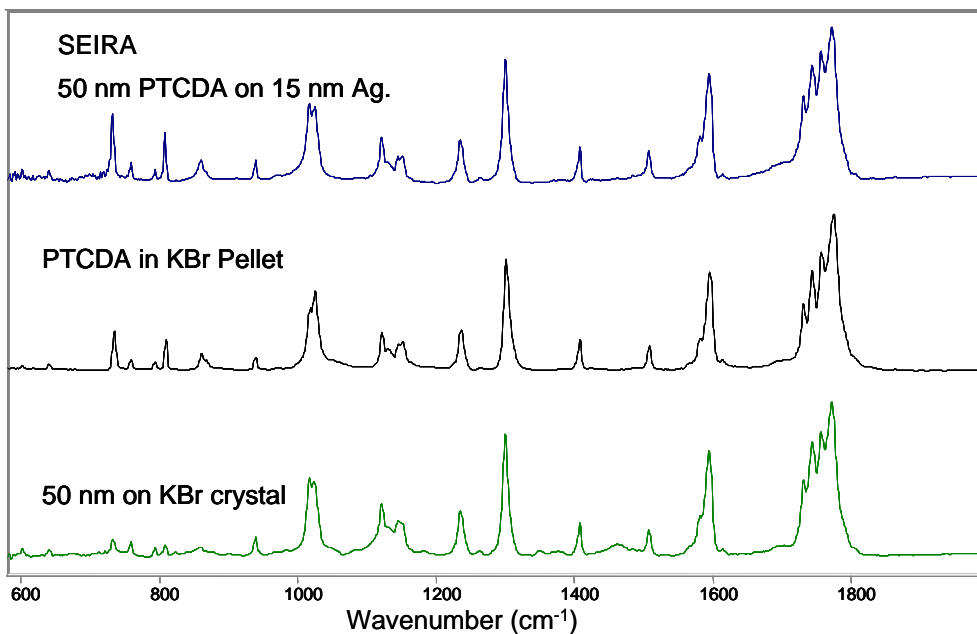
Figure 7.8. Transmission spectra. PTCDA pellet, SEIRA spectrum, and 50 nm film on KBr crystal.
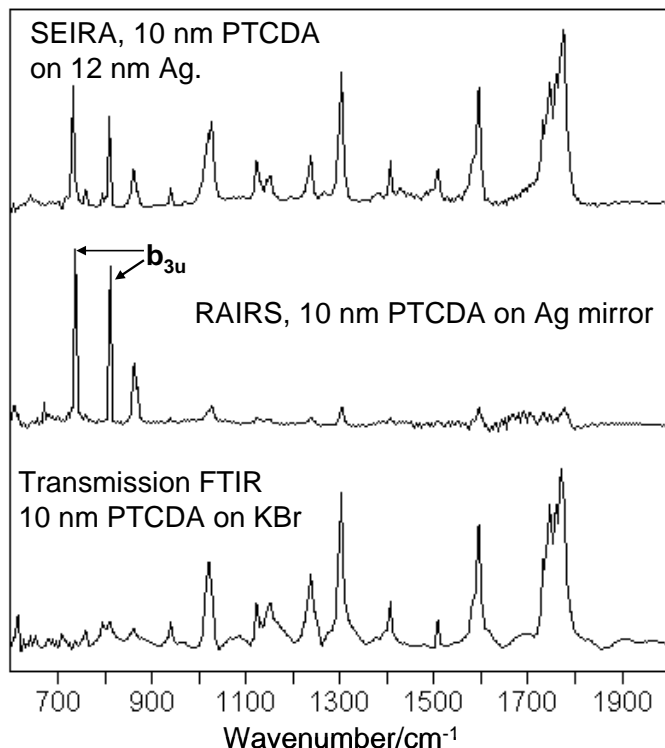
Figure 7.9. SEIRA spectrum of the 10 nm PTCDA film on 15 nm silver island film. RAIRS spectrum of the 10 nm PTCDA film on smooth silver mirror, and transmission FTIR spectrum of the 10 nm PTCDA film on KBr crystal.

Since the films used in the previous experiments were relatively "thick", we repeat the experiments using a PTCDA film of 10 nm mass thickness. The transmission spectrum of the neat PTCDA film on the KBr crystal and the SEIRA spectrum of the 10 nm PTCDA film on 15 nm silver island film were recorded under identical experimental conditions using the Bomem DA3 vacuum bench instrument. The RAIRS spectrum of the 10 nm PTCDA film on smooth silver mirror was recorded in the Bruker instrument with p-polarized light. The results are shown in Figure 7.9. It can be seen that the selection rules observed in the RAIRS spectrum unmistakably point to a flat-on molecular orientation of PTCDA with a strong relative intensity for the out-of-plane b_{3u}. Notably the SEIRA spectrum does not follow the RAIRS pattern. However, the relative intensity of the out-of-plane modes has increased with decreasing film thickness hinting to proportional increase of PTCDA molecules oriented flat-on the silver islands.

The PTCDA case presented here is of interest for researchers trying to extract molecular orientation information using SEIRA. In such cases it is advisable to carry out the RAIRS experiments[55,56] with the same species as a reference point for the SEIRA results. In conclusion, the observation of strict adherence to surface selection rules in RAIRS may not be mimicked by the SEIRA spectrum.

D. Bibliography

(1)   Aroca, R. F.; Ross, D. J.; Domingo, C. *Applied Spectroscopy* **2004**, *58*, 324A-338A.
(2)   Jeanmaire, D. L.; Van Duyne, R. P. *J. Electroanal. Chem.* **1977**, *84*, 1.
(3)   Albrecht, M. G.; Creighton, J. A. *J. Am. Chem. Soc.* **1977**, *99*, 5215.
(4)   Fleischmann, M.; Hendra, P. J.; McQuillan, A. J. *Chemical Physics Letters* **1974**, *26*, 163-166.
(5)   Moskovits, M. *Rev. Mod. Phys.* **1985**, *57*, 783-826.
(6)   Kneipp, K.; Kneipp, H.; Itzkan, I.; Dasari, R. R.; Feld, M. S. *Chem. Phys.* **1999**, *247*, 155-162.
(7)   Hartstein, A.; Kirtley, J. R.; Tsang, J. C. *Phys. Rev. Lett.* **1980**, *45*, 201-204.
(8)   Osawa, M. *Bull. Chem. Soc. Jpn.* **1997**, *70*, 2861-2880.
(9)   Nishikawa, Y.; Fujiwara, K.; Ataka, K.; Osawa, M. *Anal. Chem.* **1993**, *65*, 556-562.
(10)   Johnson, E.; Aroca, R. *J. Phys. Chem.* **1995**, *99*, 9325-9330.
(11)   Kellner, R.; Mizaikoff, B.; Jakusch, M.; Wanzenbock, H. D.; Weissenbacher, N. *Appl. Spectrosc.* **1997**, *51*, 495-503.
(12)   Bjerke, A. E.; Griffiths, P. R.; Theiss, W. *Anal. Chem.* **1999**, *71*, 1967-1974.
(13)   Aroca, R.; Price, B. *J. Phys. Chem. B* **1997**, *101*, 6537-6541.
(14)   Hahn, F.; Melendres, C. A. *Electrochim. Acta* **2001**, *46*, 3525-3534.
(15)   Zheng, M. S.; Sun, S. G.; Chen, S. P. *J. Appl. Electrochem.* **2001**, *31*, 749-757.
(16)   Anderson, M. S. *Appl. Phys. Lett.* **2003**, *83*, 2964-2966.
(17)   Andersen, P. C.; Rowlen, K. L. *Appl. Spectrosc.* **2002**, *56*, 124A-135A.
(18)   Jensen, T. R.; Van Duyne, R. P.; Johnson, S. A.; Maroni, V. A. *Appl. Spectrosc.* **2000**, *54*, 371-377.
(19)   Otto, A.; Mrozek, I.; Grabhorn, H.; Akemann, W. *Condens. Matter* **1992**, *4*, 1143-1212.
(20)   Campion, A.; Kambhampati, P. *Chem. Soc. Rev.* **1998**, *27*, 241-250.
(21)   Ross, D.; Aroca, R. *J. Chem. Phys.* **2002**, *117*, 8095-8103.
(22)   Coronado, E. A.; Schatz, G. C. *J. Chem. Phys.* **2003**, *19*, 3926-3934.
(23)   Noguez, C. *Journal of Physical Chemistry C* **2007**, *111*, 3806-3819.
(24)   Lambert, D. K. *J. Chem. Phys.* **1991**, *94*, 6237-6242.
(25)   Sinther, M.; Pucci, A.; Otto, A.; Priebe, A.; Diez, S.; Fahsold, G. *Phys. Stat. Sol. (a)* **2001**, *188*, 1471-1476.
(26)   Langreth, D. C. *Phys. Rev. Lett.* **1985**, *54*, 126-129.
(27)   Kneipp, K.; Wang, Y.; Kneipp, H.; Perelman, L. T.; Itzkan, I.; Dasari, R.; Feld, M. S. *Phys. Rev. Lett.* **1997**, *78*, 1667-1670.
(28)   Nie, S.; Emory, S. R. *Science* **1997**, *275*, 1102-1106.
(29)   Yang, W. H.; Schatz, G. C.; Van Duyne, R. P. *J. Chem. Phys.* **1995**, *103*, 869-875.
(30)   Barber, P. W.; Chang, R. K.; Massoudi, H. *Phys. Rev. B* **1983**, *27*, 7251.

(31)   Schatz, G. C.; Van Duyne, R. P. In *Handbook of Vibrational Spectroscopy*; Chalmers, J. M., Griffiths, P. R., Eds.; John Wiley: New York, 2002; Vol. Volume 1.

(32)   Gersten, J. I.; Nitzan, A. *J. Chem. Phys.* **1980**, *73*, 302.

(33)   Chang, R. K.; Furtak, T. E. *Surface Enhanced Raman Scattering*; Plenum Press: New York, 1982.

(34)   Zeman, E. J.; Schatz, G. C. *J. Phys. Chem.* **1987**, *91*, 634-643.

(35)   *Handbook of Optical Constants of Solids*; Palik, E. D., Ed.; Academic Press, 1985.

(36)   Hillenbrand, R.; Taubner, T.; Keilmann, F. *Nature* **2002**, *418*, 159-162.

(37)   Osawa, M.; Ataka, K.-I.; Yoshii, K.; Nishikawa, Y. *Applied Spectroscopy* **1993**, *47*.

(38)   Granqvist, C. G.; Hunderi, O. *Phys. Rev. B* **1977**, *16*, 3513.

(39)   Papavassiliou, G. C. *Prog. Solid State Chem.* **1979**, *12*, 185.

(40)   Normann, S.; Andersson, T.; Granqvist, C. G.; Hunderi, O. *Phys. Rev. B* **1978**, *18*, 674.

(41)   Bohren, C. F.; Huffman, D. R. *Absorption and Scattering of Light by Small Particles*; John Wiley & Sons, Inc.: New York, 1983.

(42)   Osawa, M.; Ikeda, M. *J. Phys. Chem.* **1991**, *95*, 9914-9919.

(43)   Bergman, D. J.; Stroud, D. In *Solid State Physics*, 1992; Vol. 46.

(44)   Fujiwara, H. J.; Rovira, P. I.; Collins, R. W. *Phys. Rev. B* **2000**, *61*, 10832.

(45)   Stoner, E. C. *Philos. Mag.* **1945**, *36*, 803.

(46)   Jackson, D. J. *Classical Electrodynamics*; Second ed.; Jonh Wiley & Sons, 1975.

(47)   Yoshida, S.; Yamaguchi, T.; Kimbara, A. *J. Opt. Soc. Am.* **1971**, *61*, 62.

(48)   Eagen, C. F. *Appl. Optics* **1981**, *20*, 3035-3042.

(49)   Bilboul, R. R. *J. Phys. D.* **1969**, *2*, 921.

(50)   Heutz, S.; Salvan, G.; Silaghi, S. D.; Jones, T. S.; Zahn, D. R. T. *J. Phys. Chem. B* **2003**, *107*, 3782-3788.

(51)   Akers, K.; Aroca, R.; Hor, A. M.; Loutfy, R. O. *J. Phys. Chem.* **1987**, *91*, 2954-2959.

(52)   Aroca, R.; Rodriguez-Llorente, S. *J. Mol. Struct.* **1997**, *408/409*, 17-22.

(53)   Frisch, M. J.; Trucks, G. W.; Schlegel, H. B.; Scuseria, G. E.; Robb, M. A.; Cheeseman, J. R.; Zakrzewski, V. G.; Montgomery, J. J. A.; Stratmann, R. E.; Burant, J. C.; Dapprich, S.; Millam, J. M.; Daniels, A. D.; Kudin, K. N.; Strain, M. C.; Farkas, O.; Tomasi, J.; Barone, V.; Cossi, M.; Cammi, R.; Mennucci, B.; Pomelli, C.; Adamo, C.; Clifford, S.; Ochterski, J.; Petersson, G. A.; Ayala, P. Y.; Cui, Q.; Morokuma, K.; Malick, D. K.; Rabuck, A. D.; Raghavachari, K.; Foresman, J. B.; Cioslowski, J.; Ortiz, J. V.; Stefanov, B. B.; Liu, G.; Liashenko, A.; Piskorz, P.; Komaromi, I.; Gomperts, R.; Martin, R. L.; Fox, D. J.; Keith, T.; Al-Laham, M. A.; Peng, C. Y.; Nanayakkara, A.; Gonzalez, C.; Challacombe, M.; Gill, P. M. W.; Johnson, B.; Chen, W.; Wong, M. W.; Andres, J. L.; Gonzalez, C.; Head-Gordon, M.; Replogle, E. S.; Pople, J. A.; Gaussian, Inc.: Pittsburgh PA, 1998.

(54)   Scott, A. P.; Radom, L. *J. Phys. Chem.* **1996**, *100*, 16502.

(55)   Chang, J.-h.; Xuan, G. S.; Li, C. J.; Kim, J.-H. *Abstracts of Papers, 223rd ACS National Meeting, Orlando, FL, United States, April 7-11, 2002* **2002**, COLL-244.

(56)   Zhang, J. M.; Zhang, D. H.; Shen, D. Y. *Macromolecules* **2002**, *35*, 5140-5144.

CHAPTER EIGHT
QUANTUM CHEMISTRY FOR MOLECULAR SYSTEMS

A. Nanostructures and the Observed Spectra in SER(R)S

The observed SER(R)S spectra of any molecule that is near or attached to a silver or gold nanostructure, and can sustain localized surface plasmon resonances[1,2] carries the quantum fingerprints of the molecular system. This is modulated by the molecule-nanostructure interactions and the electronic resonances (including resonances with charge-transfer electronic transitions) that may result from laser excitation. There is a wealth of information to be extracted from measured vibrational band parameters. The observed spectrum is the electromagnetically enhanced Raman spectrum of the physisorbed molecule, as well as a host of chemical products, such as: the chemisorbed molecule, newly formed molecular complexes, photodissociation products, dimers, and molecular ions. This variety of products being observed simultaneously can make the spectral interpretation quite challenging[3]. In order to interpret this data, it is necessary to go back and look at the origin of the Raman scattering that is coupling with the plasmon resonance, and revisit the theory behind our detailed knowledge of the electronic ground state and its vibrational states for molecular systems.

The classical theory of Rayleigh and Raman scattering is based on the concept that scattered light is generated by oscillating electric dipoles induced by the electric field of the electromagnetic radiation. The simplest relationship for a frequency-dependent induced electric dipole p in a linear approximation is $p = \alpha E$, where both p and E are vectors and the polarizability α is a first rank tensor[4]. This is indeed the first term, and also the largest, of power series in E, where the polarizability is the first coefficient follow by higher rank tensors (the hyperpolarizability [tensor of second rank] and second hyperpolarizability) that give rise to nonlinear Raman effects. In this thesis we are only concerned with the linear term, i.e., the origin of the Raman scattering induced by low power lasers. The three components of the induced dipole moment vector p are:

$$p_x = \alpha_{xx}E_x + \alpha_{xy}E_y + \alpha_{xz}E_z$$
$$p_y = \alpha_{yx}E_x + \alpha_{yy}E_y + \alpha_{yz}E_z \qquad (8.1)$$
$$p_z = \alpha_{zx}E_x + \alpha_{zy}E_y + \alpha_{zz}E_z$$

In matrix form:

$$\begin{bmatrix} p_x \\ p_y \\ p_z \end{bmatrix} = \begin{pmatrix} \alpha_{xx} & \alpha_{xy} & \alpha_{xz} \\ \alpha_{yx} & \alpha_{yy} & \alpha_{yz} \\ \alpha_{zx} & \alpha_{zy} & \alpha_{zz} \end{pmatrix} \begin{bmatrix} E_x \\ E_y \\ E_z \end{bmatrix} \qquad (8.2)$$

Here, the equilibrium polarizability matrix can be written as α_0. To solve the mechanical problem, we set a fixed the system of coordinates in the molecule, such that the molecule is free to vibrate but the rotational motions are left out[5-7]. We therefore have a fixed equilibrium configuration for a stable molecule in a given electronic state, which provides us with an equilibrium value of both the polarizability tensor and the dipole moment. The infinitesimal variations of this equilibrium configuration with internal vibrations will give rise to the Raman and infrared intensities. The variation of the polarizability tensor elements with the vibrational modes can be expressed in a Taylor series with respect to a set of vibrational coordinates termed normal modes of vibration[4];

$$\alpha_{\rho\sigma} = \left(\alpha_{\rho\sigma}\right)_0 + \sum_k \left(\frac{\partial \alpha_{\rho\sigma}}{\partial Q_k}\right)_0 Q_k + \frac{1}{2}\sum_{k,l} \left(\frac{\partial^2 \alpha_{\rho\sigma}}{\partial Q_k \partial Q_l}\right)_0 Q_k Q_l \ldots \qquad (8.3)$$

Notice that (8.3) applies to each of the elements in the polarizability tensor (8.2). The first term in (8.3) is the value of the polarizability tensor element at equilibrium. *Q,* represents the normal coordinate of vibration, and for a non-linear molecule there are 3N-6 of them, where N is the number of nuclei. The first derivatives are responsible for the Raman intensities of the fundamental vibrational modes (3N-6 of them), while the second derivatives correspond to combinations and overtones in the Raman spectrum. This introduces the nomenclature: $\left(\alpha'_{\rho\sigma}\right)_k = \left(\frac{\partial \alpha_{\rho\sigma}}{\partial Q_k}\right)_0$. These derivatives form a new "derived

polarizability tensor" for each vibrational mode: $\alpha_k^{'}$. For each vibrational mode "k" the total tensor (including the equilibrium tensor element) is;

$$\left(\alpha_{\rho\sigma}\right)_k = \left(\alpha_{\rho\sigma}\right)_0 + \left(\alpha_{\rho\sigma}^{'}\right)_k Q_k \tag{8.4}$$

Within the harmonic approximation, the time dependence of the normal coordinates may be expressed by: $Q_k = Q_{k0}\cos\left(\omega_k t\right)$, because the incident electric field can be a simple plane wave: $E = E_0\cos\left(\omega_0 t\right)$. In both cases, we neglected the phase factors for simplicity. The corresponding induced dipole moment p, can now be written for each vibrational mode in terms of the polarizability tensors:

$$p = \alpha_0 E_0 \cos\left(\omega_0 t\right) + \alpha_k^{'} E_0 Q_{k0} \cos\left(\omega_k t\right)\cos\left(\omega_0 t\right) \tag{8.5}$$

Using the trigonometric identity for the product of cosines, we get three oscillating dipole components:

$$p = p\left(\omega_0\right) + p\left(\omega_0 - \omega_k\right) + p\left(\omega_0 + \omega_k\right) \tag{8.6}$$

The first term in (8.6) gives rise to Rayleigh scattering, the second to Stokes Raman scattering and the third to anti-Stokes Raman scattering. Notably, the tensor α_0 or $\alpha^{Rayleigh}$ scattering tensor is always different from zero; in other words, Rayleigh scattering is *always* observed. The emission from any of the other two induced dipole requires that at least one of the elements in the derived polarizability tensor or Raman tensor ($\alpha_k^{'}$ or α^{Raman}) would differ from zero.

There is another important development that arises from the phase factor that we neglected in the treatment:

$$Q_k = Q_{k0}\cos\left(\omega_k t + \delta_k\right) \tag{8.7}$$

It can now be seen from (8.4) that the Rayleigh scattering is in phase with the incident electromagnetic wave. However, for an ensemble of molecules, the Raman scattering allows for an arbitrary phase relationship with the incident radiation. The latter is a consequence of fixing the system of coordinates on each

molecule whose orientations are not fixed and the δ_k are different for different molecules. Therefore, the Raman scattering of the ensemble is incoherent, i.e., each molecule is an emitter independent of its spatial position.

The most challenging aspect of these computations is how to explain the activity of the Raman vibrational frequencies. For this, it is necessary to recourse to the quantum mechanical treatment of the interacting molecule in Raman scattering, although the electromagnetic wave is treated classically. Because the nuclei are much heavier than the electrons, in a first approximation it is assumed that they are at rest. This enables us to later introduce their motion as a perturbation. This approach is the termed the adiabatic approximation, and allows to separate the nuclear from the electronic motions[8]. When solving the Schrödinger, the perturbation will be part of the potential energy operator. For a given electronic state, one can solve the vibrational wave equation with a Hamiltonian containing the kinetic operator of the nuclei and a potential energy operator. Assuming simple harmonic motion of the nuclei about their equilibrium positions, the solutions of the QM problem of the harmonic oscillator can be used, and the wavefunction can be written as a product of monovibrational wavefunctions, each a function of one normal coordinate:

$$\psi_{Vibrational} = \psi_1\left(Q_1\right)\psi_2(Q_2)...\psi_k(Q_k)...= \prod_k \psi_k \tag{8.8}$$

The Hamiltonian of fundamental vibrational modes is a sum of harmonic oscillators Hamiltonians:

$$\hat{H} = \frac{1}{2}\hbar \sum_{k=1}^{3N-6}\left[-\frac{\partial^2}{\partial Q^2}+Q_k^2\right]\omega_k \tag{8.9}$$

The total energy of the molecule will depend on the quantum numbers of each of the harmonic oscillators: $v_k = 0,1,2,...,$

$$E_{vibrational} = \sum_k \hbar\omega_k\left(v_k +\frac{1}{2}\right) \tag{8.10}$$

One of most important properties of the vibrational states is that they can be classified according to their symmetry properties, and this will allow a simple solution for the determination of the Raman active vibrations (or infrared active modes); the results will be the vibrational selection rules. Vibrational transitions are between two vibrational states connected by an operator. Let $\psi_k \, and \, \psi_l$ be the vibrational eigenfunctions of a lower and an upper vibrational state (non-degenerate). Then the transition associated with an electric dipole moment operator $\hat{p}$ will be allowed if and only if the matrix element; $p_{kl} = \int \psi_l^* \hat{p} \psi_k dv$, is different from zero. This is the general selection rule for the dipole moment transitions. For a given equilibrium configuration each vibrational state and the operator belong to an irreproducible representation of the molecular symmetry point group. Therefore, the vibrational transition between non-degenerate states is allowed if the triple product contains the totally symmetric representation of the point group, otherwise is forbidden. In terms of the symmetry species the selection rule can be formulated using the direct product:

$$\Gamma(\psi_l) \times \Gamma(\psi_k) \times \Gamma(\hat{p}) = totally \; symetric \tag{8.11}$$

For practical applications, the reduction of direct products can be read directly from character tables as infrared activity and Raman activity[7]. In other words, the irreducible representation for transition dipoles $\Gamma(\mu)$ components in the infrared spectrum and the transition polarizability components $\Gamma(\alpha)$ are all given in the character tables. For instance, for the D$_{2h}$ point group we can see in the corresponding character table,

$\Gamma(\mu) = B_{1u} + B_{2u} + B_{3u}$, and

$\Gamma(\alpha) = 3A_g + B_{1g} + B_{2g} + B_{3g}$

Notice that if the character tables are used as given, the implicit assumption is that there is no preferred molecular orientation in space, (i.e., random molecular orientation). A fixed molecular orientation at the metal surface (as could come about in SERS), will be sensitive to the state of polarization (direction of the electric field vector in space) of the incident electromagnetic

radiation. This gives rise to the "surface selection rules" [9], which are comparable to the situation encounters in solid state for crystal structures[10]. The surface selection rules will be discussed later for specific applications. In a common Raman scattering one uses a monochromatic radiation from a laser source, an essentially non-divergent beam completely characterized by its frequency, its polarization, its direction of the propagation vector and the irradiance. The polarization properties of elastic and inelastic scattering for different geometries are fully developed in Raman books and the results collected in very useful tables[4,10].

Using the quantum mechanical machinery (second order perturbation theory), one can get the expressions for the first order transition electric dipole moment (analogous to (8.1)), and the corresponding transition polarizability components for Rayleigh and Raman scattering[4].

A simplified form of the transition polarizability components is;

$$\left(\alpha_{\rho\sigma}\right)_{kl} = \frac{1}{\hbar} \sum_{r \neq k, l} \left\{ \frac{\langle l|\hat{p}_{\rho}|r\rangle\langle r|\hat{p}_{\sigma}|k\rangle}{\omega_{rk} - \omega_0 - i\gamma_r} + \frac{\langle l|\hat{p}_{\sigma}|r\rangle\langle r|\hat{p}_{\rho}|k\rangle}{\omega_{rl} + \omega_0 + i\gamma_r} \right\} \tag{8.12}$$

Where $\omega_{rk} = \omega_r - \omega_k$, and r – is an intermediate state.

When the intermediate state is larger than ω_k , but is not in resonance with any of the electronic states of the molecular system, we have the normal Raman scattering (RS). However, when the intermediate state is in resonance with an electronic state, the physical phenomenon is called resonance Raman scattering (RRS)[11].

It can be seen from the expressions of the transition polarizability components (or derived polarizability tensor) that the $\left(\alpha_{\rho\sigma}\right)_{kl}$ or $\left(\frac{\partial \alpha_{\rho\sigma}}{\partial Q_k}\right)_0$ (in the classical approach) are extremely sensitive functions of the electron density (i.e., the equilibrium polarizability is a volume) of the molecule. In other words, these functions act as a 'sensor' for intramolecular and intermolecular interactions. Any perturbation of the molecular electronic density will result in changes of the

vibrational frequencies (due to changes in the potential energy operator of the vibrational Hamiltonian) and the intensities. Changes in the equilibrium configuration may completely change the spectral pattern due to broken symmetries.

In all SERS experiments, the interaction of the metallic nanostructure and the target molecule is a 'necessary condition' for the observation of plasmon enhanced scattering. The 'necessary condition' refers to the molecule being under the influence the local field of the nanostructure, i.e., there is molecule-plasmon coupling. As it known from surface chemistry, there is a broad range of electronic interactions that will affect the transition polarizability components. At one end is the chemisorption, or complex formation, at the surface of the nanostructure. This produces a very different SERS spectra when compared with that of the molecule in a given phase (gas, liquid or solid), whichever is used as a reference. A molecule in the near field of a nanostructure that is not forming a chemical bond at the surface, may show minor changes in frequency and intensity due to the physical interactions with the nanostructure. All of these observed changes in SERS experiments are encompassed under the generic term of "chemical effects", "chemical contributions *to* SERS. It should be pointed out that, in addition to these changes due to electronic interactions, there are two important factors that may determine the observed SERS spectra. The first is that the dispersion of transition polarizability components, i.e., $\alpha_{\rho\sigma}(\omega)$ is a function of the incident radiation and the observed intensity pattern in the SERS spectra could be that of pre-resonance or in resonance with the excitation frequency. The latter will be, of course, RRS. The most studied of these cases is that of excitation in resonance with a charge transfer electronic transition.

The second factor that can be used to determine observed SERS spectra is the use of polarized light for the incident radiation, and the use of analysers for the scattered light. This provides polarized spectra with a wealth of information on molecular orientation, and in the case of SERS, information about the directionality of the plasmon resonances. There are a number of factors that may alter the observed SERS spectra, particularly when working in ultrasensitive

chemical analysis or single molecule detection that are the object of active discussion in the literature[12].

What follows is an illustration of the computational approach to obtain the vibrational spectra and the effect of aggregation (alanates, section B), surface-enhanced vibrational spectra in the Raman (SERS) in section C, and in the infrared (SEIRA) in section D. These are three selected examples taken from my extensive work on the subject during my doctoral studies.

B. Materials for Hydrogen Storage

During the development of this dissertation, a large number of molecular structures were calculated in tandem with the modeling of nanostructures. To illustrate some of this effort and the corresponding computational machinery used, we include here an example of the quantum mechanical computational work where the computational work of clusters is the important part of the modeling[13]. Hydrogen-based fuel cells are seen as a viable alternative to industrial society's reliance on oil, while at the same time minimizing pollution and global warming. Although high cost has been an impediment to market penetration of this technology, hydrogen sources are under extensive investigation for viability in fuel cells. Hydrogen is attractive as a fuel due to the clean combustion with air with very a high amount of energy delivered per unit of mass. The main issues with hydrogen as a fuel source are in terms of storage and safety, as very high pressures are needed to reduce hydrogen to a solid form[14]. Due to the need for safe and efficient storage of hydrogen, the use of co[8.B]mplex metal hydrides in hydrogen storage applications is becoming more attractive. With increased interest in hydrogen storing materials for applications such as fuel cells, improvements must be made on current technology to allow for compact, lightweight, and low-cost hydrogen production, while avoiding the difficulties associated with compressed or liquid hydrogen.

Complex metal hydrides, with the form ABH_4, where A is one of the alkali metals, and B is a group III atom, have been widely studied in solution as proton acceptors in organic chemistry applications. The first synthesized was $LiAlH_4$ in 1947 by Schlesinger[15], followed by other variations. Their vibrational spectra in a variety of solvents have been reported [16]. The alanate's structure and synthesis have been studied by a variety of techniques. Although the energetics, spectra, and reactivities of the complex metal hydrides are well known in solution, only recently has work been done on these materials in the solid state. Badanovic and Schwickardi[17] showed the potential use of the $NaAlH_4$ material having a

---

[8.B] The work in this section, 8.B, is the outcome of joint research with M. D. Halls, G. A. Nazri, and R. F. Aroca.

reversible absorption and desorption pathways for hydrogen through the use of a Ti catalyst. Considerable effort has been made to improve efficiency of the process through the use of techniques such as ball milling[18] in combination with differing additives[19]. The potential for $NaAlH_4$ for this use has also caused it to be studied structurally through X-ray diffraction through the decomposition stages[20], and as well theoretical studies of the crystalline structure[21].

The currently accepted process involves one intermediate phase along the absorption/desorption pathway, in the form of Na_3AlH_6. The reaction is [22]:

$$NaAlH_4 \Leftrightarrow \frac{1}{3}Na_3AlH_6 + \frac{2}{3}Al + H_2 \Leftrightarrow NaH + Al + \frac{3}{2}H_2 \qquad (8.13)$$
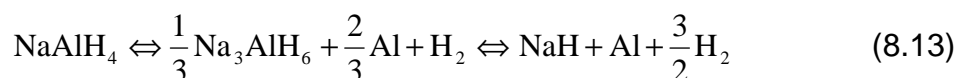
This represents a theoretical 5.6% capacity of hydrogen by mass.

Quantum chemical computations for each stage in the process can reveal structural and thermodynamic information necessary to properly characterize and improve the use of complex metal hydrides for the storage of hydrogen. Using infrared and Raman spectroscopy, the vibrational signature of the complex can be well characterized, which will further aid identification of the products and intermediate phases. A well understood vibrational fingerprint of $NaAlH_4$ material can be used as a probe for further absorption/desorption studies.

Sodium and lithium aluminum hydrides were studied previously using neutron scattering[23], revealing strong librational structure down to 92 cm^{-1}. Additionally, Raman and infrared spectra has been recorded for various AlH_4^- salts[16]. Raman spectra of librational modes in crystals have been studied in similar crystalline systems[24]. Strong Raman-active librational modes are expected due to the large polarizability change occurring from the highly dipolar $NaAlH_4$ monomers moving in the extended lattice.

Shirk and Shriver[16] studied infrared and Raman of $NaAlH_4$ in both the solid phase and in ether solutions. The lower limit to the frequency range of their Raman study was approximately 450 cm^{-1}, and a tentative assignments for the vibrational spectra in solution was offered, but difficulties were found in the solid phase due to band broadening. The lower frequency region was well studied by Temme and Waddington, by inelastic neutron scattering and FT-IR[23]. These

measurements cover a frequency range from approximately 50 cm^{-1} to 1000 cm^{-1}, and assignments for the librational and torsional modes in that region of the spectrum were made. There is still a need for reliable assignment over the complete frequency range to guide *in situ* measurements during the decomposition process of metal hydrides.

In the current work, characteristic band assignments of the observed Raman scattering spectra are made on the basis of cluster based density functional calculations and comparison to previous measurements by Raman and neutron scattering[16,23]. A cluster of molecules is built up to provide a description of the intermolecular interactions and how they modify the vibrational signature. The Raman spectra of the larger clusters can then be analyzed in reference to the spectrum of the monomer. Additionally, changes in structure and energyies of the monomer are examined in detail to help identifying trends in the cluster and solid.

Raman spectra were obtained with a Renishaw Research Raman Microscopy System RM2000 equipped with a Leica microscope (DMLM series). The excitation laser line used for the measurement was 633 nm and the laser power was of the order of 1 mW at the surface of the sample.

Sodium aluminum hydride was purified by re-crystallizing commercial $NaAlH_4$. $NaAlH_4$ was dissolved in THF and filtered through a glass frit. The filtered material was concentrated in rotaryvap under vacuum. The pure $NaAlH_4$ was precipitated by adding pentane to the concentrated $NaAlH_4$ in THF. The fine precipitate was washed with excess pentane and dried at 25 ^{o}C under vacuum.

The purified $NaAlH_4$ was also studied by X-ray diffraction in an environmental sample holder to protect the sample form exposure to air. The crystal structures were studied by powder x-ray diffraction using a Siemens 5000 x-ray goniometer equipped with CuKα radiation, operating at 40kV anodic voltage and 30mA current. The patterns were recorded over a range of 2θ angles from 5 to 85 degrees, and compared with the x-ray powder files for phase identification. All peaks were indexed to the tetragonal structure with lattice parameters of a=5.03 ^{o}A, c=11.38 ^{o}A with an excellent fit to the space group C^6_{4h} ($I4_1/a$).

Computations were performed using the Gaussian 98 suite of programs[25]. Density function theory calculations were carried out with using the hybrid functional B3-LYP, corresponding to Becke's 3-parameter exchange functional[26] along with the correlation functional developed by Lee, Yang and Parr [27]. The basis set used was a double split-valence gaussian basis set[28,29], augmented by one set of diffuse functions on heavy atoms, and also by one set of polarization functions on all atoms, or 6-31+g(d,p). Geometrical convergence was obtained with at least a tight criterion, without symmetry restrictions imposed. For comparison with experimental spectra, simulated Raman spectra were created with a gaussian bandshape. For all cluster sizes, zero point corrected energies and optimized geometrical parameters were obtained, in addition to numerical Raman intensities for each normal mode.

To obtain approximate vibrational frequencies and Raman intensities, including neighbor interactions, clusters of $NaAlH_4$ were generated by successively adding additional monomers to geometrically optimized systems. The optimized structure for a cluster of eight monomers is shown in Figure 8.1.
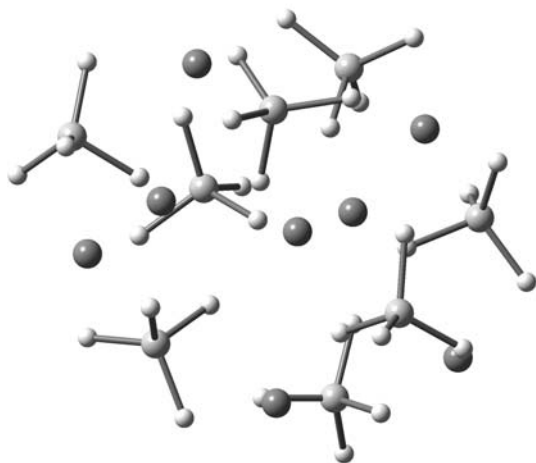
Figure 8.1. Eight monomer cluster of $NaAlH_4$ optimzed at the B3-LYP/6-31+G(d,p) level of theory.

The Raman spectrum of $NaAlH_4$ excited at 633 nm is shown in Figure 8.2. The spectrum can be broken up into three spectral regions, corresponding to different types of vibrational modes. The first is a high frequency region,

consisting of a group of bands between 1500 cm^{-1} and 1900 cm^{-1}, corresponding to the Al-H stretching modes of the $NaAlH_4$ monomer. Secondly, a middle region comprised of the various bending modes, which runs from 600 cm^{-1} to 900 cm^{-1}. Finally, a low frequency region which is made up of the various librational and torsional modes exists below 600 cm^{-1}
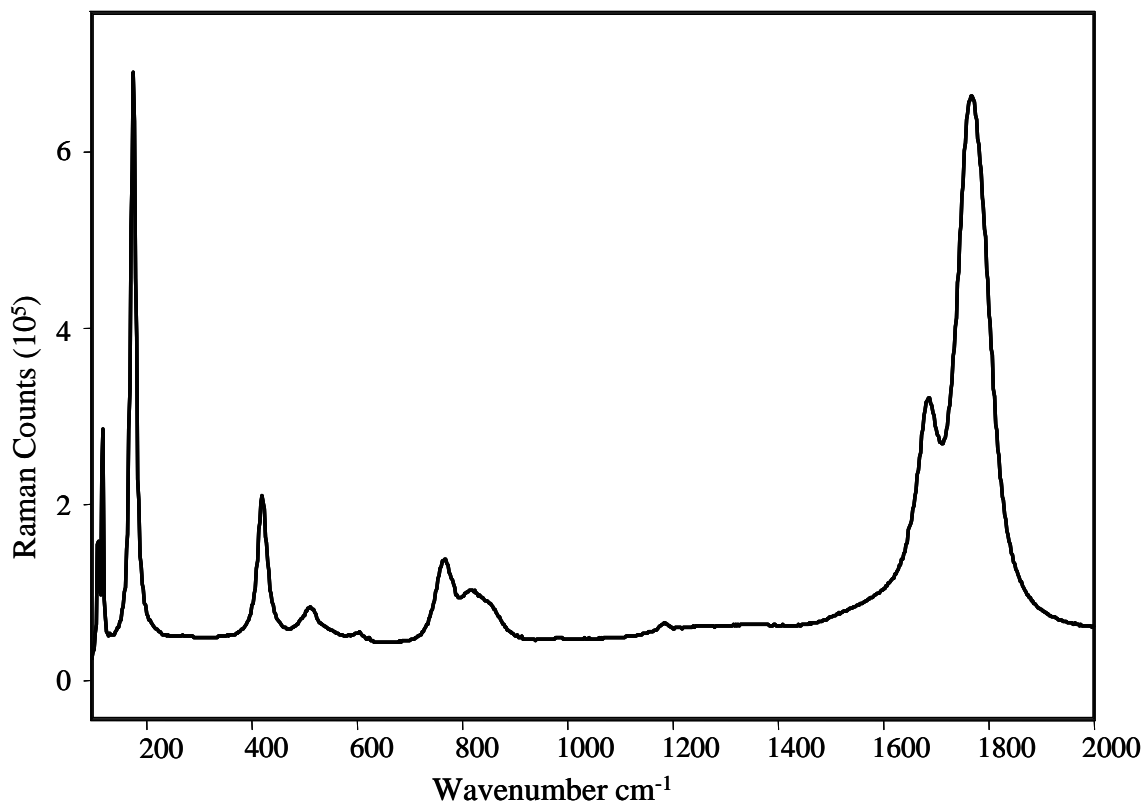
Figure 8.2. Raman scattering of $NaAlH_4$ using the 633 nm excitation line.

Notable are the Al-H symmetric and anti-symmetric peaks at 1769 cm^{-1} and 1680 cm^{-1} respectively. Also prominent are the peaks at 174 cm^{-1} and 117 cm^{-1}, with a shoulder appearing at 108 cm^{-1}. The higher frequency spectra is in good agreement with previously published Raman investigations of metal hydrides[16], although this study did not probe below 450 cm^{-1}. However, neutron scattering has shown strong librational activity in this region, and our findings are in good agreement, excepting that some frequencies observed by neutron scattering will be infrared active only.

Computation of structures and frequencies for a single monomer of sodium aluminum hydride is similar to that of an earlier study of LiAlH$_4$[30], finding three separate isomers of NaAlH$_4$. The lowest energy is a bidentate structure with a C$_{2V}$ symmetry. A tridentate form with an energy of 0.02 eV above the bidentate with a C$_{3V}$ was also found.   An energetic monodentate was found to have an enthalpy 0.56 eV above that of the bidentate, and had one doubly degenerate negative frequency, due to the C$_{3V}$ symmetry. Symmetry restrictions were placed upon the monodentate during geometry optimization to obtain this optimized form, and further optimizing without symmetry caused collapse to the more stable bidentate. The geometrical parameters and relative energies of all three configurations of NaAlH$_4$ are given in Table 8.1.

Bond Lengths (Å)	Bidentate	Tridentate	Monodentate
AlH1	1.69	1.66	1.71
AlH2	1.69	1.66	1.61
AlH3	1.60	1.66	1.61
AlH4	1.60	1.58	1.61
NaH1	2.10	2.30	1.86
NaH2	2.10	2.30	4.22
NaH3	2.68	2.30	4.22
NaH4	2.68	4.17	4.22
Al-Na	2.81	2.58	3.57
Relative Energy (eV)	0.00	0.02	0.56

Table 8.1. Geometric parameters and relative energies for monomers of NaAlH$_4$, in bidentate, tridentate, and monodentate configurations. (Lower numbered hydrogen are those bonded to Na in all three cases.)

The Al-H bond lengths for the different isomers of NaAlH$_4$ can be compared to the calculated results for LiAlH$_4$(18) as the alkali atom will not have a strong effect. The same trend in bond lengths occurs for both species, with the longest Al-H bond length occurring in the monodentate isomer, and the shortest in the tridentate. Numerically, they are very similar, with the monodentate bond

length for LiAlH$_4$ to be 1.62 Å with a BP86 density functional, compared to 1.61 Å in this work. Similarly, for the bidentate, the free Al-H bond length is 1.603 Å for the lithium aluminum hydride, and 1.60 Å for the sodium. The reported value of 1.592 Å for the LiAlH$_4$ is also very close to this value of 1.58 Å. This very similar structural feature also implies, given that the masses of these atoms are the same, that the vibrational frequencies of the Al-H stretching bands will be also very close for these two molecules.

Clusters of up to eight molecules in size were calculated. With an increase in cluster size, the vibrational spectra became increasingly complex due to splitting of individual bands. However, with larger modeled size clusters, coalescence of the spectrum occurred with overlapping multiple bands, increasing agreement with the observed Raman spectra. Figures 8.3, 8.4 and 8.5 show the computed high, middle, and low frequency regions, respectively, of the simulated Raman spectra and relative intensities for one to eight molecules, and compared to the measured Raman from a 633 nm excitation line.
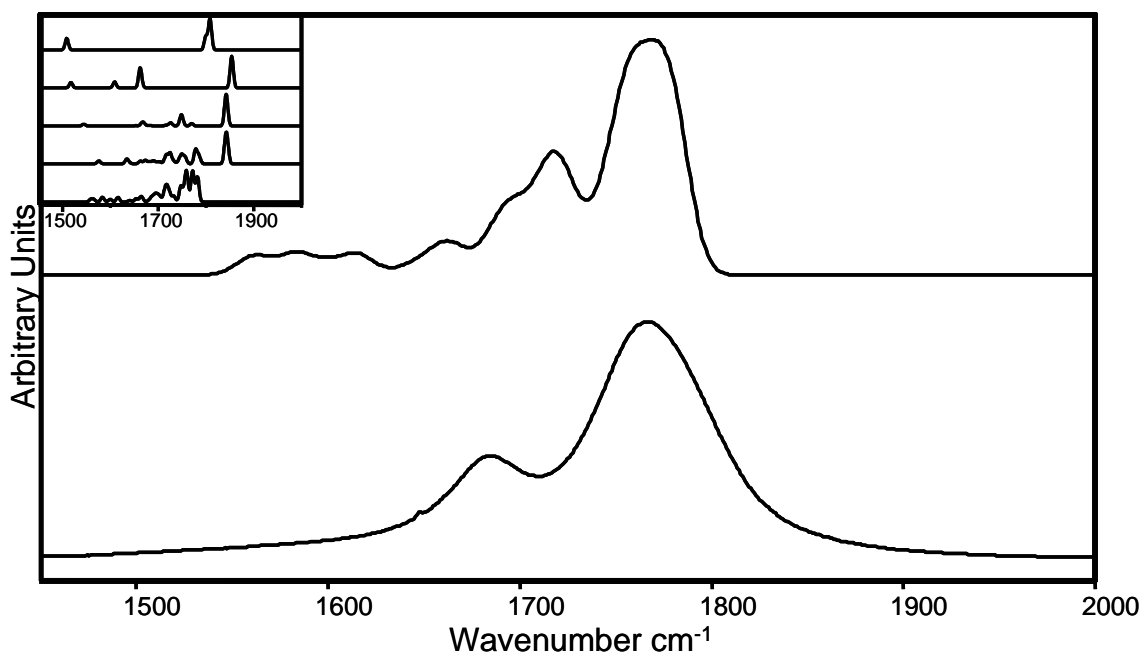
Figure 8.3. Simulated and experimental Raman spectra for the high frequency region of NaAlH$_4$ using the largest cluster model and the 633nm laser line, top and bottom trace respectively. Inset: Calculated high-frequency Raman for the one, two, four, six, and eight monomer models.
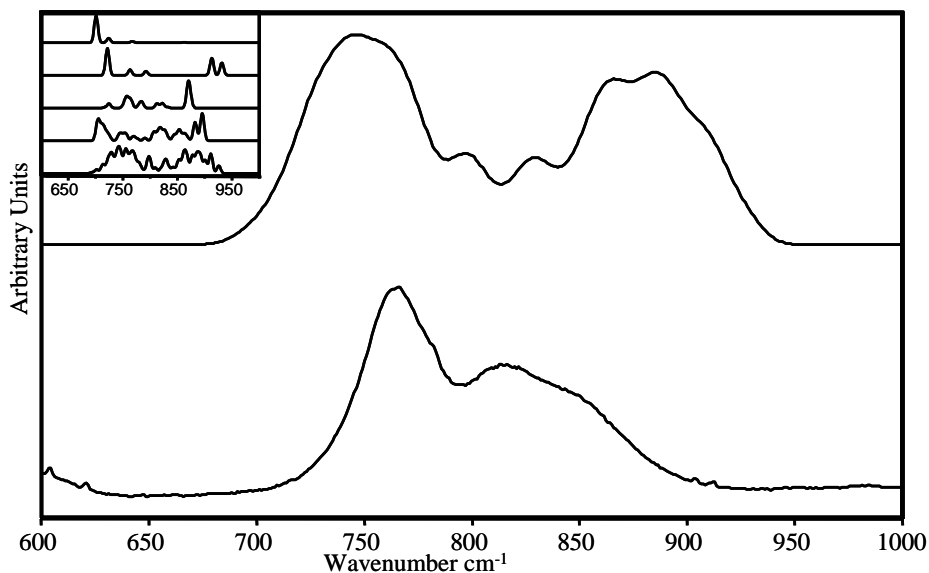
Figure 8.4. Simulated and experimental Raman spectra for the middle frequency region of $NaAlH_4$ using the largest cluster model and the 633nm laser line, top and bottom trace respectively. Inset: Calculated mid-frequency Raman for the one, two, four, six, and eight monomer models.
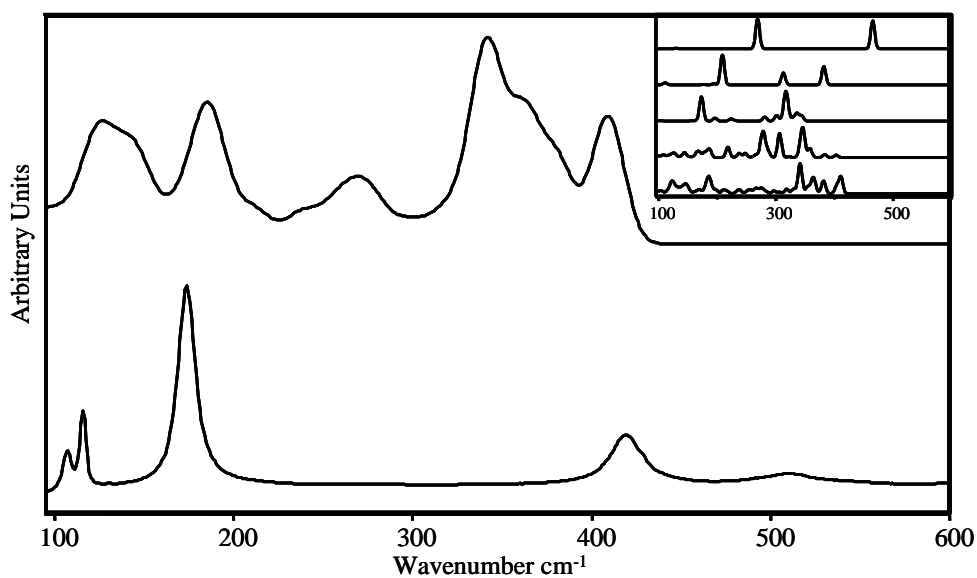
Figure 8.5. Simulated and experimental Raman spectra for the low frequency region of $NaAlH_4$ using the largest cluster model and the 633nm laser line, top and bottom trace respectively. Inset: Calculated low-frequency Raman for the one, two, four, six, and eight monomer models.

For the largest cluster, boundary conditions were applied to simulate the solid, by constraining the cluster surface hydrogens. The boundary conditions

199

bring the finite sized cluster much closer in result to the vibrational signature of the bulk. Additionally, frequency convergence is strong with the largest cluster, with bands not shifting more than 3 cm^{-1} from 6 to 8 molecules, although many new bands appeared due to distortions. The internal vibrational modes can be assigned with the aid of the theoretical results, with results summarized in Table 8.2.

Observed[a] (cm^{-1})	Relative Intensity	B3-LYP/6-31+G(d,p) Frequency[b] (cm^{-1})	Relative Intensity	Previous Raman[c] (cm^{-1})	Neutron Scattering[d] (cm^{-1})	Band Assignments
1769.2	1.00	1767.6	1.000	1763	1790	Al-H Symmetric Stretch
1680.5	0.34	1714.1	0.490	1686		Al-H Anti-Symmetric Stretch
847.5	0.06	882.9	0.051		861	Al-H-Na Symmetric Bend.
811.8	0.07	809.2	0.019	824	799	Al-H-Na Bending
764.9	0.15	746.0	0.062	767	764	Al-H-Na Bending
510.7	0.06	409.2	0.006		494	Torsion
419.4	0.27	350.5	0.011			Torsion
174.1	1.10	185.4	0.007		178	Collective Vibration
116.2	0.40	144.7	0.003			Collective Vibration
107.5	0.18	126.72	0.006			Collective Vibration

Table 8.2:. Wavenumbers and vibrational assignments of observed Raman bands of NaAlH$_4$. [a] 633 nm excitation line. [b] Harmonic frequencies scaled uniformly by 0.965. [c] From Shirk *et al.* [Ref 3]. [d] From Temme *et al.* [Ref 10].

The high frequency region, shown in Figure 8.3, shows excellent agreement between the largest cluster and the experimental spectrum. This region is comprised of the symmetric and antisymmetric stretching modes of Al-H at 1769 cm^{-1} and 1680 cm^{-1}. Coalescence of the calculated spectra towards the formation of similar bands to those observed is very clear. This region agrees

very well with the data published previously, although the band at 1680 cm^{-1} was not resolved in neutron scattering.

The Raman active frequencies in the middle frequency region can be characterized as Al-H-Na bending type modes, with the peaks appearing at 811 cm^{-1} and 764 cm^{-1} with a shoulder at 847 cm^{-1}. This calculated spectrum for the largest cluster corresponds well to the observed, with some difference in relative intensities.

The low frequency is quite rich with torsional and librational Raman active bands. The simulated spectrum can be compared to the experimental spectrum in this region to corroborate the assignments of observed bands. It is reasonable to expect that agreement in this spectral region may be worse than at higher wavenumbers since the vibrations here are characterized by long-range collective modes that may be poorly represented in a truncated cluster. The weak modes at 518 cm^{-1} and 426 cm^{-1} correspond well with torsional modes observed previously[23], which indicate that the AlH$_4^-$ ions are strongly locked into their lattice due to their high frequency. These torsional modes are computed to be at Raman active 216 cm^{-1} for two molecules, and between 350 cm^{-1} and 400 cm^{-1} for the larger model systems, illustrating an improvement in agreement with increasing cluster size. The lattice vibrations reported by neutron scattering with a peak at 178 cm^{-1} are in strong agreement with the observed Raman band at 174 cm^{-1}. The small peaks computed in that region, from 120 cm^{-1} to 200 cm^{-1} are collective, librational-type motions, with the most symmetric at 185 cm^{-1}.

On the basis of these assignments, the Raman spectrum of NaAlH$_4$ can be used to track changes in structure and concentration through non-destructive methods. The Al-H stretching peaks, which are easily observed at low laser power, will drop in intensity during the formation of the intermediate Na$_3$AlH$_6$, for which the Al-H stetching modes could be observed at a lower frequency due to the increased interaction with Na atoms.. The intensity and frequency of the librational bands, especially the observed band at 174 cm^{-1} are strongly dependant on the local environment, and during sample heating give an indication of the lattice strength.

Raman spectra of $NaAlH_4$, an important material for solid hydrogen storage applications, was taken with a 633 nm excitation line. Complete band assignments down to the librational level were made, corroborated by previously reported assignments, providing a consistent interpretation of the vibrational activity in the solid state. Characterizations were made of the basis of cluster based density functional theory calculations. In agreement with previous theoretical studies on similar systems, the bidentate structure of $NaAlH_4$ monomer is found to be the most stable, with a slightly more energetic tridentate structure, and a monodentate transition structure at a very high relative energy. With increasing cluster sizes, the computational results progressively improve in agreement with the experimentally recorded vibrational and librational spectra of $NaAlH_4$.

C. SERS Study Case

In surface enhanced spectroscopy, while it is the nanoparticle which provides the enhancement, it is the molecular system, modified by its interactions with the nanoparticle, which controls the actual spectrum that is observed, in addition to polarizations effects. To provide a clear example of some of the differences that can arise through SERS, an example of the chemical effects on a spectra are presented for two small molecules. The optimized geometries, and minimum energies for the group state are first calculated, and then the vibrational frequencies and Raman intensities. The chemical effect is modelled by examination of the silver salt of each of the two molecules, mimicking chemical adsorption onto the enhancing substrate.

The molecules: syringic acid and p-coumaric acid are shown in figure 8.6. These molecules were selected as they have similar structures, as they both have a phenyl ring as well as a OH group. The active site for adsorption to silver, however, is the carboxyl group, or COOH group. As the carboxyl group is directly off the ring in the case of syringic acid, and separated from the ring by two carbon atoms in p-coumaric, there is a natural expectation that the strongest Raman bands, corresponding to the ring breathing modes, will be modulated by the interaction with silver in different ways in the two cases. Syringic acid has a total of 24 atoms ($C_9O_5H_{10}$), for a total of 66 vibrational modes, while p-coumaric acid has 20 atoms ($C_9O_3H_8$) and 54 vibrational modes.
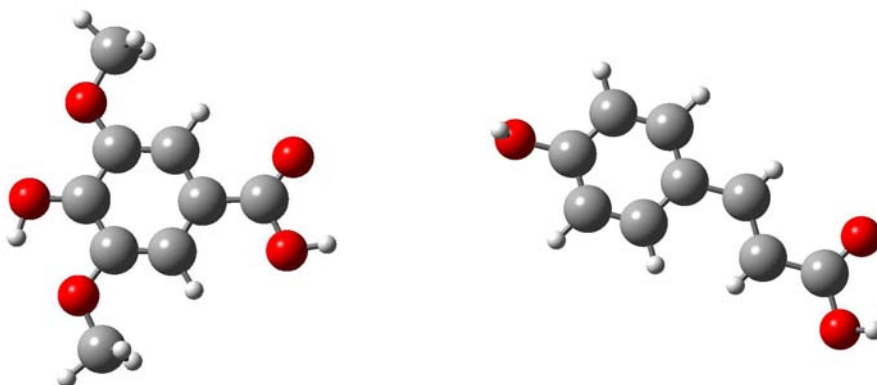
Figure 8.6: Syringic acid (left) and p-coumaric acid (right).

The molecules are first calculated using the Gaussian 03 suite of programs[31], at the B3LYP/6-311g(d,p) level of theory. Geometry optimization is done with tight convergence criteria without symmetry restrictions imposed. Harmonic frequencies and infrared and Raman intensities are taken, and scaled uniformly by a factor of 0.9669[32]. The calculated Raman bands are given a full width at half-maximum value of 5 cm^{-1}, and figure 8.7 presents the full Raman spectra for p-coumaric acid and syringic acid.
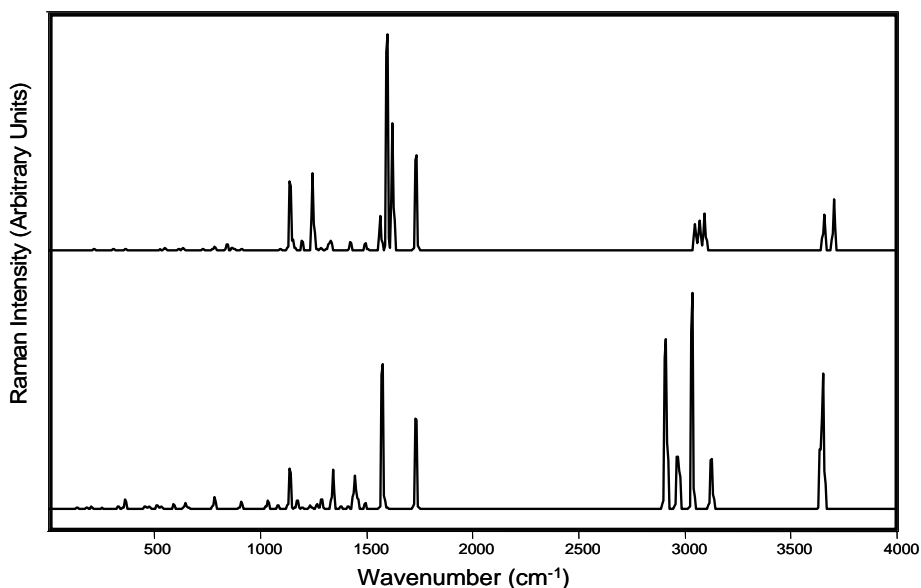
Figure 8.7: Calculated Raman spectra of: P-coumaric acid (top) and syringic acid (bottom).

Before the interaction of a silver atom and the molecule is examined, it is first necessary to have a good understanding of the spectra of the molecules. Starting with the highest frequency, each molecule has two O-H stretching modes, in the 3650 cm^{-1} region, followed by a set of C-H stretching modes centered around 3070 cm^{-1}. Although figure 8.7 has an arbitrary y axis so that the full spectrum in each case can be seen as clearly as possible, it is worthwhile noting that the C-H stretching modes for the two molecules are approximately equal in intensity, giving an idea of the scale difference. For the p-coumaric acid, the C-H modes are relatively weak, meaning that the rest of the spectrum of p-coumaric is quite a bit stronger than syringic acid. Syringic acid also has a group of modes centered at 2950 cm^{-1} corresponding to CH_3 stretching vibrations. Both

molecules also have a intense mode close to 1733 cm^{-1}, which is the C=O stretch in the COOH group. However, given the relative scale difference, this is quite a bit stronger in the p-coumaric case.

A character table for the fingerprint region (between 800 cm^{-}1 and 1800 cm^{-1}) two molecules is given in table 8.3, organized by frequency of the mode for syringic acid. Where possible, the table is organized so that vibrations of the same character are matched between the two molecules, rather than naively organizing both molecules by frequency. This causes some of the Raman frequencies for p-coumaric acid to be out of order, although the spectral differences between the molecule are clearer.

In the fingerprint region, both molecules have vibrational bands that the other does not due to the differences in structure. Syringic acid, for example, has a variety of C-H bending modes involving the CH$_3$ groups that p-coumaric does not have. The most intense bands observed in both molecules belong to the C=C stretching modes of the chain leading to the carboxyl group. Both molecules also have C-H bending modes with moderate intensity in the 1100 cm^{-1} range, although in the p-coumaric case one of them is coupled to a C-O stretching mode that causes a greater intensity.

Syringic Acid		P-Coumaric Acid		
Frequency (cm^{-1})	Raman Intensity (Å^4/AMU)	Frequency (cm^{-1})	Raman Intensity (Å^4/AMU)	Character
831.8	0.23	784.3	1.58	C-H wag
856.0	0.41	816.2	0.90	C-H wag
896.4	1.29	842.4	27.40	ip ring deformation with C-O stretch
		868.4	9.55	oop C-C bend with C-H wag
910.1	7.66			C-C stretch
		883.5	4.25	C-O stretch in carboxyl group
1083.6	3.38	912.2	2.15	C-H wag
		989.7	1.52	C-H wag
1033.8	10.45			O-CH3 stretch
1133.3	2.31			CH3 bending
1134.6	3.06			CH3 bending
		1090.8	5.09	C-H scissor
		1139.4	313.63	C-H bend and C-O stretch in carboxyl
1139.0	45.73	1154.3	45.55	C-H and O-H bend
1170.0	5.56	1159.1	4.11	C-H and O-H bend
1175.8	7.23	1196.8	40.94	C-H and O-H bend
1200.1	0.67			C-H and O-H bend
1236.6	3.41			C-H and O-H bend with ring deformation
		1247.7	354.09	C-H bend and C-C stretch
		1262.0	4.38	C-O stretch and C-H bend
1268.8	6.01			C-H and O-H bend
		1283.1	9.08	C-H bend
1289.3	11.47			C-H and O-H bend with C-O stretch
		1310.6	5.74	C-H bend and C-C stretch
		1326.3	39.44	C-H and O-H bend
		1335.0	23.08	C-H and O-H bend, and C-C stretch
1340.6	46.54			C-C stretch, C-O stretch, O-H bend
1378.2	2.27			Ring deformation and O-H bend
1411.8	3.31			CH3 umbrella and O-H bend
		1424.1	37.24	C-H and O-H bend, and C=C stretch
1439.2	6.52			CH3 umbrella and O-H bend
1442.5	17.90			CH3 bend
1444.0	16.41			CH3 bend
1445.6	2.59			CH3 bend with ring deformation
1456.0	7.43			CH3 bend
1457.9	6.60			CH3 bend
1493.9	6.22			C-O stretch and ring deformation
1574.7	174.32			C-O stretch and ring deformation
1594.7	1.35	1495.2	32.32	C-H bend and C=C stretch
		1566.4	156.77	O-H bend and C=C stretch
		1596.8	984.65	C=C stretch
		1623.7	582.60	C=C stretch
1732.2	109.15	1733.4	434.66	C=O stretch

Table 8.3: Character table of syringic and p-coumaric acid. Acronyms include ip: in-plane, and oop: out of plane.

To model chemical adsorption to a silver nanoparticle, it is assumed that these molecules will attach through the COOH group, the most chemically reactive site on both molecules. The structure is changed by the removal of the hydrogen atom, and the addition of a silver atom, making this group COOAg. The optimized structure for both molecules is shown in figure 8.8
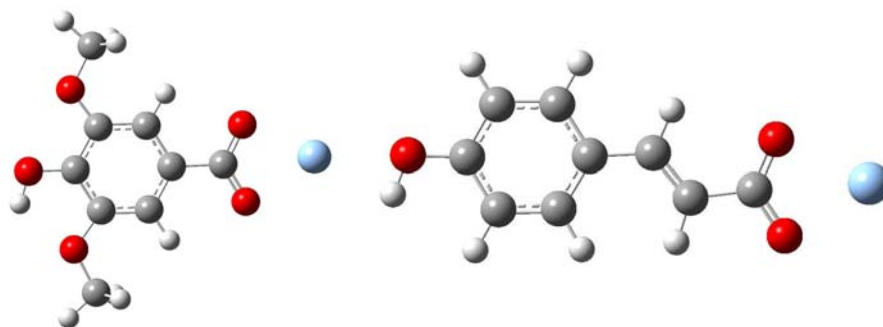
Figure 8.8: Structure of syringic acid (left) and p-coumaric (right).

The basis set used previously, 6-311g(d,p) is not implemented in Gaussian for silver, as the many electrons present would cause the calculation to become quite long. An effective core potential (ECP) is used to replace the chemically inert atoms, in this case the ECP developed by Hay and Wadt[33] at Los Alamos National Laboratories, called the Lan ECP, which includes relativistic effects. The double zeta basis set computed by the same authors for the outer orbitals (4d, 5s, and 5p) is also used, the Lanl2dz basis. The basis set for the molecule is split, so that the Lanl2dz+ECP is only used on the silver atom, and the rest of the molecule uses the same 6-311g(d,p) as before. In this way, changes in the spectra of the rest of the molecule can be attributed to electronic structure changes due to the presence of the silver atom, rather than basis set choice. The Raman spectra of syringic acid and syringic silver salt are presented in figure 8.9, where the spectra for the silver salt is offset vertically by +50 $Å^4$/amu.

There are a number of differences that are immediately apparent. First, the C=O stretching mode at 1732 cm^{-1} appears to have disappeared. Because the silver interacts with both oxygen atoms symmetrically, there is no true C=O

anymore, and portions of this band are mixed with other vibrations, including a ring deformation, making a stronger band at 1496 cm^{-1}. The electron density is shared more equally between the two oxygen atoms, and thus, the vibration is lowered in frequency. The band at 1139 cm^{-1} is also removed, as it corresponded to the O-H bending mode of the carboxyl group. Other changes include a weakening and red-shifting of the 1340 cm^{-1} vibration which included an O-H bend in the carboxyl group. New vibrations in the Raman spectrum of the salt include a moderately strong mode 400 cm^{-1}, corresponding to a distortion of the ring, a C-O$_2$ scissoring mode coupled with distortions of the ring at 748 cm^{-1}. Similar to the 748 cm^{-1} but also including C-C stretch for the carbon in the COOAg group is a new vibration at 938 cm^{-1}.
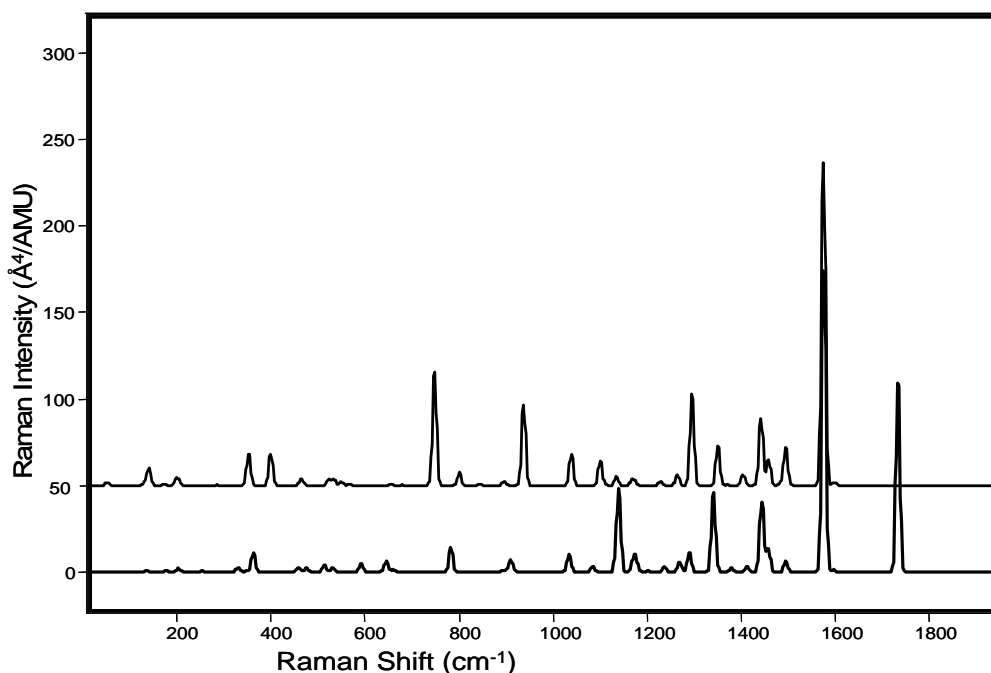
Figure 8.9: Raman spectra of syringic acid (bottom) and syringic silver salt (top). The spectrum of the syringic salt is offset for clarity.

In figure 8.10 the p-coumaric acid and its silver salt are shown. As the p-coumaric acid spectrum is dominated by a few intense modes, the differences are easier to see.   Again, all vibrations associated the O-H bending modes have

either changed or vanished. Interestingly, the strongest vibrations of the molecule, the C=C bands, are considerably stronger due to the presence of the silver, almost doubling in intensity, while they are still very clearly the same vibration, as they have not shifted significantly in frequency. The C-C stretching vibration at 1247 cm^{-1}, which is the stretching of the bond between the ring and the first carbon in the chain leading the COOH group, is red-shifted and strengthened.
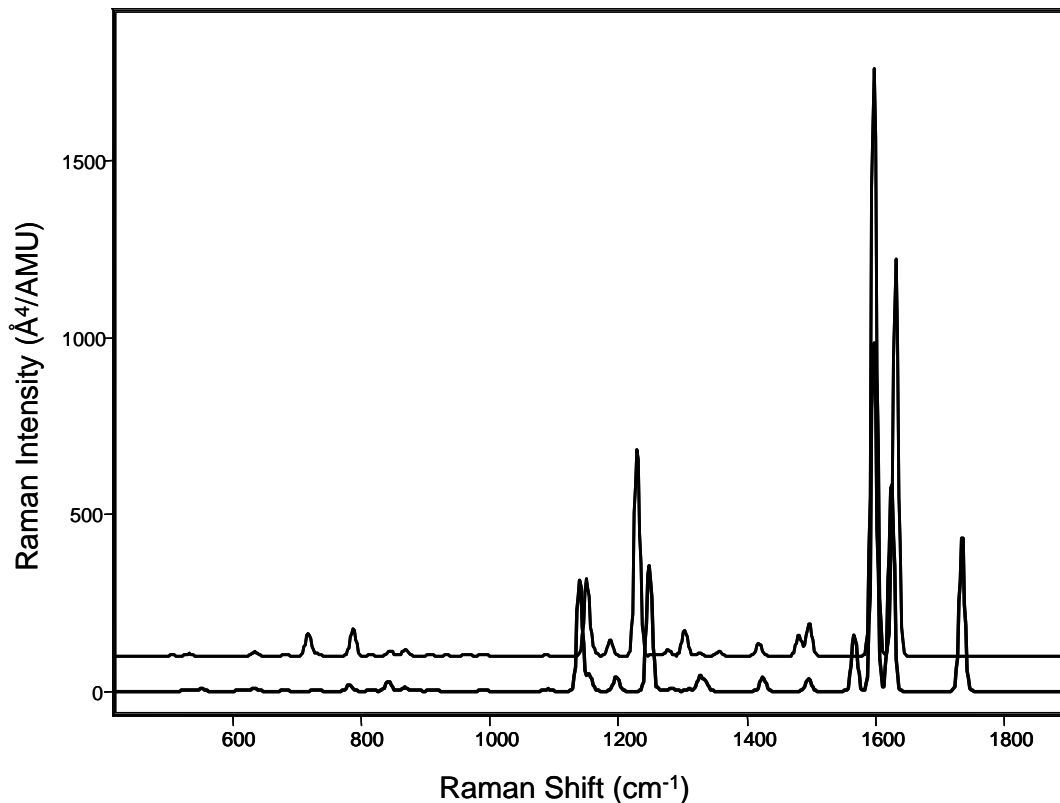
Figure 8.10: Raman spectra of p-coumaric acid (bottom) and p-coumaric silver salt (top). The spectrum of the syringic salt is offset for clarity.

The differences in the spectra between the molecule and the salt are highlighted by taking a difference, in this case defined as salt-acid, so that new bands in the salt are positive, and bands that were removed are negative. This is shown in figure 8.11. The differences in the spectra can be summarized as: 1) When the substitution of hydrogen for silver is close the ring, it is the ring modes that are most affected 2) When the substitution takes places farther from the

209

ring, it is in the atoms closest to the substitution point that undergo the most change.
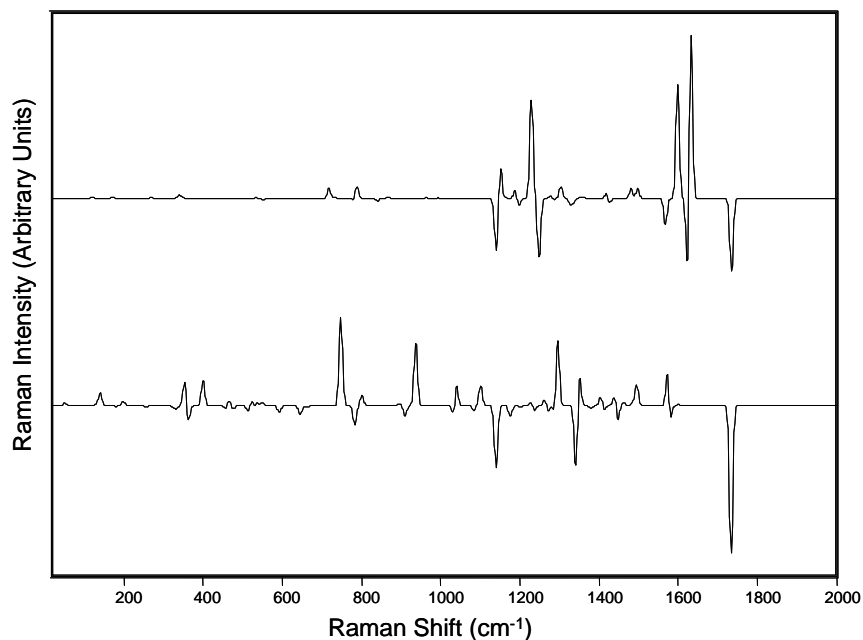
Figure 8.11: Difference spectra of p-coumaric (top) and syringic (bottom).

The study of syringic acid is in cooperation with Dr. E. Clavijo, who ran infrared, Raman and SERS spectra. This allows for comparison of the calculated Raman of syringic acid and the associated salt with experimental spectra of the molecule in solution as well as the SERS experiment. Tables 8.4 and 8.5 show the Raman and infrared experimental and computational results for the molecular and SERS cases.

Calculated	Intensity Å⁴/amu	Observed 514.5 nm	Ag-complex	Intensity Å⁴/amu	SERS	Vibrational assignment
137.1	1.15	151 (7)				Structural deformation
177.7	1.14	178 (14)				O-CH$_3$ bending
203.5	2.17	205 (7)				CH$_3$ torsion
255.2	0.72	224 (7)				O-CH$_3$ bending
285.0	0.39	295 (7)				CH$_3$ torsion
332.3	2.33	359 (18)	353.2	15.0	365 (10)	Structural deformation
363.0	11.15	383 (38)				Structural deformation
476.5	2.29	484 (5)				O-H bending
532.0	2.57	544 (8)	522.2	3.2	550 (13)	Ring deformation
592.3	5.04	585 (14)				O-H bending
645.2	6.48	687 (19)				O-C-OH scissoring
753.2	0.09	760 (1)	747.4	65.6	753(11)	C-H wag
782.7	14.15	803 (30)				Ring deformation
856.0	0.41	842 (2)				C-H wag
896.4	1.29	909 (10)				ip ring deformation with C-O stretch
910.1	7.66	937 (22)	936.6	46.2	949 (11)	C-C stretch
1033.8	10.45	1032 (37)	1038.7	18.6	1038 (12)	O-CH$_3$ stretch
1083.6	3.38	1102 (21)				C-H wag
1133.3	2.31	1115 (8)	1100.2	14.4	1109(15)	CH$_3$ bending
1134.6	3.06	1152 (7)				CH$_3$ bending
1139.0	45.73	1178 (31)				C-H bend
1170.0	5.56	1185 (19)				C-H bend
1175.8	7.23	1198 (66)				C-H bend
1236.6	3.41	1238 (6)				C-H and O-H bend with ring deformation
1289.3	11.47	1260 (13)				C-H and O-H bend with C-O stretch
1340.6	46.54	1322 (27)				C-C stretch, C-O stretch, O-H bend, and ring deformation
1378.2	2.27	1369 (24)				Ring deformation
1411.8	3.31	1388 (12)	1349.5	24.0	1389 (86)	CH$_3$ umbrella
1439.2	6.52	1424 (13)				CH$_3$ umbrella and O-H bend
1442.5	17.90	1443 (17)	1437.315	4.3498	1444(30)	CH$_3$ bend
1456.0	7.43	1454 (10)				CH$_3$ bend
1457.9	6.60	1469 (17)				CH$_3$ bend
1493.9	6.22	1520 (5)	1494.8	19.3	1523 (35)	C-O stretch and ring deformation
1574.7	174.3	1593 (81)	1574.2	187.2	1591 (100)	C-O stretch and ring deformation
1594.7	1.35	1658 (1)				C-H bend and C=C stretch
1732.2	109.15	1698 (100)				C=O stretch
2905.6	132.23	2834 (6)				C-H stretch in CH$_3$
2912.2	144.51	2859 (6)				C-H stretch in CH$_3$
2962.3	55.26	2937 (8)				C-H stretch in CH$_3$
2971.4	53.57	2944 (14)				C-H stretch in CH$_3$
3033.1	134.94	2974 (8)				C-H stretch in CH$_3$
3034.3	128.05	3036 (29)				C-H stretch in CH$_3$
3120.1	41.09	3099 (6)				C-H stretch
3127.7	48.08	3119 (2)				C-H stretch
3638.0	92.05	3378 (3)				O-H stretch

Table 8.4: Observed and calculated Raman wavenumbers (cm^{-1}) of syringic acid and its Ag-complex and SERS on Ag colloids. Experimental relative intensities are given in parenthesis.

IR (sol) cm^{-1}	IR (dioxano)	Calculated cm^{-1}	Intensity Km/mol	Vibrational assignment
	528 w	514	28.7	Ring deformation with O-H bend
	578 m	566	2.3	Ring deformation with C-H and O-H bend
	592 m	592	52.6	Ring deformation with O-H bend
	669 m	660	7.9	Ring Deformation
683 m	687 vs	645	107.1	O-C-OH scissoring
	769 s	753	64.2	C-H wag
	864 m	856	13.4	C-H wag
	908 m	910	13.7	Ring Deformation
1117 vs	1116 vs	1112	334.0	C-O Stretch and O-H bend
1181 s	1178 vs	1139	433.2	C-C stretch and O-H bend
1203 vs	1210 vs	1200	228.8	C-O stretch and O-H bend
	1247 s	1269	143.3	C-C stretch, O-H bend, and C-H bend
	1265 m	1237	39.7	C-C stretch, O-H bend, and C-H bend
	1320 s	1289	28.5	C-C stretch, O-H bend, and C-H bend
	1370 vs	1341	379.9	C-C stretch, O-H bend, and C-H bend
	1389 vs	1378	49.1	C-C stretch, O-H bend, and C-H bend
	1420 vs	1412	94.1	C-C stretch, O-H bend, and C-H bend
1464 m	1461 vs	1494	134.6	C-C stretch and C-H bend
1516 s	1523 s	1575	37.6	C-C stretch and C-H bend
1614 s	1620 s	1595	141.6	C-C stretch and C-H bend
1717 vs	1699 vs	1732	347.8	C=O stretch
	2942 m	2906	51.7	C-H stretch in CH_3
	2974 m	2912	45.6	C-H stretch in CH_3
	3030 m	3033	23.2	C-H stretch in CH_3
	3083 m	3034	21.3	C-H stretch in CH_3
3269 m	3239 s	3120	2.8	C-H stretch
3364 m	3374 s	3128	1.4	C-H stretch

Table 8.5: Observed and calculated infrared spectra of syringic acid in wavenumbers (cm^{-1}). : vs – very strong; s – strong; m – medium; w – weak , vw – very weak

The experimental SERS spectrum as tabulated in table 8.4 is much simpler than the spectrum of the molecule, and it consists of only a few bands. This is particularly striking for syringic acid as can be seen in figure 8.12.
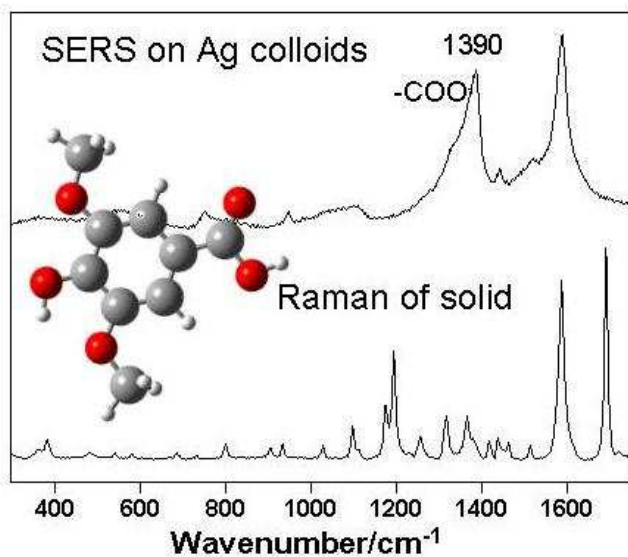
Figure 8.12. Raman and SERS spectra of syringic acid.

This is due to the directionality of the enhancement, for which the largest contribution is perpendicular to the nanoparticle surface. The calculations of the syringic acid salt with the y-axis placed from the center of the molecule to the Ag atom are done, so that the yy elements of the polarizability tensor should be the Raman terms that are most strongly enhanced. The calculated spectrum of the yy tensor elements is shown in figure 8.13, which is in good agreement with the tabulated values in table 8.4.
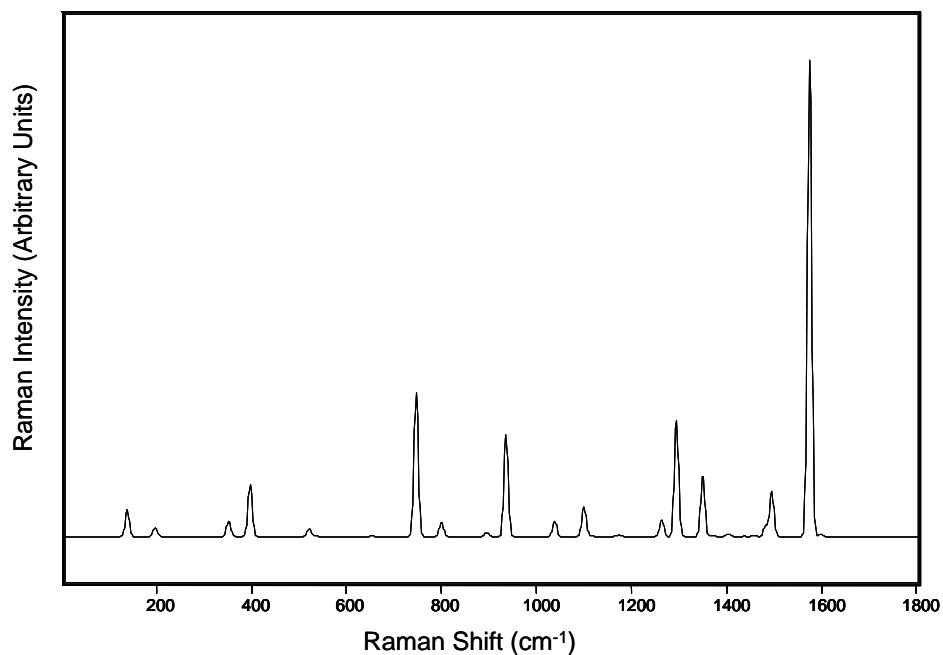
Figure 8.13: Raman intensity of yy elements of polarizability tensor of p-syringic acid.

The SERS spectra of the coumaric acid are also in good agreement with the modeled spectra using the silver complex. The SERS and the Raman are shown in figure 8.14
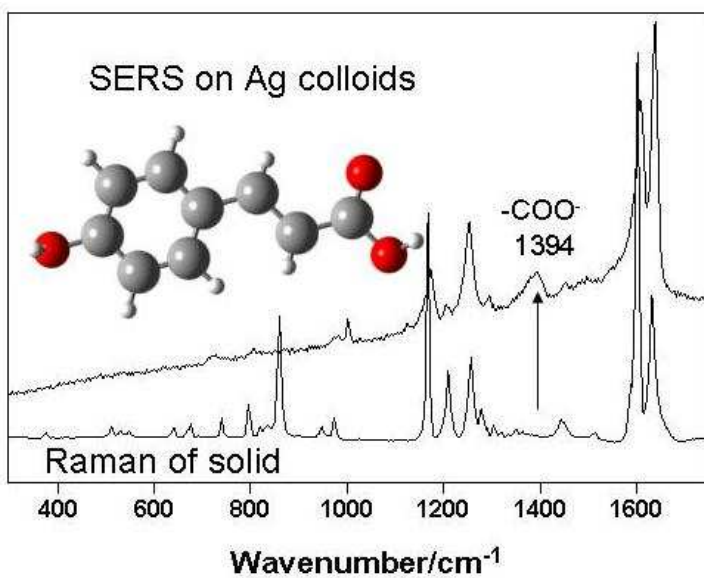
Figure 8.14: Raman and SERS spectra of coumaric acid.

D. PTCDA

The vibrational analysis of 3,4,9,10-perylene-tetracarboxylic-dianhydride (PTCDA) dye is presented here, as a supplement to the use of the molecule in SEIRA, detailed in chapter 7. PTCDA is a molecule with 38 atoms ($C_{24}H_8O_6$), and thus 108 (3N-6) vibrational degrees of freedom, although, as said before, the molecule has an inversion centre, causing only 46 of the vibrations to be infrared actve. Calculations were performed at the B3LYP/6-31g(d) level of theory, using the Gaussian 98 suite of programs[25]. Harmonic frequencies and infrared intensities were also taken, with the frequencies uniformly scaled by a factor of 0.9614[34]. Table 8.4 includes the scaled frequencies, infrared intensities, symmetry group, and character of the major infrared bands. 6 bands with relative intensities less than 0.001 are neglected.

The calculated spectrum is seen in figure 8.12. It can be roughly divided into 5 spectral regions: 1) delocalized deformations of the PTCDA backbone, the chromophore. 2) C-H bending 3) C-C stretching, or deformations of the rings 4) C=0 stretching 5) C-H stretching. Although there are a few bands which do not conform to this classification, most modes associated with each spectral region can be generalized. This can be seen in figure 8.12, where these regions are labelled.

There are 10 b_{3u} modes, corresponding to out of plane vibrations of PTCDA. The two highest regions of intensity are the C=C stretching modes (2), and the C=O stretching modes (3), none of which can be b_{3u}. The highest intensity b_{3u} mode is number twenty, with a relative intensity of 1%. The higher intensity in-plane modes, including the stretching vibrations, are distributed between the b_{1u} and b_{2u} symmetry groups.

Scaled Frequency (cm^{-1})	Infrared Intensity (Km/mole)	Relative Intensity	Symmetry	Character
36.4	5.69	0.004	b_{3u}	oop chromophore deformation along long axis
129.7	2.46	0.002	b_{3u}	oop chromophore deformation along short axis
135.3	6.67	0.005	b_{2u}	ip chromophore deformation
183.1	6.78	0.005	b_{3u}	oop chromophore deformation along short axis
206.2	4.88	0.003	b_{3u}	oop chromophore deformation along long axis
333.9	3.16	0.002	b_{2u}	ip chromophore deformation
362.3	38.82	0.027	b_{1u}	O=C-C-C-H scissoring
426.5	12.66	0.009	b_{2u}	ip chromophore deformation
432.3	17.44	0.012	b_{1u}	ip chromophore deformation
491.2	3.90	0.003	b_{1u}	ip chromophore deformation
557.9	11.32	0.008	b_{3u}	oop chromophore deformation
593.4	2.16	0.002	b_{2u}	ip chromophore deformation
621.3	6.14	0.004	b_{1u}	ip chromophore deformation
702.3	58.25	0.041	b_{3u}	oop chromophore deformation with C-H wag
738.2	12.13	0.009	b_{2u}	ip chromophore deformation
742.2	15.84	0.011	b_{3u}	oop chromophore deformation
779.1	18.54	0.013	b_{1u}	ip chromophore deformation
831.7	72.56	0.051	b_{3u}	Fully symmetric C-H wag oop
921.8	2.51	0.002	b_{2u}	H-C-C-H scissoring
954.7	1.39	0.001	b_{3u}	oop C-H wag
1028.6	503.42	0.356	b_{2u}	C-O stretch
1106.5	297.76	0.211	b_{1u}	H-C-C-H scissoring
1126.4	66.41	0.047	b_{1u}	ip C-H wag
1127.8	89.63	0.063	b_{2u}	C-H rocking ip with C-C stretch
1217.7	78.84	0.056	b_{2u}	C-H rocking ip with C-C stretch
1271.9	770.81	0.545	b_{1u}	C-H rocking ip with C-C stretch
1278.6	9.99	0.007	b_{2u}	C-C stretch
1331.0	17.66	0.012	b_{1u}	C-C stretch with C-H wag ip
1386.6	74.74	0.053	b_{1u}	ring deformation with C-H rocking ip
1401.2	19.63	0.014	b_{1u}	ring deformation with C-H rocking ip
1460.7	1.23	0.001	b_{2u}	ring deformation with C-H rocking ip
1495.9	31.23	0.022	b_{2u}	ring deformation with C-H rocking ip
1567.2	32.19	0.023	b_{1u}	ring deformation with C-H rocking ip
1581.6	550.33	0.389	b_{1u}	ring deformation
1581.6	19.49	0.014	b_{2u}	ring deformation
1750.9	740.76	0.524	b_{2u}	C=O stretch
1782.1	1414.26	1.000	b_{1u}	C=O stretch
3097.5	6.73	0.005	b_{1u}	C-H stretch
3104.0	1.41	0.001	b_{2u}	C-H stretch
3121.2	12.35	0.009	b_{2u}	C-H stretch

Table 8.6: Calculated Infrared frequencies and intensities for PTCDA at B3LYP/6-31g(d) level of theory. oop and ip are acronyms designating "out of plane" and "in plane", respectively.
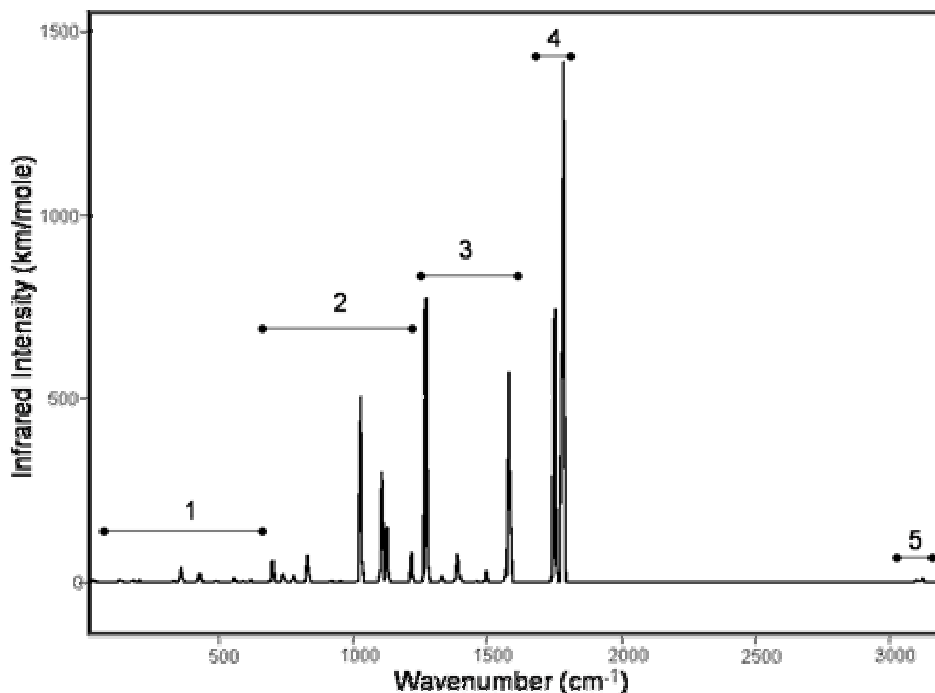
Figure 8.15. Computed infrared spectrum of PTCDA at B3LYP/6-31g(d), with classification of bands according to character.

The quantum mechanical calculations presented in this chapter form a vital part of surface enhanced spectroscopy. *Ab initio* Raman and infrared frequencies, intensities, and symmetry groups are a natural part of vibrational spectroscopy, and a complete vibrational analysis is the usual first step towards understanding the changes in the spectra that may be brought about by packing (alanates), chemical interactions (syringic and p-coumaric acids), and selection rules (PTCDA). The three examples presented here provide the molecular part of the process that includes light, nanoparticles, and molecules, known as surface enhanced spectroscopy.

E. Bibliography

(1)   Moskovits, M. *Reviews in modern physics* **1985**, *57*, 783-826.
(2)   Willets, K. A.; Van Duyne, R. P. *Annual Review of Physical Chemistry* **2007**, *58*, 267-297.
(3)   Aroca, R. *Surface-enhanced Vibrational Spectroscopy*; John Wiley & Sons: Chichester, 2006.
(4)   Long, D. A. *The Raman Effect*; John Wiley & Sons, Ltd: Chichester, 2001.
(5)   Herzberg, G. *Molecular Spectra and Molecular Structure. II Infrared and Raman Spectra of Polyatomic Molecules*; D. Van Nostrand Co., Inc.: Princeton, N.J.. 1945.
(6)   Herzberg, G. *Molecular Spectra and Molecular Structure. I Spectra of Diatomic Molecules.*; 2nd. ed.; D.Van Nostrand Co., Inc: Princeton, N.J., 1950.
(7)   Wilson Jr, E. B.; Decius, J. C.; Cross, P. C. *Molecular Vibrations; The Theory Of Infrared And Raman Vibrational Spectra*; McGraw-Hill: New York, 1955.
(8)   Davydov, A. S. *Quantum Mechanics*; Pergamon Press: Reading, 1965.
(9)   Moskovits, M. *J. Chem. Phys.* **1982**, *77*, 4408-4416.
(10)   Decius, J. C.; Hexter, R. M. *Molecular Vibrations in Crystals*; McGraw-Hill: New York, 1977.
(11)   Tang, J.; Albrecht, A. C. In *Raman Spectroscopy*; Szymansky, H. A., Ed.; Plenum Press: New York, 1970; Vol. 2.
(12)   Pieczonka, N. P. W.; Aroca, R. F. *ChemPhysChem* **2005**, *6*, 2473-2484.
(13)   Ross, D. J.; Halls, M. D.; Nazri, A. G.; Aroca, R. F. *Chemical Physics Letters* **2004**, *388*, 430-435.
(14)   Schlapbach, L. *MRS Bulletin* **2002**, *27*, 675.
(15)   Finholt, A. E.; Bond, A. C. J.; Schlesinger, H. I. *Journal of the American Chemical Society* **1947**, *69*, 1199.
(16)   Shirk, A. E.; Shriver, D. F. *Journal of the American Chemical Society* **1973**, *95*, 5904-12.
(17)   Bogdanovic, B.; Schwickardi, M. *Journal of Alloys and Compounds* **1997**, *253-254*, 1.
(18)   Zaluska, A.; Zaluski, L.; Strom-Olsen, J. O. *Journal of Alloys and Compounds* **2000**, *298*, 125-134.
(19)   Jensen, C. M.; Gross, K. J. *Applied Physics A: Mater. Sci. Processes* **2001**, *72*, 213.
(20)   Gross, K. J.; Guthrie, S.; Takara, S.; Thomas, G. *Journal of Alloys and Compounds* **2000**, *297*, 270-281.
(21)   Vajeeston, P.; Ravindran, P.; Vidya, R.; Fjellvag, H.; Kjekshus, A. *Applied Physics Letters* **2003**, *82*, 2257.
(22)   Gross, K. J.; Thomas, G. J.; Jensen, C. M. *Journal of Alloys and Compounds* **2002**, *330-332*, 683-690.
(23)   Temme, F. P.; Waddington, T. C. *Journal of the Chemical Society, Faraday Transactions 2: Molecular and Chemical Physics* **1973**, *69*, 783-90.

(24)   Shurvell, H. F.; Brown, R. J. C.; Fredericks, P. M.; Rintoul, L. *Journal of Raman Spectroscopy* **2001**, *32*, 219.

(25)   Frisch, M. J.; Trucks, G. W.; Schlegel, H. B.; Scuseria, G. E.; Robb, M. A.; Cheeseman, J. R.; Zakrzewski, V. G.; Montgomery, J. J. A.; Stratmann, R. E.; Burant, J. C.; Dapprich, S.; Millam, J. M.; Daniels, A. D.; Kudin, K. N.; Strain, M. C.; Farkas, O.; Tomasi, J.; Barone, V.; Cossi, M.; Cammi, R.; Mennucci, B.; Pomelli, C.; Adamo, C.; Clifford, S.; Ochterski, J.; Petersson, G. A.; Ayala, P. Y.; Cui, Q.; Morokuma, K.; Malick, D. K.; Rabuck, A. D.; Raghavachari, K.; Foresman, J. B.; Cioslowski, J.; Ortiz, J. V.; Stefanov, B. B.; Liu, G.; Liashenko, A.; Piskorz, P.; Komaromi, I.; Gomperts, R.; Martin, R. L.; Fox, D. J.; Keith, T.; Al-Laham, M. A.; Peng, C. Y.; Nanayakkara, A.; Gonzalez, C.; Challacombe, M.; Gill, P. M. W.; Johnson, B.; Chen, W.; Wong, M. W.; Andres, J. L.; Gonzalez, C.; Head-Gordon, M.; Replogle, E. S.; Pople, J. A.; Gaussian, Inc.: Pittsburgh PA, 1998.

(26)   Becke, A. D. *Journal of Chemical Physics* **1993**, *98*, 5648.

(27)   Lee, C.; Yang, W.; Parr, R. G. *Physical Review B* **1988**, *37*, 785.

(28)   Francl, M. M.; Petro, W. J.; Hehre, W. J.; Binkley, J. S.; Gordon, M. S.; DeFrees, D. J.; Pople, J. A. *Journal of Chemical Physics* **1982**, *77*, 3654.

(29)   Hehre, W. J.; Ditchfield, R.; Pople, J. A. *Journal of Chemical Physics* **1972**, *56*, 2921.

(30)   Asciutto, E.; Crespo, A.; Estrin, D. A. *Chemical Physics Letters* **2002**, *353*, 178-184.

(31)   Frisch, M. J.; Trucks, G. W.; Schlegel, H. B.; G. E. Scuseria; Robb, M. A.; Cheeseman, J. R.; Jr., J. A. M.; Vreven, T.; Kudin, K. N.; Burant, J. C.; Millam, J. M.; Iyengar, S. S.; J. Tomasi; Barone, V.; Mennucci, B.; Cossi, M.; Scalmani, G.; N. Rega; Petersson, G. A.; Nakatsuji, H.; Hada, M.; Ehara, M.; K. Toyota; Fukuda, R.; Hasegawa, J.; Ishida, M.; Nakajima, T.; Honda, Y.; Kitao, O.; Nakai, H.; Klene, M.; Li, X.; Knox, J. E.; Hratchian, H. P.; J. B. Cross; Bakken, V.; Adamo, C.; Jaramillo, J.; Gomperts, R.; R. E. Stratmann; Yazyev, O.; Austin, A. J.; Cammi, R.; Pomelli, C.; J. W. Ochterski; Ayala, P. Y.; Morokuma, K.; Voth, G. A.; Salvador, P.; Dannenberg, J. J.; Zakrzewski, V. G.; Dapprich, S.; Daniels, A. D.; Strain, M. C.; Farkas, O.; Malick, D. K.; Rabuck, A. D.; Raghavachari, K.; Foresman, J. B.; Ortiz, J. V.; Cui, Q.; Baboul, A. G.; Clifford, S.; Cioslowski, J.; Stefanov, B. B.; Liu, G.; Liashenko, A.; Piskorz, P.; Komaromi, I.; Martin, R. L.; Fox, D. J.; Keith, T.; Al-Laham, M. A.; Peng, C. Y.; Nanayakkara, A.; Challacombe, M.; Gill, P. M. W.; Johnson, B.; Chen, W.; Wong, M. W.; Gonzalez, C.; Pople, J. A.; Gaussian Inc.: Wallingford Connecticut, 2004.

(32)   Irikura, K. K.; Johnson, R. D. I.; Kacker, R. N. *Journal of Physical Chemistry A* **2005**, *109*, 8430-8437.

(33)   Hay, J. P.; Wadt, W. R. *Journal of Chemical Physics* **1985**, *82*, 270.

(34)   Scott, A. P.; Radom, L. *J. Phys. Chem.* **1996**, *100*, 16502.

CONCLUSION

The study of the localized surface plasmon resonances, known as the field of plasmonics, is an exciting mix of the old and the new. The basic theory has been around for a century, but it is only with modern technology that the experiment and theory have blossomed. The basic tools of plasmonics is classical electrodynamics, but the understanding and visualization of the plasmon comes from rigorous and high level computation, made possible by modern computing power. At the same time, there is unprecedented development of nanoparticle synthesis methods, both chemical and physical, as well as a host of scanning probe microscopy methods, electron microscopy and near field microscopy that have sufficient resolution to be able to detect and characterize these nanostructures. Experimentally, plasmon resonances of a single nanoparticle have been measured and the near field of nanostructured materials can be probed. The experiments are also pointing to the unique electromagnetic properties of aggregated nanostructures, nanoholes and nanojunctions. The latter is an enormous challenge to advance our understanding of these phenomena. Clearly, experiment and theoretical modeling implemented through computation are progressing together at a rapid pace.

Surface-enhanced spectroscopy combines three elements: the electromagnetic radiation, the molecular system and the nanostructure. The interaction of the electromagnetic radiation with the molecular system leads to the molecular spectra. The computational tools for this task has been used and illustrated for a variety of molecular systems and clusters. The interaction of electromagnetic radiation with nanostructures has been approached using classical electrodynamics to account for the enhanced properties in the near field and the far field (scattering, extinction and absorption). Here, a set of programs for the computational work were developed in-house and they are an important part of the results of this dissertation.   While this work can be summarized well by the title, the problem of optical properties of nanoparticles does not have a "one size fits all" solution. Spatial descritization methods such as DDA certainly

have a place, they represent the ability to model, although some fundamental features of the physical phenomena may be lost in the drive to provide model results. The Mie solution, and variations upon it presented here, provides a sound theoretical basis, although these theories themselves are not without serious limitations. The basic notion of this work was to attack the problem from both of these directions, and to develop a continuum of techniques for the understanding of plasmon resonances properties.

The difficulty is further compounded when studying the coupling of the molecule with the nanostructured material under the excitation of the electromagnetic radiation: the case of surface enhanced vibrational spectroscopy. While a molecular excitation may be treated as a classical oscillator, given a bandshape, and modeled, it is important to look for a better method. Unfortunately, the molecule is a quantum object, and understanding the interaction between a particle containing millions of atoms, and perhaps tens of millions of electrons, and a molecule is not possible within a quantum framework. While there have been studies of molecule-small cluster interactions,[1,2] these are only the beginning of what is required to treat nanoparticle-molecule interactions in a consistent way. Rather than attempt to treat them together, in this work, the molecule and the particle are treated separately: the particle through classical electrodynamics, obtaining field enhancements, and the molecule through quantum optics or quantum chemistry. The use of quantum chemistry reveals changes in the spectra due to chemical effects, while the quantum optics provides a framework for understanding the spectrum within a unified formulation including both electronic and vibrational transitions.

The use of the exact methodology here has been employed to model nanoshells grown specifically as SERS substrates[3], and as well, the approximate methods, including the use of coupled dipole equations to treat SERS due to interacting particles[4]. In addition, the use of quantum chemical methods is a valuable aid to the understanding of vibrational spectra of a variety of molecules[5,6], and enhanced spectra, especially detailing the additionally

complexity brought about by considering surface selection rules[7,8], effects of clustering[9], and adsorption to a metal[10].

Surface enhanced spectroscopy is enjoying an exponential growth, and its applications encompass biology, medicine, chemistry, physics and materials science. The analytical applications in trace analysis and single molecule detection are flourishing, and at the same there are valuable contributions to basic science, particularly in the development of macroscopic physics. Manipulating molecules and nanostructures is now a reality. However, there is a new physics in the nanometer length scales, new properties and many physical and chemical concepts of macroscopic behaviour waiting to be redefined. With the new developments in instrumentation and theory, the increasing research efforts in the nanoscale seems to indicate that the future looks bright indeed.

A. Bibliography

(1)   Cilpa, G.; Guitou, M.; Chambaud, G. *Surface Science* **2008**, *602*, 2894-2900.

(2)   Gruene, P.; Fielicke, A.; Meijer, G.; Rayner, D. M. *Physical Chemistry Chemical Physics* **2008**, *10*, 6144-6149.

(3)   Alvarez-Puebla Ramon, A.; Ross Daniel, J.; Nazri, G. A.; Aroca Ricardo, F. *Langmuir* **2005**, *21*, 10504-8.

(4)   Ross, D. J.; Rubim, J. C.; Pieczonka, N. P. W.; Aroca, R. F. *Society of Automotive Engineers, [Special Publication] SP* **2008**, *SP-2177*, 79-86.

(5)   Haro, M.; Ross, D. J.; Oriol, L.; Gascon, I.; Cea, P.; Lopez, M. C.; Aroca, R. F. *Langmuir* **2007**, *23*, 1804-1809.

(6)   Jalilehvand, F.; Mah, V.; Leung Bonnie, O.; Ross, D.; Parvez, M.; Aroca Ricardo, F. *Inorganic chemistry* **2007**, *46*, 4430-45.

(7)   Aroca, R. F.; Ross, D. J.; Domingo, C. *Applied Spectroscopy* **2004**, *58*, 324A-338A.

(8)   Ross, D.; Aroca, R. *J. Chem. Phys.* **2002**, *117*, 8095-8103.

(9)   Ross, D. J.; Halls, M. D.; Nazri, A. G.; Aroca, R. F. *Chemical Physics Letters* **2004**, *388*, 430-435.

(10)   Clavijo, R. E.; Ross, D. J.; Aroca, R. F. *Journal of Raman Spectroscopy* **Accepted**.

APPENDICIES

A. Coupled Dipole Equation Program for C++.

```
//Uses c++ due to the math library.  make sure to run c++.
//compiler name is g++ on most linux machines.
//This version is for the non-static case.
//VERSION 2.2.
#include<stdio.h>
#include<stdlib.h>
#include<cmath>
#include<complex>
#include <time.h>
using std::complex;
//long double inner_prod(complex<long double> *a,int size);
int main(void)
{
const long double pi=3.14159;
//Variable Definition
time_t start,end;long double dif;
int N;
int alpha;int beta;
int dim_a;int dim_b;
long double R_diff[3];
long double R_abs;
long double E[3];
long double n[3];
long double E_3_mag_sq;
int i;int j;int wavelengther;
int wavelengths;
time (&start);
//File operations.
FILE *input;FILE *output;

if ((input=fopen("input.txt","r"))==NULL)
      printf("Unable to open input deck\n Please see readme.");
else
{
if ((output=fopen("output.txt","w"))==NULL)
      printf("Unable to open output file.  \n Please see readme.");
else
{
printf("Welcome to Daniel's CDE program\n");
fprintf(output,"Welcome to Daniel's CDE program\n\n");
fprintf(output,"This Program is the Property of Daniel J. Ross,
Theoretician of Theoreticians.\n");
fprintf(output,"Look on This Program, Ye Experimentalists, and
Despair.\n\n");
//Read all variables from input deck.
//Number of particles.
fscanf(input, "%d\n",&N);
fprintf(output,"Number of particles=%d\n\n",N);
//Can now define everything that depends on the number of particles.
long double R[N][3];
complex<long double> E_3N[3*N];
complex<long double> x_old[3*N];
fprintf(output,"      Particle Positions\n");
fprintf(output,"    x        y        z\n");
//Positions of particles.
for (i=0;i<N;i++)
      {
      fscanf(input, "%Lf%Lf%Lf",&R[i][0],&R[i][1],&R[i][2]);
      fprintf(output,"%Lf %Lf %Lf \n", R[i][0],R[i][1],R[i][2]);
      }
```

```
//E-field in 3 space.
fscanf(input,"%Lf %Lf %Lf",&E[0],&E[1],&E[2]);
fprintf(output,"\nEfield in 3 space = %Lf %Lf %Lf\n",E[0],E[1],E[2]);
//n in 3 space (unit vector of k)
fscanf(input,"%Lf %Lf %Lf",&n[0],&n[1],&n[2]);
fprintf(output,"\nUnit propogation vector in 3 space = %Lf %Lf
%Lf\n",n[0],n[1],n[2]);
//read in polarizability and wavelength.  First read in number of
frequencies.
fscanf(input,"%d",&wavelengths);
fprintf(output,"number of wavelengths = %d\n\n",wavelengths);
fprintf(output,"Extinction coefficient (cm^2) and wavelength (nm)\n");
printf("\nStarting CG algorithm.  Please be patient.\n\n");
for (wavelengther=0;wavelengther<wavelengths;wavelengther++)
        {
       double pol_r;double pol_i;double lambda;
       fscanf(input,"%lf %lf %lf",&pol_r,&pol_i,&lambda);
       //calculate inverse polarizability directly.
       complex <long double> pol(pol_r/(pol_r*pol_r+pol_i*pol_i),-
pol_i/(pol_r*pol_r+pol_i*pol_i));
       //fprintf(output,"\nFirst frequency at Polarizability = %lf+%lfI\n
at wavelength %lf nm\n", real(pol),imag(pol),lambda);
       long double k1=2*pi/lambda;
       complex <long double> C[3*N][3*N];
       long double k_r;
       //Build the interaction matrix.
       for (i=0;i<N;i++)
               {
               complex <long double>
exponent_term1(0.0,k1*n[0]*R[i][0]+k1*n[1]*R[i][1]+k1*n[2]*R[i][2]);
               for (alpha=0;alpha<3;alpha++)
                       {
                       dim_a=3*i+alpha;
                       E_3N[dim_a]=E[alpha]*exp(exponent_term1);
                       for (j=0;j<N;j++)
                               {
                               R_abs=sqrt((R[i][0]-R[j][0])*(R[i][0]-
R[j][0])+(R[i][1]-R[j][1])*(R[i][1]-R[j][1])+(R[i][2]-R[j][2])*(R[i][2]-
R[j][2]));
                               for (beta=0;beta<3;beta++)
                               {
                               //First calculate A and B
                               dim_b=3*j+beta;
                               if (i==j)
                                       {
                                       C[dim_a][dim_b]=0;
                                       }
                               else
                                       {
                                       k_r=k1*R_abs;
                                       if (alpha==beta)
                                               {
                                               R_diff[alpha]=R[i][alpha]
R[j][alpha];
                                               complex <long double>
exponent_term(0.0,k_r);
                                               complex <long double>
A_term(pow(k_r,-1)-pow(k_r,-3),pow(k_r,-2));
                                               complex <long double>
A=A_term*exp(exponent_term);
                                               complex <long double> B_term(-
pow(k_r,-1)+3.0*pow(k_r,-3),-3.0*pow(k_r,-2));
                                               complex <long double>
B=B_term*exp(exponent_term);
```

```
                                                     C[dim_a][dim_b]=k1*k1*k1*(-A-
B*R_diff[alpha]*R_diff[beta]/(R_abs*R_abs));
                                              }
                                       else
                                              {
                                              R_diff[alpha]=R[i][alpha]-
R[j][alpha];
                                              R_diff[beta]=R[i][beta]-R[j][beta];
                                              complex <long double>
exponent_term(0.0,k_r);
                                              complex <long double> B_term(-
pow(k_r,-1)+3.0*pow(k_r,-3),-3.0*pow(k_r,-2));
                                              complex <long double>
B=B_term*exp(exponent_term);
                                              C[dim_a][dim_b]=k1*k1*k1*(-
B*R_diff[alpha]*R_diff[beta]/(R_abs*R_abs));
                                              }
                                      }
                              }
                       }
               }
       }
//fprintf(output,"\nThe interaction Matrix, C\n");
for (i=0;i<3*N;i++)
       {
       for (j=0;j<3*N;j++)
              {
              if (i==j)
                     C[i][j]=pol;
              //fprintf(output,"%Lf %Lfi ",real(C[i][j]),imag(C[i][j]));
              }
       //fprintf(output,"\n");
       }
//fprintf(output,"\n\nEfield in 3N space is:\n");
for (i=0;i<3*N;i++)
       {
       //fprintf(output,"%Lf%+f ",real(E_3N[i]),imag(E_3N[i]));
       }
//fprintf(output,"\n\n");
       //The CG algorithm
       //Variable declaration first.
complex <long double> z[3*N];
complex <long double> x_new[3*N];
complex <long double> w_old[3*N];complex <long double> w_new[3*N];
complex <long double> g_old_part[3*N];complex <long double>
g_new_part[3*N];
complex <long double> g_old[3*N];complex <long double> g_new[3*N];
complex <long double> p_old[3*N];complex <long double> p_new[3*N];
complex <long double> v_old_part[3*N];complex <long double>
v_new_part[3*N];
complex <long double> v_old[3*N];complex <long double> v_new[3*N];
long double alpha_N;
long double alpha_D;
long double alpha;
long double beta_N;
long double beta_D;
long double beta;
complex <long double> x_diff;
if (wavelengther==0)
{
       //fprintf(output,"\n Born guess for first point");
       for (i=0;i<3*N;i++)
              {
```

```
                complex <long double> erect_pol(pol_r,pol_i);
                x_old[i]=erect_pol*E_3N[i];
                /*fprintf(output,"\n%Lf
%Lf\n",real(x_old[i]),imag(x_old[i]));*/
                }
        }
for (i=0;i<3*N;i++)
        {
        z[i]=0.0;
        w_old[i]=0.0;
                for (j=0;j<3*N;j++)
                {
                z[i] += conj(C[i][j])*E_3N[j];
                w_old[i] +=C[i][j]*x_old[j];
                }
        //fprintf(output,"%Lf+%Lf ",real(z[i]),imag(z[i]));
        }
        for (i=0;i<3*N;i++)
                {
                g_old[i]=0.0;
                g_old_part[i]=0.0;
                for (j=0;j<3*N;j++)
                        g_old_part[i] +=conj(C[i][j])*w_old[j];
                g_old[i]=z[i]-g_old_part[i];
                p_old[i]=g_old[i];
                }
        //fprintf(output,"\n\n");
        for (i=0;i<3*N;i++)
                {
                v_old[i]=0.0;
                for (j=0;j<3*N;j++)
                        v_old[i] +=C[i][j]*g_old[j];
                }
        /*fprintf(output,"Punching CG vectors initial vectors in column
format\n");
        fprintf(output,"          x0                    g0                    w0
v0\n");
        for (i=0;i<3*N;i++)
                {
                fprintf(output,"%Lf %LfI  ",real(x_old[i]),imag(x_old[i]));
                fprintf(output,"%Lf %LfI  ",real(g_old[i]),imag(g_old[i]));
                fprintf(output,"%Lf %LfI  ",real(w_old[i]),imag(w_old[i]));
                fprintf(output,"%Lf %LfI  ",real(v_old[i]),imag(v_old[i]));
                fprintf(output,"\n");
                }*/
        int counter=0;
        x_diff=1.0;
        while (real(x_diff)>0.002)
                {
                counter++;
                alpha_N=0.0;
                alpha_D=0.0;
                beta_N=0.0;
                beta_D=0.0;
                for (i=0;i<3*N;i++)
                        {
                        x_new[i]=0.0;
                        w_new[i]=0.0;
                        g_new_part[i]=0.0;
                        g_new[i]=0.0;
                        p_new[i]=0.0;
                        v_new_part[i]=0.0;
                        v_new[i]=0.0;
                        x_diff=0.0;
```

```
        alpha_N+=real(g_old[i])*real(g_old[i])+imag(g_old[i])*imag(g_old[i
]);

        alpha_D+=real(v_old[i])*real(v_old[i])+imag(v_old[i])*imag(v_old[i
]);
                }
        beta_D=alpha_N;
        alpha=alpha_N/alpha_D;
        if (alpha_D==0.0)
                {
                alpha=0.0;
                }
        for (i=0;i<3*N;i++)
                {
                x_new[i]=x_old[i]+alpha*p_old[i];
                w_new[i]=w_old[i]+alpha*v_old[i];
                x_diff+=abs(alpha*p_old[i]);
                }
        for (i=0;i<3*N;i++)
                {
                g_new_part[i]=0.0;
                for (j=0;j<3*N;j++)
                        {
                        g_new_part[i]+=conj(C[i][j])*w_new[j];
                        }
                g_new[i]=z[i]-g_new_part[i];
                }
        for (i=0;i<3*N;i++)
                {

    beta_N+=real(g_new[i])*real(g_new[i])+imag(g_new[i])*imag(g_new[i]
);
                }
        beta=beta_N/beta_D;
        if (beta_D==0.0)
                {
                beta=0.0;
                }
        for (i=0;i<3*N;i++)
                {
                p_new[i]=g_new[i]+beta*p_old[i];
                v_new_part[i]=0.0;
                for (j=0;j<3*N;j++)
                        {
                        v_new_part[i]+=C[i][j]*g_new[j];
                        }
                v_new[i]=v_new_part[i]+beta*v_old[i];
                g_old[i]=g_new[i];//Reassignment of 'new' to old, to
restart iteration.
                v_old[i]=v_new[i];
                x_old[i]=x_new[i];
                w_old[i]=w_new[i];
                p_old[i]=p_new[i];
                }
        /*fprintf(output,"Punching CG vectors vectors at each
iteration, in column format\n");
        fprintf(output,"alpha%d= %Lf, beta%d= %Lf, x_diff=%Lf
\n",counter-1,alpha,counter-1,beta,real(x_diff));
        fprintf(output,"beta_N=%LE beta_D=%LE \n",beta_N,beta_D);
        fprintf(output,"          x%d                    g%d
p%d          w%d
v%d\n",counter,counter,counter,counter,counter);
        for (i=0;i<3*N;i++)
```

```
                    {
                    fprintf(output,"%Lf %LfI
",real(x_old[i]),imag(x_old[i]));
                    fprintf(output,"%Lf %LfI
",real(g_old[i]),imag(g_old[i]));
                    fprintf(output,"%Lf %LfI
",real(p_old[i]),imag(p_old[i]));
                    fprintf(output,"%Lf %LfI
",real(w_old[i]),imag(w_old[i]));
                    fprintf(output,"%Lf %LfI
",real(v_old[i]),imag(v_old[i]));
                    fprintf(output,"\n");
                    }
            fprintf(output,"\n");*/
            }
    long double C_ext_term;long double C_ext;
    C_ext_term=0.0;
    for (i=0;i<3*N;i++)
            C_ext_term+=imag(x_new[i]*conj(E_3N[i]));
    E_3_mag_sq=E[0]*E[0]+E[1]*E[1]+E[2]*E[2];
    C_ext=C_ext_term*8.00000*pi*pi/E_3_mag_sq/lambda/100000000000000;
    //fprintf(output,"The extinction cross section at %Lf is (in cm2):
\n",lambda);
    fprintf(output,"%lf %Le\n",lambda,C_ext);
    printf("The number of iterations at frequency %lf is
%d\n",lambda,counter);
}//This brace closes the frequency iteration.
fprintf(output,"Attempt to have a good day\n");
time (&end);
dif = difftime (end,start);
fprintf(output,"\nThe program took %.2f seconds to run",dif);
printf("Don't look here.  look for output.txt\n");
}//This brace closes the if statement for file closing.
} //This brace closes the if statement for file opening.
return 0;
}
/*long double inner_prod(complex<long double> *a,int size)
{//This function is for the magnitude of the unknown size complex vector
    long double ip=0.0f;
    for (int i=0;i<size;i++)
            ip+=100*real(a[i])*real(a[i])+100*imag(a[i])*imag(a[i]);
    return ip/100;
}*/


//requires input deck in same directory, called input.txt
//input file contains N, blank line, particle list in carts.
//output will be called output.txt
```

B. Mie Scattering, Extinction, and Near Field Calculations in Maple

The purpose of this worksheet is to do Mie calculations for metal
nanospheres. The result is either integrated scattering cross sections,
extinction cross sections, and when the difference is taken, absorption
cross sections. Finally, this also calculates field intensities, both
frequency dependent, and a map over a surface.
The assumptions take here are:

Non-Magnetic material,
Well seperated Spheres.

Also, if the size factors get too big, the calculation will start taking
long periods of time, but this program is very useful for spheres in the
nm range, for optical wavelengths.
```
> restart;
```
We define the region of interest, v is in nm.We define the particle
size, the index of refraction of the host medium. Then bring in the
dielectric function, and take the square root to get the index of
refraction. Also compute all size factors, and set the number of terms
for convergence, from B&H.
```
> reader:=readdata("c:/daniel/input
data/silveruv.int",2):vstart:=350;vstop:=700;radius:=10;N0:=1;for v from
vstart to vstop do e1:=reader[v-199,1]+I*reader[v-
199,2];m1[v]:=sqrt(e1)/N0;k[v]:=evalf(2*Pi*N0/v);x1[v]:=k[v]*radius;mx[v
]:=x1[v]*m1[v];od:x_max:=k[vstart]*radius;nend:=round(x_max+4*x_max^(1/3
)+1);
```
Define the Associated Legendre polynomials, and thus the spherical
harmonics by recursion.
```
> LegendreP2[0,0]:=1;LegendreP2[1,0]:=cos(theta);LegendreP2[1,1]:=-
sin(theta);for n from 2 to nend+1 do LegendreP2[n,n]:= simplify((-
1)^n*doublefactorial(2*n-1)*(sin(theta))^n);LegendreP2[n,n-
1]:=cos(theta)*(2*(n-1)+1)*LegendreP2[n-1,n-1];for m from 0 to n-2 do
LegendreP2[n,m]:=simplify(1/(n-m)*(cos(theta)*(2*n-1)*LegendreP2[n-1,m]-
(n+m-1)*LegendreP2[n-2,m]));od;od:for n from 1 to nend+1 do for m from 1
to n do LegendreP2[n,-m]:=LegendreP2[n,m]*(-1)^m*(n-m)!/(n+m)!;od;od;for
n from 0 to nend+1 do for m from -n to n do LegendrePD[n,m]:=
diff(LegendreP2[n,m],theta); dummy[n,m]:=sqrt((2*n+1)/4/Pi*(n-
m)!/(n+m)!)*LegendreP2[n,m]*exp(I*m*phi);dummy2[n,m]:=sqrt((2*n+1)/4/Pi*
(n-
m)!/(n+m)!)*LegendrePD[n,m]*exp(I*m*phi);LegendreP3[n,m]:=unapply(Legend
reP2[n,m],theta);Legendre_o_s[n,m]:=LegendreP3[n,m](theta)/sin(theta);Le
gendre_o_sin[n,m]:=unapply(Legendre_o_s[n,m],theta);LegendreP3D[n,m]:=un
apply(LegendrePD[n,m],theta);Y[n,m]:=unapply(dummy[n,m],theta,phi);YD[n,
m]:=unapply(dummy2[n,m],theta,phi);Y_o_sin_times_m[n,m]:=unapply(m*Y[n,m
](theta,phi)/sin(theta),theta,phi);od:od:
```
Define plane wave expansion coefficients,
```
> theta1:=0;phi1:=0;for n from 1 to nend do for m from -n to n do
C[m,n,1]:=simplify(2*Pi*I^n/n/(n+1)*(-(I*E0[1]-E0[2])*sqrt((n+m+1)*(n-
m))*(-1)^(m+1)*Y[n,-m-1](theta1,phi1)-(I*E0[1]+E0[2])*sqrt((n-
m+1)*(n+m))*(-1)^(m-1)*Y[n,-m+1](theta1,phi1)+2*I*m*E0[3]*(-1)^m*Y[n,-
m](theta1,phi1)));
C[m,n,2]:=simplify(2*Pi*I^n/n/(n+1)*(n*sqrt((n+m+1)*(n+m+2)/(2*n+1)/(2*n
+3))*(I*E0[1]-E0[2])*(-1)^(m+1)*Y[n+1,-m-1](theta1,phi1)-n*sqrt((n-
m+1)*(n-m+2)/(2*n+1)/(2*n+3))*(I*E0[1]+E0[2])*(-1)^(m-1)*Y[n+1,-
m+1](theta1,phi1)-(n+1)*sqrt((n-m-1)*(n-m)/(2*n-1)/(2*n+1))*(-
I*E0[1]+E0[2])*(-1)^(m+1)*Y[n-1,m+1](theta1,phi1)-(n+1)*sqrt((n+m-
1)*(n+m)/(2*n-1)/(2*n+1))*(I*E0[1]+E0[2])*(-1)^(m-1)*Y[n-1,-
m+1](theta1,phi1)+2*I*E0[3]*(n*sqrt((n+m+1)*(n-m+1)/(2*n+1)/(2*n+3))*(-
1)^m*Y[n+1,-m](theta1,phi1)-(n+1)*sqrt((n+m)*(n-m)/(2*n-1)/(2*n+1))*(-
1)^m*Y[n-1,-m](theta1,phi1)));od;od; psi:=(n,x)-
>(sqrt(Pi*x/2)*BesselJ(n+1/2,x)):chi:=(n,x)-
>(sqrt(Pi*x/2)*BesselY(n+1/2,x)): j1:=(n,x)-
>(sqrt(Pi/(2*x))*BesselJ(n+1/2,x)): psiD:=(n,x)-
```

```
>1/4*2^(1/2)/(Pi*x)^(1/2)*BesselJ(n+1/2,x)*Pi+1/2*2^(1/2)*(Pi*x)^(1/2)*(
-BesselJ(n+3/2,x)+(n+1/2)/x*BesselJ(n+1/2,x)): chiD:=(n,x)-
>1/4*2^(1/2)/(Pi*x)^(1/2)*BesselY(n+1/2,x)*Pi+1/2*2^(1/2)*(Pi*x)^(1/2)*(
-BesselY(n+3/2,x)+(n+1/2)/x*BesselY(n+1/2,x)):
xiD:=(n,x)->psiD(n,x)+I*chiD(n,x):
unassign('n','x','dummy');      h1[0]:=unapply(-
I*exp(I*x)/x,x):xi[0]:=unapply(-I*exp(I*x),x):
h1[1]:=unapply(-exp(I*x)*(1+I/x)/x,x): xi[1]:=unapply(-
exp(I*x)*(1+I/x),x):h1D[0]:=unapply(exp(I*x)*(x+I)/x^2,x):xiD[0]:=unappl
y(simplify(h1[0](x)+x*h1D[0]),x): h1D[1]:=unapply(-exp(x*I)*(x^2*I-2*x-
2*I)/x^3,x):xiD[1]:=unapply(simplify(h1[1](x)+x*h1D[1]),x):h1D2[1]:=unap
ply(h1[1](x)+x*h1D[1](x),x):for dummy from 1 to nend do
h1[dummy+1]:=unapply(simplify((2*dummy+1)/x*h1[dummy](x)-h1[dummy-
1](x)),x); xi[dummy+1]:=unapply(simplify(x*h1[dummy+1](x)),x);
h1D[dummy]:=unapply(simplify(1/2*(h1[dummy-1](x)-h1[dummy](x)/x-
h1[dummy+1](x))),x);
xiD[dummy]:=unapply(simplify(h1[dummy](x)+x*h1D[dummy](x)),x);
h1D2[dummy]:=unapply(simplify(h1[dummy](x)+x*h1D[dummy](x)),x):od:
```
Calculate Mie Coefficients. Calculate terms numerically first, as they are repeated. Writing these down seems anticlimatic after the previous definitions, but that work makes this section easy.
```
> for v from vstart to vstop do for n from 1 to nend do
Pmx:=evalf(psi(n,mx[v]));Px:=evalf(psi(n,x1[v]));PDx:=evalf(psiD(n,x1[v]
));PDmx:=evalf(psiD(n,mx[v]));Xx:=evalf(xi[n](x1[v]));XDx:=evalf(xiD[n](
x1[v])); a_mie[v,n]:=(m1[v]*PDx*Pmx-Px*PDmx)/(m1[v]*XDx*Pmx-Xx*PDmx);
b_mie[v,n]:=(m1[v]*Px*PDmx-PDx*Pmx)/(m1[v]*Xx*PDmx-XDx*Pmx);od;od;
```
Calculate the cross sections.
```
> for v from vstart to vstop do for n from 1 to nend do
Cterm[n,v]:=10^(-
14)*evalf(2*Pi/k[v]^2)*(2*n+1)*((abs(a_mie[v,n]))^2+(abs(b_mie[v,n]))^2)
; Exterm[n,v]:=10^(-
14)*evalf(2*Pi/k[v]^2)*(2*n+1)*Re(a_mie[v,n]+b_mie[v,n]);od;
unassign('dummy');Csca[v]:=sum(Cterm[dummy,v],dummy=1..nend);Cext[v]:=su
m(Exterm[dummy,v],dummy=1..nend);Cabs[v]:=Cext[v]-
Csca[v];od:Sca_plot:=[seq([v,Csca[v]],v=vstart..vstop)]:Ext_plot:=[seq([
v,Cext[v]],v=vstart..vstop)]:Abs_plot:=[seq([v,Cabs[v]],v=vstart..vstop)
]:
> plot([Ext_plot,Sca_plot,Abs_plot]);
>writedata("E:/diss/organized/5_results/Mie_isolated/silver_30nm_ext.prn
",Ext_plot,float);writedata("E:/diss/organized/5_results/Mie_isolated/si
lver_30nm_sca.prn",Sca_plot,float);writedata("E:/diss/organized/5_result
s/Mie_isolated/silver_30nm_abs.prn",Abs_plot,float);
```
Field Spectra Calculations. Choose the point of interest, and the electric field. The light, by default, is from the z, which is assumed. The field is calculated only the xy plane.
```
>with(LinearAlgebra):unassign('dummy');dimen:=sum(2*dummy+1,dummy=1..nen
d);E0:=Vector(3,[1,0,0]);point_of_int:=Vector(3,[radius,0,0]);rf:=Norm(p
oint_of_int,2);phi:=arctan(point_of_int[2],point_of_int[1]);theta:=Pi/2;
spher_to_cart:=Matrix(3,[[sin(theta)*cos(phi),cos(theta)*cos(phi),-
sin(phi)],[sin(theta)*sin(phi),cos(theta)*sin(phi),cos(phi)],[cos(theta)
,-sin(theta),0]]):
for v from vstart to vstop do T[v]:=Vector[row](2*dimen); for p to 2 do
for n to nend do if p=1 then mie_term:=b_mie[v,n];else
mie_term:=a_mie[v,n];fi;for m from -n to n do T[v][dimen*p-
dimen+n*(n+1)+m]:=evalf(mie_term*C[m,n,p]);od;od;od;for n from 1 to nend
do for m from -n to n do
VSH3[v,m,n,1]:=evalf(Vector(3,[0,I*Y_o_sin_times_m[n,m](theta,phi)*h1[n]
(k[v]*rf),YD[n,m](theta,phi)*h1[n](k[v]*rf)]));VSH3[v,m,n,2]:=evalf(Vect
or(3,[n*(n+1)*h1[n](k[v]*rf)/k[v]/rf*Y[n,m](theta,phi),-
h1D2[n](k[v]*rf)/k[v]/rf*YD[n,m](theta,phi),I*Y_o_sin_times_m[n,m](theta
,phi)*h1D2[n](k[v]*rf)/k[v]/rf]));for dummy from 1 to 2 do
VSH3_cart[v,m,n,dummy]:=spher_to_cart
.VSH3[v,m,n,dummy];od;od;od;WE3:=Matrix(2*dimen,3):for p from 1 to 2 do
for n from 1 to nend do for m from -n to n do for dummy from 1 to 3 do
```

```
WE3[dimen*(p-
1)+n*(n+1)+m,dummy]:=simplify(VSH3_cart[v,m,n,p][dummy]);od;od;od;od;Es[
v]:=T[v]
.WE3;Es_mag[v]:=Norm(Es[v],2);od:Es_spec:=[seq([v,Es_mag[v]],v=vstart..v
stop)]:writedata("E:/diss/organized/5_results/Mie_isolated/silver_30nm_f
ield.prn",Es_spec,float);
```
Field Calculations: Map. At a specific frequency, calculate field at
points on a grid. Because of the symmetry, we only need a 1/4 grid.
The radius must be an integer or half integer.
```
> v:=350;T[v]:=Vector[row](2*dimen); for p to 2 do for n to nend do if
p=1 then mie_term:=b_mie[v,n];else mie_term:=a_mie[v,n];fi;for m from -n
to n do T[v][dimen*p-
dimen+n*(n+1)+m]:=evalf(mie_term*C[m,n,p]);od;od;od;unassign('dummy');di
men:=sum(2*dummy+1,dummy=1..nend);E0:=Vector(3,[1,0,0]);for x from 0 to
2*radius do print(x);for y from 0 to 2*radius do
phi:=arctan(y,x);rf:=evalf(sqrt(x^2+y^2));if rf>radius then
spher_to_cart:=evalf(Matrix(3,[[cos(phi),0,-
sin(phi)],[sin(phi),0,cos(phi)],[0,-1,0]])):for n from 1 to nend do for
m from -n to n do
VSH3[v,m,n,1]:=evalf(Vector(3,[0,I*Y_o_sin_times_m[n,m](theta,phi)*h1[n]
(k[v]*rf),YD[n,m](theta,phi)*h1[n](k[v]*rf)]));VSH3[v,m,n,2]:=evalf(Vect
or(3,[n*(n+1)*h1[n](k[v]*rf)/k[v]/rf*Y[n,m](theta,phi),-
h1D2[n](k[v]*rf)/k[v]/rf*YD[n,m](theta,phi),I*Y_o_sin_times_m[n,m](theta
,phi)*h1D2[n](k[v]*rf)/k[v]/rf));for dummy from 1 to 2 do
VSH3_cart[v,m,n,dummy]:=spher_to_cart
.VSH3[v,m,n,dummy];od;od;od;WE3:=Matrix(2*dimen,3):printlevel:=1;for p
from 1 to 2 do for n from 1 to nend do for m from -n to n do for dummy
from 1 to 3 do WE3[dimen*(p-
1)+n*(n+1)+m,dummy]:=simplify(VSH3_cart[v,m,n,p][dummy]);od;od;od;od;Es_
vec:=T[v] .WE3;Es_mag[x,y]:=Norm(Es_vec,2);else
Es_mag[x,y]:=0;fi;od;od;for y from 0 to 2*radius do
Eenh_spec1[round(y)]:=[seq([x,Es_mag[x,y]]
,x=0..2*radius)];saver:=cat('"e:/diss/organized/5_results/Mie_isolated/a
g1_377_r30_"',y,".prn");writedata(saver,Eenh_spec1[y],float);od:
```

C. Copyright Releases

234

their respective officers, directors, employees and agents, from and against any and all claims arising out of your use of the licensed material other than as specifically authorized pursuant to this license.

11. No Transfer of License: This license is personal to you and may not be sublicensed, assigned, or transferred by you to any other person without publisher's written permission.

12. No Amendment Except in Writing: This license may not be amended except in a writing signed by both parties (or, in the case of publisher, by CCC on publisher's behalf).

13. Objection to Contrary Terms: Publisher hereby objects to any terms contained in any purchase order, acknowledgment, check endorsement or other writing prepared by you, which terms are inconsistent with these terms and conditions or CCC's Billing and Payment terms and conditions. These terms and conditions, together with CCC's Billing and Payment terms and conditions (which are incorporated herein), comprise the entire agreement between you and publisher (and CCC) concerning this licensing transaction. In the event of any conflict between your obligations established by these terms and conditions and those established by CCC's Billing and Payment terms and conditions, these terms and conditions shall control.

14. Revocation: Elsevier or Copyright Clearance Center may deny the permissions described in this License at their sole discretion, for any reason or no reason, with a full refund payable to you. Notice of such denial will be made using the contact information provided by you. Failure to receive such notice will not alter or invalidate the denial. In no event will Elsevier or Copyright Clearance Center be responsible or liable for any costs, expenses or damage incurred by you as a result of a denial of your permission request, other than a refund of the amount(s) paid by you to Elsevier and/or Copyright Clearance Center for denied permissions.

LIMITED LICENSE

The following terms and conditions apply to specific license types:

15. **Translation**: This permission is granted for non-exclusive world **English** rights only unless your license was granted for translation rights. If you licensed translation rights you may only translate this content into the languages you requested. A professional translator must perform all translations and reproduce the content word for word preserving the integrity of the article. If this license is to re-use 1 or 2 figures then permission is granted for non-exclusive world rights in all languages.

16. **Website**: The following terms and conditions apply to electronic reserve and author websites:
Electronic reserve: If licensed material is to be posted to website, the web site is to be password-protected and made available only to bona fide students registered on a relevant course if:
This license was made in connection with a course,
This permission is granted for 1 year only. You may obtain a license for future website posting,
All content posted to the web site must maintain the copyright information line on the bottom of each image,
A hyper-text must be included to the Homepage of the journal from which you are licensing at http://www.sciencedirect.com/science/journal/xxxxx or, for books, to the Elsevier homepage at http://www.elsevier.com;
Central Storage: This license does not include permission for a scanned version of the material to be stored in a central repository such as that provided by Heron/XanEdu.

17. **Author website** for journals with the following additional clauses:

All content posted to the web site must maintain the copyright information line on the bottom of each image, and

235

From:	Daniel J. Ross [rossn@uwindsor.ca]
Sent:	Wednesday, December 17, 2008 4:36 PM
To:	Office@S-A-S.org
Subject:	copyright release for dissertation?

Society for Applied Spectroscopy,

I am a graduate student at the University of Windsor, working with Ricardo Aroca. I am hoping to secure a copyright release for the material we published in Applied Spectroscopy for use only in my Ph.D. dissertation, specifically:

R. F. Aroca, D. J. Ross, and C. Domingo,
"Surface-Enhanced Infrared Spectroscopy," Appl. Spectrosc. 58, 324A-338A (2004)

What is the process to obtain a copyright release for this work? Going through the links on your website leads me to http://www.copyright.com/, and none of the options presented there seem to apply. So I am slightly confused on how to proceed.

Best Regards,
Daniel J. Ross

Daniel J. Ross
email: rossn@uwindsor.ca
University of Windsor,
Department of Physics
Windsor, ON
Canada N9B 3P4 http://www.uwindsor.ca/units/materials-and-surface-science/mass.nsf/
"Before I came here I was confused about this subject.
Having listened to your lecture, I am still confused.
But on a higher level." --Enrico Fermi

Permission granted for the use requested above:
Permission granted this 19th **day of**
Dec 2008. **Full citation required.**

SAS Bonnie A. Saylor, Executive Director

VITA AUCTORIS

NAME:	Daniel Joseph Ross
PLACE OF BIRTH:	Scarborough, Ontario
YEAR OF BIRTH:	1976
EDUCATION	St. Thomas of Aquinas High School, Oakville, Ontario 1993-1995
	University of Windsor, Windsor, Ontario 1995-1999 B.Sc/B. Ed.
	University of Windsor, Windsor, Ontario 2000-2003 M.Sc.
	University of Windsor, Windsor, Ontario 2003-2009 Ph.D.

Refereed Publications

(1)   Cilpa, G.; Guitou, M.; Chambaud, G. *Surface Science* **2008**, *602*, 2894-2900.
(2)   Gruene, P.; Fielicke, A.; Meijer, G.; Rayner, D. M. *Physical Chemistry Chemical Physics* **2008**, *10*, 6144-6149.
(3)   Alvarez-Puebla Ramon, A.; Ross Daniel, J.; Nazri, G. A.; Aroca Ricardo, F. *Langmuir* **2005**, *21*, 10504-8.
(4)   Ross, D. J.; Rubim, J. C.; Pieczonka, N. P. W.; Aroca, R. F. *Society of Automotive Engineers, [Special Publication] SP* **2008**, *SP-2177*, 79-86.
(5)   Haro, M.; Ross, D. J.; Oriol, L.; Gascon, I.; Cea, P.; Lopez, M. C.; Aroca, R. F. *Langmuir* **2007**, *23*, 1804-1809.
(6)   Jalilehvand, F.; Mah, V.; Leung Bonnie, O.; Ross, D.; Parvez, M.; Aroca Ricardo, F. *Inorganic chemistry* **2007**, *46*, 4430-45.
(7)   Aroca, R. F.; Ross, D. J.; Domingo, C. *Applied Spectroscopy* **2004**, *58*, 324A-338A.
(8)   Ross, D.; Aroca, R. *J. Chem. Phys.* **2002**, *117*, 8095-8103.
(9)   Ross, D. J.; Halls, M. D.; Nazri, A. G.; Aroca, R. F. *Chemical Physics Letters* **2004**, *388*, 430-435.
(10)   Clavijo, R. E.; Ross, D. J.; Aroca, R. F. *Journal of Raman Spectroscopy* **Accepted**.

Conference Presentations

(1) Daniel J. Ross, Joel C. Rubim, Nicholas P. W. Pieczonka, and Ricardo F. Aroca. SAE International, Detroit, Michigan, April **2008**. Paper 2008-01-1267.
(2) Daniel Ross, Maryam Nazri, Ricardo Aroca and Gholam-Abbas Nazri. MRS spring meeting March 28th, **2005**, San Fransico, Abstract GG1.5
(3) Ross, Daniel J.; Halls, Mathew D.; Nazri, Abbas G.; Aroca, Ricardo F. 87th Canadian Chemistry Conference and Exhibition. May 29th – June 1st, **2004**. London, Ontario. Abstract 00001281.
(4) Daniel J. Ross and Ricardo F. Aroca. 39th IUPAC Congress and the 86th Conference of the Canadian Society of Chemistry. August 10th – August 15th, **2003**. Ottawa, Ontario. Abstract AE.6.P083.
(5) C.J.L. Costantino, S. Hadi, D. Ross, T. Lemma, and R Aroca**.** 84th Canadian Society for Chemistry Conference and Exhibition, May 26-30, **2001**. Montreal, Quebec. Abstract 120.